Non-local Modelling of Radial Transport in the Tokamak Edge and SOL

Theodore Emmanuel Gheorghiu

Doctor of Philosophy

University of York,
Department of Physics, Engineering and Technology

December 2024

Abstract

The Scrape-Off Layer (SOL) is a fascinating region which links the core plasma of the tokamak to the material components of the tokamak device. Understanding transport in this region is essential to the design of fusion devices. The SOL is influenced strongly by conditions at the turbulent edge, and characterised by the presence of non-local phenomena. While the solution of full transport equations of the SOL is possible, these tend to be intensive in both labour and computing time - Simplest possible analytical modelling is then worth pursuing. Advection-Diffusion models have been attempted with limited success - but models which incorporate the statistical behaviour of the non-local phenomena present have been promising.

On this basis, we develop an 'observational' random walk. The key element of this approach is a jump function which determines the probability of a random walker making a particular jump during an observation interval of duration τ. We show that non-Gaussian jump functions result in behaviour that cannot be characterised with an advection-diffusion model, and find evidence that such jump functions may be observed in SOL simulations dominated by coherent structures.

We construct a stochastic flux equation which relates the jump function to the flux. Through use of the general central limit theorem, we prove that in the case that the jump function converges to the Levy-α stable (LαS) distribution, the transport behaviour may be described by a non-local 'fractional-advection, fractional-diffusion' equation (FADE) - of which the classical advection-diffusion equation is just one specific case.

We apply the work to simulations of the 2D SOL. The measured jump functions appear to be inhomogeneous, anisotropic, and non-Gaussian - and indeed, belong to the LαS distribution. Numerical solutions of FADEs obtained from the jump functions match well to the average radial density profiles generated by the 2D SOL simulations.

Declaration

I declare that this thesis is a presentation of original work and I am the sole author. This work has not previously been presented for a degree or other qualification at this University or elsewhere. All sources are acknowledged as references.

Acknowledgements

I have had enormous intellectual fun over the course of this PhD. It is truly a privilege to have been encouraged and supported in the pursuit of research, and I will be forever grateful to those who enabled me - some of whom I must thank explicitly:

This work exists as is thanks to my supervisor Fulvio Militello, with whom it has been a pleasure to formulate ideas and execute research plans - and who I can always turn to for assistance with physical intuition, or to help hammer out useful ideas from my (occasionally) cryptic remarks.

It is thanks to David Dickinson - my supervisor at York - that this thesis makes sense due to his tireless and exacting proof-reading. He has consistently provided much needed perspective in my work, and has always been there to help, as well as reminding me to take holiday.

Of course, it is thanks to the patience and knowledge of Jens-Juul Rasmussen that the project developed as it has - his comprehensive knowledge of what has worked or not worked before has been immensely useful, and we have established a fruitful collaboration which I hope lasts many years.

Thanks to the people at CCFE - to John Omotani and his assistance with high-performance computing and computing in general; to Stefan Mijin and our wide-ranging physics bus conversations which baffle our fellow travellers - and to the members of my TAP panel, Irene D'Amico and István Cziegler, for useful insights and their support.

I owe a huge amount to my family - thank you Mum and Dad for raising me well.

Finally and most importantly: I must thank my wife Emma, who has supported me throughout my PhD - even when I am speaking entirely in indecipherable nonsense.

Contents

List of Figures

List of Tables

1 Introduction

1.1 Motivations for Pursuing Nuclear Fusion as an Energy Source

Nuclear Fusion was first put forward as the source of power for stars in 1920 by Eddington, following Aston's observations of the mass defect between Helium and four Hydrogen atoms [11], and thus started a journey of over a century to take advantage of this energy. For motivation as to the pursuit of fusion power - beyond the sheer Promethean dream of having the power of the stars at our command - I will put forward two primary reasons, both wholly anthropocentric. The first is that we have many problems of our current energy supply. Secondly, we have the longer term concern for the survival of human (and other) life as we know it in a fickle universe; This requires a degree of pragmatism and forward planning to manage appropriately.

The growing population of Earth, and a strong desire for an increase in living standards in many populations undergoing such population increases, is resulting in a substantially increased demand for energy [12]. The current and historical use of fossil fuels has likely resulted in measurable change to the climate, which will result in reduced habitability of various areas internationally, and cause harm to human and animal populations - this is expected to drive human competition for energy sources, land, and other resources in such a manner that international stability may be damaged [13].

The global energy supply in 1973 was 254 EJ, with 87% of that provided by fossil fuels, and had more than doubled to 606 EJ by 2019 - with 80.9% provided by fossil fuels [14]. With current trends and technology, it is expected that emissions and consumption will increase up to 2050, largely driven by increasing demand in non-OECD Asian countries; while renewable energy sources are expected to increase as a proportion of the energy supply, fossil fuels are expected to continue to provide a large proportion [12]. Despite strong commitments by governments at the UN Climate Change Conference in 2015, emissions have continued to grow year on year - the budget for carbon emissions to keep global average temperatures from exceeding 2 degrees above pre-industrial levels by 2100 is shrinking, and substantial action is required [15]. Action is not simply required for environmental reasons, however - fossil fuels are finite by nature, and based on the reserves-to-production ratio and current consumption rates, it is estimated that there is on the order of 50 years availability for both oil and gas, and approximately 140 years for coal [16].

For the full technical assessment of the impact of well-mixed greenhouse gases on the environment, I refer the reader to the International Panel on Climate Change (IPCC) report 2021, which is perhaps the most comprehensive single document on the matter, with over 2400 pages of material [13]. Abridging substantially, there has been an observed increase in global temperatures of approximately 1.25 degrees centigrade since 1850, which cannot be explained solely by variations in solar output and other natural processes. The examination of ice core samples allows us to study the both global temperatures and the concentration of greenhouse gases (GHG) over thousands of years, and finds that these are strongly positively correlated. The IPCC report concludes that enhanced GHG emissions since the start of the industrial age ($\sim$ 1750) have contributed to enhanced global (average) temperatures. The IPCC expects the impact of this to include: A substantial increase in the number and severity of extreme weather events, such as storms, heatwaves, floods and droughts (which have already been observed to occur); sea level rise due to thermal expansion, and the melting of glaciers and ant/arctic ice (which already endangers certain island habitats, which may be seen in chapter 15 of [13]). These are expected to continue to intensify if emissions are not curtailed. If GHG emissions do not peak and begin to decline by 2050, it is very likely that we will see global warming of over 2 degrees in the long term. Due to the chaotic nature of the atmosphere, even relatively small increments in temperature can result in substantial increases in the frequency of extreme events. This presents a threat to global stability, as certain regions are expected to get much more arid and warm, and so less habitable, which is likely to prompt mass population displacement. This may also have a significant impact on agriculture, as crops and livestock are highly dependent on the local water cycle and temperatures.

Fossil fuels, particularly coal, diesel and petroleum, do not combust cleanly - particulates are produced in addition to the greenhouse gases [17], which are a health risk in themselves [18]. These can be categorised in terms of size, and the impact of particulate combustion by-product on health can be investigated. Estimates from the OECD environment directorate estimated that there were on the order of a million latent fatalities in the year 2000 as a direct consequence of airbourne particulates, of which 30% were attributable to energy sources. More recent (2021) analysis of the health impact of particles of size PM2.5 originating solely as fossil fuel combustion products estimates that 8.7 million premature deaths result annually, globally, with a particularly high contribution from east Asia and India [18] - China and India by themselves accounted for 70% of the increase in coal demand in 2021 [16]. If demand for cheap coal continues to increase, we may then expect a corresponding increase in the premature deaths in those nations taking advantage of this energy source.

It is then clear that emissions due to fossil fuel dependence not only have severe environmental impact and thus indirect impact on the population due to sea level rise, extreme weather, etc, but also direct and ongoing health impacts on the population. The current solution would seem to be other sources which are currently available - renewable sources such as wind, and low emission/high energy density sources such as nuclear fission. It may also be necessary to extract GHG's from the environment to actually meet climate targets, for which abundant energy will be required.

Renewable sources in 2019 accounted for approximately 11.4% of global production [14]. The theoretical global capacity for renewable energy generation is significantly larger - projections indicate that by 2027, renewable sources could make up 38% of energy generating capacity. Some of this (especially in Europe) has been driven by a desire to increase energy security - European nations wish to reduce reliance on imported oil [19]. While sources of renewable energy such as wind, solar, hydroelectric, and biofuels provide far less environmentally damaging sources of energy, these can be unpredictable - a reliable and scalable source of energy is required to provide for energy demand when renewable sources are unable to meet it; as such, substantial power storage infrastructure is required to smooth out production variation in wind and solar, which requires investment in technology such as pumped storage and battery storage solutions - technologically, it seems that we already have the capability to accomplish this [20]. However, in order to meet the Paris Agreement's goal of limiting average temperature rise to 2 degrees (Preferably 1.5), substantial changes in investment would have to be made, which has not currently been done. This is addressed in IRENAs 2020 report [20].

Many renewable resource plans feature some reliable power source to provide a baseline level of production. This can be provided by conventional nuclear fission, for a time - The IAEA and NEA report in 2020 makes clear that there are sufficient current uranium reserves to last for 135 years from 2019 at current levels of production and consumption [21] - and that despite the real capability of nuclear fission to provide low carbon power in abundance, in Europe, the actual fission capacity is expected to decline. Nuclear fission carries a risk of the proliferation of nuclear weapons, especially in fuel reprocessing and recycling, and more advanced reactor designs may carry a proliferation risk which requires careful consideration to mitigate [22]. There is also a seeming lack of public awareness of the ability of nuclear fission to assist with reducing greenhouse gas emissions, as well as difficulty in changing public opinion. Nations which use nuclear energy are more supportive generally [23], but due to several high profile nuclear incidents, there is opposition and a negative perception

of nuclear fission - despite the fact that it is typically far safer than fossil fuels, resulting in considerably less latent deaths relative to energy density [24] even when the most severe incidents are included. Ultimately, nuclear fission makes use of finite fissile fuel reserves, and must inevitably be phased out of the energy make up in much the same way as fossil fuels.

It is reasonable to conclude that the energy crisis could be resolved for the near term with current technology, and indeed renewable energy sources are becoming increasingly dominant due to their relatively low costs and abundance. It seems that the primary barrier to resolving the short term energy and environmental crisis is simply a lack of political and financial will [20], about which the pursuit of nuclear fusion can do little - and indeed, it is possible that presenting nuclear fusion as a viable solution to the current energy crisis may dampen motivation to tackle it via other means. That said, there is a real and material logistical requirement to provide a base power supply to supplement renewable energy sources, the role of which is currently filled by nuclear fission. This role is certainly one which nuclear fusion power potentially has the capability to occupy, especially given that supplies of fissile fuel are finite. As such, we have our first compelling reason to develop nuclear fusion - to provide a base power source to supplement renewable power in place of nuclear fission.

But this is very short term thinking. Society as we know it has been able to develop following the last ice age - a period lasting almost 100 millennia, and ending only around 11 millennia ago. The environment can change in ways which fundamentally alter the ability of humans and other species to survive, *through no fault of humanity* - the several last mass extinctions demonstrate this beyond any doubt. If we wish to avoid extinction, we must consider the longer term prospects of humanity, and how they may be ensured. Our species is currently very vulnerable - all humans, our supporting biosphere, reside on a single planet. A single mass extinction event has the potential to eradicate life as we know it; a particularly large asteroid, some solar event, or even a singularity wandering a bit too close to our star system throwing it into chaos - we are fortunate to have evolved in an islet of environmental stability, which cannot be taken for granted. While we have not been the most careful with regards to the exploitation of resources, as demonstrated by the nature of our current energy crisis, humanity is in the unique position of being the only known species which both has the capability to conduct large scale engineering projects such as travelling to nearby celestial bodies, and the imagination to conceive of travelling further afield. If humans wish to continue existing, then we must look to guaranteeing our survival indefinitely. Furthermore, developing the capability to avoid or survive extinction events may in principle benefit our environment; if humanity can mitigate events causing mass extinction, this constitutes an

act of environmental protection. Likewise, if humanity develops the capacity to travel further afield, this also suggests the capability to take samples of our local flora and fauna with us. Successful propagation of such samples elsewhere would likewise constitute a mitigation of extinction risk.

Humans may choose to mitigate extinction events in two ways. *One*, we may cause the extinction event to stop - for example, by causing a small spacecraft to collide with an asteroid, therefore changing its orbit, as demonstrated on the 26th of September 2022 [25] as part of the Asteroid Impact and Deflection Assessment missions [26]; *Two*, we do not put all our eggs in one basket: This can be done by spreading ourselves and our biosphere to other worlds, in other places. We have now found strong evidence for the existence of planets outside our home system, with over 5000 exoplanets identified - two exoplanets of a size similar to Earth have been identified as existing within the habitable zone of their star a mere 16 light-years distant [27], strongly suggesting that there exists a possibility of finding a world humans could live on with relatively little adaptation or terraforming.

Option One may be achievable in part, as demonstrated - however, there are a hideous number of ways for extinction to occur, and it is entirely feasible to consider many which it simply may not be possible to prevent with present technology. Option Two is achievable only once humanity achieves interplanetary and interstellar travel. This is not a fanciful notion. Interstellar travel in a reasonable time does seem viable with current technologies. This is currently being explored in the form of the "Breakthrough Starshot" project, based on using a large laser with output on the order of 70 GW to accelerate a small probe with a laser-sail to $0.2c$; such a probe would reach nearby star-systems on the order of decades [28]. However, to accomplish interstellar travel in reasonable times for a reasonable payload that is several orders of magnitude larger than a small probe requires extreme amounts of energy and very high energy densities: chemical bonds possess energy on the order of 1 eV, and to viably reach the relativistic velocities required for interstellar travel, we would require on the order of 1 GeV per chemical bond [28].

Renewable energy sources do not typically work in space, with the exception of solar power - however, that rapidly becomes less effective with the input falling off with a factor of $\frac{1}{r^2}$ from our Sun - while solar power may in principle be used around other stars, it might be expected that it would provide only a trace amount of power in interstellar space. Chemical propulsion would require prohibitive amounts of fuel, given the energy released from the breaking of chemical bonds. The laser-sail propulsion method outsources the propulsion

method to exterior sources, but requires low mass payloads - while payloads of arbitrary sizes are possible, they fail at the 'reasonable time' constraint; in practice, a payload of 100 Mg would be able to achieve only on the order of 0.002c, which would take substantially more than a human lifetime to reach nearby stars by a factor of 10 or so. Other propulsion methods have been devised based on nuclear fission, first devised by Everett and others in 1955 [29] which essentially consisted of throwing nuclear weapons out of the back of a spaceship and detonating them, culminating in the infamous "Project Orion". Project Orion suggested that it was technically feasible for nuclear pulse propulsion to achieve rapid interplanetary and even interstellar travel with large payloads [30]: It appears that nuclear fission does in fact possess the energy density required to achieve our long term survival goals - however, a major downside is the dependence on fissile materials, which are quite rare in the universe: as mentioned previously, we have current exploitable reserves on Earth for only 135 years, and they are not expected to be particularly more abundant elsewhere in the universe given their expected mechanism of formation. In contrast, nuclear fusion can be fuelled by the most abundant elements and isotopes in the universe, and is capable of releasing substantially more energy than nuclear fission. Nuclear fusion pulsed rockets such as that proposed in "Project Daedalus" are in theory capable of using high-gain fusion pellets to send a payload of 450 Mg on a one-way trip to Barnard's star at $0.12c$, taking only on the order of fifty years [31]. Non-pulsed approaches such as the Bussard ramjet [32] are also, in theory, as capable as the pulsed approach - but again, are heavily contingent on achieving a mastery of nuclear fusion. Fusion based methods allow for feasible interstellar and interplanetary travel - a return trip to Jupiter could take on the order of a few hundred days, in comparison to current, chemically powered missions taking many years, and interstellar missions taking only decades, as opposed to taking tens of thousands of years with chemical propulsion.

There are several fusion reactions, but some of the most energetically favourable are the D-He3 and D-T fusion reactions. If we can achieve D-He3 fusion viably, then we have extensive reserves of fusion fuel throughout the solar system - deuterium abundance on the comet *Rosetta* is three times higher than that in our oceans [33], and it is in high abundance on Jupiter, with 22.5 deuterons per million protium. Helium-3 is likewise present in large quantities on Jupiter [34]. Presuming that Jupiter is typical of gas giants, and that gas giants are relatively common, then we may reasonably infer that we have abundant fuel for fusion throughout the universe.

As such; if we can achieve net-energy positive fusion, and then achieve sufficient mastery of the technology - then we can not only use this to our advantage in the short term, but

in the long term also. Preliminary studies exist indicating that nuclear fusion can make both interplanetary and interstellar travel viable even with large payloads, in timespans shorter than a human lifetime. If this can be achieved and exploited to allow humanity and its supporting ecosphere to expand throughout the galaxy, humanity will have massively increased its chances of long-term survival. This is the second compelling reason to pursue nuclear fusion.

1.2 Thermonuclear Fusion

Nuclear fusion is the process of causing nuclei to come sufficiently close together such that the nuclei merge and so produce different nuclei. A mass defect exists between the nucleons and the nucleus of atoms - that is, atomic nuclei have a mass which is smaller than the sum of the individual nucleons which compose them. This can be interpreted using the concept of mass-energy equivalency, in which we can say that a mass has an energy given by Einstein's equation $E = mc^2$. It has been demonstrated that as a result of this, reactants with fewer nucleons than Fe-56 typically fuse and result in net energy being released (exothermic reactions), while reactants with more nucleons typically result in net energy loss (endothermic reactions). There are a very large number of fusion reactions which are possible, but our interest lies in a small subset of these reactions for reasons which will become clear shortly. We give a selection of reactions, reproduced from [35]:

$$D + Li^6 \longrightarrow 2He^4_{22.4\ MeV} \tag{1}$$

$$D + He^3 \longrightarrow He^4_{3.6\ MeV} + p_{14.7\ MeV} \tag{2}$$

$$D + T \longrightarrow He^4_{3.5\ MeV} + n_{14.1\ MeV} \tag{3}$$

$$He^3 + T \longrightarrow \begin{cases} He^4_{4\ MeV} + p_{4\ MeV} + n_{4\ MeV} & 51\% \\ He^4_{4.8\ MeV} + D_{9.5\ MeV} & 43\% \\ He^5_{1.89\ MeV} + p_{9.46\ MeV} & 6\% \end{cases} \tag{4}$$

In order for nuclei to fuse successfully, the Coulomb barrier must be overcome. This is the electrostatic repulsion between the (positively charged) nuclei. Reacting nuclei must come sufficiently close together such that the strong nuclear force becomes dominant. In order to overcome the Coulomb barrier via collision, from the classical perspective, it is clear that the relative kinetic energy must meet or exceed that exerted by the Coulomb force. From the quantum perspective, since Gamow's discovery of quantum tunnelling, there is a probability of fusion occurring even for lower kinetic energies due to a chance to tunnel through the Coulomb barrier [36] - practically, this can be accounted for in our reaction cross-sections. The most obvious attempt to achieve fusion from the perspective of overcoming the Coulomb barrier is to accelerate an ion beam of reactant at a reactant target. A particularly useful quantity would be the specific reaction rate, R - fusion reactions per volume per time. Ergo, for a beam of density n_1 travelling at velocity v_b, intersecting a target with density n_2, with a reactant interaction cross-section σ_c, then we can show through geometric considerations that:

$$R = n_1 n_2 \sigma_c v_b \tag{5}$$

Unfortunately, the Deuterium-electron cross-section is very high in comparison to reaction cross sections of fusion reactions [37]. In the cases of other fuels, in order to ensure sufficient number of collisions to generate energy, one would require a solid target. This was investigated in the case of $p + B^{11}$ fusion [38] however the proton beam constituents undergo recombination and so lose significant energy - with the challenge of accelerating heavy ions to significant velocities, as well as other losses, beam-target fusion seems inefficient to the point of being nonviable.

The second most obvious attempt to achieve nuclear fusion is then by heating the reactants to very high temperatures, such that the thermal kinetic energy is sufficient to fuse the reactants - this typically results in the creation of a plasma - an ionised gas, locally quasi-neutral, which exhibits collective behaviour due to long-range electromagnetic forces. We

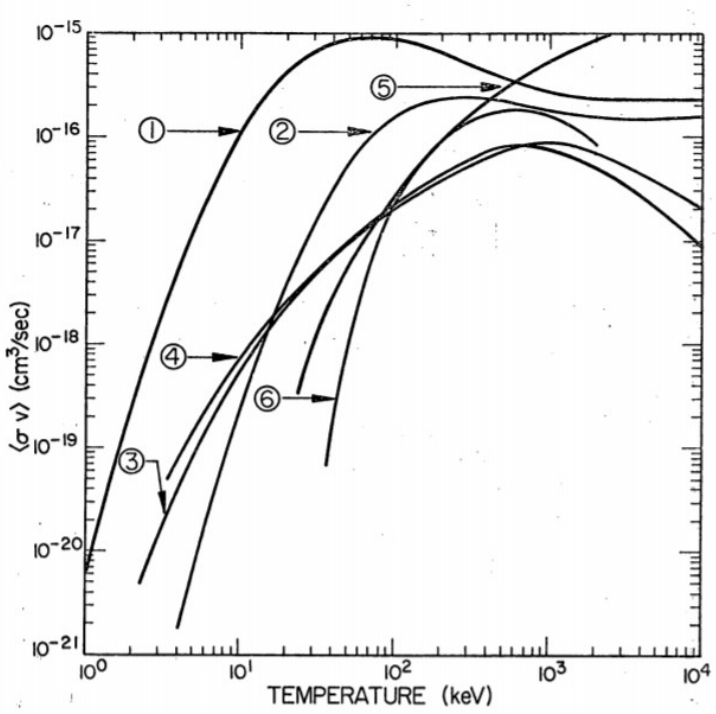

Figure 1: A number of thermo-nuclear cross-sections $< \sigma v >$, reproduced from [1]. 1: D-T reaction, 2: D-He_3 reaction, 3: D-D reaction, 5: T-He_3, and 6: Proton-B_{11}

may still use Eq. 5, but instead perform an averaging procedure over the cross section and velocity distribution[1] - this allows us to have a thermal nuclear cross-section, $\langle \sigma v \rangle$, and so define a thermal reaction rate R_{th}. A selection of thermal cross-sections are given in Fig. 1, over a range of temperatures. It can be seen that the largest reaction cross-section for temperatures below $600\ keV$ is for the Deuterium-Tritium reaction, which has its highest reaction rate at around $60\ keV$.

We can see then that the most readily achievable form of fusion is the D-T reaction, since it has the highest reaction cross-section for lower temperatures. In order to achieve any of the other, lower cross-section reactions, it is reasonable to think that we must first master the D-T reaction.

Importantly, we know it is possible to achieve fusion with net energy yield on Earth - this was first demonstrated with Ivy-Mike in 1952 [39], where a nuclear fission weapon was used to provide the energy for a liquid deuterium fusion stage - later thermonuclear weapons use D-T reactions almost exclusively. This does not yet demonstrate mastery, as this is not

[1]This is typically assumed to be Maxwellian

controlled fusion[2].

There are issues with D-T fusion; while Deuterium is abundant, as discussed in Sec. 1.1, Tritium is unstable and has a half-life of only 12.3 years - as such it must be created, and this can be done by bombarding various things with neutrons. The CANDU reactors produce and sell small quantities of Tritium for use by Fusion-oriented organisations via neutron bombardment of heavy water. It is also possible to use the reaction in Eq. 6 to create Tritium, though other reactions are possible. A review is given in Ref. [40], which discusses Tritium production via a 'breeder blanket', an as-yet untested unit that is proposed to sit within a hypothetical fusion reactor and create the Tritium needed to fuel the fusion reactor. This is of critical importance to reactor design, but will not be a focus of this thesis.

$$Li^6 + n \longrightarrow T + He^4 + 4.8\ MeV \tag{6}$$

The need to produce fuel within the reactor provides many further engineering challenges. While the neutrons are necessary to create fuel and to heat the breeder to produce usable output energy, the high-energy neutrons produced by the D-T reaction damage the reactor structure by displacing atoms[3], and can activate the walls. Returning to our table of thermonuclear cross-sections, the next easiest achieved reaction for much of the $10 - 100\ keV$ is the D-He_3 reaction, which we can see from Eq. 2 produces a high-energy proton rather than a neutron, and requires relatively abundant He_3 rather than Tritium. While it is less obvious as to how useful energy may be extracted from the reactor in this case, this sidesteps many of the challenges presented by use of the D-T reaction and its neutron products, at the expense of requiring greater mastery of fusion reactions. Consequently, as a first step to other forms of fusion, we should first master D-T fusion.

We consider an idealised D-T fusion reactor with no regards as to the interior dynamics. Assuming we have a temperature, $T = T_e = T_i$[4] (in Kelvin), then we can give the internal energy of the plasma to be $E_u = 3nk_BT$, summing over electrons and ion species. We can then define an energy confinement time, τ_E, in terms of the power lost from the reactor, P_{loss}:

[2]clearly a stove is much more desirable than a forest fire in terms of application

[3]The engineering properties of Steels are highly dependent on their microstructural properties

[4]Where T_e and T_i denote electron and ion temperature

$$P_{loss} = \frac{E_u}{\tau_E} \tag{7}$$

Then, in order to remain in thermodynamic equilibrium we should maximise τ_E. From Eqn. 3, we see that the output products are a neutron, with a very low chance of interaction with our D-T mix, and an He_4, or an alpha particle, with energy $E_\alpha = 3.5\ MeV$ - provided this remains confined within the plasma for a sufficiently long time, this can then provide the energy required to balance the energy loss[5]. This begets the concept of *ignition*, a condition achieved when all of the required heating power is provided by the fusion product alpha particles - where this power is simply the product of the reaction rate and the energy output due to that particular reaction. Assuming that $n_T = n_D = \frac{1}{2}n$, we can then find our ignition criterion as:

$$n\tau_E \geq \frac{12k_BT}{\langle\sigma v\rangle\, E_\alpha} \tag{8}$$

This condition tells us that we should maximise $n\tau_E$ while minimising $T/\langle\sigma v\rangle$. A further useful consideration is that $\langle\sigma v\rangle \propto T^2$ for certain ranges of T, which then leads to the concept of the *triple product*, $nT\tau_E$, which is a good benchmark by which to judge experimental fusion performance. For D-T reactions, for $10 \leq T \leq 20\ keV$, $\langle\sigma v\rangle$ may be represented by equation 9, where T is in keV, to an accuracy of around 10% [41].

$$\langle\sigma v\rangle \cong 1.1 \times 10^{-24} T^2\ \mathrm{m^3\,s^{-1}} \tag{9}$$

This suggests that we may reasonably expect ignition conditions for $nT\tau_E \geq 3.1{\times}10^{21}\ m^{-3}keVs$. The ignition condition does not tell us about the power output of the reactor with relation to the input - for that, we must consider the situation in which the power output must also provide the power input, through some kind of conversion process. The current plan is to use the output neutrons to "boil a kettle" - a Carnot-cycle thermodynamic process in which we use steam turbines to generate electricity. This typically has a conversion efficiency on the order of $\eta = 40\%$, so we see we must have substantially higher output to 'waste' [6]. The

[5] In reality, it is not this simple - there are other effects at play

[6] another reason we would like to proceed beyond D-T to D-He_3 reactions is that it is possible to use *Direct Energy Conversion* to convert output directly to electricity, with potentially much higher conversion

break-even condition is met when the (converted) electricity output is capable of providing sufficient energy to make up for the power loss and so maintaining the reactor temperature, given some conversion efficiency, η. Based on this, we may then find Lawson's (break-even) criterion [43] as:

$$n\tau_E = \frac{1-\eta}{\eta}\frac{12k_BT}{\langle\sigma v\rangle E_{D-T}} \tag{10}$$

Which has identical scaling to the ignition criterion in terms of $T/\langle\sigma v\rangle$ and $n\tau_E$, and we note that the break-even is typically substantially easier to achieve than ignition given $E_{D-T} = 17.6\ MeV$ and $E_\alpha = 3.5\ MeV$. To achieve ignition, in terms of the fusion triple product, we can go for a very short confinement time and very high densities and temperatures; or a longer confinement time $\tau_E \sim 1\ s$ with, for example $T \sim 20\ keV$ and $n \sim 1.5 \times 10^{20}\ m^{-3}$.

There are a number of approaches to fusion. The current methods under serious consideration are Inertial Confinement Fusion (ICF), Magnetic Confinement Fusion (MCF), and Magnetised Liner Inertial Fusion (MAGLIF).

ICF is inertia-based, and operates on the principle of achieving very high densities and temperatures for a very short period of time.

It should be noted that ICF's first iteration can be considered to be the Hydrogen bomb - and so once we achieved net gain that way, it was a rational development to move to a non-fission driver, due to the twin benefits of less extreme requirements for power-plants and not having to breach various international treaties. ICF has two main variants - Direct Drive, and Indirect Drive. Both methods typically use a fuel capsule consisting of an exterior ablator layer and filled with fusion fuel, and can use either an array of lasers or an array of heavy ion beams. Direct Drive targets the fuel capsule directly using the beams, ablating the ablator layer - the ablated material rapidly heats and expands, therefore applying a radially inward force to the capsule, thereby causing the remainder of the capsule to implode and the fuel to fuse. Indirect Drive uses an intermediate target - a Hohlraum - constructed from a high-z material such as gold or depleted uranium. The Hohlraum interior is targeted with the lasers, which generates x-rays, which in turn cause the fuel capsule ablator to ablate. Many articles have reported on the National Ignition Facility (NIF) achieving "ignition" in

efficiencies [42] - however, this is also requires development

December of 2022, when as a matter of fact it has achieved target net gain, Q_{target}, equal to 1.54, having produced 3.15 MJ of energy from 2.05 MJ of energy delivered to the target [44] - this is a remarkable achievement and a first for fusion, however this is still a long way off delivering net power from fusion: one must first consider that only $10 - 20\%$ of the laser energy is actually delivered to the capsule [45] - considering this to be the facility laser gain, $Q_{laser} = 0.31$, it is then clear that target gain will have to be significantly higher to actually achieve net power.

MCF devices however, operate on the principle of having longer confinement time with substantially lower $n\tau_E$ than those required for ICF. There are numerous types of MCF devices, but the primary methods in active development are the Tokamak and the Stellarator. Tokamaks such as JET, MAST-U, DIII-D and Alcator-C Mod consist of a toroidal chamber in which plasma resides, which is confined with a toroidal magnetic field and a poloidal magnetic field [46]. The poloidal magnetic field is induced by a central solenoid driving a toroidal current, in a manner not dissimilar to a transformer where one winding is the solenoid and the other the plasma (there are problems with this, but these will be discussed later) - and so achieving confinement. Stellarators such as Wendelstein 7-X and the Large Helical Device differ from Tokamak devices in that no plasma current is externally driven, and instead confinement is achieved solely through use of a geometrically complicated set of magnets. In principle, Stellarators are entirely steady-state devices: this is as opposed to Tokamaks, which must have their poloidal field driven by induction, therefore requiring a time-varying solenoidal current - however, the self-generated "Bootstrap" current is a phenomenon which may be exploited in Tokamak devices to achieve steady state operation. This is only one example of a non-inductive current drive approach; other examples include electron- or ion- cyclotron resonance heating (E/ICRH), and neutral beam injection (NBI), all of which may be used to induce currents and establish particular scenarios in the Tokamak.

MAGLIF, like ICF, is an inertia-based method. It is an evolution of the Z-pinch concept, by which a column of plasma is subjected to a radial Lorentz force through application of a current along the axis - Z-pinch fusion is very vulnerable to "kink" and "sausage" instabilities, which greatly reduce the effective density reachable by the kink. The liner is introduced to suppress the instabilities, and an axial magnetic field is also introduced to suppress radial heat transfer [47, 48].

None of the methods above have succeeded in achieving net gain in a reactor setting, yet substantial progress has been made towards this goal. A main barrier is the creation of

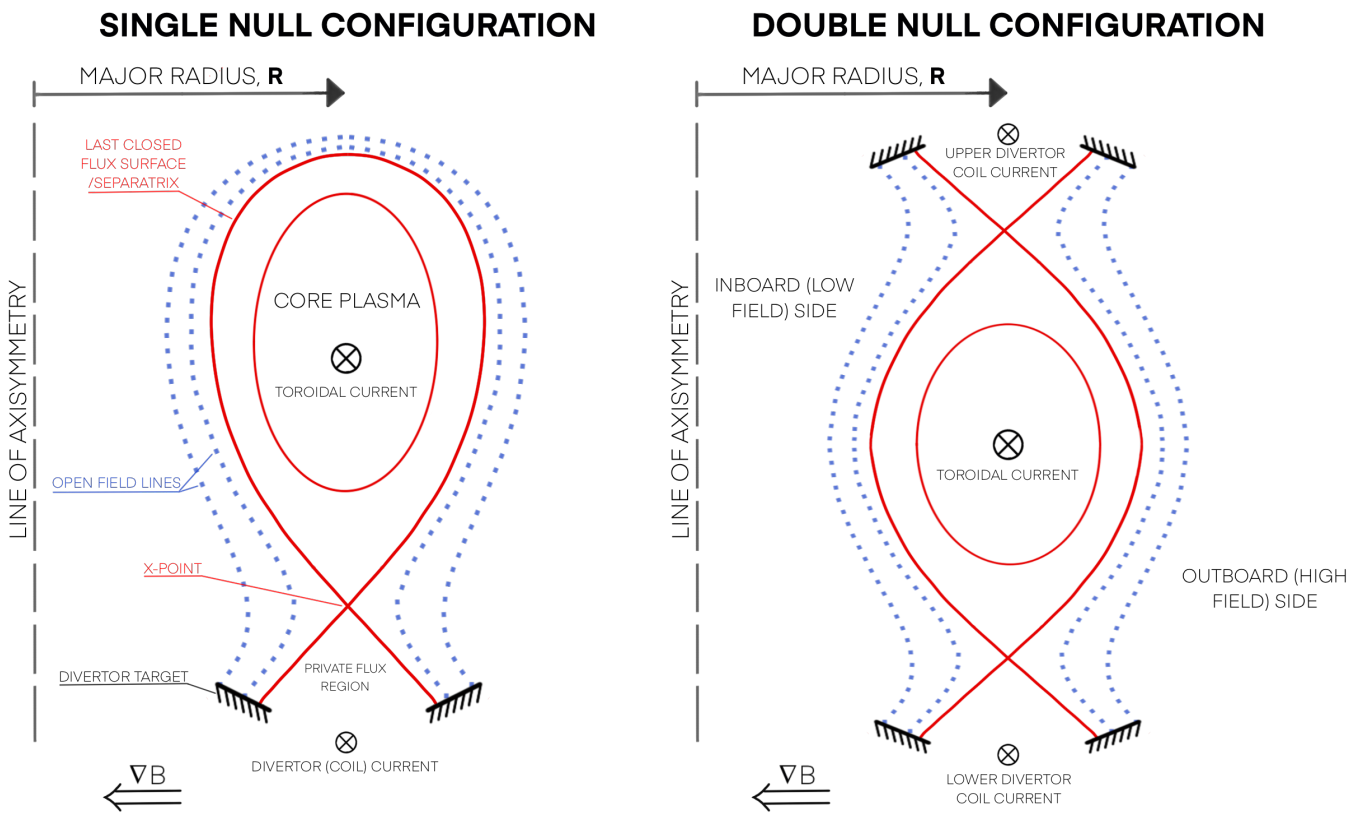

Figure 2: A simplified radial cross-section of two different modern Tokamak configurations. Left: Single-Null Diverted Configuration. Right: Double-Null Diverted Configuration

Tritium - the breeder blanket technology required to satisfy the Tritium fuel requirements is expected to be tested on the ITER tokamak device - which is expected to prove the technology for use: additionally the UKAEA has begun the LIBRTI programme that aims to demonstrate that Tritium breeding is viable [49]. Power extraction from ICF must be engineered around the intrinsically pulsed nature of the technology - Pulsed methods of fusion introduce cyclical thermomechanical stresses into the device [50, 51, 52], which will result in a higher maintenance burden than steady state operation if the effects cannot be mitigated.

In the author's opinion, steady-state solutions are more elegant than pulsed ones when it comes to power generation - with Stellarators and Tokamaks being the most likely avenues to success in that regards. As such we concern ourselves with the Tokamak.

1.3 Tokamak Devices

We consider some key aspects of the Tokamak, creating some general definitions, and introducing key concepts in relation to the Edge, Scrape-off layer and divertor region for broad reference.

The Tokamak was developed in the 1950's, with the first pilot tokamak built in the USSR in 1955 [53]. Following confirmation of the improved performance in comparison to other toroidal devices, the Tokamak saw extensive development. The plasma is magnetically confined by the application of two magnetic fields, a poloidal one and a toroidal one. A stronger B-field is typically good for confinement - due to the plasma being composed of charged particles, they gyrate about the B-field lines: with smaller radius of gyration (gyroradius or Larmour radius, ρ) for lower temperatures and higher B-field. The gyroradius, ρ can be shown to be $\propto B^{-1}$, with relation $\rho = \frac{mv_\perp}{qB}$.

We see in Fig. 2 cross-sections of the single- and double- null configurations of a Tokamak, with devices such as JET using the single-null and devices such as MAST-U capable of operating in both configurations. The major radius, R is measured from the line of axisymmetry, whereas the minor radius r, is measured from the centre of the torus. There are two key geometric areas: areas within the separatrix, or last closed flux surface (LCFS), within which all the magnetic field lines do not interact with material surfaces (are closed); and areas just beyond the separatrix/LCFS, where the magnetic field lines are open and terminate on a material surface. The core plasma is the region in the centre of the torus, in contact only with the plasma edge but otherwise isolated. The edge is a term typically used to refer to the outermost part of the plasma in the core, and is the link between plasma on the open field lines to the core plasma. Plasma on the open field lines flows along the lines towards the material, for reasons we will discuss shortly, and is known as the scrape-off layer (SOL)[7]. The divertor legs are the sections of the SOL below the x-point. As the strength of the magnetic field generated scales with $1/R$, the field is stronger for smaller R - leading naturally to the concept of the inboard/low field side and outboard/high field side.

[7] A name remaining from previous Tokamak designs, in which a component called a limiter was used, which was a physical obstruction limiting the radial extent of the plasma

1.3.1 Confinement

If we consider that the confinement device has a certain scale in the relevant direction, it is obvious that if the gyroradius is larger than that, the particle will collide with the device and so not be meaningfully confined. The size of the gyroradius relative to the device scale is therefore an important quantity to consider in design. Charged particles in a magnetic field do not have any obvious limitation on their movement along the magnetic field [8]. The magnetic field is composed of a poloidal and a toroidal component by design - these have the effect of 'twisting' the field lines such that particles undergo both toroidal and poloidal motion (in addition to guiding centre motion), and allows the definition of a safety factor, q, which must be > 1 in the tokamak edge[9]. The effect of introducing both a poloidal and toroidal magnetic field is to mitigate particle guiding centre drift effects that cause charge separation - and therefore destruction of confinement, if a purely toroidal field was used - are mitigated.

The confinement is not perfect - particles escape confinement: this can be due to collisional diffusion, where a gyrating particle experiences a collision and then continues gyrating, therefore experiencing a net motion and undergoing a random walk process. A more detailed description is available due to neoclassical transport - a specific collisional process that can be shown to occur in magnetic confinement devices in which particles undergo so-called banana orbits due to the magnetic mirror effect; and the effect of instabilities. Instabilities may be small, or much larger, and cause the total collapse of confinement and subsequent extinction of the plasma - large instabilities are avoided as much as possible. The smaller instabilities may be essentially unavoidable and are responsible for creating turbulence in the plasma which vastly enhances cross-field transport; this is one of the forms of transport referred to as "anomalous" in plasma physics - This usage of the term anomalous is inconsistent with its usage in other fields which we will be referring to; in kinetic theory, anomalous transport typically relates to the transport found in the case that particles undergo non-normal transport. For clarity, in this thesis, we will refer to the kinetic 'anomalous transport' as *strange transport* and anomalous transport will refer to the type of enhanced transport caused by microturbulence. The plasma edge is particularly vulnerable to instabilities due to the steep gradients in this region - steep gradients that may very well be necessary to

[8] except where there is variation in the magnetic field in the direction parallel to the field, which results in the confinement of a proportion of particles due to the magnetic mirror effect

[9] q may be considered to be the number of times a confined particle performs a poloidal orbit, per toroidal orbit around the device

ensure a good τ_E, and which may also keep the reactor volume to a reasonable size [54, 55]. Escaped particles carry energy, and consist of "burnt" fuel (Helium 'ash' in the case of a D-T reaction), Deuterium and Tritium, which will interact with material surfaces if allowed to escape unchecked. We would like to minimise the interactions they have with the wall of the device, and prevent both Tritium absorption, and material erosion: Tritium absorption in the wall would be very undesirable, as it would render the wall radioactive, as well as constitute a temporary loss of Tritium inventory; material erosion can result in the injection of high-Z material into the plasma, which can cause significant energy loss due to radiative emission.

There are two major confinement modes in Tokamak operation, which were defined following the discovery of a high-confinement mode, or *H-mode*, in which the τ_e has been observed to increase by a very substantial factor [56] - this H-mode is likely caused by an edge transport barrier associated with the formation of sheared flow in the edge, and results in much higher gradients in the edge of the tokamak [54]. This mode is opposed to low-confinement mode, or L-mode, which has much lower gradients at the edge and in the SOL. While the enhanced τ_e of H-mode is highly desirable for an effective reactor, H-mode is vulnerable to spontaneous breakdown by Edge Localised Modes (ELMs) [57, 55] which may cause damage to the reactor.

In L-mode, the gradients present in the edge are fuel to the fire of turbulence - strong turbulence. There have been many attempts to understand transport in the edge region, as well as the nature of the transport barriers, their formation and dynamics, with many aspects of the physics remaining not fully understood. However, if we are ever to achieve the improvements in Tokamak devices that may possibly allow us to move towards (aneutronic) D-He_3 fusion, it is of great importance to fully understand the physics the various confinement modes.

1.3.2 Plasma-Surface Interactions

The interaction of plasmas and material surfaces is particularly important - as confinement is not perfect, we will always have a certain amount of matter which escapes, and something must be done with it. Where a material surface is placed close to the plasma, it rapidly forms a plasma sheath with a net plasma flow into the sheath - the simplest treatments give a sonic flow into the sheath. The reason for this is that plasma near a conducting material will experience a localised charge separation. This is as a result of the much lower mass of

electrons - they will have a much higher thermal velocity than ions for a given temperature. Electrons will then impact the surface with greater frequency. So, for any degree of surface absorptivity, a negative potential develops at the wall, causing the development of a sheath as the bulk plasma moves to maintain quasi-neutrality. Collision of plasma with material typically causes sputter (amongst other things) - where particles are ejected into the plasma; if they are high-z particles, and they are close enough to be ejected into the core plasma, they will radiate energy - consequently reducing τ_E. As such, we would like to move the material surfaces that escaped plasmas interact with far away from the confined plasma. One option is to make very large reactors, with the plasma held somewhere in the centre, far from any surfaces - however, this is not very practical due to the large fields that would need to be generated for confinement: additionally, 'pinch' effects may occur which may result in transport of impurities into the core, regardless of size. Less impractical options consist of the modern diverted configurations in Tokamak devices - this ensures much greater purity of the core plasma, with much less interaction with things that would otherwise degrade the τ_e.

1.3.3 Energy Exhaust

The material surfaces the scrape-off layer flow towards are named the Divertor, and typically consist of tungsten "cassette tapes" which must be designed to withstand the high heat and particle flux loads resulting from the contact. The location where the separatrix intersect the divertor targets (or other material surfaces if the reactor operation has gone wrong) is known as the *strike point*. Particularly important quantities in the study of the scrape-off layer and its consequences are the *heat-flux width*, λ_q, which is the length scale (in the radial direction) of the heat flux profile in the scrape-off layer; and the *wetted area* of the target, A_w, which is the area in the vicinity of the strike point in which the exhaust power from the reactor, transmitted through the SOL, is deposited. The λ_q is small for many MCF devices, typically on the order of mm or cm [58] at the midplane. Given the expected exhaust power output from the ITER reactor may be on the order of $\sim 100\ MW/m^2$, it is very clear that we must understand the laws governing the heat flux profile, the influences on the wetted area, and how to increase this without also impairing reactor performance. Also important to maintaining the material properties of the divertor targets is minimising the particle flux. High particle flux may alter the atomic structure of the divertor targets, thereby negatively impacting its mechanical properties. There are a number of ways to mitigate the impact of the fluxes to the wetted area, perhaps the most obvious being by

manipulating the magnetic geometry such that the wetted area is larger - the double-null configuration is such a method [59, 58]. Another promising method to mitigate the impact of fluxes is through radiative detachment [60], a process by which the plasma in the divertor leg neutralizes near the divertor target, and the plasma is no longer in direct contact with the target - this significantly reduces fluxes to the targets.

1.3.4 Divertor Regimes

To mitigate the power and particle flux delivered to the wetted area, it may not simply be enough to alter the divertor geometry - the plasma will still be confined by the magnetic fields. However, by making use of radiative, collisional and molecular processes, it is possible to allow the energy in the divertor leg to escape confinement by transferring it into other forms - and thereby reducing the fluxes to the wetted area [58, 61]. These processes are primarily collisional processes, and therefore the collisonality, $\nu*$, typically expressed as a ratio of the relevant spatial scale to the mean free path, plays an important role in determining different regimes of operation in the divertor - there are three key regimes in divertor operation; these are the sheath-limited regime, the conduction-limited regime, and the detached regime [61, 62]. The sheath-limited regime occurs for low collisionality values, in which the plasma maintains a very similar profile throughout the SOL, all the way to the target, and has small gradients throughout. Due to low collisonality, heat is conducted to the wall highly effectively - the only thing separating the plasma from the wall is the sheath, which acts to insulate the wall, and limits the energy flux into the targets; hence the divertor properties are limited by the sheath. The conduction-limited regime occurs when transport to the target is predominantly limited by the (Spitzer-Harm) thermal conductivity of the plasma throughout the divertor and SOL rather then the properties of the plasma sheath at the target - this results in a thermal gradient throughout.

Ideally we wish to distribute energy lost from the core via the SOL and divertor to the maximum spatial extent possible, and so have a regime which allows us to do this. Hence, if we are to protect the material surfaces of the divertor, we must prevent much of the flux from reaching it - and should therefore operate in the high collisionality mode. Unfortunately, the control parameters we have to reach this mode are limited and may impact other aspects of confinement in the core. This is the motivation for operation in the detached regime of divertor operation, occurring with very high collisionality and low temperatures at the divertor target, and characterised by substantial energy transfer from the plasma into radiation

and neutral particles; this primarily reduces the particle fluxes to the surface, which reduces the power dissipated on the plasma surfaces via surface recombination [62].

1.3.5 Coherent Structures, Turbulence and Non-Locality

Understanding the relationships between core properties, edge properties, in the pursuit of maximising τ_E while making conditions tolerable for real engineering materials must be our goal. We have brushed over just a few reasons why this is important. We have already mentioned the problem of anomalous transport, and its likely cause rooted in the turbulence generated by the steep gradients in the edge. Unfortunately for the fusion community, solving or partly solving the problem of strong turbulence appears to be an integral part of creating an operational MCF power plant, and this has substantial consequences - one consequence is a deep and field-wide reliance on numerical simulations of turbulence and transport in order to both understand relevant phenomena and make predictions for future MCF reactors. But the scales involved make realistic simulations prohibitively expensive, and in some cases beyond the current capability of computing resources. It has been known for over 20 years that the radial transport in the SOL may be strongly influenced by the radial propagation of filaments, a type of coherent structure which propagates radially and results in transport characterised by non-local and non-diffusive effects - understanding of which is therefore critical to understanding the balance of transport along the divertor to the target and radially to the wall. Simulations and models of plasma turbulence in the edge and core indicate that coherent structures such as zonal flows form, and that these may be strongly associated with the H-mode of confinement. It has been known that macroscopic coherent structures such as these have been the cause of strange transport in other areas of study. Understanding the impact on transport of coherent structures such as these, as well as their dynamics, may be instrumental in developing simplified, reduced models of transport that allow understanding and prediction without having to resort to expensive simulations.

As such, the goal of this thesis is to understand whether there is scope to develop reduced models of edge and SOL transport, determine how this may be done, and begin doing so.

1.4 Outline of Thesis

This project consists of the development and application of random walk methods to model radial transport in the Scrape-Off Layer. As such, the thesis will be structured in such a way as to provide a narrative of this process.

Chapter 2: We establish the problem we seek to address and identify similar problems in other fields. The edge and Scrape-Off Layer (SOL) of magnetic confinement fusion devices are discussed in order to understand the importance of this region to the dynamics of the MCF device. Following this, we cover in detail the existence of non-local phenomena and non-local transport in this region as well as the experimental evidence for these phenomena. We then discuss theories of turbulence and coherent structures, since this will be required in the work.

Chapter 4: We introduce random walk models. We present a new random walk model, characterised by a jump function with characteristic observation interval. Its development is justified, and it is compared to other random walk models. We consider the construction of a jump function from first principles, and the conditions for stable distributions to occur, as well as demonstrate that we may actually recover the previous random walk models by making the appropriate assumptions about the jump function.

Chapter 5 & 6: We measure the jump function by tracking the motion of Lagrangian tracers undergoing $\mathbf{E} \times \mathbf{B}$ motion on potential fields. We examine this on synthetic turbulence fields expected to generate normal diffusion, which it does so. We then consider the (Charney-)Hasegawa-Wakatani equations as a simple model of drift-wave turbulence present in MCF devices. We are able to demonstrate the existence of anomalous transport when coherent structures are present.

Much of the contents of chapter 3, 4, and 5 are the basis for a manuscript published in the journal 'Physics of Plasmas' [63].

Chapter 6: We construct a stochastic flux equation that defines the instantaneous flux in terms of the jump function and the transported quantity. We demonstrate that it may be used to directly prove Fick's first law and the non-local extensions thereof. The transform pair of the stochastic flux equation proves particularly useful in deriving a (non-local) fractional -advection, -diffusion equation (FADE), which follows from the consideration of the

general central limit theorem, and of which the standard (local) advection-diffusion equation is a specific case.

Chapter 7: We consider the numerical solution of FADEs using explicit schemes. We compare to an example problem and find good agreement. We note particular challenges in considering boundary conditions for non-local equations. However, the work completed in this chapter allows us to continue with the key work of this thesis.

Chapter 8: We consider simulations of the SOL using STORM2D and examine jump functions. These are uniformly non-Gaussian and anisotropic. Fits to the jump functions indicate that they are well-described by a Levy-α Stable distribution, and hence suggest that a FADE could describe transport. We solve the appropriate FADEs and find that they match the mean profiles well in a number of cases.

The contents of chapters 6, 7, and 8 are the basis for a manuscript in preparation for submission.

Chapter 9: We conclude the thesis, and discuss future work.

2 Establishing the Problem

2.1 Overview

We have considered tokamak devices in very broad terms. We will now cover the subjects needed in order to investigate the nature of cross-field transport in the outer edge and Scrape-off Layer (SOL). This is a large field of knowledge and so the full details are beyond the scope of this document. We will consequently abridge somewhat, focusing only on the subjects directly informing our research.

We will first consider the available evidence relating to SOL transport, and what this tells us about the models and the underlying assumptions. Following this, we will introduce the models used to understand transport in the SOL, as well as the underlying physics that has been applied. We will then examine the theory and phenomenology of turbulence and coherent structures in other fluid systems for two reasons: To establish the basics of turbulent theory, and to identify any parallels between our edge/SOL and other fluid systems. This will make clear the reasons for which we have taken the random walk approach to transport.

2.2 Coordinates in a Tokamak Device

Selecting a set of reference coordinates in a Tokamak device is not totally straightforward - full discussion of a variety of coordinate systems that may be used are discussed in "Flux Coordinates and Magnetic Field Structure" [64], which is an invaluable reference on the topic. We use right-handed coordinate systems in this case. Globally, it is useful to use a cylindrical coordinate system R, Θ, Z, where Θ is the toroidal direction - we can also define a poloidal direction, φ. This global coordinate system is shown in figure 3.

At the edge of a device, it is useful to use a field-aligned coordinate system; as the B-field is important in the consideration of numerous effects, we use it as as the basis for the field aligned system. This field-aligned coordinate system is defined in terms of the local B-field and the local radial coordinate, where the radial coordinate specifies a specific flux surface, which then gives us a binormal coordinate which is orthogonal to both - this is typically used when considering "flux tubes" rather than the whole device

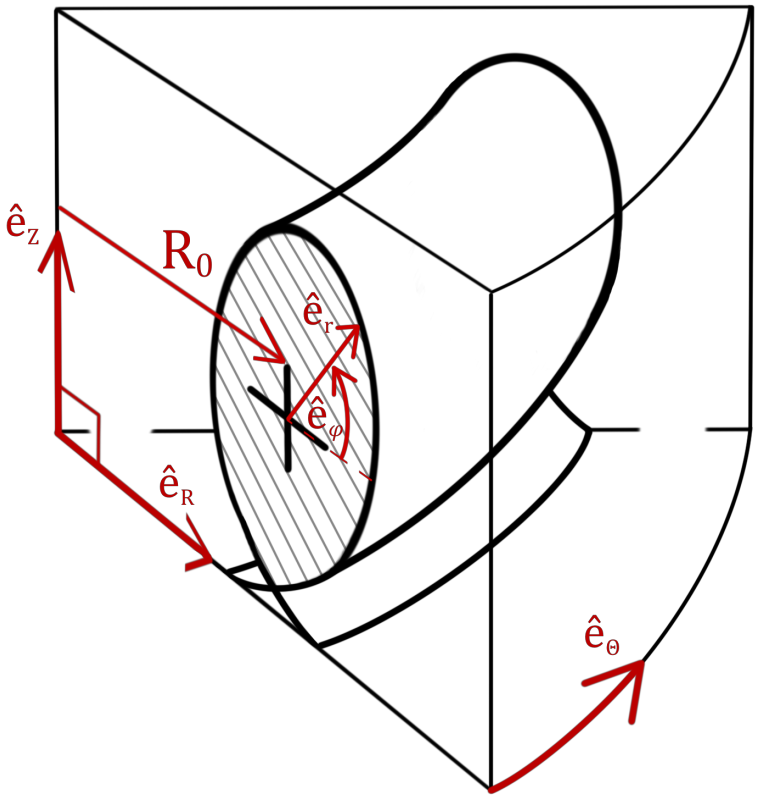

Figure 3: Segment of an idealised single-null diverted Tokamak, with unit vectors for the global cylindrical coordinate system $\hat{e}_R$, $\hat{e}_\Theta$, $\hat{e}_Z$. R_0 denotes the major radius, and the minor radius is located at $r = a\hat{e}_r$

2.3 Importance of understanding Scrape-Off Layer Transport

The Scrape-Off Layer (SOL) is the interface between the core plasma and the plasma facing surfaces, and consequently understanding the balance of radial and parallel transport of both density and temperature is critical. The SOL heat flux width, $\lambda_{q,SOL}$ has been investigated carefully and experimental scaling laws generated from reactor data [65, 66] due to its expected impact on the divertor - projections of the heat flux width are primarily experimental, although significant work has been done (primarily via gyrokinetic simulations) to predict $\lambda_{q,SOL}$ over a wider range of conditions.

Multiple regressions against different machine parameters reveal many possible regression selections which fit data well [65] but it is clear that these will really only be valid for projection if interpolating within the data rather that extrapolating - the strongest correlation appears to be $\lambda_q \propto \frac{1}{B_{pol}}$. Many of the projections for ITER, even with divertor spreading due to flux expansion, yield $\lambda_{q,Div} \sim 1\ mm$ - which would yield a heat flux to the divertor on

the order of $10MWm^{-2}$, a value intolerable to existing engineering materials. Consequently, understanding SOL heat transport is critical to reactor design.

Access to the detached regime is a way of mitigating the extreme loads on the divertor, and it is clear that this, too, is dependent on SOL parameters [67, 68] - as well as neutral gas injection and divertor magnetic topology, of course.

Mass transport is also of importance - the Main Chamber Recycling regime [69] demonstrates that in certain circumstances we may have anomalously high neutral pressure in the main chamber at the plasma facing surfaces as a consequence of anomalous transport of matter in the SOL. Observation of a similar phenomena in JET [70] demonstrate well the importance of understanding such matter transport - It was observed that significant hot-spots were observed on the main chamber wall near the NBI port, which declined only when the NBI was deactivated or the neutral density in the main chamber declined. The explanation for this is that due to the high neutral density near the wall, the NBI beam can undergo partial re-ionization due to collisions with the neutral gas, and the resultant ion beam is deflected into the wall by the device B-field. Neutral density in the main chamber can have an impact on edge dynamics, and consequently understanding radial transport of plasma, and the resultant recycling is important to developing a full picture of the reactor.

A particle within the last closed flux surface would experience oscillations about a magnetic field line, and move relatively unobstructed along it. Charged particles in the open field line region would find themselves oscillating about a open field line - any motion in either direction, at any fraction of the sound speed, c_s, would ensure they rapidly collide with a divertor target (or the sheath, at least, into which it can be demonstrated that particles flow at around c_s [71, 72, 73, 61]). A mechanism by which a particle may cross the separatrix, and move from a closed field line onto an open field line would then result in the particle escaping confinement. The simplest mechanism for a change in a particles field line would be a collision with another particle - repeated collisions between particles would result in a random walk, and so this behaviour is well described by a diffusive process: this is referred to as classical transport [73]. There are other diffusive mechanisms which may be considered, such as those due to neoclassical effects, so it does not seem unreasonable to consider transport into the open field lines to be of a diffusive nature overall.

Unfortunately, this picture of radial transport is significantly less amenable to this form of simplification than we would like, as we will discover.

2.4 Phenomenology of Non-Local Transport in the Edge and Scrape-Off Layer

If we wish to develop reduced models of edge and SOL plasma transport, we must first understand the nature of transport in that area, so from that infer what effects a reduced model should incorporate. The majority of existing models implicitly rely on local features having local effects. Numerical models, by taking appropriate grid sizes and step times such that all relevant phenomena are represented faithfully, may solve local transport equations and still retain non-local effects by propagating features over the whole domain - a very simple example of this is Conway's "game of life" which has purely local laws, and yet the interaction with previously stored states results in long-range phenomena. A more relevant example is in the field of radiation hydrodynamics, where non-locality introduced by radiation transport is incorporated into solvers (note that in this case, there is a scale separation between the local fluid transport and the non-local transport of energy by radiation). In order to have a suitable reduced model of a phenomenon, it is then the case that non-local effects, where present, be properly incorporated into the model in a physical manner. Models incorporating non-local interactions can prove powerful tools to understanding the dynamics of tokamak devices; for example, we may consider the two-point model discussed in section 2.6 to be a reduced model incorporating non-local effects, as it relates conditions at one point upstream to the point downstream, thereby implicitly assuming that the conditions at the target are strongly dependent at conditions at a spatially distant location.

As such, to develop appropriate reduced models, we must first establish a few points: Is there evidence for non-local transport in tokamak devices? And, is the transport on such a scale and of a kind that it cannot be neglected or treated with corrective alterations to existing models? There are several experiments demonstrating the existence of phenomena that indicate non-local transport in the SOL, and in tokamak devices more generally. The first and second parts relate to the SOL exclusively, discussing first filamentary transport in tokamak devices, and then the flux-Gradient relationship in the SOL. In the third and fourth part we discuss first cold-pulse propagation experiments, and then evidence for avalanche-like transport phenomena - both of these are related to the core plasma rather than the edge, and so will be covered only briefly, however will indicate the domain of applicability for aspects of the findings of this project.

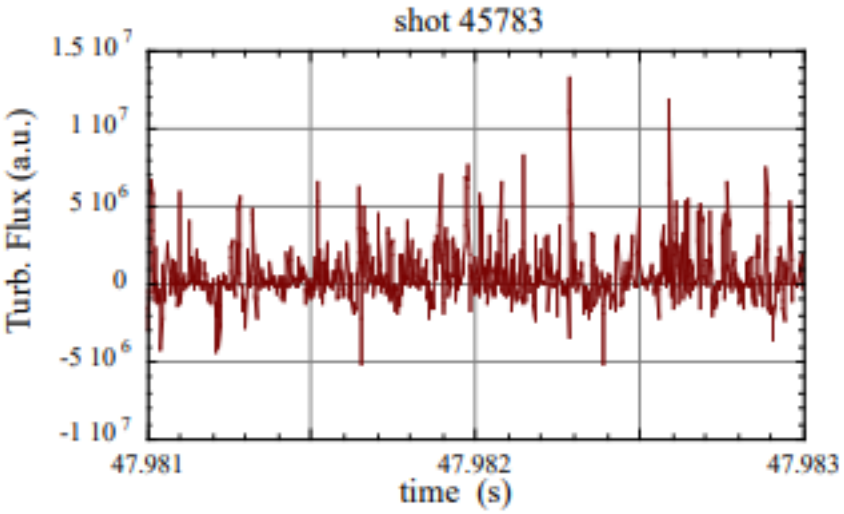

Figure 4: $E \times B$ Flux as measured by a Langmuir probe 2cm inside the JET LCFS on shot 45783. Reproduced from [2]

2.4.1 Filamentary Transport in Tokamak Devices

Examining the nature of turbulence in the edge and SOL then tells us the nature of turbulence in that region. This is of particular importance in determining the radial and parallel transport of matter and energy, as turbulence typically has significant impacts on the nature of transport in general. It has been known for a long time that the edge of tokamak devices are rarely quiescent, and prone to becoming turbulent [74], that the fluxes cannot be explained with the neoclassical theories of transport alone [75], and that the resultant fluxes have a significant impact on confinement time such that these anomalous behaviours cannot be ignored [76].

Diagnostics used to examine edge conditions typically include: vertically- and horizontally-scanning (Langmuir) probes to obtain density, temperature and floating potential profiles; Mach probes to infer plasma velocity from the ratio of ion saturation currents; Thomson scattering diagnostics to infer electron density and temperature profiles; Optical spectroscopy examining D_α and Lyman$_\alpha$ emission may obtain emissivity profiles, which can be used to infer density in some circumstances. Gas puff imaging, where a neutral gas is injected into the plasma along the line of sight of an imaging array can be used to enhance the contrast of features that may be present, and so allow for observation of fine features.

Evidence emerged pre-2000 on numerous devices - tokamaks and stellarators both - that

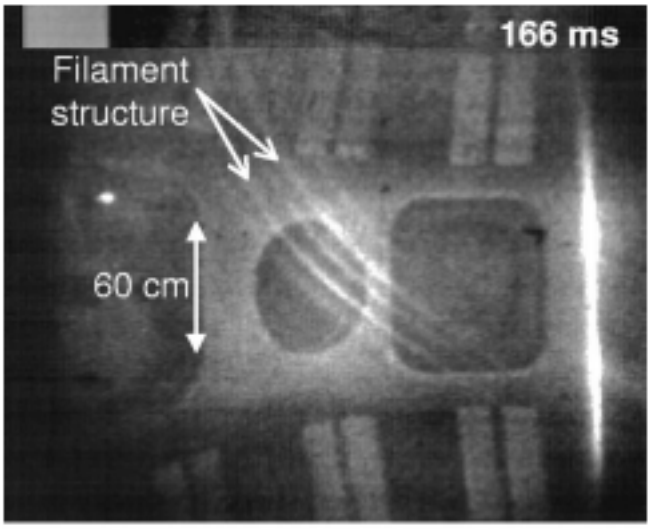

Figure 5: 'Filamentary' structures observed in the poloidal plane of NSTX on discharge 101533. Reproduced from [3]

there were high levels of fluctuation driven transport in numerous devices [2]. It was noted on experiments in JET, DIII-D, ASDEX-U, TCV, MAST (and others!) that the turbulent flux as measured by Langmuir probe arrays was 'bursty' or intermittent [2, 3, 77, 78, 79, 80, 81, 82] and showed very similar characteristics between devices [83]. The intermittency is demonstrated in figure 4, which shows the measured turbulent flux at a point identified to be 2cm inside the LCFS while running in limited configuration. While both positive and negative fluxes are observed, the magnitude of radially outward fluxes significantly exceeds those going inwards; a high degree of coherence in the outward flux was also noted by examining the radial coherence length (Note that the flux is identified from the ion saturation current at a Langmuir probe).

Initial imaging on NSTX supported the intermittency, with highly intermittent 'filamentary' structures observed at the edge of the NSTX device (see figure 5 using gas puff imaging, a finding that has been commonly replicated [3]), and it was found that these were well-aligned with the magnetic field. A particularly interesting finding from Alcator C-Mod obtained using a horizontal scanning probe through the SOL was able to identify distinct regions of intermittent behaviour [77]: in the near-SOL region, where there is a large gradient in the average density profile, there are small, random fluctuations in the ion saturation current; where the gradient of the average density profile begins to become small, the nature of the fluctuations begins to take on the intermittent character observed in JET, with high correlation times likewise also observed. Statistical analysis of the probability density function

(PDF) of the radial flux in TEXTOR confirmed this observation, finding that while inward transport was relatively Gaussian, the flux PDF's had a positive skew overall, indicating a deviation from Gaussian statistics towards more intermittent behaviour, which increased from the near to the far SOL [80].

This last observation naturally leads to a division of the Scrape-Off Layer into the 'Far SOL' dominated by this intermittent and highly correlated behaviour, and the 'near SOL' which has less intermittent/correlated behaviour.

It was also found in numerous devices that transport due to this intermittent behaviour accounted for a high proportion of the radial transport in the SOL in both L- and H- mode discharges, across a variety of machines [84, 7, 79, 80]. In a study investigating "intermittent plasma objects" in DIII-D, it was found that the intermittent structures were responsible for some significant proportion of the radial transport in the far SOL [84], and that these objects were formed at or near the LCFS, with density dependent on the conditions at formation. Radial transport had been higher than expected in a number of devices, and was the cause of routine 'main wall recycling' in Alcator-C mod, and there is strong evidence that this intermittency is responsible.

Krasheninnikov proposed a theory of transport by filamentary structures in the open field line region of Tokamak devices [85], where charge separation driven by the ∇B drift in isolated filaments aligned with the **B**-field (terminating on the wall at each end) (an ambipolar drift) would result in a consequent $E \times B$ drift of the whole filament in the radial direction. It was proposed these filaments originated near the LCFS and were formed by turbulence originating from the edge, and once formed would propagate outwards; this would thus explain the intermittent behaviour of the observed flux, as well as its biased nature in a number of experiments.

Simulations of interchange turbulence and comparison with SOL measurements [86, 4] found excellent agreement with experiment on the TCV device, and appeared to demonstrate that SOL transport was indeed dominated by filaments - and that they are primarily generated by interchange turbulence within the LCFS. Studies on linear devices directly confirmed the existence of filaments far from the confined plasma, travelling at velocity consistent with derived scalings, and demonstrating the skewed statistics observed in Tokamak devices [81]. "Blobs" or "Filaments" have been observed to be ubiquitous in MCF devices where an ambipolar drift is present at the edge of the confined region, and there is a mechanism by

which plasma may be ejected into this region i.e. turbulence - a particularly comprehensive review on the subject is given by D'Ippolito et al. [87]. Moreover, they have been observed in the private flux region as well as in the diverted region of tokamak devices such as MAST [88].

If filaments are formed in the edge, and then propagate radially outward, then this constitutes a form of non-local transport: the transport of heat and particles is dependent on the transport of filaments, which in turn is dependent on conditions in the turbulent plasma at the edge of the device. To confirm this, we examine SOL profiles and the flux-gradient relationship.

2.4.2 The Flux-Gradient Relationship in the SOL

Fick's laws of diffusion have been used to characterise transport for fluids in numerous cases. Fick's first law, equation 11 was initially observed experimentally for characterising concentration gradients, but has seen broad application in fluids; transport due to turbulence can be simply characterised in numerous cases by encoding it with a diffusion coefficient, and this proves useful in analytic models of fluid-surface interactions. Contemporary codes for transport in the field of magnetically confined fusion which are used in the design workflow for future reactors such as ITER include the interaction of plasmas, atomic effects, and molecular effects (such as SOLPS [89]) do not - and indeed cannot - treat turbulence self-consistently, and so must use spatially varying convection and diffusion coefficients to model transport in the regions of interest.

$$\Gamma_n(x,t) = -D\frac{\partial n(x,t)}{\partial x} \tag{11}$$

Fick's first law is a statement that the local flux of a quantity, Γ_n, is proportional to the local gradient of that quantity, n, and the diffusion coefficient, D. It may also be modified to include an advective term, $vn(x,t)$ to represent local bulk motion. As such, there is a flux-gradient relationship which may be defined in systems where the transport can be considered a combination of advective and diffusive terms.

Scrape-Off Layer (SOL) transport has been examined in these terms in order to attempt

to characterise the transport in that region [77, 90, 86, 4, 91, 5], with examination of an "effective" diffusion coefficient, D_{eff}, to parameterize SOL transport. The advantage of this is obvious; if this can be defined and linked to plasma parameters, then we have a reduced model of radial transport.

The flux-gradient relation may be written as:

$$\frac{\Gamma_n(r)}{n(r)} = V_{eff} - \frac{D_{eff}}{n(r)}\frac{\partial n(r)}{\partial r} \tag{12}$$

and we may define a radial density scale length, λ_n, as:

$$\lambda_n \equiv -\frac{n}{\frac{\partial n}{\partial r}} = -\frac{1}{\frac{\partial ln n}{\partial r}} \tag{13}$$

Which is appropriate for use assuming profiles with exponential form - in such cases is λ_n is the e-folding length. This is also easily extended to scale lengths for other quantities

The flux-gradient relation may then be examined directly in numerical or physical experiment, by collecting measurements of the flux, density and then the density gradient at the same point. This has been done using numerically using the ESEL code, which produces output based on a model of simplified interchange turbulence [92], and then compared with the output of conditions in the TCV tokamak [4], which may be seen in figures 6 and 7. Figure 6 demonstrates a high spread in the datapoints taken from TCV during L-mode discharge with filamentary behaviour present - it is difficult to justify the use of the flux-gradient relation to characterise the observed profile, as there is no strong correlation. The same is true for the data plotted in figure 7, which is taken from simulation, which suggests that the same flux may be attributed to quite different gradients. In the case of both graphs it is the *local* density gradient which is related to the *local* flux - these data then indicate that the local flux-gradient relation does not hold, and consequently this is then strong evidence that filamentary transport in the SOL is the cause of non-local behaviour.

Experimental work on Alcator C-mod and DIII-D sheds light on the radial variation of transport coefficients, D_{eff} and V_{eff}, that would be required for the flux-gradient relation to be consistent with data [77, 90]. The coefficients would both have to steadily increase

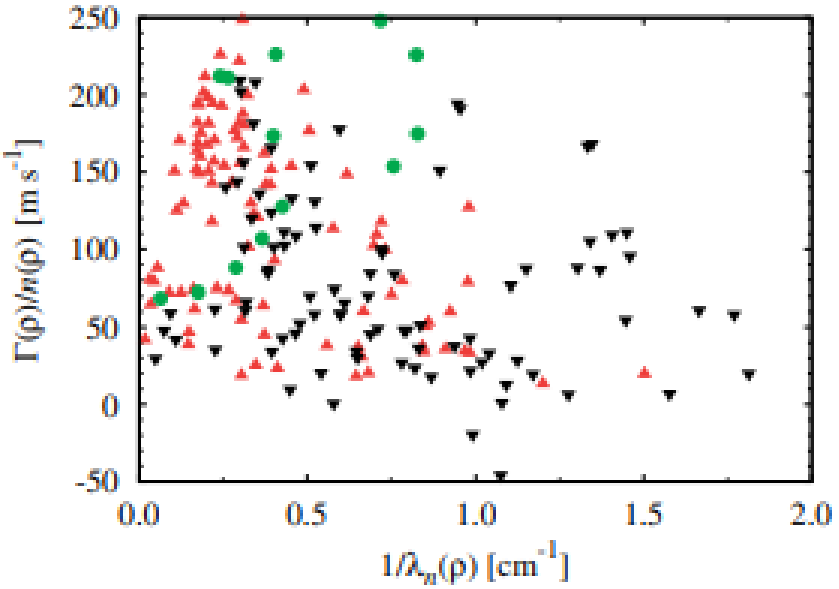

Figure 6: Flux-gradient plot for Low-density TCV discharge (black), high-density TCV discharge (red), and for ESEL with the same conditions (green). Reproduced from [4].

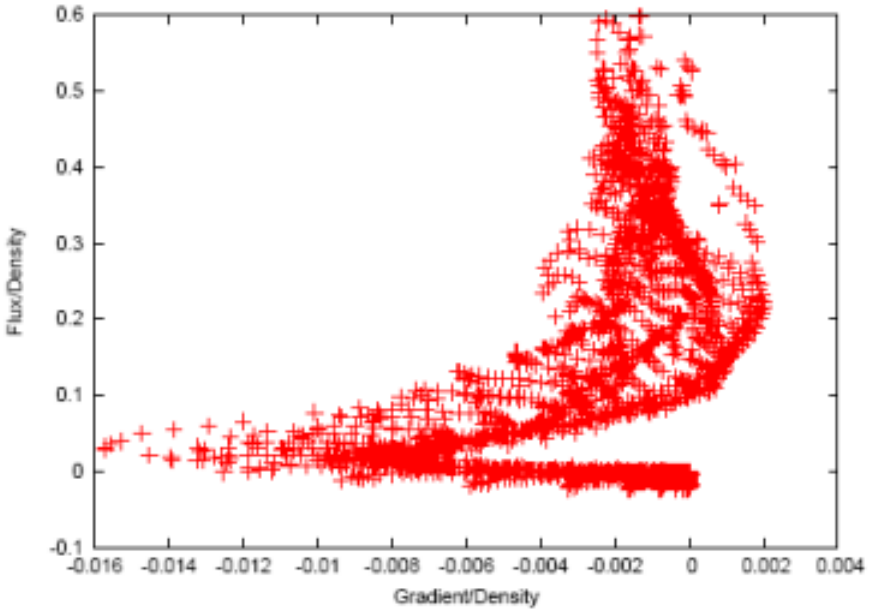

Figure 7: Flux-gradient plot found by sampling over a numerical experiment using ESEL. Reproduced from [5].

across the SOL, becoming un-physically large in the case of D_{eff} in the far-SOL, whereas the V_{eff} remained at reasonable values and relatively consistent in the far-SOL across devices, for a range of core plasma parameters. These suggest that the far-SOL is dominated by convection phenomena only, and that it is relatively insensitive to changes in parameters. In the near-SOL it is found that D_{eff} is well-correlated with the local electron mean-free-path [77] and transport behaviour is not quite the same as that in the far-SOL, demonstrating dependence on at least one local parameter.

The conclusion here may then be twofold: The flux-gradient relation breaks down in the SOL such that transport is distinctly non-local; the nature of transport changes across the SOL, and so any radial transport model must be able to take this into account.

To develop a reduced model we must understand how the nature of transport changes across the SOL, and the underlying mechanism(s) thereof. This is discussed in section 2.6.

2.4.3 Cold Pulse Propagation Experiments

Experiments conducted on various devices to examine the transport of a change in a property radially through devices have been conducted, which may be used to infer the nature of transport present in a device. Typically, the temperature in the edge of a device is varied by injection of impurities, or by the firing of a fuel pellet (a significantly larger impurity), and then the propagation of the radial variation in temperature is studied (e.g. by examining the electron temperature using electron cyclotron emission (ECE)), and then compared to models of such transport.

This type of experiment was first conducted on the Texas Experimental Tokamak (TEXT) which introduced carbon impurities into the device via gas puff [93, 94] such that radiation dissipated sufficient energy to cause a perturbation on the order of 60 % of the temperature in the edge. These investigations produced unintuitive results - a sudden and rapid decrease in the plasma edge temperature caused by the impurity injection, accompanied a rapid and significant increase in the core temperature. Edge and core ECE data were examined. The edge data were compared to the solution of a conventional (local) electron transport equation with various coefficients given an initial equilibrium profile which was a fit to the initial experimental profile, and it was found that the model was incapable of replicating the experimental data without unphysically large transport coefficients [93]. In the core

plasma, the data was totally inconsistent with the transport model used, and suggested that small changes in the edge could cause very large effects - additionally, the data suggested near instantaneous change in temperature across all radii. An ad-hoc non-local transport model with variation in the transport coefficient does provide a reasonable fit to the data, suggesting that local models are not appropriate in this case.

More detailed investigation on TEXT [94] considering a wider range of parameters including pressure variation appeared to confirm the earlier findings. Using experimental data, it was possible to infer the necessary variation in transport coefficients which would be required to model the phenomena, and this required a sudden variation in these coefficients over the whole radius of the device. This indicated that transport at any point depends on the variation of global variables, not simply local properties - and hence is non-local.

A review of cold pulse propagation experiments and theory up to 2015 is given in Ida et al. 2015 [95]. The findings of non-locality appear to be robust, with replication in the Rijnhuizen Tokamak Project (RTP) and the Large Helical Device (LHD) (a stellarator), and nearly all other devices - with a rapid increase in the core temperature following edge cooling via impurity injection. Initial explanations for this particular behaviour involving variation in the q-profile appear to be precluded by the LHD results: Stellarator devices maintain careful control over the device q-profile, hence the replication of the results in the LHD suggest another mechanism is responsible for the phenomenon - the authors suggest coupling of turbulence is the likely driver of non-local behaviour. Overall, in light of the experimental evidence in the core the review considers that the perspective that transport is influenced only by local properties to be inconsistent, and that we must necessarily use non-local approaches to model such transport. The cause of the non-locality is expected to be turbulence, and more specifically due to the nature of the interaction between different scales of turbulence in confined plasmas of this nature.

That core transport is non-local has been challenged [96, 97]. Rodruiguez-Fernandez et al. 2022 [97] explicitly challenge the conclusions that non-local transport models are required:

> "[experimental and computational work] has provided an explanation to the cold-pulse mystery without the need of nonlocal transport effects. Purely local transport models used nowadays to study and predict tokamak behavior are demonstrated to be enough to explain these effects, as long as multi-channel transport interactions are accurately captured within the model assumptions."

Prima facie this would appear to contradict earlier works as it would suggest that the apparently non-local effects are, in fact, not non-local and transport indeed does depend purely on local quantities in the case of cold pulse propagation. It is important to evaluate this paper specifically, as it may suggest an alternative approach to dealing with seemingly non-local effects, and indeed obviate the need to deal with them at all.

First, it is important to note that Rodruiguez-Fernandez et al. 2022 [97] do not actually challenge the findings of previous works directly, stating *"we recognize that such [non-local] models can provide the basis for the fast propagation and reversal of cold pulses in tokamak plasmas"*. The challenge is therefore indirect, via the claim that their local model accurately models the cold pulse phenomena without needing non-locality - and so, the cold pulse behaviour is therefore local in nature.

The local model presented is referred to as the trapped Gyro-Landau fluid (TGLF) quasilinear model, which solves EM gyro-fluid linear equations for each plasma species of relevance, using a spectral solver [98]. It appears to solve a slightly different equation for trapped vs non-trapped particles. One of the core distinctions between other, similar models appears to be the reliance of the TGLF model on a database of outputs from fully nonlinear gyro-kinetic simulations:

> The saturated intensity of the potential fluctuations is not computable from first principles but must be obtained from a formula fit to nonlinear turbulence simulations

(From [98]). This database is used to predict the saturation level of fluctuations that arise from modes which are linearly unstable.

This is an important feature: the TGLF model relies on a database - equivalent to providing a look-up table or slide rule - without which it could not perform the simulations, and this slide rule is calculated from fully nonlinear and gyro-kinetic simulations. Full equations resolved at the appropriate scale are capable of propagating phenomena non-locally due to the action of the transport equations upon computing memory; TGLF, by taking into account sufficient channels of interaction, is able to model enough features of the physics such that the non-linear dynamics that lead to what appears to be non-local transport are also modelled. This does not preclude the idea that transport may be described as non-local.

The success of the TGLF model to describe the core transport does not appear to be inconsistent with the presence of non-local effects - especially given non-local models of transport have also had success in describing the results of cold-pulse propagation experiments. This particular disagreement can perhaps be resolved by considering the approaches to be complementary, with different purposes: Non-local models can incorporate unusual phenomena in a reduced manner; use of software such as TGLF can model the full equations exactly - and, if it predicts the outcomes well enough as selected, is in some sense equivalent to the non local model. As such, it may be possible to find the non-local parameters from such simulation.

Overall, it does seem as though the cold pulse phenomenon can be described both by appeals to non-locality, as well as by modelling of a sufficiently large number of variables - that is, by incorporating and properly modelling multi-channel transport and interactions thereof. The latter does not necessarily preclude the former, and the former should be primarily viewed as a way of simplifying the expression of a problem. There is still uncertainty here, and it may be that further work reveals new subtleties in future.

2.4.4 Avalanche-like transport

The archetypal avalanche is the seemingly spontaneous onset of (quite large) amounts of snow down an incline like a mountain, where the initiation conditions can be sensitive to small or distant phenomena, like loud noises or distant earthquakes. When transport is described as being avalanche-like, then it is characterised by the transport of a quantity occurring primarily through spontaneous, intermittent events, which tend to rapidly propagate in the direction opposing the local gradient of said quantity.

What do avalanches have to do with non-local transport? Avalanche-like transport is local near the avalanche event - however, the circumstances triggering the avalanche are dependent on conditions at the origin of the avalanche, and so transport in all regions reachable by the avalanche is dependent on both the conditions at the avalanche origin, and on the local conditions of the avalanche: consequently, this is a form of non-local transport.

Avalanche-like transport has been observed in MCF devices, with some of the earliest observations occurring in the DIII-D tokamak [99, 100] and the TJ-II stellarator [101].

Avalanches were first searched for in the core plasma of the DIII-D tokamak, using ECE to examine temperature profiles over the radius [99] using pure Deuterium plasma in L-mode. The authors examine fluctuations in the electron temperature during a quiet period of steady-state operation (No sawteeth modes, no MHD activity, no edge localised modes), and observes large, discrete, rapid fluctuations which appear to remain correlated over a large range of the plasma minor radius, hence demonstrating an avalanche-like behaviour. Additionally, by examining the power spectrum of the ECE signal, the authors are able to observe that the spectrum has a $1/f$ dependence - this suggests a self-similar scaling behaviour, and is sometimes called fractal noise as a consequence. An approach to quantify this behaviour in 2-d is by measurement of the Hurst exponent[102][10] that by saying that Examining the Hurst coefficient, H, of the autocorrelation functions, the author finds evidence of $H \neq 0.5$, which is indicative of long time autocorrelation, which further supports the existence of avalanche-like transport in the core.

A follow-up study of avalanche-like transport in DIII-D by the same author examined the magnitude of transport due to avalanche events in the core [100]. This was a more comprehensive study, looking at quiet periods of steady state operation, using the ECE, a beam emission spectroscopy (BES) diagnostic to probe density fluctuations, and a microwave reflectometry diagnostic which may also be used to probe density fluctuations. Again, autocorrelated, discrete, and long-range temperature fluctuations were observed propagating over the minor radius, with velocities on the order of $\sim 300\ ms^{-1}$. Again, the signals demonstrated a $1/f$ spectrum, and Hurst parameters $H \neq 0.5$. As well as providing more robust findings in support of avalanche-like behavior, the key result in this study indicated the magnitude of radial core transport that these avalanches may be responsible for - the energy flux was estimated as being $\sim 0.39\ MW$ in a particular case where the estimated sum of the total electron and ion power was $\sim 1.02\ MW$. Consequently, this provides evidence that during quiet periods in DIII-D, avalanche-like transport is responsible for a significant fraction of energy transport.

The outward transport of heat pulses in the TJ-II stellarator is studied in a lucid paper by B. P. van Milligen et al. [101], who examined both cold pulse propagation radially inward, and hot pulse propagation radially outwards. They note quite a high degree of experimental uncertainty on the order of $\sim 30\%$ in the hot pulse, much higher uncertainty than in the cold

[10] If a measurement demonstrates self-similarity, it exhibits the same statistical behaviour on multiple scales; the assumption is that there is a scaling relation that can be used to find the magnitude of the statistical behaviour between different scales, and that this scaling relation is given by a constant to the power of a characteristic exponent: the Hurst exponent.

pulse case as a consequence of the hot pulse being a much smaller fraction of the background in comparison; the authors then find evidence for ballistic transport in both radial directions. The authors note attempts to tackle this with the introduction of an ad-hoc pinch term to local diffusive models, which is essentially an advection term, but demonstrate that this approach is inconsistent with the evidence - estimation of the magnitude of the pinch velocity given the data suggests $\sim 1\ ms^{-1}$, whereas the actual pulse propagation velocity is an order of magnitude larger at least; consequently concluding that local models are not appropriate in this case for modelling the avalanche-like behaviour, without ad-hoc coefficient variation.

A recent review of avalanche-like transport in the core of MCF devices is given in section 4 of K. Ida et al. 2022 [103]

2.4.5 Implications and Inferences from phenomenology

We have considered the phenomenology relating to radial transport in the scrape-off layer (SOL), edge, and core of MCF devices. The evidence for non-local transport in the SOL is compelling: transport is mediated by filaments, emitted from the edge into the open field line region, which are responsible for significant fractions of mass and energy transport in the radial direction. This transport is not well characterised by the local, Fickian, advection-diffusion equations except by attempting to fit ad-hoc coefficients to experimental data - this is always possible, but it is difficult to physically explain the necessary variation in the transport coefficients; consequently it is difficult to see a path forward towards predictive modelling using this approach. In the edge and core, there is also evidence for non-local transport in the form of the radially propagating avalanche-like heat transport and the inwardly propagating cold pulse, which again is responsible for a significant part of the energy transport; there is some disagreement that this requires a non-local mechanism for explanation, however, non-local models are indeed consistent with experiment.

Given observed non-local phenomenology present almost universally across MCF devices, and the magnitude of transport following from these phenomenon, it is clear it cannot be neglected: non-local models are necessary in the understanding and development of future MCF devices.

To develop appropriate non-local models of the SOL, we must first understand the behaviours of the SOL, relevant phenomena, and then also consider other areas in which non-local

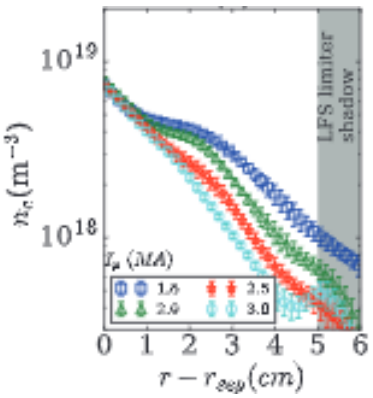

Figure 8: Formation of a shoulder in the JET SOL, characterised by distinct flattening of the density profile, in response to the variation in plasma current, I_p. Reproduced from [6].

phenomena have been studied, to see whether there are relevant concepts and approaches that have been applied to analogous problems which may also be applicable in this case.

2.5 Transport behaviour in the near- and far- SOL

Following from section 2.4.2, we are particularly interested in understanding how transport behaviour varies across the SOL, and upon what this has been observed to depend on. Fortunately, there are numerous experimental studies addressing this topic specifically across all major Tokamak devices in a variety of conditions: Alcator C-mod [69, 77, 7], DIII-D [79, 104], TCV [105, 106], JET [6], MAST [107], EAST [108], as well as multimachine comparisons [109, 110] - it is worth noting that the SOL transport has been primarily observed in L-mode due to issues conducting observations during inter-ELM periods in H-mode; nonetheless a more recent study has been completed during H-mode [110]. SOL behaviour was first separated into distinct near- and far- SOL behaviours on JT-60 [111] in high-density L-mode discharges, where it was noted that there was a distinct flattening of the density profile after a certain distance into the SOL. This may be diagnosed by examining the e-folding length of the density profile; the "second SOL" [111] or "shoulder" [69], and the point where the near-SOL behaviour transitions into far-SOL behaviour is occasionally called the "break point". It is worth noting also that a shoulder is observed in temperature too, which may be diagnosed in the same way [112]. An illustration of the density shoulder in JET is given in figure 8

Early experiments have been conducted for a range of core Greenwald fractions [77, 7, 105].

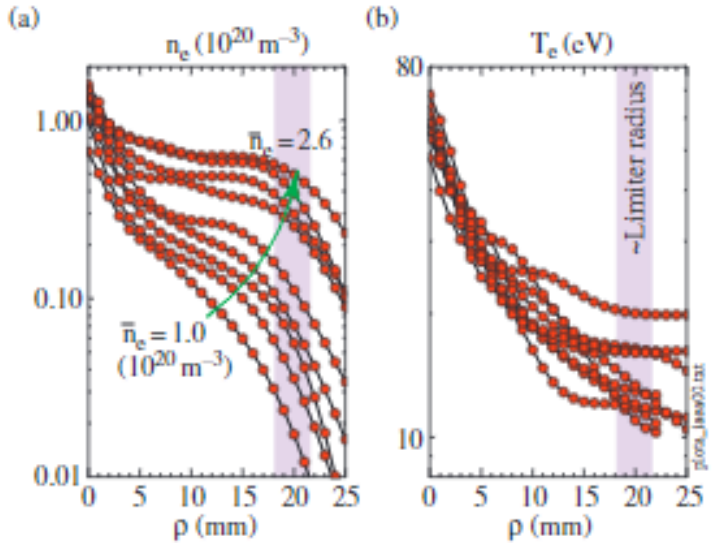

Figure 9: SOL parameters over a range of core densities, corresponding to the range $0.17 \leq n_g \leq 0.45$ *in Alcator C-Mod L-mode. Reproduced from [7].*

Typically it is found that the break-point of the density and temperature shoulder moves further inward with higher Greenwald fraction, such that for high Greenwald fraction, the far-SOL behaviour extends to the separatrix. A particularly good demonstration of this effect is seen in 9 where the data was gathered from Alcator C-mod over a range of core densities - in this case the near-SOL is defined for $\rho \leq 5$ mm, where a distinctly steeper profile is observed. The flattening of the profile in the electron density profile is very clear, but is less obvious in temperature. Similar behaviour is observed in the TCV device [105] for the particle density profile over a range of core densities - the distinct near-SOL/far-SOL behaviours are present for core densities at a low fraction of the Greenwald density, and for core density near the density limit, the flattened profile associated with far-SOL behaviour extended all the way to the separatrix. The ratio of the density limit at which the near-SOL/far-SOL behaviour becomes a shoulder varies somewhat between devices: in JT-60 it occurs at Greenwald fraction ~ 0.55 [111], whereas in TCV it appears between ~ 0.25 and ~ 0.6 [105], and in Alcator C-mod the behaviour seems to demonstrate the distinct near-SOL/far-SOL behaviours for Greenwald fraction < 0.5 [77].

It has been hypothesised that the two-region SOL is a consequence of a difference in filament parallel connectivity between the two regions, and that the transition from the two-region SOL to the shoulder dominated SOL is therefore a consequence of an alteration in that interaction [105, 113] - with low collisionality, filaments exist such that the current flowing within is limited by the plasma sheath at the wall - by contrast, at high collisionality the

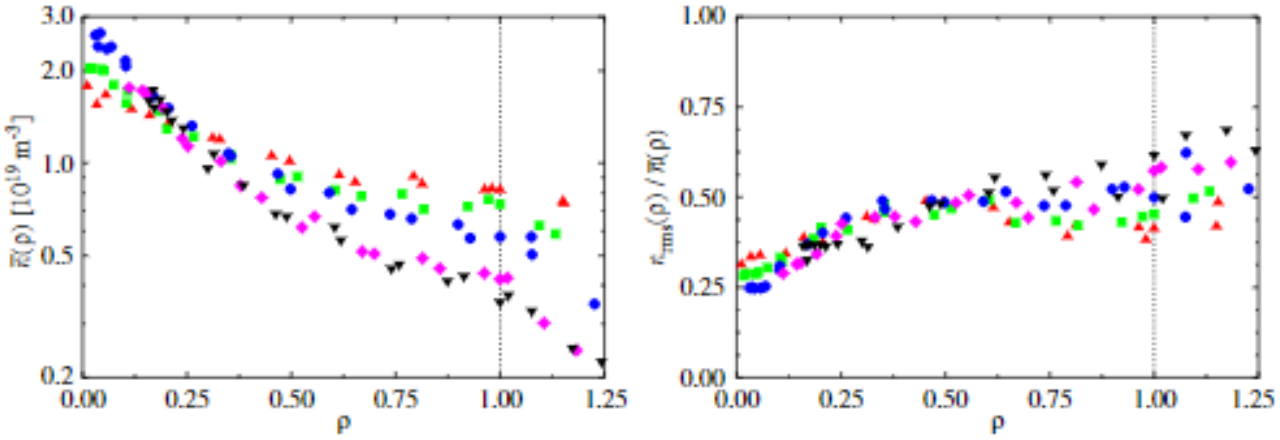

Figure 10: Average particle density (Left), relative fluctuation level (Right), in the TCV SOL over a range of plasma currents $I_p \in [220, 380]$ kA, where the red triangles correspond to the lowest I_p and black to the lowest I_p. ρ corresponds to distance from the separatrix normalised to the wall shadow distance. Reproduced from [8].

influence of the sheath is less significant, and filaments exist in an inertial regime.

The effect of the transition from L- to H- mode on the SOl profiles has been examined [7, 108]. In Alcator-C mod the transition occurred within the same shot, and conditions were observed before and after. The effective density diffusivity near the separatrix has been observed to decline from L- to H- mode, which is consistent with better plasma confinement. It is worth noting that during an ELMy H-mode as observed on DIII-D [79, 104] that fluxes to the wall substantially increase as a consequence of very large plasma blobs being transported to the wall. Since it is expected that we will operate future reactors without ELMs, this is not considered to be "typical" SOL behaviour.

Plasma current also plays a role in the SOL behaviour [79, 107, 8]. A plasma current scan performed on TCV [8] found that the impact on the radial density profile, fluctuation statistics was very similar to the effect of a scan in core density, but further the standard deviation of the estimated radial velocity appeared to increase as the plasma current decreased, throughout the SOL, as depicted in figure 10 - it should be noted that as the plasma current decreases, the collisionality also increases, supporting the role of collisionality and wall detachment in SOL shoulder behaviour. A study on JET [6] also supported this finding, that the density shoulder increased as I_p was reduced.

An early comparison between COMPASS, JET, and AUG on this subject [109], which was

based on observation of SOL properties given a scan in core density found that JET and AUG underwent shoulder formation at a Greenwald fraction of $\sim$ 0.5, and this was observed to occur at a similar time to detachment of the divertor - however in COMPASS, neither detachment nor shoulder formation were observed for the same range.

The effect of divertor configuration upon SOL profiles has also been studied [109, 107, 106, 6, 108], since $\Lambda_{divertor}$ has been described as being $\Lambda_{divertor} \propto L_{||}$ [113], where $L_{||}$ is the parallel connection length - altering the divertor configuration provides a reasonably straightforward way of altering the parallel connection length. A study was conducted in TCV [106] where the parallel connection length was varied by altering the degree of flux expansion in the divertor leg, and appeared to show that despite an increase in divertor collisionality the measured e-folding length in the near-SOL, λ_n, was not observed to substantially change, and nor was a $L_{||}$-dependence observed; the far-SOL e-folding length was observed to increase for $\Lambda_{divertor} > 1$, as seen elsewhere, but these results seem to demonstrate that filament disconnection from the divertor target as indicated by $\Lambda_{divertor}$ values is not a sufficient condition to result in the flattening of the SOL profile in TCV. A similar study on JET [6] also found that the divertor collisionality condition of shoulder formation, $\Lambda_{divertor} > 1$, was not sufficient to predict the formation of a shoulder. By sweeping the divertor leg across the divertor plates, and thus changing the parallel connection length (but in such a way that the divertor collisionality was unaffected) it was found that changes in SOL profiles were observed with no changes in divertor collisionality. Further, the study in JET indicated that changes in neutral density in the divertor were also indicative of shoulder formation or alterations. Study of L-mode discharges in MAST [107] operating in double-null configuration found that shoulder formation can occur with neither detachment nor wall recycling, again suggesting that the current models do not quite capture all effects that affect the SOL behaviour. This study also highlighted the distinction between heat transport and density transport - diffusive models gave a good match for heat flux e-folding width at the midplane based on the widths at the divertor, but not for the density. While operating in H-mode, EAST operators [108] reduced the neutral pressure in the lower divertor while maintaining a high Greenwald fraction, as well as maintaining a $\Lambda_{divertor} > 1$; in this case, the density shoulder did not form until the end of the discharge, strongly suggesting the influence of neutrals in shoulder formation.

To summarise the studies of SOL profile phenomenology: the scrape-off layer has been observed to have two distinct regions, the near- and far- SOL, which are typically characterised based on their density scale lengths. A distinct flattening in the far-SOL occurs, which is

found to move closer to the separatrix with increased Greenwald fraction, as determined by line-averaged core densities. Experiments observed a link between divertor neutral densities and shoulder formation; this indicates that shoulder formation could be related to other physical processes, such as variation in parallel transport dynamics or alteration in the behaviour of radial electric fields in the edge, which may influence edge turbulence.

It is worth mentioning here work on the generation of filaments. This is hard to investigate experimentally due to the difficulty in identifying and tracking filaments, although methods to track filaments have been developed [114]. However, it has been suggested that there is a relation between the filament generation rate and the qualities of edge turbulence [115].

2.6 Modelling the Scrape-Off Layer

The computational approach to modelling plasmas is very powerful, but in some cases significant progress can be made by considering simple models. This is done to consider the present work and scope in such reduced models. The two point model [71][61] provides a simple relation between conditions at the last-closed flux surface and the divertor targets. A simple version provides three equations - these may be rearranged to find target conditions in terms of upstream conditions, and thus find scaling relations. This is a very simple model of the problem, essentially a 'black box' plus conservation equation approach like that favoured by engineers - however this simplicity makes it very useful, as it provides a highly interpretable representation of dynamics, and allows predictions to be made simply. Consequently, two-point models are widely used, despite their over-broad assumptions. In a recent example of this, a refined two-point model expanded to incorporate plasma-neutral interactions - still simple, still analytical - was found to have an excellent agreement with simulations on GBS, which solves the drift-reduced Braginskii equations [116].

A model describing the transport of SOL filaments was proposed by S. I. Krasheninnikov in 2001 [85]. As soon as plasma is ejected into the SOL, it is no longer confined in the parallel direction except by the plasma facing surfaces and any effects arising thereof. Consequently, the $\nabla \mathbf{B}$ drift acts to polarize the filament of plasma, and then the $\mathbf{E} \times \mathbf{B}$ drift acts to move the charged particles composing the now-polarized filament. Papers comparing theory and experiment [117, 87] finds good agreement with these approximations, finding that filaments do appear to follow these scalings to a significant degree - suggesting that the model does

capture well the key elements dominating filament behaviour.

2.6.1 The Statistical SOL model

The filamentary transport model is not sufficient in itself to describe the statistical properties of the SOL - such as mean radial density profile and radial flux - which are required to describe the average radial transport in the SOL. This is as a consequence of the filamentary transport model consisting of a description of the behaviour of individual filaments, rather than a description of the large ensemble of filaments which we presume dominates the behaviour of the SOL. A next rational step is to attempt to describe the behaviour of this ensemble of filaments, a method by which to do so was first proposed by O. E. Garcia [118], and developed further or rediscovered more recently [119, 120, 121, 122].

We follow [119] in the derivation of the statistical SOL model. Consider a plane perpendicular to $\mathbf{B}_{tot}$ beyond the LCFS. Assume this region is well described by an ensemble of filaments propagating in the radial direction. Further assume that these filaments are non-interacting, and that the distribution of filament characteristic sizes, a_f, is a well-behaved distribution. Assume that the filaments undergo a drainage process, due to parallel losses. Assume that filaments have a characteristic shape which is re-scaled rather than substantially altered over the filament lifetime. We do not consider the details of filament formation, and instead consider them to pop into existence, fully formed, at the LCFS, with initial value of thermodynamic variable for a particular filament i as $\eta_{0,i}$. A shape function, $\Lambda = \Lambda(x, a_{f,i})$, which is dependent on the filament characteristic size, and a loss term $L_i = L_i(t)$ may be defined which represents the effect of the parallel losses. The dependence of the thermodynamic variable, $\eta_i(x,t)$, on the initial value for a given filament may be written as:

$$\eta_i(x,t) = \eta_{0,i} L_i(t) \Lambda \left(x - \int_0^t V_i(\xi) dt\xi,\ a_{f,i} \right) \tag{14}$$

Another assumption is that the velocity, V_i, and loss terms are set only by the initial filament characteristic size, $a_{f,i}$, and parameter value $\eta_{0,i}$. At a given radial position, x, and time t, an ideal probe which measures η would experience a signal, $\eta_s(x,t)$, composed of the contribution of each filament:

$$\eta_s(x,t) = \sum_{i=1}^{K} \eta_i(x, t - t_i) \tag{15}$$

Where t_i is the time at which the i'th filament crosses the LCFS, and we have K filaments crossing the separatrix in a time δt. If the crossing times for each filament are independent of each other and can be modelled at a constant rate, then the distribution of t_i may be described with a Poisson distribution, such that:

$$P_t = \lambda^K e^{-\lambda} \frac{1}{K!} \quad \lambda = \frac{\delta t}{\tau_f} \tag{16}$$

Where τ_f is the mean waiting time between filaments.

So far, this stochastic model results in a statistical quantity related to the ensemble behaviour of filaments, and has ways of incorporating key filament physics; the filament physics discussed in 2.4.1 can be used to create the loss term and set the dependence of the velocity distribution on the filament characteristic size. We may then acquire mean profiles of quantities in the SOL by considering the time average over the interval δt - $\overline{\eta_s}$ - in the limit $\delta t \longrightarrow \infty$.

Key quantities that must be introduced to develop this further are probability density functions (PDFs) of filament initial amplitudes, P_η and characteristic size, P_a. Considering the contribution of the PDFs to the average, we may then write:

$$\overline{\eta_s}(x) = \int_0^\infty P_\eta \int_0^\infty P_a \sum_{K=1}^{\infty} P_t \sum_0^K \frac{1}{\delta t} \int_0^{\delta t} \eta_i(x, t - t_i)\ dt_i\ d\eta_{0,i}\ da_f \tag{17}$$

Applying Campbell's theorem [121], a key part of Eqn. 17 may be simplified to:

$$\lim_{\delta t \to \infty} \sum_{K=1}^{\infty} P_t \sum_0^K \frac{1}{\delta t} \int_0^{\delta t} \eta_i(x, t - t_i)\ dt_i = \frac{1}{\tau_f} \int_{-\infty}^{\infty} \eta_i(x,t) dt \tag{18}$$

and so finally:

$$\overline{\eta_s}(x) = \frac{1}{\tau_f} \int_{-\infty}^{\infty} \int_{0}^{\infty} \int_{0}^{\infty} P_\eta(\eta_0) P_a(a_f) \eta(x,t)\ da_f\ d\eta_0\ dt \tag{19}$$

Where the indices have been dropped. Examining different moments of $\overline{\eta_s}(x)$ permits scrutinisation of different quantities, such as variance, skewness, and kurtosis - which may be compared to experimental measurements. A typical shape function to consider is an exponential distribution with a leading vertical edge, such that $\Lambda(x,w) = e^{\frac{x}{a_f}} H(-x)$ [118, 119], and with a loss term with a characteristic time, t_L such that $L(t) = e^{-\frac{t}{\tau_L}}$. The application of this model to JET data [120] met with some success, however, the simple model fails to capture the SOL profile flattening/shoulder formation in the SOL without adjustment. It was possible to fit the model in the cases of shoulder formation by adjusting, locally, the parallel drainage time τ_L, or by considering a variation in the filament velocity. While it is possible to tune the statistical model parameters to fit experiment, no simple relation was captured when the profiles are broadened, suggesting that there is physics missing from the simple model [120].

While a simple and intuitive model, capturing filament of behaviour and in principle permitting the expression of the SOL profile given the knowledge of a few probability distributions, there is comparison with experiment suggests that the simple model is not a full description, and that further modification is required in order to obtain agreement with experiment. It does, however, demonstrate the power of statistical approaches to model behaviour

2.7 Approaches to non-locality and transport in fluid systems

Examination of the nature of transport in the edge of tokamak devices suggests it is turbulent, and the SOL is dominated by structures known as filaments, which are generated, presumably, as a consequence of the plasma dynamics near the LCFS. It is not unreasonable therefore to suspect that the distribution of filament properties and transport in the SOL more generally is fundamentally influenced by the conditions of turbulence in the edge - and indeed, approaches to the problem of SOL transport from the perspective of turbulence transport have been of particular interest of late [123, 124]. Unfortunately for us, large scale turbulence is an as-yet unsolved problem in general - although there has been significant

progress in a number of specific cases.

To formulate our problem more explicitly: we are particularly concerned by transport across fluids dominated by large coherent structures, and also the relation of the properties of the coherent structures to turbulence in the edge. Coherent structures, their formation and properties, their link to turbulence have all been considered in the field of fluid mechanics - and so we will briefly review some of the more relevant work in this field in order to gain an insight into the nature of the problem in tokamak devices; we also examine non-locality in fluids, where it occurs, how it is related to fluid conditions, and examine several methods by which researchers have attempted to find models of transport in such fluids.

2.7.1 Turbulence in neutral fluids

In this section we have primarily used "The Physics of Fluid Turbulence" [125] and "Turbulence" [126] as reference.

When modelling neutral fluids, the Navier-Stokes equations are the starting point of many treatments. The Navier-Stokes (NS) equations are often evaluated by decomposing the quantities involved into a time-averaged and fluctuating quantity, referred to as Reynolds decomposition, e.g. for a $f(x,t)$:

$$f(x,t) = \bar{f}(x) + \tilde{f}(x,t) \tag{20}$$

This averaging process simplifies the NS equations to the Reynolds-Averaged-Navier-Stokes (RANS) equations, and allows us to find the mean profiles. Unfortunately, we run into a closure problem - the (kinematic) Reynolds stress term appears:

$$R_{ij} = \overline{\tilde{u}_i \tilde{u}_j} \tag{21}$$

Where u denotes the velocity of the flow, and we are using index notation. The term in which the Reynolds stresses appear represents the transport of momentum due to turbulent fluctuations, and so represents the un-closed part of the RANS equations. Most approaches

to computing or analysing turbulence therefore require assumptions to be made regarding the Reynolds stress tensor. The diagonal terms of the Reynolds stress are normal stresses, and the off-diagonal terms are shear stresses.

The Boussinesq hypothesis is one such attempt at simplifying the Reynolds stress tensor: One may make an assumption that the local Reynolds stress is related to the local mean velocity shear - it introduces an effective (turbulent) eddy viscosity, ν_t, related to the mean strain tensor - and the turbulent kinetic energy, $k = R_{ii}\frac{1}{2}$, such that:

$$R_{ij} = \frac{2}{3}k\delta_{ij} - \nu_t\left(\frac{\partial \bar{u}_i}{\partial x_j} + \frac{\partial \bar{u}_j}{\partial x_i}\right) \tag{22}$$

In combination with Prantl's mixing length model, this has been used to study the flow of fluids near walls, and has been a highly successful reduced model.

Approaches which model an effective eddy viscosity are commonly used in computational fluid dynamics to model transport affected by turbulence - a common approach is the $k-\epsilon$ model, where ϵ is the rate of dissipation of (kinetic) energy, $\epsilon \equiv \frac{dk}{dt}$, or models which transport the Reynolds stresses directly, which may be constructed by taking the appropriate moment of the NS equations.

The subject of turbulent kinetic energy and its dissipation rate in isotropic media was addressed by Kolmogorov, who devised the Kolmogorov theory; Turbulent kinetic energy is transferred from large scales to small scales, where the energy is dissipated by molecular viscosity. The energy is therefore distributed over the range of available scales. Once energy is transferred to a scale that is sufficiently small with respect to the system size, the distribution of energy among scales should be universal. This leads to the (second) Kolmogorov hypothesis, which states that the distribution of turbulent kinetic energy among wavenumbers, $E(k)$, should become independent of viscocity as the Reynolds number [11] tends to infinity, and:

$$E(k) \propto \epsilon^{-\frac{2}{3}}k^{-\frac{5}{3}} \tag{23}$$

[11] Where the Reynolds number is the ratio of inertial forces to viscous forces

An important distinction with two dimensional turbulent flows as opposed to three dimensional turbulent flows, is that the energy spectrum can be demonstrated to have different behaviour due to the conservation of both energy and enstrophy in the incompressible two-dimensional case. This is discussed extensively by Kraichnan [127], and it can be demonstrated that the constraint of enstrophy conservation results in a cascade of energy from small scales to large scales following Kolmogorov's $E(k) \propto \epsilon^{2/3} k^{-5/3}$ and an additional transfer of energy to smaller scales following $E(k) \propto \eta^{2/3} k^{-3}$. The k^{-3} transfer regime is known occasionally as the enstrophy inertial range. This particular two-dimensional energy cascade behaviour is frequently referred to as the dual cascade. While this may seem a limitation on the use of 2-D fluid simulations, there are physical cases of the dual cascade occurring in some models of physical systems such as in the Hasegawa-Mima equation [128], and in atmospheric systems [129].

2.7.2 Coherent Structures in fluids

There is a zoo of coherent structures that have been observed - two particular types of coherent structure that are of direct interest to us consist of transport barriers [130, 103], and filaments - filaments can be considered a form of dipole vortex, composed as they are of two counter-rotating vortices [131][12]. Coherent structures are particularly fascinating because they are not self-evident from the PDE's with which we model systems - they are perhaps one of the archetypal examples of emergent complexity, and so a subject of great interest.

Coherent structures, a term seemingly coined by Brown and Roshko [135] when describing the appearance of structures in a jet, have been observed in real and simulated flows of many kinds and are readily visually identified. While seemingly easily identifiable by humans using subjective methods, there is no universal, agreed upon rigorous definition of a coherent structure. Some properties were proposed by Weiss and McWilliams [136] as follows - coherent structures are:

- recurrent in the system

[12]While generation of structures is beyond the scope of this work, it is certainly worth noting that 'bursty' structure generation processes have long been observed in turbulent boundary layers [132, 133, 134] which have a few parallels to the generation of filaments

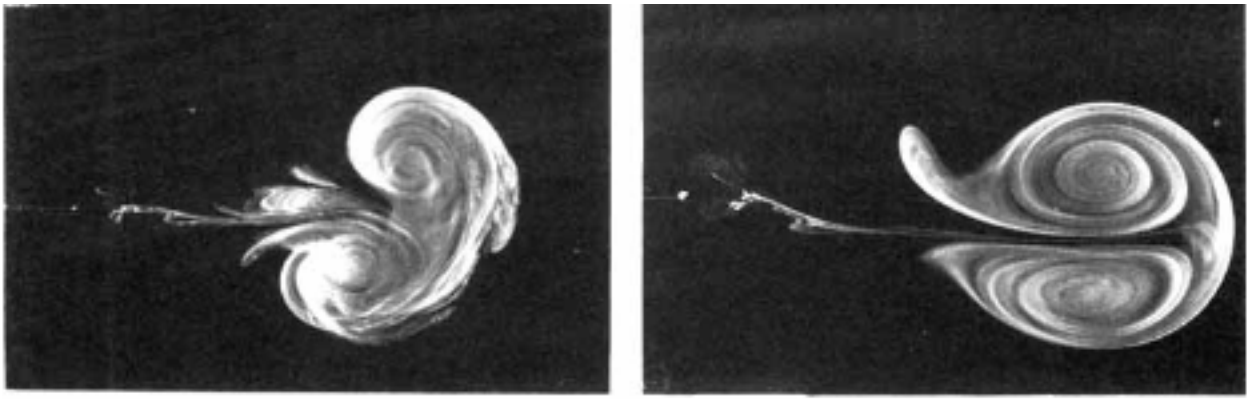

Figure 11: Two images of a dipolar vortex in a stratified fluid - tracer particles were injected, and allow observation of the flow structure. Reproduced from [9]

- spatially localised and isolated
- a preferred state of nonlinear dynamics
- self-organising
- persist for a time longer than the Eulerian timescale

Coherent structures are typically generated from an instability in the system [137] - perhaps the most simple being the unipolar vortex, from which can be constructed the dipole vortex, which comprises of two counter-rotating vortices which then result in propagation [9] - please see Fig. 11 for an example. In a sense the dipole vortex is the two-dimensional fluid analogue to the glider found in Conway's game of life - a self propagating structure.

The importance of vorticity and shear flow in delineating the boundaries of coherent structures has been recognised for some time [137], and has been investigated extensively - primarily in the case of unipolar vortices in two-dimensions [138, 139, 140, 141].

The Okubo-Weiss parameter, typically denoted Q [142, 138] can be demonstrated to separate a fluid flow instantaneously into hyperbolic and elliptic regions, where:

$$Q = s^2 - \omega^2 \tag{24}$$

where s is the deformation and ω is the vorticity, as acquired through decomposing the 2D

velocity gradient into a deformation and rotation component as:

$$\omega = \frac{\partial v}{\partial x} - \frac{\partial u}{\partial y} \tag{25}$$

and

$$s^2 = \left(\frac{\partial u}{\partial x} - \frac{\partial v}{\partial y}\right)^2 + \left(\frac{\partial v}{\partial x} + \frac{\partial u}{\partial y}\right)^2 \tag{26}$$

Where u and v denote the x and y component of the velocity vector. This was proposed on the basis that in regions with strain rates larger than rotation rate, the vorticity would experience substantial shear, whereas in regions with rotation rate exceeding the strain rate, the vorticity would be advected. The Okubo-Weiss parameter is particularly enlightening as to some characteristics of coherent structures - analysis of simulated 2D flow fields identified elliptic regions with $Q < 0$, or the vorticity dominated regions and hyperbolic regions with $Q > 0$, or shear dominated regions [13][14]. Vortices were found to typically consist of a periphery with very large positive Q - highly hyperbolic - with a core of very large negative Q, so strongly elliptic [140]. The propagation of tracer particles in such a field revealed that the boundaries of vortices were found to act as barriers to particle transport, demonstrating great impermeability to exterior particles. Similarly, particles remain trapped within coherent structures. Interactions between coherent structures was typically responsible for particle ejection from vortices [140].

Of particular interest for us, is that due to the impermeability of coherent structures, tracer particles are typically carried with the structure - and consequently, may affect the dynamics of transport. A particularly excellent demonstration of this is done by Weeks et al. [10] who examined the transport of tracer particles in an experimental quasi-geostrophic flow set-up [15], finding that tracer particles undergo anomalous transport due to trapping in vortices - that is, they experience (variously) both long flights across the system and periods of

[13] A flaw in this approach is that the Q parameter is too sensitive, and classifies all regions as elliptic or hyperbolic - to identify vortices only, it is necessary to set a subjective Q threshold...

[14] More recent work by Haller et al. [143] allows identification of coherent structures with less subjectivity - however it is significantly more computationally intensive than evaluating Q; it is also found that Q is the short time limit of the Haller approach.

[15] Geostrophic flow is analogous to the Hasegawa-Wakatani equations, as we will discuss in section 5

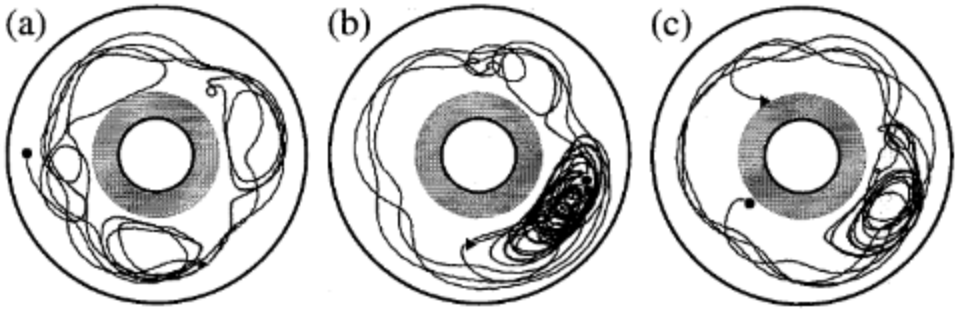

Figure 12: Trajectories of three tracers observed in the experimental apparatus. In (b), a particle is observed trapped in the same vortex, which moves erratically. Reproduced from [10]

'sticking'.

An important aspect of transport by coherent structures is that due to the structures remaining coherent over long timescales, this results in long-time correlations - and consequently, introduces non-locality to the system: A coherent structure generated at a point, will have been created as a consequence of conditions at that point; consequently, if it travels a long way, transport will be influenced strongly by conditions at a distant location. To predict transport in a system dominated by coherent structures, one must consider the nature of coherent structures in the system, their generation and propagation, in a self consistent manner.

2.7.3 Attempts at treating non-locality in neutral fluids

Anomalous diffusion in fluids was (seemingly) first addressed by L. F. Richardson [144] who considered how particles may feasibly undergo non-Fickian diffusion. The particular case considered was the transport of particles in the atmosphere - the observations noted were that the rate of diffusion appeared to increase with the increasing separation of diffusing particles; This was inferred to be due to the action of eddies. It was noted that Fick's second law:

$$\frac{\partial n}{\partial t} = D\frac{\partial^2 n}{\partial x^2} - \overline{u}\frac{\partial n}{\partial x} \tag{27}$$

...where D denotes a diffusion coefficient, and $\overline{u}$ denotes a mean velocity, appeared incapable of describing transport in such cases; this form of transport being referred to as 'non-Fickian'.

S. Corrsin in particular [145] recognised that the significant majority of fluid equations are primarily dependent on Fick's first law:

$$\Gamma(x,t) \equiv -D\frac{\partial n(x,t)}{\partial x} \tag{28}$$

..which was postulated initially on the basis of experimental results, and is a statement that the local flux, $\Gamma(x,t)$, of a quantity, $n(x,t)$, should be proportional to the local gradient of that quantity. This assumption of Fickian transport for most quantities has resulted in *almost all transport equations used consisting of gradient transport models.* A key assumption of gradient transport models is that the knudsen number, Kn is small, or otherwise that the characteristic scale of transport must be small in comparison to the distance over which the mean gradient changes. Corrsin suggests that it is remarkable that gradient transport models generally work. It is suggested that random walk models, however, may be able to deal with these issues and furnish us with a better description - and indeed, in certain limits these deliver us the telegraph equation [146], as well as the Fokker-Planck equation - and so have demonstrated their usefulness already. It is important to note that random walk models are Lagrangian models of transport rather than Eulerian, and so can tell us something different about the nature of turbulence and transport; indeed, nearly all experimental visualisations of fluid flow - and especially turbulence - make use of Lagrangian tracers to highlight fluid motion, and to provide an intuitive sense of the processes occurring [147].

A challenge to the gradient-transport model came from Fiedler [148] and Berkowicz [149], who proposed an integral model [16] for the relation between the turbulent flux, and the local gradient, as:

$$\Gamma_{turb}(x,t) = \overline{vn}(x,t) = \int D(z,z')\frac{\partial n}{\partial z'}dz' \tag{29}$$

Where Γ_{turb} denotes the turbulent flux, and $D(z,z')$ denotes an eddy diffusivity. This emerged due to observations of flux-gradient relation breaking in numerical LES simula-

[16] Or, occasionally referred to as the spectral turbulent diffusivity

tions of boundary layers of various kinds, and the failure of local eddy diffusivity models to explain up-gradient transport. The Eqn. 29 is a non-local relation; the turbulent flux at x may depend on the gradient across the whole domain in the case that the kernel $D(z, z')$ does not vanish with distance sufficiently quickly - as such, there may be a contribution to the flux at x from the gradient across the whole system. However, it remained within the realms of experimental observation to determine the form of $D(z, z')$.

Quite similar is the transilient turbulence approach [150], where a scalar (say, n, for ease of comparison) is transported as:

$$\overline{n_i(t + \Delta t)} = \sum_{j=1}^{n} c(t, \Delta t)_{ij} \overline{n_j(t)} \tag{30}$$

Where c_{ij} is the transilient [17] matrix. Note that this is, again, a non-local approach depending on the from of c_{ij}. This is, in a sense, equivalent to the spectral turbulent diffusivity approach. Measurements of the transilient matrix were conducted by injecting (Lagrangian) tracer particles into LES simulations of mixed layers, and it was found that the matrix demonstrated quite skewed transport - but again, it was not obvious how to find the transilient matrix from first principles. A review of transilient turbulence theory [152] covers the phenomenology of the transilient matrix in different conditions in more detail, but there is as yet no clear first principles approach to finding this kernel. It was noted in the case of large eddies in fluid systems, the transilient matrix was non-Gaussian, however reduced to the Gaussian distribution when eddies were typically quite small [151].

Continuing in this vein Hamba [153], considers the non-local transport of the Reynolds stress, due to a non-local eddy viscocity; this non-local approach was more successful than a local approach, and provided a good model of turbulent shear flow near a boundary - however, it was not obvious how to find the non-local eddy viscocity from first principles. Similarly, a non-local eddy diffusivity approach was compared with DNS [154] and found to compare favourably - however, it was still not obvious how to find the non-local parameter from first principles.

Isichenko [155] considers the effectiveness of random walk models of particles on lattices of various kinds allow the calculation of effective transport coefficients and transport equations

[17] NB: the word 'transilent' derives from Latin, meaning 'leap across' [151]

across various kinds of complex geometries - highlighting the importance of the consideration of statistical topologies when considering transport across various kinds of media; indeed, one may infer from Isichenko that the presence of structure is not necessarily a barrier to developing reduced models of transport, provided that the nature of structure is sufficiently statistical in nature.

2.7.4 Attempts at treating non-locality in plasmas

The challenge of non-local transport in plasmas has been recognised and approached with neutral fluid or non-local methods previously (e.g. [156, 157, 158, 159, 160]). Recognising the similarity to neutral fluids, a turbulence spreading model based on the $k - \epsilon$ approach (that is, transport of turbulent kinetic energy) was developed [160], and developed to a correlation-based model [159], which similarly to the integral transport and transilient approach results in an integral kernel approach, delivering equations analogous to the telegraph equations which appear able to propagate filaments with dynamics similar to the statistical filaments of section 2.6.1. This suggests that an effective diffusion coefficient may be derived, but as the equations to solve would be local equations, the effective diffusion coefficient may have to vary radially.

Transport in plasmas by use of fractional order derivatives was attempted[156, 157, 158], however the generalisation from integer order derivatives to time and space fractional derivatives lacked any kind of physical justification [156], or clear relation to underlying physical phenomena - while the research indicated that the proposed equations may explain aspects of transport behaviour, without a rigorous explanation for the appearance of these non-local equations, this cannot be used as a basis for a predictive model.

2.8 Section Summary

The flux-gradient relationship does not work in the SOL, or in the core plasma. Uphill transport is observed, too. We have strong turbulence, shear effects at play, as well as the propagation of coherent structures (filaments) dominating transport. Existing models of filaments make strong use of statistical topological approaches, such as the statistical SOL model, which, combined with an understanding of the dynamics of individual structures,

allows reasonable modelling. Non-locality is emphasised; the two-point model, and the statistical SOL model, are both intrinsically non-local approaches, by necessity.

The effects observed in the SOL and core plasma are not unprecedented. Very similar phenomena in the boundary layers of neutral fluids have troubled scientists and engineers for a while, and both phenomena concerning us in plasmas - flux-gradient breaking and up-hill transport - have been observed and analysed in neutral fluids: The successful approaches to reduced modelling of these phenomena has depended upon the creation of non-local eddy diffusion and viscosity models, $k-\epsilon$ models, or the transilient matrix approach. Measurement of the transilient matrix has been accomplished by the observation of tracer particles in the fluid systems of relevance, and this has been able to provide useful qualitative explanation of some aspects. The motion of Lagrangian tracers is emphasised as one of the key ways of understanding turbulence. One issue, however, has been a lack of success in creating the non-local kernels required for the non-local approaches (or to compose the transilient matrix).

As a consequence of all of this, it seems highly likely that it is possible to model transport by using a random walk approach - from which it is possible that we will see non-locality emerge. We begin this approach in the next chapter.

3 The Random Walk Approach to Transport

Random walk models, and the application of random walk models in physical sciences, is an extensive field which has impacted many varied disciplines, and for a broad overview the author directs you to work by R. Metzler & J. Klafter [161], R. Kutner & J. Masolivier [162]. The term 'random walk' was coined by Karl Pearson [163] in 1905, which seems to be the first explicit mention of the subject and its study in mathematics. Full review of this area grows quite challenging after 1965 due to the impact of E. Montroll and G. Weiss' paper [164], which has been cited in an exponential fashion and was cited over 32,000 times by 2015 [162] - this possibly makes the Montroll-Weiss paper one of the most cited papers of all time [165] - as they developed what was later known as the continuous-time random walk (CTRW), which has broad application [18].

[18] Although, it appears that many of their results appear first in work by Chandrasekhar [166]

The observation of the irregular, jittery, motion of light particles - dust, or pollen - is not unusual, described by Lucretius in 60BC [167]. This property was noted by J. Ingenhousz in 1785, as well as J. Brown in 1827 [167], and came to be known as 'Brownian Motion'. The link between Brownian motion and mathematical statistical models began at the end of the 19th century: Initially with the work of T.N. Theile in 1880, who was particularly concerned with measurement error in optical telescopes - he inferred that the error was likely random, independent, and was likely normally distributed around the immediately previous position; Theile's work anticipated later work, such as that by N. Weiner [168].

One of the most significant advances was the mathematical work of L. Bachelier in 1900 [169], who was concerned with the motion of the financial markets, derived the Bachelier equation, and using this was able to demonstrate that this resulted in a "Fourier equation" - or a diffusion equation, and found the result that the root-mean squared displacements of the random walk is proportional to the square root of time, $RMS(\Delta x) \propto \sqrt{t}$. This contribution is widely recognised in financial mathematics [170], but not in physics - with whom the development of diffusion is more closely associated with A. Einstein [171] [19], who considered the same phenomena in relation to the motion of particles rather than the motion of stock prices.

Broadly, the approach to the random walk is of two kinds: Classical Random Walk (CRW) models, and Continuous-Time Random Walk models (CTRW) [167]. The CRW typically takes time as no more that a dummy variable, measuring the number of steps taken, and the CTRW introduces a characteristic waiting time between steps taken by a random walker. We consider first the CRW and CTRW, and consider their application to fluid systems. We then consider the Bachelier and Einstein formulation of the random walk. Finally, we consider an 'observational' random walk.

[19] One may postulate that this is a consequence of Einstein's work receiving an English translation

3.1 The Classical and Continuous-Time Random Walks

3.1.1 The Classical Random Walk

The archetypal presentation of the random walk problem is that of a random walker upon a 2D structured grid with increments of equal size [166, 163][20]. The random walker has an assigned probability of 'jumping' or 'walking' to an adjacent point on the grid. It becomes an interesting problem to consider what happens to the particle after N jumps, given certain conditions imposed on the random walker. The most important and essential property of the random walker in this formulation is the probability of moving to a particular grid point with each step. While it is possible to assign an arbitary probability of moving to *any* grid point, the probability assigned is that of moving to the adjacent grid point in a particular dimension.

Therefore in the classical formulation, the defining aspects of the problem are the translational degrees of freedom of the random walker, and the (homogeneous) probability of motion along those degrees of freedom which is typically considered to be isotropic, and independent of previous steps.

The simplest case to consider is the case where the random walker may move in one dimension, with a probability of moving either left or right. We may write that $P_L = \frac{1}{2}$, and $P_R = \frac{1}{2}$. We may label each point on the grid in the range $s \in [-N, N]$ where $N \in \mathbb{N}$, and the walker begins its walk at $s = 0$.

Given all steps are independent, the probability of any particular sequence of steps is $P_a = \frac{1}{2}^N$. The probability of a walker being at a particular grid point, s, given it takes N jumps to get there, $P(s|N)$ is then the sum of probabilities of all possible paths to that point.

This is then a combinatoric problem. Given 2 degrees of freedom (left or right), there are then 2^N possible paths, given N jumps. Every path that gets to a point s must have taken a sum of right jumps and left jumps that sums to s. Therefore:

$$r - l = s \tag{31}$$

[20] specifically, a drunk person walking home after a night out [163]

And:

$$r + l = N \tag{32}$$

So then:

$$r = \frac{1}{2}(N + s), \quad l = \frac{1}{2}(N - s) \tag{33}$$

Given N steps, we must then know the number of ways of picking r from them, or $\binom{N}{r}$. Then, the probability $P(s|N)$ may be written as:

$$P(s|N) = \binom{N}{\frac{1}{2}(N+s)} P_a = \frac{N!}{\{\frac{1}{2}(N+s)\}!\{\frac{1}{2}(N-s)\}!} \left(\frac{1}{2}\right)^N \tag{34}$$

This is equivalent to the binomial distribution, and so we can find various statistical properties of the random walk if we would like. One question of relevancy is; what is the behaviour of $P(s|N)$ in the limit $N \to \infty$? By application of Stirlings approximation [172]:

$$n! \approx \sqrt{2\pi n}\; n^n e^{-n} \tag{35}$$

it may be shown that [166]:

$$P(s|N) = \lim_{N\to\infty} (\frac{2}{N\pi})^{\frac{1}{2}} e^{-\frac{s^2}{2N}} \tag{36}$$

Other statistics, such as the first time a random walker passes a particular point, may also be found. Interesting modifications of the classical random walk are possible - for example, one may consider the impact of non-isotropic jump probabilities, non-homogenous jump probabilities, or combinations thereof: one of the most obvious modifications which may represent a physical scenario consists of boundary conditions of various kinds. As such, the CRW provides a very flexible paradigm from which to consider various kinds of problem.

There are several limitations to the CRW approach:

- Time does not feature directly; it can only be incorporated if one takes the number of jumps taken by a random walker as a proxy
- The classical random walk assigns probabilities of jumping only to neighbouring grid-points
- Walkers can occupy only discrete locations on a lattice

The fact that time can only be introduced by proxy rather than directly has some consequences, especially if one wishes to consider the statistical properties of multiple (and then an ensemble) of random walkers. We consider a thought experiment which clarifies the issue.

Consider we have two random walkers. These undergo random walks on a structured lattice, as before, with a homogeneous and isotropic probability of making a jump to a nearest neighbouring grid point. As there is no system time defined in the random walk, time can only be measured by the number of jumps made by a random walker. If the walkers are assumed to jump synchronously, then it is easy to define a system time - each walker takes the nth jump concurrently, moving to an adjacent grid point with each step. This situation is identical to specifying that both walkers have an identical speed.

In the consideration of the movement of particles or other physical objects, we would quite like to model the random walkers as possessing a distribution of speeds.

Consider our two random walkers again; this time, they have a different speed. If the walkers are limited to moving only to neighbouring grid points, then the faster random walker must undertake more jumps in the same time as the slower random walker in order to be faster - however this is not possible unless a system time is defined which is not linked to the number of jumps any specific walker makes. Alternatively, if one still wished to use the number of jumps of one of the walkers as a measure of time and picked the 'slowest' walker, then one would need to move the faster walker a further distance in the same time - that is, there would then need to be a probability of not just jumping to a nearest neighbour, but to any grid-point, depending on the distance. Additionally, given that the walker is moving on a lattice, the lattice spacing would restrict the possible ratios of velocities of the random walkers.

Therefore classical random walk as it is seems too much of a simplification if we wish to model fluid phenomena.

3.1.2 The Continuous-Time Random Walk

The Continuous-Time Random Walk (CTRW) is the next step in the development of the classical random walk, attempting to deal with the time issue. We follow the treatment in 'Random Walks on Lattices II' [164]. It should be noted that the particular field that the CTRW is developed to deal with is solid-state physics, in which there are many problems which are well described by random walk of a walker on a discrete lattice. Many lattices are well-defined, such as the face-centred cubic lattice or the simple cubic lattice: as such, only a relatively small modification to the classical random walk is required to tailor it to this application.

We consider a random walker on a lattice. The lattice is 'toroidal' in geometry, i.e. periodic in every direction. Specifically, where we have labelled our lattice points $(x_1, x_2, ..., x_k)$, where k is the dimensionality of our lattice. Periodicity can be enforced as follows:

$$(x_1, x_2, ..., x_k) = (x_1 + j_1 N, x_2 + j_2 N, ..., x_k + j_k N) \tag{37}$$

Where $N, j \in \mathbb{Z}$ and we then have N^k lattice points. This may be extended to the (countably) infinite lattice by assuming $N \to \infty$.

A probability is defined, $P_n(\mathbf{x})$, which is the probability that a random walker is at $\mathbf{x}$ after the nth jump on its walk. We can then define a discrete recursion relation:

$$P_{n+1}(\mathbf{x}) = \sum_{\Delta\mathbf{x}} q(\Delta\mathbf{x}) P_n(\mathbf{x} - \Delta\mathbf{x}) \tag{38}$$

Where $q(\mathbf{x})$ is the probability density of a random walker experiencing a jump of length $\mathbf{x}$. $q(\Delta\mathbf{x})P_n(\mathbf{x} - \Delta\mathbf{x})$ then represents the probability of a walker present at $\mathbf{x}$ making a jump length $\Delta\mathbf{x}$, and so the sum over all $\Delta\mathbf{x}$ represents the sum over all possible paths to $\mathbf{x}$. The Fourier series of $q(\mathbf{x})$ is defined as the structure function.

Note that already the CTRW already overcomes one of the shortcomings of the CRW: jumps are not limited to neighbouring lattice-points. Consideration, however, is still limited to a

single random walker.

The continuous-time part of the CTRW is introduced by assuming that the walker makes jumps at random times, $t_0, t_1, t_2, \ldots$, where the intervals are:

$$\Delta t_1 = t_0 - t_1, \quad \Delta t_2 = t_1 - t_2, \ \ldots \ , \Delta t_i = t_{i-1} - t_i \tag{39}$$

And the intervals are given by a distribution $q_{\Delta t}(\Delta t)$. We may then say that the probability of a particle 'waiting' a time Δt at a particular point is then:

$$\psi(\Delta t) = 1 - \int_0^{\Delta t} q_{\Delta t}(t')dt' = \int_{\Delta t}^{\infty} q_{\Delta t}(t')dt' \tag{40}$$

We now have the tools to derive the Montroll-Weiss equation [173], which we do following Vlahos et al [167]. First, define the distribution of turning points $Q(\mathbf{x}, t)$, which are the set of points at which the random walker arrives at and begins a random walk jump:

$$Q(\mathbf{x}, t) = \int \int_0^t Q(\mathbf{x} - \Delta x, t - \Delta t) q_{\Delta t}(\Delta t) q_{\Delta x}(\Delta x) d\Delta t d\Delta x + \delta(t) P(\mathbf{x}, t = 0) \tag{41}$$

And $P(\mathbf{x}, t)$ is the probability that the walker is at $\mathbf{x}$, at time t. Note we now have not only the probability of making a jump of spatial length $q_{\Delta x}(\Delta x)$, but also our distribution of time intervals. Using this, we may then write our $P(\mathbf{x}, t)$, as the probability of our walker being at a turning point spatially located at $\mathbf{x}$, and then waiting there until time t:

$$P(\mathbf{x}, t) = \int_0^t Q(\mathbf{s}, t - \Delta t) \psi(\Delta t) d\Delta t \tag{42}$$

We may variously take the Fourier transform in space, and the Laplace transform in time of the previous few equations to acquire:

$$\widetilde{\hat{P}}(k, s) = \widetilde{\hat{Q}}(k, s) \widetilde{\psi}(s) \tag{43}$$

$$\hat{\widetilde{Q}}(k,s) = \hat{\widetilde{Q}}(k,s)\hat{q}_{\Delta x}(k)\widetilde{q}_{\Delta t}(s) + 1 \tag{44}$$

And then we may solve for $\hat{\widetilde{P}}(k,s)$ to find:

$$\hat{\widetilde{P}}(k,s) = \frac{1}{s}\frac{1-\widetilde{q}_{\Delta t}(s)}{1-\widetilde{q}_{\Delta t}(s)\hat{q}_{\Delta x}(k)} \tag{45}$$

By making careful assumptions about $q_{\Delta x}(\Delta x)$ and $q_{\Delta t}(\Delta t)$, and inverse-transforming, one may find a transport equation. For example, one may assume that $\widetilde{q}_{\Delta t}(s) = e^{-|s|^{\beta}}$ and $\hat{q}_{\Delta x}(k) = e^{-|k|^{\alpha}}$: that is, the distribution of spatial steps and times are given by symmetric Levy-α Stable distributions (see Section 6.4 for more details). If this is the case, then in the small-k, small-s limits, one can show that:

$$D_t^{\beta} P(x,t) = D_x^{\alpha} P(x,t) \tag{46}$$

There are still limitations to the CTRW approach shared with the CRW approach, which remain that time is still only present by proxy, as it is still incorporated by counting the numbers of jumps made by a particular particle; if one wished to consider an ensemble of random walkers, then the way the CTRW is constructed means that they must all share the same waiting times (i.e. jump synchronously), or one has to introduce a probability of 'seeing' a random walker between turning points [167]. Additionally, walkers are still considered to occupy discrete positions on a lattice - the product of this consideration is the waiting time distribution.

Considering particles in a fluid, we realise that since there are no well-defined positions which particles can occupy, the concept of a waiting time distribution is not appropriate. Hence, if we wish to consider the more general problem of the bulk properties of the random walk undertaken by an ensemble of particles not confined to a lattice, we need to consider a free-space approach that discards the waiting time. We do this in section 3.3.

3.2 Bachelier and Einstein's Random Walk

Bachelier and Einstein's approach is an approach which is not lattice-limited, considers an ensemble of particles, and makes no specific assumptions about time - as such, it seems to be a natural starting point for our task in the next section. The authors' French is limited, so we refer to [171] primarily. assume:

- a fluid contains 'n' particles, and '$f(x,t)$' is the number of particles per unit volume
- in a time interval, 'τ', the x-coordinate of each particle increases by a 'Δ'

Then the distribution of particles at $t+\tau$ can be written as in equation 47 - the Bachelier-Einstein equation.

$$f(x,t+\tau) = \int_{-\infty}^{\infty} f(x+\Delta,t)q(\Delta)d\Delta \tag{47}$$

$q(\Delta)$ is here assumed to have a number of properties.

- symmetry:
$$q(\Delta) = q(-\Delta) \tag{48}$$
- 0th moment:
$$\int_{-\infty}^{\infty} q(\Delta)d\Delta = 1 \tag{49}$$
- first moment (due to symmetry) :
$$\int_{-\infty}^{\infty} \Delta q(\Delta)d\Delta = 0 \tag{50}$$
- second moment
$$\int_{-\infty}^{\infty} \Delta^2 q(\Delta)d\Delta = 2D\tau \tag{51}$$
- ...that $q(\Delta)$ differs from zero only for small values of Δ

Armed with these assumptions, the LHS is expanded in time, and the RHS is expanded in terms of space, both using the 1-D Taylor expansion.

$$f(x, t+\tau) = f(x,t) + \tau \frac{\partial f(x,t)}{\partial t} \tag{52}$$

$$f(x+\Delta, t) = f(x,t) + \Delta \frac{\partial f(x,t)}{\partial x} + \frac{\Delta^2}{2!} \frac{\partial^2 f(x,t)}{\partial x^2} + ... \tag{53}$$

these are then substituted into Eqn. 47, to obtain:

$$f(x,t) + \tau \frac{\partial f}{\partial t} = f(x,t) \int_{-\infty}^{\infty} \phi(\Delta) d\Delta + \frac{\partial f(x,t)}{\partial x} \int_{-\infty}^{\infty} \Delta \phi(\Delta) d\Delta + \frac{1}{2!} \frac{\partial^2 f(x,t)}{\partial x^2} \int_{-\infty}^{\infty} \Delta^2 \phi(\Delta) d\Delta + ... \tag{54}$$

Terms are then either eliminated due to symmetry, or the assumption that "...Each subsequent term is very small compared with the one preceding it", which the paper states results in the diffusion equation:

$$\frac{\partial f}{\partial t} = D \frac{\partial^2 f(x,t)}{\partial x^2} \tag{55}$$

The paper goes on to find that for non-interacting particles which are conserved, and have a distribution which obeys equation 55, the Gaussian distribution is found: it may also be observed that the root mean displacement is proportional to the square root of the time in the system, which follows from Eqn. 51.

3.3 The Observational Random Walk

We introduce an 'observational' random walk, which is a formalism designed to deal with the general problem of an ensemble of random walkers in free space, with time not simply a proxy for the number of steps a random walker takes, but some reference time.

Physically, if our random walker is a particle in a fluid system, it does not seem appropriate

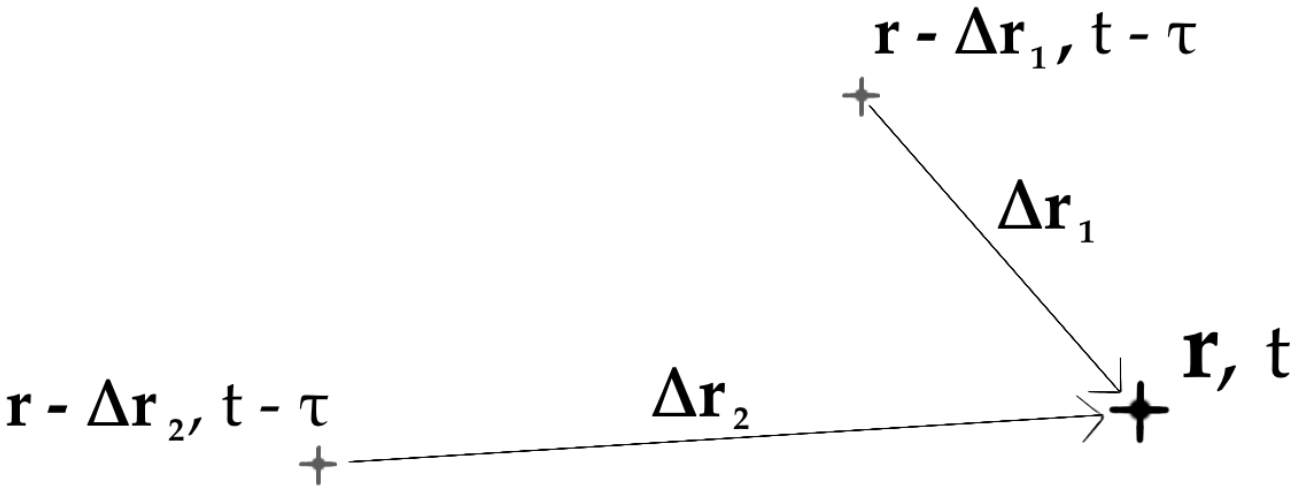

Figure 13: The current particle position, $\boldsymbol{r}, t$, and two possible prior positions

to consider its motion in terms of distinct jumps, or in terms of a distinct waiting time at a particular position.

It is much more intuitive to consider the physical random walker in terms of observations; if one is observing a random walker, its behaviour is characterised by recording its positions at different times, separated by an observation interval, which we denote τ. This line of thought is readily extended to an ensemble of particles; in the same observation interval, one may record all their positions concurrently. This then conveniently introduces an intrinsic time, τ, which may be readily linked to other physical phenomena.

Observing our ensemble of random walkers, and recording their positions every observation interval, we may be interested in the distribution of jumps made by the ensemble in an observation interval. We name this distribution of random walker jumps in observation time τ the *jump function*, denoted $q(\Delta\mathbf{r}, \tau)$. This is well defined for both an ensemble, and for a single random walker.

Using the same rationale as Bachelier, we may then construct a recursion relation, which relates current and past states of the ensemble. At a previous observation time, $t - \tau$, the particle could have been at a set of positions, $\mathbf{r} - \Delta\mathbf{r}$ - as in Fig. 13.

Conservation of random walkers is assured via equation 56, which is effectively a statement that a particle will have some jump, including a zero length jump, over an observation interval.

$$1 = \int_{-\infty}^{\infty} q_{\Delta\mathbf{r},\tau}(\Delta\mathbf{r},\ \tau)\ d\Delta\mathbf{r} \tag{56}$$

Considering the position of interest, $\mathbf{r}$, τ, the only way a walker exists there at a current observation is if a walker at a previous observation, $\mathbf{r} - \Delta\mathbf{r}_1,\quad t - \tau$, was displaced by an $\Delta\mathbf{r}_1$. A jump of this length has a probability $q_{\Delta\mathbf{r},\tau}(\Delta\mathbf{r}_1,\ \tau)$. So, the probability density of a walker being found at a current point of interest, $P(\mathbf{r}_c,\ t_c)$, is then the sum over all paths, appropriately weighted.

By permitting summing over all possible paths to $\mathbf{r}_c,\ t_c$, we find:

$$P(\mathbf{r}_c,\ t_c) = \int_{-\infty}^{\infty} P(\mathbf{r}_c - \Delta\mathbf{r},\ t_c - \tau) q_{\Delta\mathbf{r},\tau}(\Delta\mathbf{r},\ \tau)\ d\Delta\mathbf{r} \tag{57}$$

It can be shown that in the spatially one-dimensional case, using two-dimensional (space and time) Taylor expansion and making the assumption that the first moment of the jump function is zero, and the second moment is σ^2 (equivalent to assuming a Gaussian jump function), we recover the equation governing the evolution of $P(x_c,\ t_c)$:

$$\frac{\partial P(x_c,\ t_c)}{\partial t_c} = \frac{\sigma^2}{2\tau}\frac{\partial^2 P(x_c,\ t_c)}{\partial x_c^2} - \frac{\sigma^2}{2}\frac{\partial^3 P(x_c,\ t_c)}{\partial x_c^2 \partial t_c} \tag{58}$$

This reduces to the classical diffusion equation when Eqn. 59 is satisfied, which suggests that the smaller the time between observations, the more time variation of P is permitted before the rightmost term in Eqn. 59 begins to be significant.

$$\frac{1}{\tau} \gg \frac{1}{P(x_c,\ t_c)}\frac{\partial P(x_c,\ t_c)}{\partial t_c} \tag{59}$$

Note that if we consider the limit of locality as being the 'hardest' case, given that the jump function is the distribution of jumps that are physically possible, then it becomes obvious that for a given lab observation interval τ, the maximum possible distance that can be moved by a non-interacting particle is $|\Delta\mathbf{r}| = c\tau$, where c is the speed of light in the medium. As such, the probability of a particle being observed to make a jump greater than

this magnitude must be zero. It is then possible to see that in the very small limit $\tau \longrightarrow 0$, the jump function will tend toward a delta distribution. This is simple recognition of the fact that as observation interval tends to zero, the particle will be increasingly likely to appear closer and closer to the location of the previous observation, which can be represented in the zeroth moment of the jump function as:

$$1 = \int_{-\tau c}^{\tau c} q_{\Delta\vec{r},\tau}(\Delta\vec{r},\ \tau)\ d\Delta\vec{r} \tag{60}$$

The 1-D case is a convolution, with a Fourier representation (where $x_c \longrightarrow k$) as:

$$\hat{P}(k,\ t_c) = \hat{P}(k,\ t_c - \tau)\hat{q}_{k,\tau}(k) \tag{61}$$

In order to be able to apply Fourier analysis, we assume that $P(x)$ and $q(\Delta x)$ tend to zero as $x,\ \Delta x \longrightarrow \infty$, which is a reasonable assumption in many physical systems.

To find the equation for P, all that has to be done is the two dimensional Taylor series expansion of 61, followed by an inversion to find the x_c space representation. The two dimensional expansion captures the cross terms, and results in the appearance of the time derivative. For example, in the case of a Gaussian-like jump function with characteristic function (the Fourier transform of the jump function) as in Eqn. 62, we can recover Eqn. 63, which is then the full solution of the recursion relation relation for the case that observations are at a constant interval, with Gaussian character and no net drift.

$$\hat{q}_{k,\tau}(k) = e^{-Z|k|^{\zeta}},\quad \zeta = 2 \tag{62}$$

$$\sum_{j=1}^{\infty}(-1)^{j+1}\frac{\tau^j}{j!}\frac{\partial P(x_c,\ t_c)}{\partial t_c^j} = \sum_{j=0}^{\infty}\frac{\tau^j}{j!}\frac{\partial}{\partial t_c^j}\left\{\sum_{n=1}^{\infty}\frac{Z^n}{n!}\frac{\partial^{2n}P(x_c,\ t_c)}{\partial x_c^{2n}}\right\} \tag{63}$$

It can be shown that by neglecting terms of $O(x_c^4), O(\tau^2)$ or greater, we return an equation of the form of Eqn. 58 with the same conditions on tending to the Fickian diffusion equation.

Table 1: Table of coefficients, $c_{a,b}$, for the first three temporal and first five spatial derivative orders, in the case that the jump function is Gaussian

s-order	0th t-order	1st t-order	2nd t-order
0	$c_{0,0} = \frac{A-1}{2\pi}$	$c_{0,1} = -\frac{A\tau}{2\pi}$	$c_{0,2} = \frac{A\tau^2}{2!\ 2\pi}$
1	$c_{1,0} = \frac{B}{2\pi}$	$c_{1,1} = -\frac{B\tau}{2\pi}$	$c_{1,2} = \frac{B\tau^2}{2!\ 2\pi}$
2	$c_{2,0} = \frac{A\alpha}{2\pi}$	$c_{2,1} = -\frac{A\alpha\tau}{2\pi}$	$c_{2,2} = \frac{A\alpha\tau^2}{2!\ 2\pi}$
3	$c_{3,0} = \frac{B\beta}{2\pi}$	$c_{3,1} = -\frac{B\beta\tau}{2\pi}$	$c_{3,2} = \frac{B\beta\tau^2}{2!\ 2\pi}$
4	$c_{4,0} = \frac{A\alpha^2}{2!\ 2\pi}$	$c_{4,1} = -\frac{A\alpha^2\tau}{2!\ 2\pi}$	$c_{4,2} = \frac{A\alpha^2\tau^2}{2!2!\ 2\pi}$

Eqn. 63 represents an infinite series. For the normally diffusive case, only certain terms are relevant, based on the magnitude of the coefficients and differential order. However, should the jump function not possess a Gaussian character, then it may be the case that other terms are relevant - so, we can define a general differential equation composed of all possible combinations of the partial integer order derivatives in both directions, as in equation 64, with a differential coefficient, $c_{a,b}$, for each order derivative. The coefficient may be found from the particular version of Eqn. 63 which arises from the jump function.

$$0 = c_{0,0}f + c_{1,0}\frac{\partial f}{\partial x} + c_{0,1}\frac{\partial f}{\partial t} + c_{1,1}\frac{\partial^2 f}{\partial x \partial t} + c_{2,0}\frac{\partial^2 f}{\partial x^2} + c_{0,2}\frac{\partial^2 f}{\partial t^2} + ... + c_{i,i}\frac{\partial^{2i} f}{\partial t^i \partial x^i} \tag{64}$$

In this case, the first subscript indicates the coefficient belonging to the spatial derivative, with the value of the coefficient indicating derivative order, and the second is the same but for the time derivative. Some of these terms feature in equations describing phenomena across various disciplines in the sciences, so we call '$c_{0,0}$' the damping term, '$c_{0,1}$' the Fickian term, '$c_{0,2}$' the telegraphers term, '$c_{1,0}$' the advection term, and '$c_{2,0}$' the diffusion term. Odd spatial derivatives tend to have an advection-like character, while even derivatives tend to have a diffusion-like character.

the classical diffusion term is then easily expressed in terms of the coefficients,

$$d = -\frac{c_{2,0}}{c_{0,1}} \tag{65}$$

Based on the assumption of a Gaussian jump function with drift - a jump function of Gaussian character, but a non-zero mean - we can find the coefficients of each differential term. In the one dimensional case drift is easily imposed using the Fourier shift identity.

$$FT\left\{q_{\Delta x-\mu_s,\tau}(\Delta x-\mu_s)\right\} \longrightarrow e^{-ik\mu_s}\hat{q}_{k,\tau}(k) \tag{66}$$

Eqn. 62 is easily modified to incorporate particle drift. It is then possible to express the characteristic function of the jump function as the sum of a real and imaginary part, which for the shifted-Gaussian jump function can be shown to have the form:

$$\hat{q}_{k,\tau}(k) = Ae^{-\alpha k^2} + ikBe^{-\beta k^2} \tag{67}$$

The imaginary component originates entirely from the drift in the jump function. Some of the coefficients of the general differential equation for the jump function with characteristic function of form 67 are presented in table 1.

By acquiring some jump function of any form, it is possible to find an evolution equation. For a jump function well described by:

$$q_{\Delta x,\tau}(\Delta x) = \Gamma e^{-\gamma \Delta x^2} \tag{68}$$

this is Fourier transformed to equation:

$$\hat{q}_{k,\tau}(k) = \Gamma\sqrt{\frac{\pi}{\gamma}}e^{-\frac{k^2}{4\gamma}} \tag{69}$$

Via substitution we may find the damping, Fickian, and diffusion terms using table 1 and equation 67, and so find the classical diffusion coefficient. Due to the zero-value of the

imaginary terms in this case, by inspection of table 1 it is clear that all the highest order odd derivatives are equal to zero - hence the previous reference to odd derivatives being advection-like, and even ones being diffusion-like.

$$c_{0,0} = \left(\Gamma\sqrt{\frac{\pi}{\gamma}} - 1\right)\frac{1}{2\pi} \tag{70}$$

$$c_{0,1} = -\frac{\tau\Gamma}{\sqrt{4\pi\gamma}} \tag{71}$$

$$c_{2,0} = \frac{\Gamma\gamma^{-\frac{3}{2}}}{8\sqrt{\pi}} \tag{72}$$

$$d = \frac{1}{4\gamma\tau} \tag{73}$$

Enforcing the zeroth moment condition of equation, and introducing the standard deviation (σ), we then have:

$$\Gamma = \frac{1}{\sigma\sqrt{2\pi}}, \quad \gamma = \frac{1}{2\sigma^2} \tag{74}$$

Which can then be used to recover the classical result $d = \frac{\sigma^2}{2\tau}$, and that $c_{0,0} = 0$, in addition to the fact that higher orders are much less significant. The forms of the differential coefficients become more cumbersome with less ideal jump functions, but the Fourier method allows any form provided the jump function is well characterised. Note that we find a significantly more elegant way of doing this in section 6, that also furnishes a derivation of Fick's first law for arbitrary jump function, and we use that approach going forwards.

Using the observational random walk (ORW), if we can identify or construct a jump function between system states then we can find an equation governing the evolution of the system. It is not subject to the limitations of the CRW or CTRW, and indeed it is very possible to alter the jump function such that the ensemble moves on a lattice.

One point to note is that the elimination of the waiting time in the ORW means that time-fractionality cannot be introduced in the ORW as there is in the CTRW (see Eqn. 46) - an analogous way of introducing time-fractionality in the ORW would be to have a statistical

observation interval, τ, drawn from a LαS distribution; however, the jump function would also change self-consistently with τ. It would be of interest to consider the physical origin of time-fractionality in ensembles of random walkers, and especially whether we can identify conditions under which it arises, as it is not obvious.

3.4 The Central Limit Theorem and Conditions for Stable Random Walks

For a given physical system it should be possible to define a jump function, $q_{\Delta x,\tau}(\Delta x, \tau)$, for the ensemble of random walkers. We have demonstrated that the diffusion equation must arise in cases where the jump function is Gaussian. It is then sensible to question why this should be the case, and under what conditions. To do so, we will construct the single walker and ensemble jump function from first principles using the ORW. We will then consider the short-time case, and then the long-time case. We will then demonstrate how the CRW and CTRW can be obtained directly from the long-time ORW formalism. Finally, we will consider the central limit theorem (CLT) and general central limit theorem (GCLT), and see that when considered with the ORW, allows us to understand the long-time behaviour.

3.4.1 The Short-Time ORW

Consider a particle moving with a constant velocity, $\mathbf{v}$. The observational random walk formalism immediately allows us to characterise this population with a jump function:

$$q(\Delta\mathbf{x}, \tau) = \delta(\Delta\mathbf{x} - \mathbf{v}\tau) \tag{75}$$

For an ensemble of non-interacting ballistic particles which are not acted on by an external force, such that $v_i(t) = v_i(t + \tau) \ \ \forall\ \tau$, and with particles, n_i, with $i \in [0, N]$, each with a velocity, v_i, we may then construct the jump function as:

$$q(\Delta\mathbf{x}, \tau) = \frac{1}{N}\sum_{i=0}^{N} \delta(\Delta\mathbf{x} - v_i\tau) \tag{76}$$

In the small time limit, such that no collisions have occurred and that motion is purely ballistic, one may therefore write the jump function of an ideal gas as in Eqn. 76, with the v_i corresponding purely to the initial distribution of particle velocities. A particular measure used to judge whether the transport of particles is anomalous is the mean squared displacement, $\overline{|x(t) - x(0)|^2}$ - or, the absolute value of the relative dispersion, squared, averaged over all particles. This may be calculated using our jump function. Denoting our absolute relative displacement over the observation interval in one dimension as $|q(\Delta x, \tau)|$, we may write:

$$|q(\Delta x, \tau)| \equiv q(\Delta x, \tau) + q(-\Delta x, \tau), \quad \Delta x > 0 \tag{77}$$

Which still maintains all the required properties of a PDF. The statistical moments of $|q(\Delta x, \tau)|$ may be written as:

$$\overline{|q(\Delta x, \tau)|^n} = \int_0^\infty \Delta x^n |q(\Delta x, \tau)| d\Delta x \tag{78}$$

And we identify:

$$\overline{|q(\Delta x, \tau)|^2} \equiv \overline{|x(\tau) - x(0)|^2} \tag{79}$$

considering a single particle with velocity $v_i > 0$, we may then write the second moment as:

$$\overline{|q(\Delta x, \tau)|^2} = \int_0^\infty \Delta x^2 \delta(\Delta x - v_i \tau) d\Delta x = v_i^2 \tau^2 \tag{80}$$

and for an ensemble we may write:

$$|q(\Delta x, \tau)| = \frac{1}{N} \sum_{i,\ v_i \geq 0} \delta(\Delta x - v_i \tau) + \frac{1}{N} \sum_{i,\ v_i < 0} \delta(-\Delta x - v_i \tau) \tag{81}$$

so:

$$\overline{|q(\Delta x,\tau)|^2} = \frac{1}{N}\int_0^\infty \sum_{i,\ v_i\geq 0} \Delta x^2 \delta(\Delta x - v_i\tau)d\Delta x + \sum_{i,\ v_i<0} \Delta x^2\delta(-\Delta x - v_i\tau)d\Delta x \tag{82}$$

therefore:

$$\overline{|q(\Delta x,\tau)|^2} = \frac{1}{N}\sum_{i,\ v_i\geq 0}(v_i\tau)^2 + \sum_{i,\ v_i<0}(-v_i\tau)^2 = \tau^2\frac{1}{N}\sum_{i=0}^{N} v_i^2 = \overline{v_i^2}\tau^2 \tag{83}$$

We find an MSD $\propto \tau^2$, which is the short time limit for particle diffusion in an ideal gas - this kind of diffusion is referred to as ballistic diffusion.

3.4.2 The Long-Time ORW

In the long time, a random walker undergoes a sequence of jumps, which may be in arbitrary directions. We say that in each observation interval, the particle may undergo multiple changes in velocity, $\partial v_{i,j+1}^k$, with k changes for $k \in [0,\infty]$. At the next observation, the particle will be observed with velocity:

$$\mathbf{v}_{i,j+1} = \mathbf{v}_{i,j} + \partial\mathbf{v}_{i,j+1}, \quad where \quad \partial\mathbf{v}_{i,j+1} = \sum_k \partial\mathbf{v}_{i,j+1}^k \tag{84}$$

so the jump function at time $t = \tau(j+1)$ will then be:

$$q_{i,j+1}(\Delta\mathbf{x},\tau) = \delta(\Delta\mathbf{x} - (\mathbf{v}_{i,j} + \partial\mathbf{v}_{i,j+1})\tau) \tag{85}$$

this may be expressed as:

$$q_{i,j+1}(\Delta\mathbf{x},\tau) = \delta(\Delta\mathbf{x} - \mathbf{v}_{i,j}\tau) * \delta(\Delta\mathbf{x} - \partial\mathbf{v}_{i,j+1}\tau) \tag{86}$$

where the $*$ denotes the convolution operator, and after m observation intervals:

$$q_{i,m}(\Delta\mathbf{x},\tau) = \delta(\Delta\mathbf{x} - \mathbf{v}_{i,0}\tau) \overset{m-1}{*} \delta(\Delta\mathbf{x} - \partial\mathbf{v}_{i,m}\tau) \tag{87}$$

Then, the average jump function for all particles at m is then:

$$q_m(\Delta\mathbf{x},\tau) = \frac{1}{N}\sum_{i=0}^{N} q_{i,m}(\Delta\mathbf{x},\tau) \tag{88}$$

This encompasses all possible random walks. To specify any random walk, what is required is the specification of the distribution of k; the probability that a change in the walker trajectory occurs - and the specification of the distribution of $\mathbf{v}_{i,j}^k$; that is, the details of the change in walker trajectory, should a change in trajectory occur. It is reasonable to use spherical coordinates in 3D or cylindrical coordinates in 2D to specify $\partial\mathbf{v}_{i,j}^k$, such that:

$$\partial\mathbf{v}_{i,j}^k = r_{i,j}^k(cos\theta_{i,j}^k\hat{\mathbf{e}}_x + sin\theta_{i,j}^k\hat{\mathbf{e}}_y) \tag{89}$$

The random walk is then fully specified once one has defined $P(r)$ and $P(\theta)$ - or the probability of a net radial velocity change r, and scattering angle θ - as well as $P(k)$ in relation to τ.

If we wish to specify the CRW on a square lattice in this formalism, where a lattice has uniform and isotropic lattice spacing a, we specify that $k = 1$, $v_{i,0} = 0$, $\partial\mathbf{v}_{i,j}^k = \frac{a}{\tau}$ and:

$$P(\theta) = \frac{1}{4}\left[\delta(\theta) + \delta(\theta - \frac{\pi}{2}) + \delta(\theta - \pi) + \delta(\theta - \frac{3\pi}{2})\right] \tag{90}$$

The CTRW for the same lattice has the same $P(\theta)$. To introduce the waiting time, one has

to set an appropriate $P(k)$ with $k \in [0,1]$ and dependent on the residence time in terms of τ. $P(r)$ may then be set in terms of the lattice spacing as with the CRW.

3.4.3 Conditions for Stable Random Walks

In the long time m, if the jump function converges, then we expect there to be an m_{crit} such that:

$$q_{m_{crit}}(\Delta\mathbf{x}, \tau) \approx q_{m_{crit}+1}(\Delta\mathbf{x}, \tau) \tag{91}$$

Which is the long-time jump function, which is simply then referred to as $q(\Delta\mathbf{x}, \tau)$. There is a question of what m_{crit} and $q(\Delta\mathbf{x}, \tau)$ are, and under what conditions they converge.

The central limit theorem may be stated as: the sum of (properly normalised) statistically independent and identically distributed (iid) random variables converges to a normal distribution, provided that their variance is finite [174]. Practically, this means that if we have iid random variables $X_1, X_2, ...X_n$ which are sampled from a population which has a mean, μ, and variance, σ^2, then the sample mean $\bar{X} = \sum_i^n \frac{X_i}{n}$ possesses the property that:

$$\frac{\bar{X} - \mu}{\sigma/\sqrt{n}} \longrightarrow N(0,1) \; as \; n \to \infty \tag{92}$$

The general central limit theorem, in contrast, considers the distributions to which iid random variables converge to, in the case that the variance is infinite. This was first discussed in English by Gndenko and Kolmogorov in 'Limit Distributions for Sums of Independent Random Variables' [175], to which we refer.

Essentially, it can be demonstrated that in the case that the variance is not necessarily well defined, the only convergent distribution is the stable, or Levy-α Stable (LαS), distribution[21]. Consequently, given $q_m(\Delta\mathbf{x}, \tau)$ can be expressed in terms of the sum of trajectory changes and these are iid, then if there is an m_{crit}, it must belong to the LαS.

[21] Please see section 6.4 for definition and details thereof

In terms of our ORW formalism then, for convergence we require our $\partial \mathbf{v}_{i,j}^k$ to belong to a process which is iid. If this has a variance which is not well defined, then it will belong to the LαS distribution. If the variance is well defined, then it will belong to the normal distribution.

In the case of an isotropic and homogeneous fluid, it is reasonable to think that our $\partial \mathbf{v}_{i,j}^k$ will be iid with a well-defined variance due to thermalisation. Less obvious are the cases that there are large changes in mean free path, density, temperature or other variables, and how these impact the assumptions of iid, or what the impact of turbulence or coherent structures should be on the jump function. These require careful consideration. As such, we begin with measurement in certain systems, in order to demonstrate that that the LαS case is of relevance.

4 Measuring Jump Functions in an Ideal System

Using the recursion relation, Eqn. 57, or the stochastic flux equation 198, it is possible to infer a transport equation with knowledge of the jump function, q, or its pair $\hat{q}$.

Aside from construction of the jump function from first principles, we may also obtain the jump function by direct consideration of the motion of appropriate random walkers. For example, we may identify a jump function by observing the motion of tracers in a system of interest.

We may estimate the jump function over an observation interval, τ, by considering the motion of tracer particles in a statistically stationary system as follows:

1. Propagate a statistically significant number of test particles on the system.
2. Separate the acquired time series of particle locations into non-overlapping sections with length τ.
3. For each time series of length τ, calculate the absolute dispersion - the distance between the initial and final location - for each particle.

4. The jump function over the observation interval is the probability distribution of the absolute dispersion over the interval τ.

5. Examine the jump function and find the most appropriate fit. Alternatively, one may find the Fourier transform of the jump function (the complementary function), and find the fit in Fourier space. This may be more appropriate since the Symmetric α-Stable distributions are well defined in Fourier space.

To test this, we should examine an ideal system and see whether we obtain reasonable results.

4.1 Jump Functions in Simple Isotropic Synthetic Turbulence

We consider 10^5 Lagrangian tracers in an isotropic 2D 'turbulent' system at steady state. A synthetic field, ϕ, is generated on a grid of n_x, n_z cells in each dimension, and n_{out} output steps. The field is initialized such that features exist at every scale, and given by:

$$\phi = \sum_{n=1}^{n_x} \sum_{m=1}^{n_z} \cos(xk_x + \xi_x) \cos(zk_z + \xi_z) \tag{93}$$

where:

$$k_x = \frac{2\pi n}{n_x}, \quad k_z = \frac{2\pi m}{n_z} \tag{94}$$

and:

$$\xi_x = \mathbf{a}^x_{n,m,n_{out}} \pi, \quad \xi_z = \mathbf{a}^z_{m,n,n_{out}} \pi \tag{95}$$

Where $\mathbf{a}$ can be understood to be an array of phases. The approach here is somewhat similar to synthetic fields used previously in the literature for a similar purpose, e.g. Pettini et al [176][22]. For pure white noise, the phases in $\mathbf{a}$ for all output steps are unrelated, and selected from a normal distribution with zero mean and standard deviation equal to unity - we refer to this case as zero correlation. Brownian noise is implemented by selecting the $n_{out} = 0$ as for white noise for both $\mathbf{a}$, then generating the subsequent n_{out} values for $\mathbf{a}$ based on the previous values but adding a value selected from a Gaussian distribution with zero mean,

[22]More sophisticated synthetic fields are conceivable - such as those targeting a particular turbulent spectrum [177], and it would be extremely interesting to study these dynamics too. This is outside the scope of this thesis, but seems a rich area of study

and standard deviation being a proportion of the standard deviation used to generate the initial values, typically 0.1. The Brownian generation of **a** leads to a system which evolves with a finite correlation, such that randomly generated structures on various scales can be observed propagating across the system in a manner similar to the characteristic behaviour of turbulence - we refer to this case as finite correlation. The effects of this are visible in Fig. 14 and 15, which show snapshots of zero correlation ϕ-field and finite correlation ϕ field respectively.

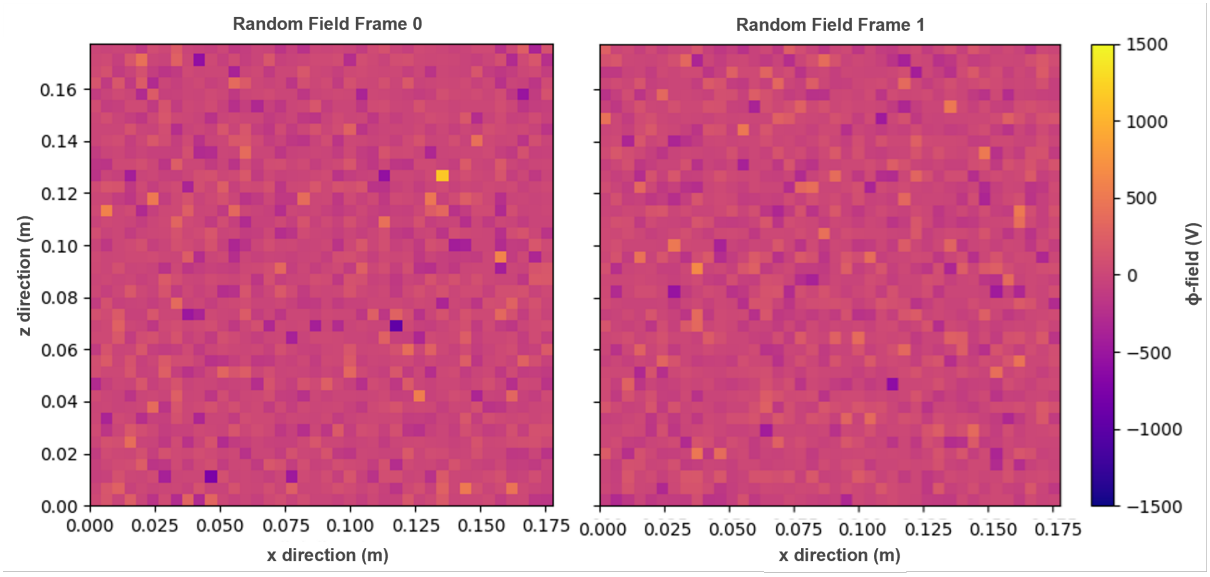

Figure 14: Evolution of the zero correlation synthetic field between two frames on a 50x50 grid. Frames appear to share no similar features

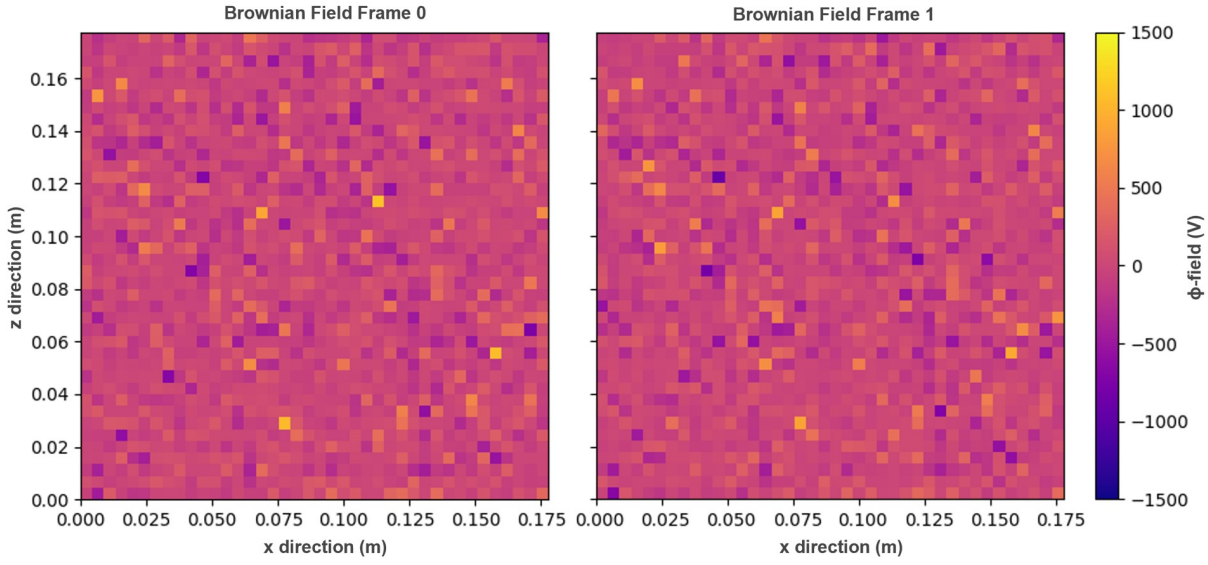

Figure 15: Evolution of the finite correlation synthetic field between two frames on a 50x50 grid. Similar features can be seen in both frames

Once the synthetic ϕ-field is generated, we propagate tracers on top. Massless particles are propagated by the ExB drift velocity as in equation 96. A third-order Adams-Bashforth integrator was used. We consider the ExB drift as this is particularly relevant in MCF plasmas. It arises due to gradients in the electric potential, which occur spontaneously. Other drifts can also be considered, but the ExB velocity is reasonable for the case of ideal massless particles with zero inertia - this is standard for tracking passive particles in plasmas [178].

$$x_{i+1} = x_i + \int_{t_i}^{t_{i+1}} \vec{v}_{E\times B}(x,t) \cdot \hat{x}\ dt \tag{96}$$

where:

$$V_x = -\frac{\mathbf{E}\cdot\hat{z}}{B_0}, \qquad V_z = \frac{\mathbf{E}\cdot\hat{x}}{B_0} \tag{97}$$

and:

$$\mathbf{E} = -\nabla\phi \tag{98}$$

Here the unit vectors are denoted $\hat{x}$ and $\hat{z}$. $\mathbf{E}$ for each particle is calculated from the grid value of ϕ at the position of the particle, and $\mathbf{E}$ is calculated using a second order central difference method. Due to a focus on plasma systems, it is convenient to specify some parameters largely used for (Bohm) normalisation: $B_0 = 0.5\ T$, $T = 40\ eV$, $\delta t = 1\times10^{-9}\ s$, $\Omega_i = \frac{eB_0}{m_i}$, $c_s = \sqrt{\frac{eT}{m_i}}$, $\rho_s = \frac{c_s}{\Omega_i}$. The size of cells is determined by $dx = \frac{L_x}{n_x}, dz = \frac{L_z}{n_z}$, where L_x, L_z are set in units of ρ_s (the ion Larmour radius at the electron temperature). In the context of the edge of a plasma device, x is the radial direction in which equilibrium gradients occur, and the direction perpendicular to the plane (y) would be the direction of the magnetic field, and z is the binormal direction. The zero correlation case has uncorrelated velocity and a time average of zero, as expected, with the mean velocity for each timestep having $\frac{V_x}{\sigma_x} << 1$. The finite correlation case contains some correlation in the velocity fields, but again has a time average of zero. There is a small net ExB field in each frame similar in magnitude to the white noise case, and these are due to numerical error.

We can consider the Eulerian single-point velocity correlation as in Eqn. 99, which in this case is the spatially averaged auto-covariance of the velocities at the grid points - a measure of how the field varies with itself:

$$E_v(t) =< \tilde{v}(t_1)\tilde{v}(t_1+t) >_{t_1} \tag{99}$$

Where we define the fluctuation part of f as:

$$\tilde{f} = f - < f >_a \tag{100}$$

where the average, $< f >_a$ is as:

$$< f >_a = \frac{1}{L_a} \int f da \tag{101}$$

and L_a is a normalising length in the a-direction.

In the homogeneous, Gaussian, and stationary turbulence case we expect the synthetic field to have the auto-covariance of form as [179]:

$$E_v(t) \sim e^{-\frac{t}{R_c}} \tag{102}$$

This is indicative of pattern persistence in the system. R_t is the correlation time, the measure of how long a system retains correlation - a system observed at intervals much longer than its correlation time will appear to have little similarity.

The Eulerian velocity correlations of the finite correlation synthetic field (averaged over the grid) are displayed in Fig. 16. The fits suggest a correlation time of $R_c \sim 10$ timesteps. The same graph for the zero correlation synthetic field has a correlation time $R_c = 0$, as expected.

Propagated particles experience periodic boundary conditions such that once they pass over any boundary they reappear on the opposite boundary. The primary output data from particle tracking are absolute coordinates in z-x at every time step, the absolute displacement in infinite space from the initial seeded location, and a record of whether the particle crossed a boundary or boundaries during a particular step. We generally use particle systems of 10^5 particles. The PDF's of the velocities experienced by the particles (Lagrangian) and at the grid centres (Eulerian) are shown in Fig. 17. We see they are nearly identical, which suggests the tracer statistics are a good proxy for the field statistics, as discussed by Basu et al [178].

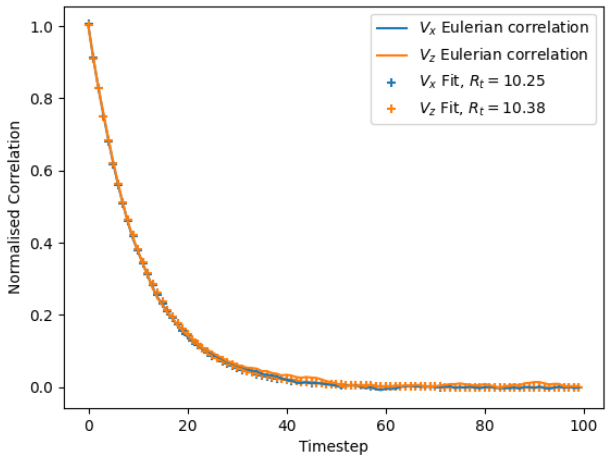

Figure 16: Normalised Eulerian velocity correlation over timesteps, finite correlation synthetic field on 200x200 grid.

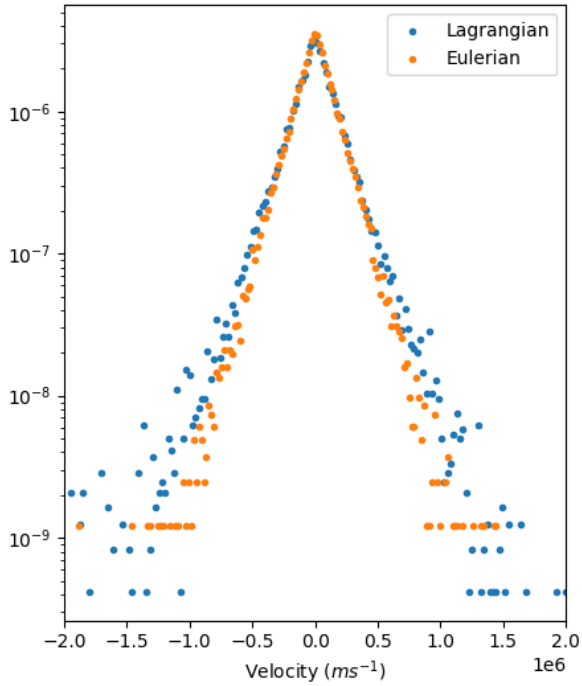

Figure 17: PDF's of the Lagrangian and Eulerian velocities in the x-direction

Table 2: Table of regimes of the MSD

Regime	Value of η
Sub-diffusive	$\eta < 1$
Diffusive	$\eta = 1$
Super-diffusive	$\eta > 1$
Ballistic	$\eta = 2$

This setup is similar to thought experiments that lead to the Brownian motion concept - particles being driven by random impulses. We have a system which evolves - the particles on the synthetic ϕ field which develops. Provided the statistical properties of the particle evolution remain approximately the same over the system time, and that it remains isotropic, then we can consider applying the ORW to the system.

As discussed in section 3.2, we expect diffusive particles to have a scaling such that we may define a general mean-squared displacement:

$$< r^2(t) > \sim t^{\eta} \tag{103}$$

Where it is calculated from particle positions as:

$$< r^2(t) >= \frac{1}{N} \sum_{i=1}^{N} |r_i(t) - r_i(0)|^2 \tag{104}$$

In the diffusive case, we expect $\eta = 1$, and in the case of ballistic random walkers, we expect $\eta = 2$ (see Eqn. 80). As such, we may characterise the MSD as in table 2:

Where subdiffusion represents a regime in which random walkers propagate slower than they would in a diffusive system, and superdiffusion represents a regime in which random walkers propagate faster than they would in a diffusive system [10], and these more unusual values of η have been observed [161].

As discussed in section 3.2, the diffusion coefficient is directly related to the mean squared displacement such that:

$$d = \frac{< r^2(t) >}{2t} \tag{105}$$

As particles propagate, we expect them to display initially ballistic behaviour, followed by a diffusive behaviour *if* the long-time behaviour is diffusive, for the reasons discussed in section 3.4.

The MSDs for both the zero and finite correlation cases are as shown in Fig. 18. The behaviour in both cases tends to a constant diffusion coefficient, approximately 13.7 $m^2 s^{-1}$ for the zero correlation case and approximately 37.3 $m^2 s^{-1}$ for the finite correlation case, calculated from the gradient of the Mean Square Displacement.

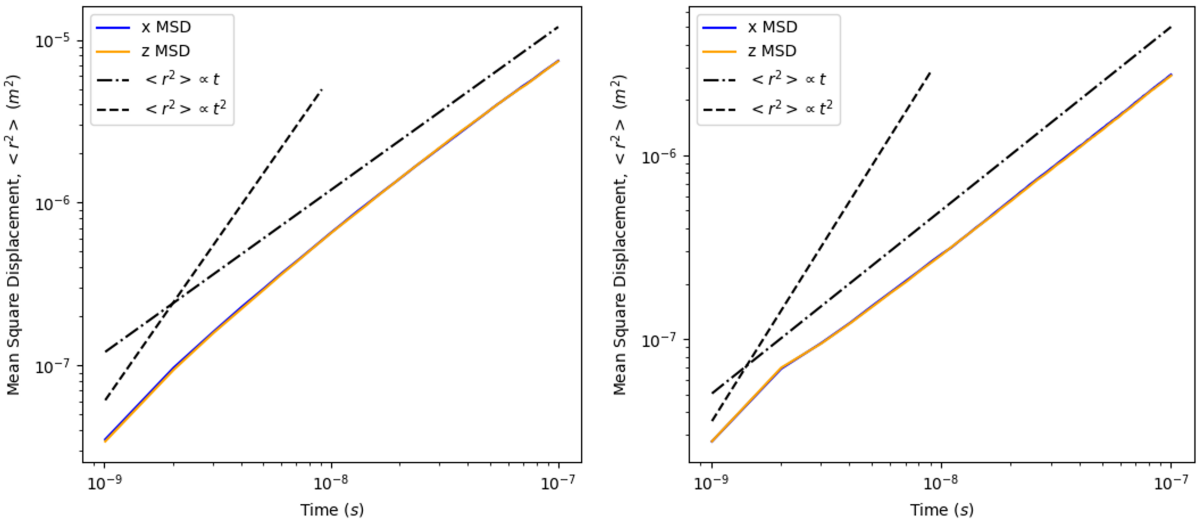

Figure 18: Mean Square Displacements for Brownian evolved (Left) and White noise evolved (Right) synthetic fields

The mean squared displacement tends to linear, indicating a constant diffusion coefficient which is consistent with $\eta = 1$ and so is representative of a normally diffusive process occurring. There also appears to be a short time ballistic regime, which is expected [23]. This synthetic field is then ideal for testing our numerical tools. We expect for the isotropic normally diffusive case, that the jump function be spatially separable - we assume the jump functions are statistically independent - and have a Gaussian shape, since this is a core assumption that leads to normal diffusion in section 3.3. We find that this is essentially the case, both for particles evolved on the finite correlation ϕ field, and for particles on the zero correlation ϕ case, and that the jump function is well described as being spatially separable.

[23] Short-time ballistic transport and long-time diffusive transport are also found for systems governed by the telegraph equation [159]

We collected histograms of the jump function and found the discrete Fourier transform, over a variety of timesteps, assuming no spatial dependence. This suggested that the imaginary component is essentially zero except for a small amount of noise - corresponding to zero advection.

From table 1, we expect that for small α, increasing even spatial orders will get smaller quickly. Ideally $A = 1$, as this is essentially a measure of conservation of the transported quantity - $A \sim 0.90$ at the first timestep, but by timestep 17 it exceeds 0.99 and then reaches an approximately constant value. This would seem to correspond with the fitting error. α typically takes a value on the order of 10^{-4} to 10^{-5}, so higher spatial orders are negligible. Our timestep is equal to 1×10^{-9} s, and since we have run for 100 timesteps, the maximum time we may observe a particle over is 1×10^{-7} s. We find the diffusion coefficient via Eqn. 64 and a fit to the jump function in the finite correlation case to be $d_x \sim d_z = 37.7$ $m^2 s^{-1}$, and in the zero correlation case to be $d_x \sim d_z = 14.3$ $m^2 s^{-1}$ which in both cases are within 5% of the value found with the mean squared displacements. For these cases, the coefficients are independent of the observation interval for observation intervals larger than the correlation time.

This fitting to the complementary function of the Jump function then delivers transport coefficients similar to those provided by previous methods in this simple case. The relative scalings indicate that other forms of transport are essentially negligible in comparison with diffusion, which also confirms the assumption of normal diffusion in these isotropic cases.

5 Transport on Drift Wave Simulations

Satisfied that the particle tracking approach delivers suitable and expected results in the simple isotropic synthetic turbulence case, we move on to a more realistic system. We wish to investigate non-local transport. As discussed in section 2.7.2, coherent structures appear to be related to non-local transport, and they are observed in MCF devices (see section 2.4). As such, an ideal system to investigate would be one that models aspects of transport in MCF devices, and which has well-defined coherent structures.

In this case, we have selected the (Charney-)Hasegawa-Wakatani equations, due to their ability to model certain types of drift-wave turbulence relevant in MCF devices, and the

formation of large-scale coherent structures (zonal flows) in certain cases. We hypothesise that the presence of zonal flows in the system will significantly modify transport, inducing non-local transport.

In this section, we discuss the HWE equations, then we discuss their simulation and results, and then finally we examine the propagation of Lagrangian tracers on the HWE system.

5.1 The (Charney-)Hasegawa-Wakatani Equations and their Modification

The modified (mHWE) and classical (Charney-)Hasegawa-Wakatani equations (cHWE) are used contemporaneously to study aspects of turbulence ([180, 178], etc), and are specifically used as a model of drift-wave turbulence. The assumptions are constant magnetic field, an inhomogeneous plasma with a radially varying density which is exponential and determines the strength of the gradient drive term such that $\kappa \equiv \frac{\partial}{\partial x} ln n$, and constant isotropic temperature. Electron-ion collisions and ion viscocity terms are included.

The classical Hasegawa-Wakatani equations are:

$$\frac{\partial n}{\partial t} + \{\phi, n\} = C(\phi - n) - \kappa \frac{\partial \phi}{\partial z} - D_n \nabla^4 n \tag{106}$$

$$\frac{\partial \zeta}{\partial t} + \{\phi, \zeta\} = C(\phi - n) - D_\zeta \nabla^4 \zeta \tag{107}$$

where D are dissipation coefficients, C is a measure of conductivity/adiabaticity, and κ is the density gradient drive/coefficient[24].

The vorticity is as:

$$\zeta = \nabla^2 \phi \tag{108}$$

The Poisson bracket is defined as:

$$\{a, b\} = \frac{\partial a}{\partial x}\frac{\partial b}{\partial z} - \frac{\partial a}{\partial z}\frac{\partial b}{\partial x} \tag{109}$$

[24]We use hyper-viscous dissipation terms, in order to introduce grid-scale dissipation.

In the limit $C \to \infty$ such that the system becomes adiabatic and $\phi \sim n$, it can be shown that the system of equations tends to the Hasegawa-Mima system, also known in geostrophic fluid dynamics, and so this system is occasionally called the Charney-Hasegawa-Mima system [181]. In the limit $C \to 0$, the two equations become decoupled, resulting in the hydrodynamic regime, characterised by long-lived coherent vortices [180, 182, 183].

The modified HW equations are:

$$\frac{\partial n}{\partial t} + \{\phi, n\} = C(\tilde{\phi} - \tilde{n}) - \kappa \frac{\partial \phi}{\partial z} - d_n \nabla^4 n \tag{110}$$

$$\frac{\partial \zeta}{\partial t} + \{\phi, \zeta\} = C(\tilde{\phi} - \tilde{n}) - d_\zeta \nabla^4 \zeta \tag{111}$$

Where the quantities with the over-tilde are defined as the quantity minus the binormal mean (or a zonal average).

The modification is introduced as a consequence of carefully considering the adiabatic electron response [184] in 2D. When in toroidal tokamak geometry where we may define a flux surface, we have conditions in which variation in the potential on the flux surface should be countered by parallel electron motion, so that there is no contribution to the parallel current from the average zonal components. This therefore should be eliminated and so:

$$\tilde{\phi} = \phi - < \phi >_z \tag{112}$$

$$\tilde{n} = n - < n >_z \tag{113}$$

where the zonal average is defined as in Eqn. 101, but with L_z a normalising length in the z-direction. Without the modification, we would observe a net radial transport of electrons which would 'short' the radial electric field. In a 3D simulation there should not be a need for the modification, as the correction would occur naturally as a consequence of appropriate boundary conditions.

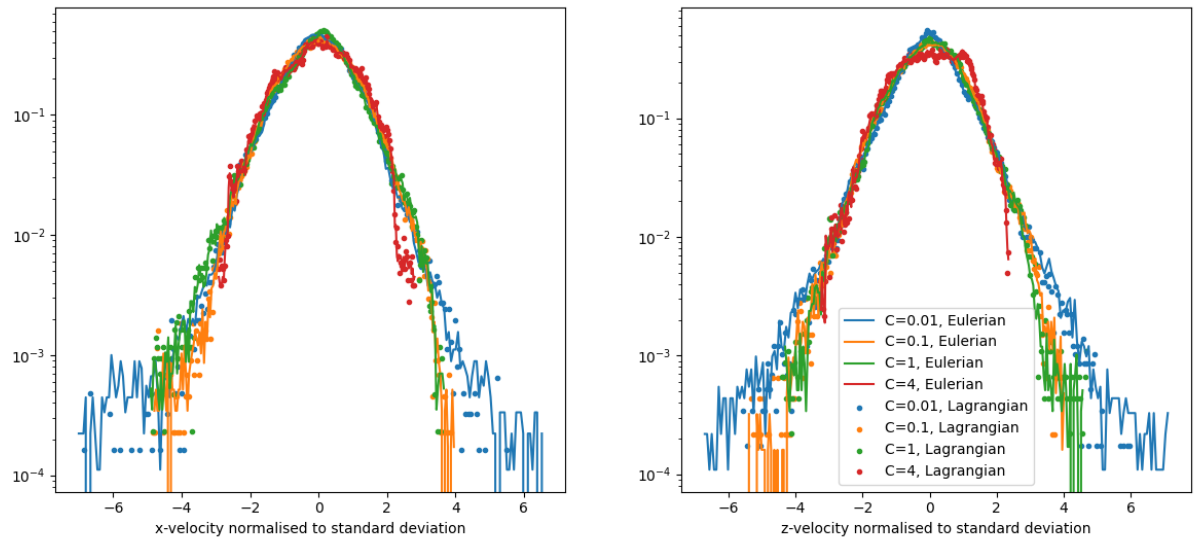

Figure 19: Normalised velocity probability density for the classical HWE system

5.2 Simulation of the Modified and Classical HW Equations

The cHWE and mHWE systems are both solved using the BOUT++ code [185], on a double periodic (or toroidal) space, with a cyclic Fourier solution method used to solve the Laplacian. The systems are first run to a steady state, and then we propagate the particles on the backgrounds simulated after steady state.

We use the Bohm normalization, with parameters: $B_0 = 0.5\ T$, $T = 40\ eV$, $\delta t = 1 \times 10^{-8}\ s$, $\Omega_i = \frac{eB_0}{m_i}$, $c_s = \sqrt{\frac{eT}{m_i}}$, $\rho_s = \frac{c_s}{\Omega_i}$. The size of cells is determined by $dx = \frac{L_x}{n_x}, dz = \frac{L_z}{n_z}$. Our mHWE and cHWE simulations are conducted on a grid of $nx = 512$ by $nz = 256$, with $L_x = 32\pi$ and $L_z = 16\pi$, and use a $d_\zeta = d_n = 10^{-4}$ and $\kappa = 0.2$. We vary the adiabaticity from $C = 0.01 \sim 4$, as this accesses a range of flow regimes [180], for both the mHWE and cHWE systems, giving us a total of 8 simulations, four each of mHWE and cHWE. As in the synthetic field section, we examine the behaviour of 10^5 particles initially dispersed uniformly over the space.

We examine the Lagrangian and Eulerian velocity probability density functions (PDFs) at the end of each simulation, with the velocity normalised to the data-set standard deviations, in order to ensure the particle statistics can be considered as being representative of the system statistics and to gain a basic understanding of the system behaviour. These are seen in Fig. 20 (corresponding to the mHWE system) and 19 (corresponding to the cHWE

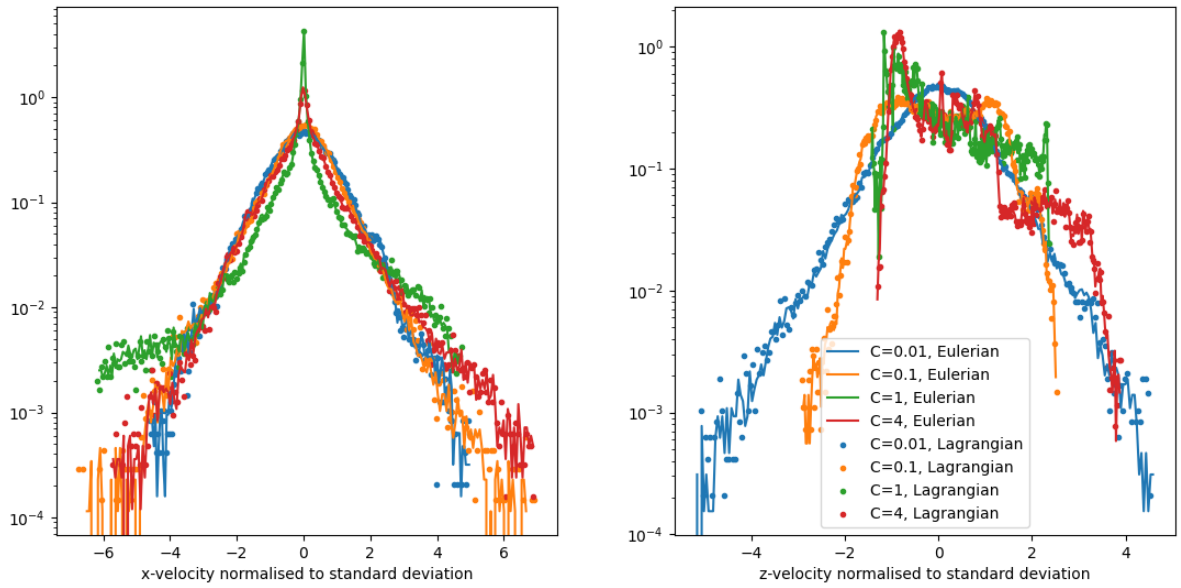

Figure 20: Normalised velocity probability density for the modified HWE system

system). The Lagrangian and Eulerian distributions correspond very well with each other in both the mHWE and cHWE cases. This indicates that the tracer particles accurately reproduce the velocity dynamics, throughout the simulations.

The cHWE case PDFs demonstrate substantial self-similarity over values of C, retaining approximately Gaussian shape. There is vanishing asymmetry, and the velocity variation is similar in both directions and so demonstrating vanishing anisotropy. We then expect these to have normal diffusion.

In the mHWE case, the x-velocity distribution tends to be symmetric, while the z-velocity is less symmetric for larger C. The asymmetric cases demonstrate skewness, as they retain a near-zero mean. The x- and z- velocity distributions in the $C = 0.01$ case are close to Gaussian with similar velocity variation, indicating isotropic normal diffusion. The $C = 1$ to $C = 4$ cases display clear anisotropy - from inspection, the $C = 0.1$ case appears approximately Gaussian, but does display a heavier tail than in the $C = 0.01$ case. Generally the mHWE x-velocity PDFs demonstrate heavier-tailed behaviour, as well as a distinct spike in the centre in the $C = 1$ and $C = 4$ cases, both of which are indicative of non-Gaussian behaviour.

Comparing Fig. 19 and 20, we see that the C=0.01 cases have similar profile and variation,

which is to be expected when both the cHWE and mHWE tend to the hydrodynamic case for small C.

A snapshot of each simulation is presented in Fig. 21, with the path of a single particle selected at random displayed for illustrative purposes. The distinct bands due to the zonal flows in the mHWE system are visible in (a)-(d) in contrast to the more isotropic turbulence in the cHWE system (e)-(h). The particle paths occur over 500 timesteps for all simulations.

In the mHWE cases, the zonal motion of the particles is distinct and clear in comparison with the cHWE cases in which the traced particle appears to express more isotropic motion. We note also that (a) lacks distinct bands and is visibly more isotropic than (b)-(d), which then seems to justify the near Gaussian velocity PDF in the $C = 0.01$ case.

The non-Gaussian velocity PDFs seem to correspond to the cases in which we observe the presence of zonal flows, especially the $C = 1$ and $C = 4$ cases. If zonal flows are indicative of non-Gaussian velocity PDFs, then this indicates that the $C = 0.1$ should also be non-Gaussian, but this is less obviously the case than in the $C = 1$ and $C = 4$ cases.

We examine the mean square displacements (MSDs) for the different simulations, in Fig. 22 and 23, the cHWE and mHWE respectively. Note the comparative dotted lines (black) which are $\propto t^2$ and $\propto t$, corresponding to ballistic and normal diffusion respectively.

The cHWE simulations have MSDs which are ballistic for small time, and reasonably $\propto t$ for long time in the cases $C = 0.01$-1, in both x- and z- directions. A transition from ballistic in the early time to normal diffusive behaviour after the Lagrangian correlation time is expected, as for small scales particles simply convect with minimal interaction, whereas for larger times they would interact with structures in the field. These cases therefore demonstrate the attributes of normal diffusion. Particles experience a similar displacement in both directions over a similar time, apparently relatively isotropic for the $C = 0.01$ case - there is a small but persistent anisotropy for the $C = 0.1$ case. For the $C = 1$ case, particles appear to travel approximately one order of magnitude further in the z-direction than the x-direction, and along with $C = 4$ appears to be anisotropic. The $C = 4$ case features a decline in the MSD beyond $t = 0.5 \times 10^{-4}$ s. Note that a similar phenomenon is observed for the case of passive tracers seeded in a 2 dimensional turbulence dominated by coherent structures in a study by Elhmaidi et al [186] for tracers seeded in a coherent structure.

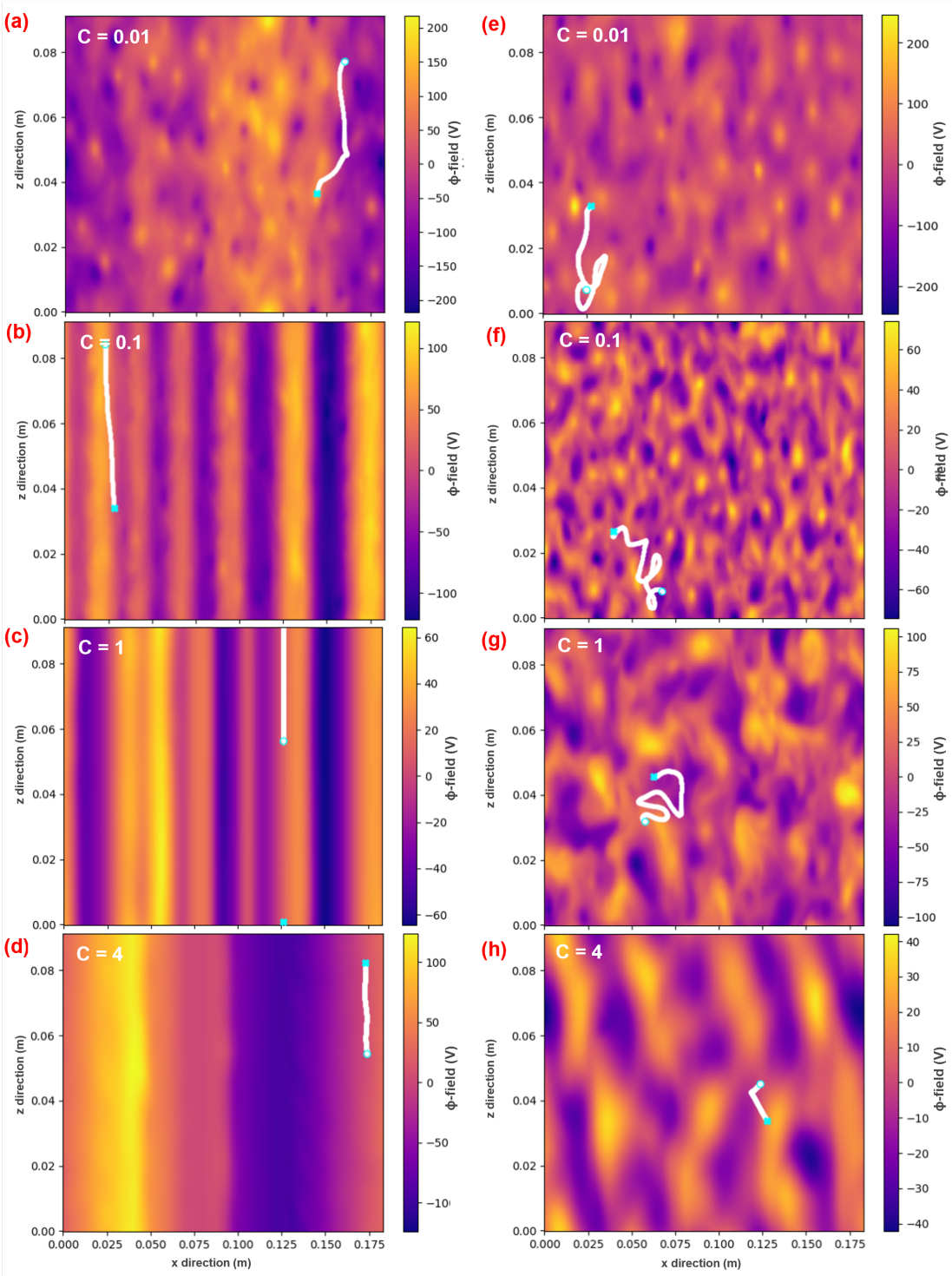

Figure 21: Particle tracks over first 500 timesteps, corresponding to 5×10^{-6} s. (a)-(d) are the mHWE cases, and (e)-(h) the cHWE cases. The particle motion starts at the full cyan cross, and ends at the empty cyan point, with the displayed frame being the end frame.

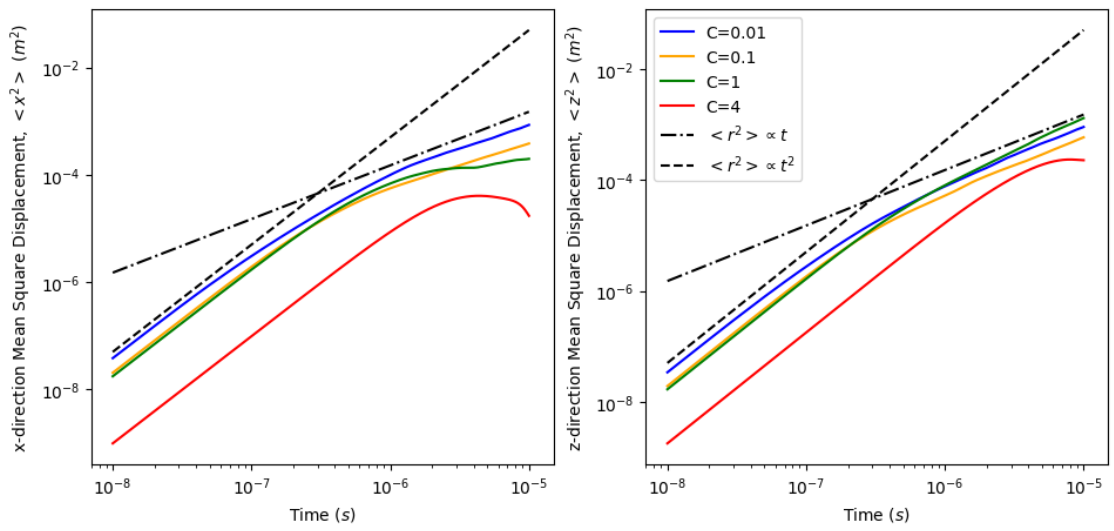

Figure 22: Mean Square Displacements for the classical HWE simulations, with x MSD (left) and z MSD (right), with reference.

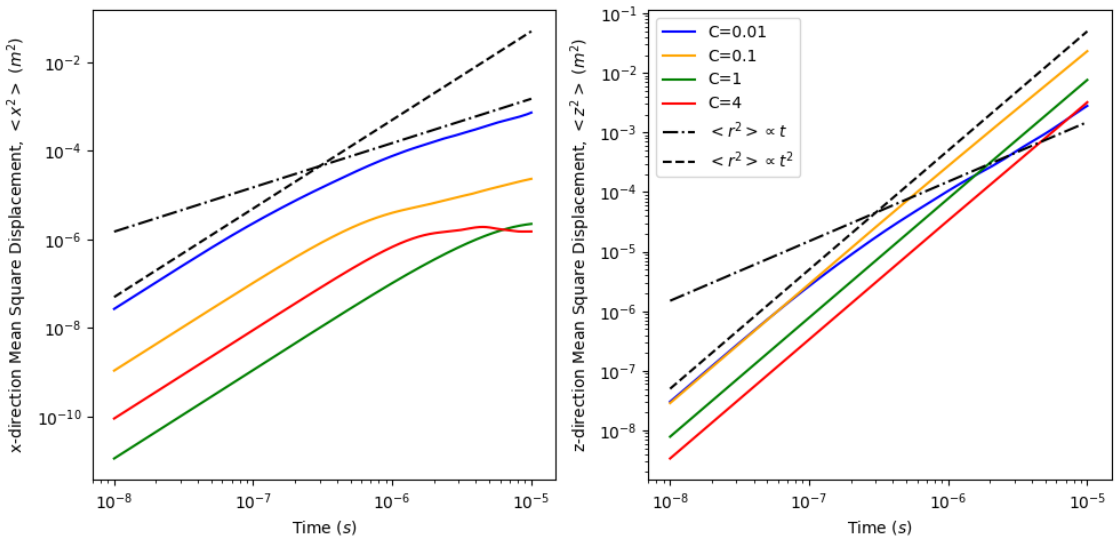

Figure 23: Mean Square Displacements for the modified HWE simulations, with x MSD (left) and z MSD (right), with reference.

We surmise that the reason for this MSD behaviour in the mHWE case is due to trapping by the zonal flows which persist over the simulation time, consequently limiting the dispersion. We also note in Bos et al [187] similar behaviour for $C = 4$ case - a key difference between this work and the work of Bos et al is that they do not disaggregate the MSD into the x- and z- components. In Bos et al, we note a slight decay of the MSD before the long time superdiffusive behaviour becomes predominant, which suggests a similar behaviour to what we have observed here. Given that the cHWE tends to the Hasegawa-Mima (HM) system for large C, it is perhaps the case that wave-like behaviour will be observed - If there is an element of periodicity, this does suggest that these simulations cannot be completely considered as being examples of steady state turbulence over the time. In the Mima limit of the cHWE equations, there is no inherent instability - towards the limit, the growth rate is therefore decreasing towards zero.

The mHWE simulations demonstrate clear anisotropy in their MSDs. Bulk displacement of particles in the z-direction is universally greater than in the x-direction by at least an order of magnitude. Comparison to the reference indicates that the x-direction MSD has the initial ballistic phase, followed by a decline to more $\propto t$ behaviour. The z-direction MSD seems to remain ballistic for all cases except in the $C = 0.01$ case which seems to become more normally diffusive for long time, but is still superdiffusive for the considered time. Given the presence of the zonal flows in the $C = 0.1$, $C = 1$, & $C = 4$ cases, superdiffusive MSDs in the z-direction may be expected. The x-MSDs overall demonstrate marked decline in transport with increasing C, which is far more pronounced than any similar decline for the x-MSDs in the cHWE cases. Note that subdiffusion in the presence of zonal flows is also observed in [188], which is exactly the phenomenon observed in the x-MSDs here. The $C = 0.01$ case seems to demonstrate similar dispersive behaviour for both cHWE and mHWE cases; in the x-MSDs, $< r^2 > \sim 10^{-4}$ at $t = 10^{-6}$, as well as having a final x-displacement on the order of 10^{-6}. The z-MSDs for the $C = 0.01$ case suggest that the mHWE case does have greater transport in the z-direction than for the cHWE case, with a fitted line having a gradient 4 times greater than in the cHWE case in long time, suggesting anisotropic behaviour despite the lack of distinctive zonal flow bands and Gaussian velocity PDFs.

The correlation times are estimated as in the Sec. 4. In the cHWE $C = 0.01$ case, the correlation times in x and z are similar, being 51.4 and 43.6 timesteps respectively. The x and z correlation times diverge for increasing adiabaticity, staying at ≈ 39 timesteps in x for the $C = 0.1$ and $C = 1$ cases, but with z correlation times increasing from 57.3 to 86.5 timesteps respectively. The $C = 4$ case demonstrates long time correlations.

The mHWE cases show long range correlations in the z-direction for $C \geq 0.1$. In the mHWE $C = 0.01$ case we have x and z correlation times of 33.2 and 82.0 timesteps respectively. The mHWE $C = 0.1$ case has x correlation time of 11.38 timesteps, the $C = 1$ case has x correlation time of 49.8 timesteps, and the $C = 4$ case has x correlation time of 104.2 timesteps.

5.3 Jump statistics of Lagrangian tracers

We now examine the jump statistics of particles seeded in the mHWE and cHWE systems. Previous study indicates that the use of Lagrangian tracers to examine the statistics of the HWE system is reasonable; further details on the connection between tracer particles and plasma density transport can be found in Basu et al [189].

Diffusion coefficients can be inferred from the mean square displacements in the $C = 0.01, 0.1$ cHWE cases, as we appear to be having normal diffusion in those cases over relevant timescales. We may also infer normal diffusion coefficients in the x-direction the $C = 0.01$ case of the mHWE. We will then be using these coefficients, found from fits, to compare to the MSD's and so confirm that the fitting method is working in this case.

We first examine whether the jump functions are stationary or not, which is done by examining 10 jump functions at 10 different start points covering the simulation time, each with $\tau = 100$ timesteps - this is typically larger or on the order of the x correlation time. Each jump function will then contain the statistical information about the displacement of particles for 10% of the simulation - smaller variation will therefore not be captured. By way of example, we provide the $C = 0.1$ case for cHWE and for mHWE in Fig. 24, in both x- and z- directions. The $C = 0.1$ case is used as it is the first case in the mHWE where the zonal structures are distinct, so the key differences between the cHWE and mHWE jump functions should be evident.

Barring statistical noise, the jump functions seem to have very stationary behaviour. This is common to all the data sets barring cHWE $C = 1$ and $C = 4$, suggesting that considering the systems to be in a statistical steady-state is reasonable, and so our current ORW model is applicable. The cHWE $C = 0.1$ case demonstrates slightly anisotropic behaviour, with very similar jump functions in both the x- and z- directions, as well as both being highly Gaussian.

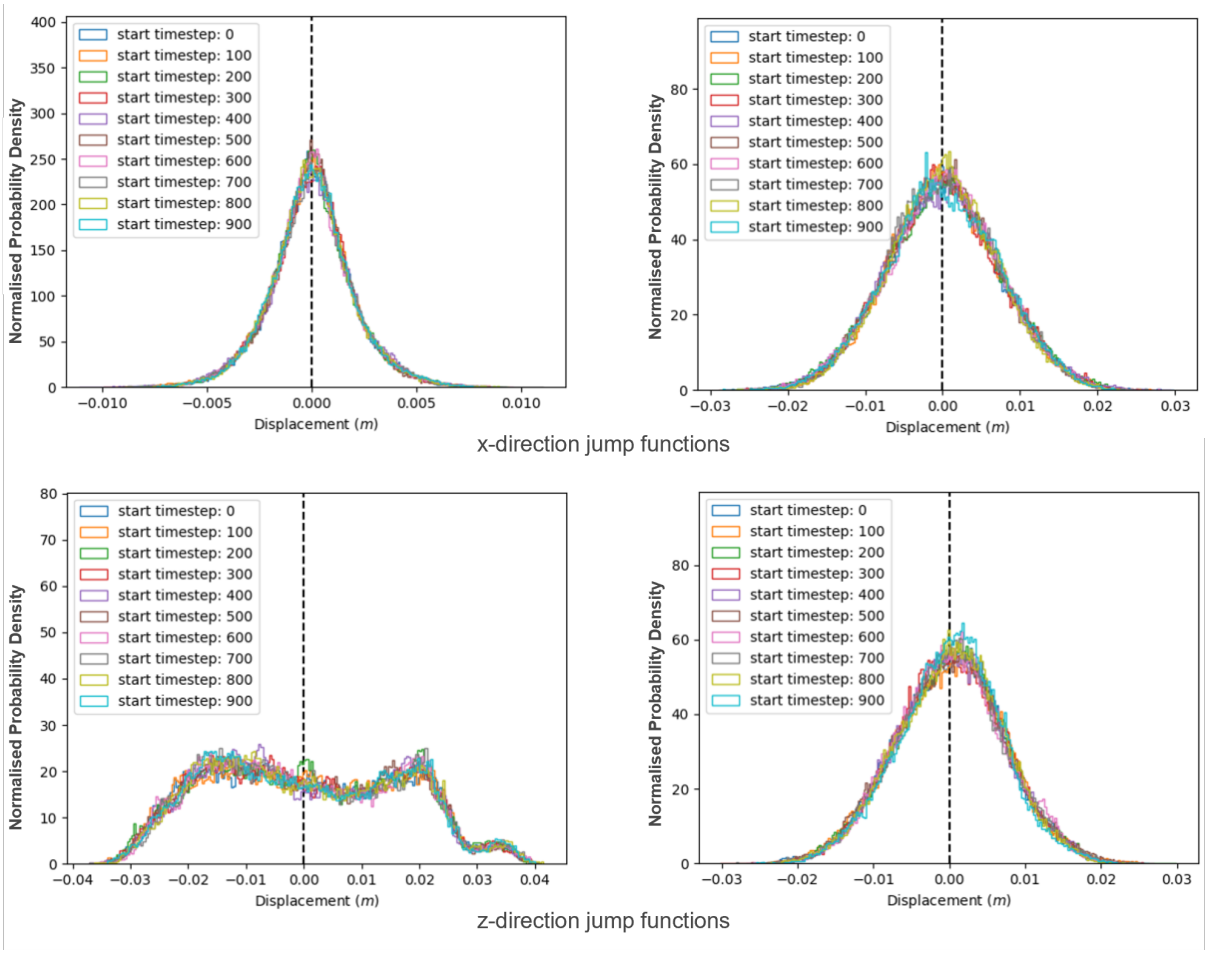

Figure 24: mHWE (left column) and cHWE (right column) jump functions for the $C = 0.1$ case, with progressing start timesteps, covering the simulation time

We can confirm this by examining the standardised moments. The 3rd standardised moment (skewness) of a Gaussian is 0, and 4rd standardised moment (kurtosis) of a Gaussian is 3. The x jump function in the cHWE case has a skewness of 0.058 and a kurtosis of 2.95, and the z jump function has a skewness of -0.041 and a kurtosis of 2.93. Both jump functions have a mean on the order of 10^{-5}, and standard deviations on the order of 10^{-3}

The mHWE $C = 0.1$ case is obviously anisotropic, and the z jump function demonstrates approximately an order of magnitude greater transport than in the x direction. This feature is common in all the mHWE simulations with the exception of the $C = 0.01$ case, which is relatively isotropic. This is consistent with superdiffusive behaviour in the z direction of the mHWE cases, as suggested in the MSDs.

Examining the standardised moments in the $C = 0.1$ case, the x jump function has a mean of 4.8×10^{-7}, standard deviation of of 2.01×10^{-3}, skewness of 0.036 and kurtosis of 4.09; the z jump function has a mean of 1.9×10^{-4}, standard deviation of of 0.016, skewness of 0.17 and kurtosis of 2.01. We see from the standardised moments that the jump function for the mHWE $C = 0.1$ case are not straightforward Gaussian distributions. The kurtosis of all the mHWE x jump functions are significantly in excess of 3, with the exception of the $C = 0.01$ case, which has kurtosis of 2.93.

The z-jump function demonstrates a variety of features, indicating a variety of particle behaviours, and this is again a feature of all the mHWE cases with distinct zonal bands. Given that the zonal bands can be described as anisotropic in the x-direction, and that the jump functions are acquired from the aggregate particle behaviour regardless of location, the z-jump functions are then incorporating all these behaviours into a single jump function. While this is then an accurate descriptor of the z displacements in the mHWE cases on average, we suggest that this could indicate spatial non-uniformity in the jump function which would become evident if we examined it in subsets of the x dimension.

We are particularly interested in the impact of the zonal structures on x transport, so we will consider fits to the x-jump functions in the mHWE cases. Given that the system is statistically stationary, we take the ensemble average of the 10 jump functions for each case as being representative of the jump function overall, a measure taken to reduce statistical noise. A wide variety of fits were considered, and it was found that a particularly good fit was achieved in general for the $C = 0.1$, $C = 1$, and $C = 4$ cases with a fit in fourier space corresponding to the sum of a symmetric Levy distribution (see Eqn. 209, section 6.4) and

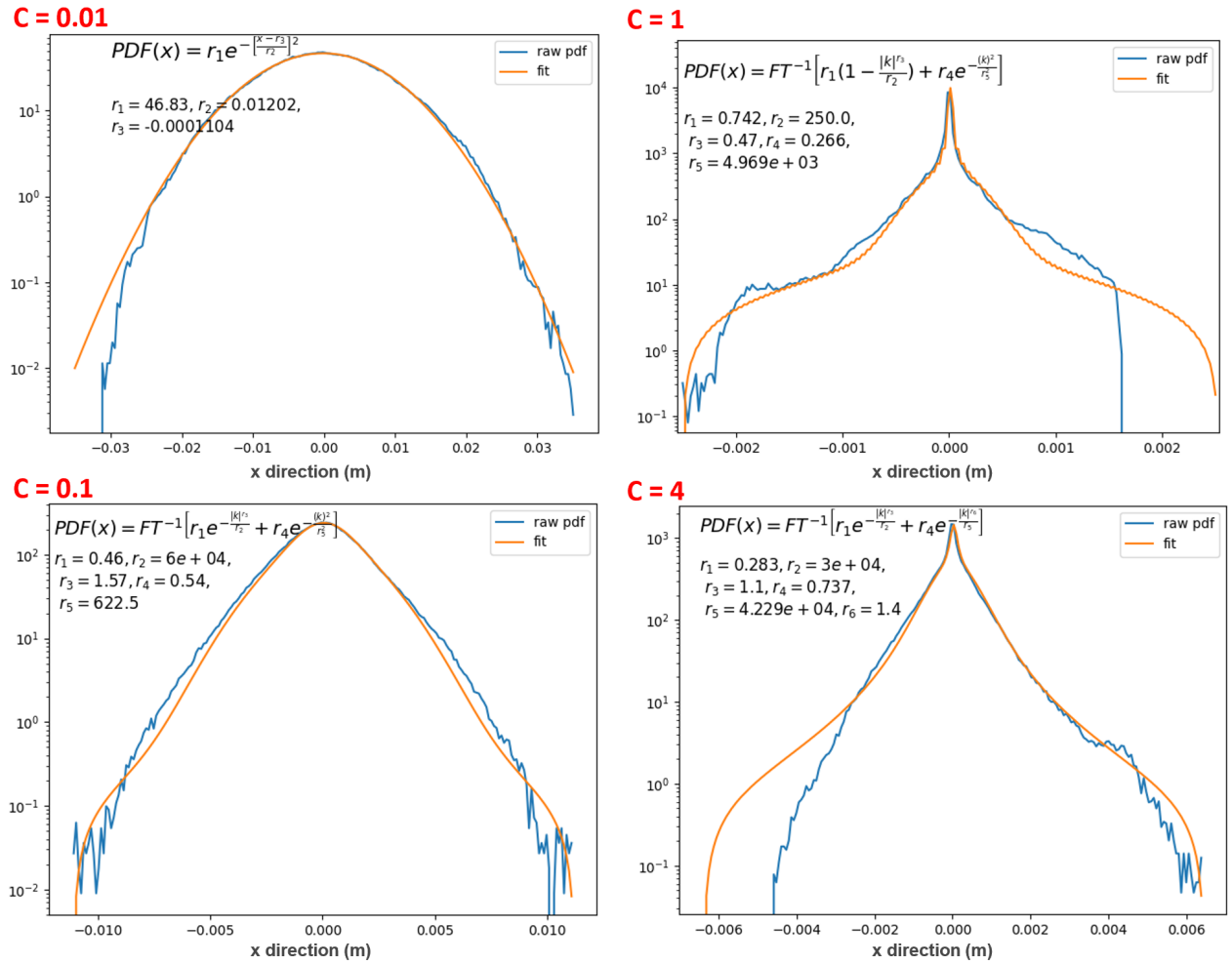

Figure 25: Fits to the ensemble averaged x jump functions for the mHWE case, semilog plot

a symmetric normal distribution.

These fits are displayed in Fig. 25. The $C = 0.01$ case is well described with a simple Gaussian distribution down to nearly two orders of magnitude from its peak. The $C = 0.1$ case is very well described by a pure symmetric Levy distribution at almost every scale, and both $C = 1$ and $C = 4$ cases are well described by equation 106 down two orders of magnitude from the peak at least.

The fits in Fourier space are given in table 3. We estimated the error of fit parameters by examining the covariance matrix of the fit and taking the square root of the diagonal values, and then propagating those quantities through the analysis.

Table 3: Table of Fourier fits and fit coefficient values for the ergodic x-Jump functions

System	Fourier Space Fit	Coefficient values
mHWE, C=0.01	$\hat{q}_{k,\tau}(k) = g_1 e^{-g_2 k^2}$	$g_1 = 0.998 \pm 0.00144$, $g_2 = (3.61 \pm 0.0121) \times 10^{-5}$
mHWE, C=0.1	$\hat{q}_{k,\tau}(k) = l_1 e^{-\frac{\lvert k\rvert^{l_3}}{l_2}} + g_1 e^{-g_2 k^2}$	$l_1 = 0.46 \pm 0.0117$, $l_2 = (6 \pm 1.16) \times 10^4$, $l_3 = 1.57 \pm 0.0245$, $g_1 = 0.54 \pm 0.0109$, $g_2 = (2.58 \pm 0.0258) \times 10^{-6}$
mHWE, C=1	$\hat{q}_{k,\tau}(k) = l_1 \left[1 - \frac{\lvert k\rvert^{l_3}}{l_2}\right] + g_1 e^{-g_2 k^2}$	$l_1 = 0.742 \pm 0.00718$, $l_2 = 250 \pm 21.2$, $l_3 = 0.470 \pm 0.00722$, $g_1 = 0.266 \pm 0.0053$, $g_2 = (4.05 \pm 0.0571) \times 10^{-8}$
mHWE, C=4	$\hat{q}_{k,\tau}(k) = l_1 e^{-\frac{\lvert k\rvert^{l_3}}{l_2}} + l_4 e^{-\frac{\lvert k\rvert^{l_6}}{l_5}}$	$l_1 = 0.283 \pm 0.00853$, $l_2 = (3 \pm 1.07)) \times 10^4$, $l_3 = 1.09 \pm 0.0296$, $l_4 = 0.737 \pm 0.00961$, $l_5 = (4.229 \pm 0.529) \times 10^4$, $l_6 = 1.40 \pm 0.0166$
cHWE, C=0.01	$\hat{q}_{k,\tau}(k) = g_1 e^{-g_2 k^2}$	$g_1 = 0.995 \pm 0.002$, $g_2 = (4.26 \pm 0.0196) \times 10^{-5}$
cHWE, C=0.1	$\hat{q}_{k,\tau}(k) = g_1 e^{-g_2 k^2}$	$g_1 = 0.998 \pm 0.0015$, $g_2 = (2.657 \pm 0.00904) \times 10^{-5}$

Using the highest order expansion, we are able to find effective transport equations using the jump function.

For the mHWE C=0.01 case:

$$\frac{\partial f}{\partial t} = d_x \frac{\partial^2 f}{\partial x^2}, \quad d_x = 36.1 \pm 0.108 \ m^2 s^{-1} \tag{114}$$

The half-gradient of the MSD should give us the diffusion coefficient. The half gradient in the mHWE $C = 0.01$ case is 35.23 $m^2 s^{-1}$, which is very close to d_x in this case.

For the mHWE C=0.1 case:

$$\frac{\partial f}{\partial t} = d_x \frac{\partial^2 f}{\partial x^2} + (7.59 \pm 1.52) D^{1.57}_{|x|} f, \ d_x = 1.4 \pm 0.042 \ m^2 s^{-1} \tag{115}$$

For the mHWE $C = 1$ case:

$$\frac{\partial f}{\partial t} = d_x \frac{\partial^2 f}{\partial x^2} + (2900 \pm 249) D^{0.47}_{|x|} f, \ d_x = 0.011 \pm 0.0003 \ m^2 s^{-1} \tag{116}$$

For the mHWE $C = 4$ case:

$$\frac{\partial f}{\partial t} = (8 \pm 2.94) D^{1.097}_{|x|} f + (17 \pm 2.17) D^{1.399}_{|x|} f \tag{117}$$

For the cHWE $C = 0.01$ case, we find $d_x = 42.6 \pm 0.2 \ m^2 s^{-1}$ and $d_z = 40.0 \pm 0.15 \ m^2 s^{-1}$. The half-gradient of the x and z MSDs in the cHWE $C = 0.01$ case are 42.64 $m^2 s^{-1}$ and 45.27 $m^2 s^{-1}$ respectively which closely match the diffusion coefficients found using a Gaussian fit to the jump function, strongly supporting the assumption of isotropic normal diffusion in this case.

For the cHWE $C = 0.1$ case, we find $d_x = 26.6 \pm 0.09 \ m^2 s^{-1}$ and $d_z = 25.6 \pm 0.07 \ m^2 s^{-1}$ respectively. The half-gradients in this case are 18.65 $m^2 s^{-1}$ in the x MSD and 29.20 $m^2 s^{-1}$ in the z MSD. While reasonably close in the z direction, there is disagreement in the x-direction, suggesting that the assumption of a Gaussian distribution does not fully capture the tracer transport in the x-direction: however, the diffusion magnitude does agree closely

with the magnitude from the MSD.

The fits to the complementary function of the Jump functions typically return the classic Fickian diffusion equation when expected, which occurs when the Jump function is well fit by a Gaussian distribution. This is very clear in the $C = 0.01$ cases of both mHWE and cHWE systems, which are closer to the hydrodynamic regime.

Particularly interesting, however, is that when the distinct zonal flow bands appear in the mHWE simulations with $C \geq 0.1$, we see a marked difference in the transport. Superdiffusive behavior is observed in the z-direction, and the x-direction begins to be marked by non-Gaussian heavy-tailed behaviour in the jump function, which typically requires symmetric Levy-type distributions or similar in addition to a Gaussian distribution to achieve a reasonable fit - analysis of which recovers transport equations with significant fractional transport, often in addition to a classic Fickian transport term.

5.4 Section Summary

Use of Lagrangian tracer particles seems to be a reasonable way to extract jump functions from simulations, provided care is taken. This reproduces the expected results in the case of fields evolved with brownian and white noise.

Of more significant interest is the measurement of jump functions in the classical and modified Hasegawa-Wakatani cases. The key observation in this case is that we observe non-Gaussian jump functions when zonal flows are present in the system. This confirms the relevance and existence of non-Gaussian jump functions, and suggests strongly that they have an association with coherent structures.

6 The Stochastic Flux Approach

Given the findings of 5, there is indeed evidence to support the existence of non-Gaussian equilibrium jump functions in certain cases. We should then seriously consider the case of non-Gaussian equilibrium jump functions in MCF relevant plasmas. Of particular impor-

tance to tokamak dynamics is flux, and given previous evidence of non-Fickian fluxes in the edge and SOL of tokamak devices, it would seem timely and relevant to consider models of flux which can take into account non-Gaussian jump functions. We then seek to relate our ORW to flux, in the hope of being able to describe flux in terms of a distribution of particles and a jump function.

We restate Fick's first law so we may keep it foremost in our mind:

$$\Gamma(x) = -D\frac{\partial P(x)}{\partial x} \tag{118}$$

where $\Gamma(x)$ is the flux at a point x, D is the diffusion coefficient, and $P(x)$ is the background field. Simply, Fick's first law states that the local flux is proportional to the gradient of the local distribution of particles.

In section 6.1 we construct the stochastic flux equation from first principles. In section 6.2, we obtain Fick's first law from the stochastic flux equation. In section 6.3, we find the Fourier transform pair of the stochastic flux equation. In section 6.4, we examine the transform pair, consider its properties, and determine in what limits we may find Fick's first law. Finally, in section 6.5 we consider the validity of truncation to low order.

6.1 Constructing the Stochastic Flux Equation

We consider the transport of a distribution of particles, $P(x)$, by a jump function, $q(\Delta x)$, over an observation interval τ. We consider particles emanating from a point, x_n, and impose a wall, w, located at position x, as in figure 26. The jump function is a probability distribution, and so consequently we may define the probability of a single particle crossing w in terms of the jump function:

$$p_w = \int_w^{+\infty} q(\Delta x) d\Delta x \tag{119}$$

Which is equivalent to the hatched area. If we are to consider the distribution of particles,

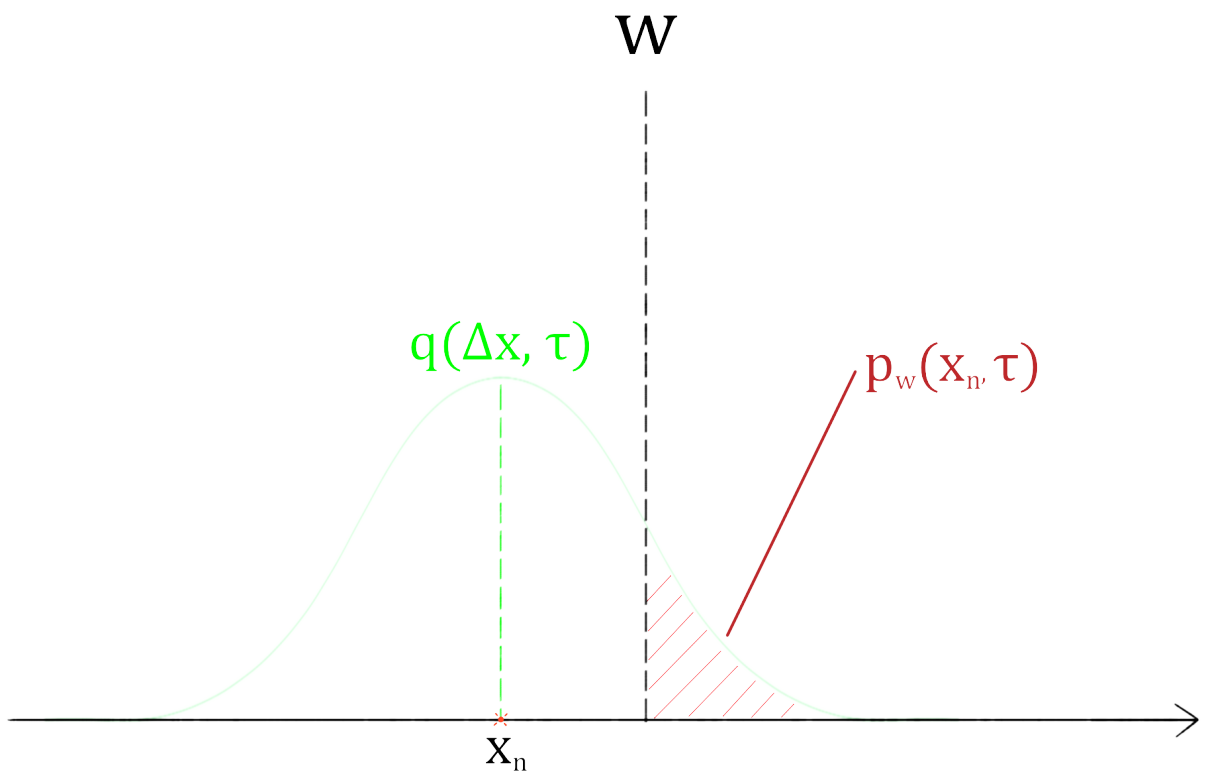

Figure 26: Probability of particles at point x_n crossing w over the observation interval, τ

we can then state that the number of particles emanating from x_n crossing the wall (or the flux) over the observation interval is:

$$\Gamma_{w,L}(x_n, t) \equiv \frac{1}{\tau} P(x_n, t) p_w \tag{120}$$

Where $\Gamma_{w,L}(x_n, t)$ is defined as the instantaneous left flux at t due to the contribution of point x_n.

Now, it is clear that the net flux across w, $\Gamma(x, t)_w$, is the sum of all fluxes across w, from all x_n on both sides of the wall. An intuitive way to construct this that gives us nice coordinates to work in is to consider the net flux due to pairs of points around the wall (for reference, see Fig. 27) and then consider the contribution of all pairs. We may write the left flux due to the contribution of the point on the left side of the wall at $x - x_n$ as:

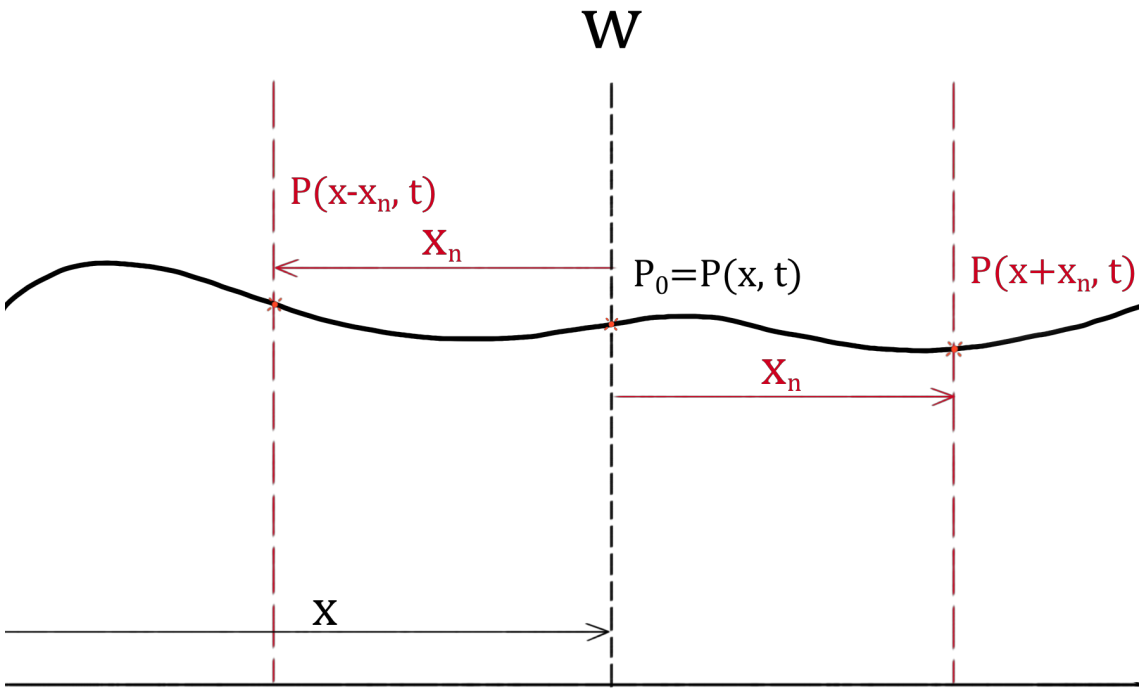

Figure 27: A background distribution, with wall w located at x, collocated with P_0. We consider the contribution of a single pair of points, symmetrically located at $P(x \pm x_n, t)$, to the flux across w

$$\Gamma_{w,L}(x, x_n, t) \equiv \frac{1}{\tau} P(x - x_n, t) \int_{x_n}^{+\infty} q(\Delta x) d\Delta x \tag{121}$$

and we may define the instantaneous right flux across w due to the contribution of a point on the right side of the wall at $x + x_n$ as:

$$\Gamma_{w,R}(x, x_n, t) \equiv \frac{1}{\tau} P(x + x_n, t) \int_{x_n}^{+\infty} q(-\Delta x) d\Delta x \tag{122}$$

And so the net instantaneous flux across w due to the pair of points $x \pm x_n$ is:

$$\Gamma_w(x, x_n, t) = \Gamma_{w,L}(x, x_n, t) - \Gamma_{w,R}(x, x_n, t) \tag{123}$$

And finally, the contribution due to all pairs is simply the sum over all x_n, from zero to infinity, such that:

$$\Gamma_w(x,t) = \int_0^{+\infty} \Gamma_w(x, x_n, t) dx_n \tag{124}$$

And we may equivalently write this as in Eqn. 125.

$$\tau\Gamma_w(x,t) = \int_0^{+\infty} \left[P(x - x_n, t) \int_{x_n}^{+\infty} q(\Delta x) d\Delta x - P(x + x_n, t) \int_{x_n}^{+\infty} q(-\Delta x) d\Delta x \right] \; dx_n \tag{125}$$

Where we call Eqn. 125 the *stochastic flux equation*. Thus, we have found an equation for the instantaneous flux at an arbitrary point, depending only on the particle distribution and the jump function, as desired.

Perhaps the most significant property we may infer by directly examining 125 is that the contribution of the particle distribution for pairs further away from the point of interest is increasingly weighted by the tail of $q(\Delta x)$. We may then see that for jump functions with tails weighted heavily in comparison to the centre we will have a long-range contribution to the flux, and conversely, jump functions with very small tails in comparison to the centre will have the local contribution to the flux predominate.

Additionally, we would like to note that the stochastic flux equation is quite straightforward to compute, provided a jump function can be defined for a distribution. In equilibrium systems, we expect the jump function to belong to the class of Levy α-stable (LαS) distributions as a consequence of the generalised central limit theorem: This limits the range of possible jump functions we may have to consider. However, the LαS distributions have well defined Fourier space expressions only, so in order to consider these properly we should find the transform pair of the stochastic flux equation. We shall consider this in section 6.3. First, we should check that the stochastic flux equation returns Fick's first law in circumstances in which we would expect Fick's first law to apply.

6.2 Fick's First Law using the Stochastic Flux Equation

In this section, we demonstrate that we can find Fick's first law from the stochastic flux equation. First, we simplify the representation of our stochastic flux equation. We define:

$$I(x_n) \equiv \int_{x_n}^{+\infty} q(\Delta x) d\Delta x \tag{126}$$

and:

$$I'(x_n) \equiv \int_{x_n}^{+\infty} q(-\Delta x) d\Delta x \tag{127}$$

We then write Eqn. 123 as

$$\tau \Gamma_w(x, x_n, t) = P(x - x_n, t) I(x_n) - P(x + x_n, t) I'(x_n) \tag{128}$$

We can straightforwardly expand $P(x \pm x_n, t)$ using the one-dimensional Taylor series, as in Eqn. 129.

$$P(x \pm x_n, t) = P(x, t) \pm x_n \frac{\partial P(x,t)}{\partial x} + \frac{1}{2!} x_n^2 \frac{\partial^2 P(x,t)}{\partial x^2} \pm \frac{1}{3!} x_n^3 \frac{\partial^3 P(x,t)}{\partial x^3} + ... \tag{129}$$

and by substitution of Eqn. 129 into Eqn. 128 we may then find:

$$\begin{aligned} \tau \Gamma_w(x, x_n, t) = P(x,t) \left[I(x_n) - I'(x_n) \right] - x_n \frac{\partial P(x,t)}{\partial x} \left[I(x_n) + I'(x_n) \right] \\ + \frac{x_n^2}{2!} \frac{\partial^2 P(x,t)}{\partial x^2} \left[I(x_n) - I'(x_n) \right] + ... \end{aligned} \tag{130}$$

If $q(\Delta x)$ is an even function such that $q(\Delta x) = q(-\Delta x)$, given the definitions in equations

126 and 127, then $I(\Delta x) - I'(\Delta x) = 0$ and $I(\Delta x) + I'(\Delta x) = 2I(\Delta x)$ for any $q(\Delta x)$. For a jump function with zero drift and symmetry, this clearly suggests we only have odd derivatives present. In the case of a jump function with net drift, i.e. asymmetric and with non-zero mean, we would have all terms present.

Now, we consider the case that we have a Gaussian jump function, such that:

$$q(\Delta x) = \frac{1}{\sigma\sqrt{2\pi}} e^{-\frac{(\Delta x - \mu)^2}{2\sigma^2}} \tag{131}$$

where μ and σ have the usual interpretations. We find $I(\Delta x)$ for the case of a Gaussian jump function:

$$I(x_n) = \int_{-\infty}^{+\infty} q(\Delta x) d\Delta x - \int_{-\infty}^{x_n} q(\Delta x) d\Delta x \tag{132}$$

And since the jump function is a probability distribution:

$$I(x_n) = 1 - \int_{-\infty}^{x_n} q(\Delta x) d\Delta x \tag{133}$$

by using the properties of the error function, $erf(x)$, (defined in Eqn. 135), we may write:

$$I(x_n) = \frac{1}{2}[1 - erf\left(\frac{x_n - \mu}{\sigma\sqrt{2}}\right)] \tag{134}$$

where the error function has the properties $erf(\infty) = 1$, $erf(0) = 0$, and is an odd function.

$$erf(x) \equiv \frac{2}{\sqrt{\pi}} \int_0^x e^{-t^2} dt \tag{135}$$

We find $I'(x_n)$ for the case of a Gaussian jump function similarly:

$$I'(x_n) = \int_{-\infty}^{+\infty} q(-\Delta x) d\Delta x - \int_{-\infty}^{x_n} q(-\Delta x) d\Delta x \tag{136}$$

so:

$$I'(x_n) = \frac{1}{2}[1 - erf\left(\frac{x_n + \mu}{\sigma\sqrt{2}}\right)] \tag{137}$$

consequently we may write:

$$I(x_n) - I'(x_n) = \frac{1}{2}\left[erf\left(\frac{x_n + \mu}{\sigma\sqrt{2}}\right) - erf\left(\frac{x_n - \mu}{\sigma\sqrt{2}}\right)\right] \tag{138}$$

and:

$$I(x_n) + I'(x_n) = \frac{1}{2}\left[2 - erf\left(\frac{x_n + \mu}{\sigma\sqrt{2}}\right) - erf\left(\frac{x_n - \mu}{\sigma\sqrt{2}}\right)\right] \tag{139}$$

In order to find the net flux across w, we must sum over all pairs, as in Eqn. 124. Consequently, we may write:

$$\tau\Gamma_w(x,t) = P(x,t)\int_0^{+\infty} I(x_n) - I'(x_n) dx_n - \frac{\partial P(x,t)}{\partial x}\int_0^{+\infty} x_n \left[I(x_n) + I'(x_n)\right] dx_n + ... \tag{140}$$

We consider the case of small x_n, such that we keep only the highest order terms. The integral for the zeroth order term is as:

$$I_\alpha \equiv \int_0^{+\infty} I(x_n) - I'(x_n) dx_n \tag{141}$$

This is straightforward to solve via geometric considerations. We simply write its value:

$$I_\alpha = \mu \tag{142}$$

The integral for the first order term is:

$$I_\beta \equiv \int_0^{+\infty} x_n[I(x_n) + I'(x_n)]dx_n \tag{143}$$

Or:

$$I_\beta = \int_0^{+\infty} x_n dx_n - \int_0^{+\infty} \frac{1}{2} x_n erf\left(\frac{x_n + \mu}{\sigma\sqrt{2}}\right) dx_n - \int_0^{+\infty} \frac{1}{2} x_n erf\left(\frac{x_n - \mu}{\sigma\sqrt{2}}\right) dx_n \tag{144}$$

defining the transforms:

$$z \equiv \frac{x_n - \mu}{\sigma\sqrt{2}}, \qquad z' \equiv \frac{x_n + \mu}{\sigma\sqrt{2}} \tag{145}$$

then:

$$\begin{aligned} I_\beta = +\infty &- \frac{\sigma\sqrt{2}}{2} \int_{\frac{\mu}{\sigma\sqrt{2}}}^{+\infty} \sigma\sqrt{2} z' erf(z') - \mu\ erf(z') dz' \\ &- \frac{\sigma\sqrt{2}}{2} \int_{-\frac{\mu}{\sigma\sqrt{2}}}^{+\infty} \sigma\sqrt{2} z\ erf(z) + \mu\ erf(z) dz \end{aligned} \tag{146}$$

We may find the indefinite integrals required here using integration by parts:

$$\int x\ erf(x) dx = \frac{1}{4}\left[(2x^2 - 1) erf(x) + \frac{2x}{\sqrt{\pi}} e^{-x^2}\right] + C \tag{147}$$

$$\int erf(x)dx = x\ erf(x) + \frac{1}{\sqrt{\pi}}e^{-x^2} + C \tag{148}$$

so, for the first integral on the RHS of Eqn. 146:

$$\int_{\frac{\mu}{\sigma\sqrt{2}}}^{+\infty} z' erf(z')dz' = \frac{1}{4}\left[(2\infty^2 - 1) - (2\frac{\mu}{\sigma\sqrt{2}}^2 - 1)erf(\frac{\mu}{\sigma\sqrt{2}}) - \frac{2}{\sqrt{\pi}}\frac{\mu}{\sigma\sqrt{2}}e^{-\frac{\mu}{\sigma\sqrt{2}}^2}\right] \tag{149}$$

and:

$$\int_{\frac{\mu}{\sigma\sqrt{2}}}^{+\infty} erf(z')dz' = \left[\infty - \frac{\mu}{\sigma\sqrt{2}}\ erf(\frac{\mu}{\sigma\sqrt{2}}) - \frac{1}{\sqrt{\pi}}e^{-\frac{\mu}{\sigma\sqrt{2}}^2}\right] \tag{150}$$

then for the final integral on the RHS of Eqn. 146:

$$\int_{-\frac{\mu}{\sigma\sqrt{2}}}^{+\infty} zerf(z)dz = \frac{1}{4}\left[(2\infty^2 - 1) - (2\frac{\mu}{\sigma\sqrt{2}}^2 - 1)erf(-\frac{\mu}{\sigma\sqrt{2}}) + \frac{2}{\sqrt{\pi}}\frac{\mu}{\sigma\sqrt{2}}e^{-\frac{\mu}{\sigma\sqrt{2}}^2}\right] \tag{151}$$

and:

$$\int_{-\frac{\mu}{\sigma\sqrt{2}}}^{+\infty} erf(z)dz = \left[\infty + \frac{\mu}{\sigma\sqrt{2}}\ erf(-\frac{\mu}{\sigma\sqrt{2}}) - \frac{1}{\sqrt{\pi}}e^{-\frac{\mu}{\sigma\sqrt{2}}^2}\right] \tag{152}$$

After substituting equations 149-152 into equation 146, we find:

$$I_\beta = \frac{\sigma^2}{2} \tag{153}$$

Finally, substituting I_α and I_β into equation 140, we may then write:

$$\Gamma_w(x,t) = \frac{\mu}{\tau}P(x,t) - \frac{\sigma^2}{2\tau}\frac{\partial P(x,t)}{\partial x} + ... \tag{154}$$

Where $\frac{\mu}{\tau}$ is the mean displacement over interval τ, which is then the average velocity, V, and $\frac{\sigma^2}{2\tau}$ can be demonstrated to be equivalent to the diffusion coefficient, D, in the case of a Gaussian jump function. Consequently:

$$\Gamma_w(x,t) = VP(x,t) - D\frac{\partial P(x,t)}{\partial x} + ... \tag{155}$$

Which is Fick's first law, equation 118.

6.3 The Spectral Stochastic Flux Equation

There are a number of reasons we may wish to have the Fourier transform pair of the stochastic flux equation. The first is that the form may be quite simple in Fourier space, and perhaps even analytically tractable - at least, more so than the un-transformed pair. The second is a corollary of the first: the Fourier transform is relatively easy to compute numerically, and so if the pair has a simple form, it may be that the flux is numerically straightforward to calculate. The third is that operators such as the Reisz fractional derivative - which may be used to describe non-local transport - have representations in Fourier space (see B); consequently, the transform of the stochastic flux equation may indicate the presence of non-integer diff-integrals in the untransformed space.

Using identities 126 & 127 for $I(x_n)$ and $I'(x_n)$ respectively, we re-write the stochastic flux equation.

$$\tau\Gamma_w(x,t) = \int_0^{+\infty} P(x-x_n,t)I(x_n)\ \ dx_n - \int_0^{+\infty} P(x+x_n,t)I'(x_n)\ \ dx_n \tag{156}$$

As written in Eqn. 156, it is clear that the stochastic flux is a kind of convolution of P with I. We use the definition of the spatial Fourier transform:

$$\hat{f}(k) \equiv FT\{f(x)\}(k) \equiv \int_{-\infty}^{\infty} f(x)e^{-ikx}dx \tag{157}$$

Which has inverse:

$$f(x) \equiv FT^{-1}\{\hat{f}(k)\}(x) \equiv \frac{1}{2\pi}\int_{-\infty}^{\infty} \hat{f}(k)e^{ikx}dk \tag{158}$$

Evidently the transforms are integrals over the whole domain, $-\infty \longrightarrow \infty$, whereas the stochastic flux is over $0 \longrightarrow \infty$. We use the Heaviside step function, $\theta(x)$, to deal with this. The Heaviside step function is defined as:

$$\theta(x) = \begin{cases} 1 & x \geq 0 \\ 0 & x < 0 \end{cases} \tag{159}$$

So then, we may write equation 156 as:

$$\tau\Gamma_w(x,t) = \int_{-\infty}^{+\infty} \theta(x_n)P(x-x_n,t)I(x_n)\ \ dx_n - \int_{-\infty}^{+\infty} \theta(x_n)P(x+x_n,t)I'(x_n)\ \ dx_n \tag{160}$$

Then we may write the Fourier transform of the stochastic flux, $\hat{\Gamma}(k,t)$, as:

$$\begin{aligned} \tau\hat{\Gamma}(k,t) = &\int_{-\infty}^{+\infty} e^{-ikx} \int_{-\infty}^{+\infty} \theta(x_n)P(x-x_n,t)I(x_n)\ \ dx_n\ dx \\ &- \int_{-\infty}^{+\infty} e^{-ikx} \int_{-\infty}^{+\infty} \theta(x_n)P(x+x_n,t)I'(x_n)\ \ dx_n\ dx \end{aligned} \tag{161}$$

This is somewhat familiar - nearly a convolution of some sort. We will define:

$$l \equiv x - x_n \qquad l' \equiv x + x_n \tag{162}$$

so:

$$\begin{aligned}\tau\hat{\Gamma}(k,t) = &\iint_{-\infty}^{+\infty} e^{-ikx} P(l,t)\theta(x-l)I(x-l) \;\; dl \; dx \\ &- \iint_{-\infty}^{+\infty} e^{-ikx} P(l',t)\theta(-(x-l'))I'(-(x-l')) \;\; dl' \; dx\end{aligned} \tag{163}$$

We may exchange the order of integration without too much fuss, as the limits are identical:

$$\begin{aligned}\tau\hat{\Gamma}(k,t) = &\int_{-\infty}^{+\infty} P(l,t) \int_{-\infty}^{+\infty} e^{-ikx}\theta(x-l)I(x-l) \;\; dx \; dl \\ &- \int_{-\infty}^{+\infty} P(l',t) \int_{-\infty}^{+\infty} e^{-ikx}\theta(-(x-l'))I'(-(x-l')) \;\; dx \; dl'\end{aligned} \tag{164}$$

Or:

$$\begin{aligned}\tau\hat{\Gamma}(k,t) = &\int_{-\infty}^{+\infty} P(l,t) FT\{\theta(x-l)I(x-l)\}(k) \; dl \\ &- \int_{-\infty}^{+\infty} P(l',t) FT\{\theta(-(x-l'))I'(-(x-l'))\}(k) \; dl'\end{aligned} \tag{165}$$

We need to go on a little diversion with regards to the inverse convolution identity. Defining $\hat{h}(k)$ as:

$$\hat{h}(k) \equiv \int_{-\infty}^{+\infty} \hat{f}(v)\hat{g}(k-v)dv \equiv (\hat{f} * \hat{g}) \tag{166}$$

Then finding the inverse transform:

$$FT^{-1}\{\hat{h}(k)\}(x) = FT^{-1}\{(\hat{f} * \hat{g})\}(x) \tag{167}$$

And using the identity for the Fourier transform of a convolution:

$$FT^{-1}\{\hat{h}(k)\}(x) = 2\pi f(x)g(x) \tag{168}$$

So:

$$FT\{f(x)g(x)\}(k) = \frac{1}{2\pi}(\hat{f} * \hat{g}) \tag{169}$$

and so:

$$FT\{f(x)g(x)\}(k) = \frac{1}{2\pi}(FT\{f(x)\} * FT\{g(x)\}) \tag{170}$$

The shift identity is given as:

$$FT\{f(x-a)\}(k) \equiv e^{-iak}\hat{f}(k) \tag{171}$$

Taken together, we may then re-write parts of the first term of Eqn. 165:

$$FT\{\theta(x-l)I(x-l)\} = \frac{1}{2\pi}(FT\{\theta(x-l)\} * FT\{I(x-l)\}) \tag{172}$$

Applying the shift identity to equation 172:

$$FT\{\theta(x-l)I(x-l)\} = \frac{1}{2\pi}(e^{-ilk}\hat{\theta}(k) * e^{-ilk}\hat{I}(k)\}) \tag{173}$$

And then using the convolution identity:

$$\begin{aligned} FT\{\theta(x-l)I(x-l)\} &= \frac{1}{2\pi}\int_{-\infty}^{+\infty} e^{-ilv}\hat{\theta}(v)\ e^{-il(k-v)}\hat{I}(k-v)\ dv \\ &= \frac{1}{2\pi}\int_{-\infty}^{+\infty} e^{-ilk}\hat{\theta}(v)\hat{I}(k-v)\ dv \end{aligned} \tag{174}$$

And similarly, for the relevant parts of the last term of equation 165:

$$FT\{\theta(-(x-l'))I'(-(x-l'))\} = \frac{1}{2\pi}(e^{-il'k}\hat{\theta}(-k) * e^{-il'k}\hat{I}'(-k)\}) \tag{175}$$

Then:

$$FT\{\theta(-(x-l'))I'(-(x-l'))\} = \frac{1}{2\pi}\int_{-\infty}^{+\infty} e^{-il'k}\hat{\theta}(-v)\hat{I}'(v-k)\ dv \tag{176}$$

Substituting equations 174 and 176 into equation 165, we find:

$$\begin{aligned} \tau\hat{\Gamma}(k,t) =& \frac{1}{2\pi}\int_{-\infty}^{+\infty} P(l,t)\int_{-\infty}^{+\infty} e^{-ilk}\hat{\theta}(v)\hat{I}(k-v)\ dv\ dl \\ &- \frac{1}{2\pi}\int_{-\infty}^{+\infty} P(l',t)\int_{-\infty}^{+\infty} e^{-il'k}\hat{\theta}(-v)\hat{I}'(v-k)\ dv\ dl' \end{aligned} \tag{177}$$

Which may be rearranged to:

$$\begin{aligned} \tau\hat{\Gamma}(k,t) =& \frac{1}{2\pi}\int_{-\infty}^{+\infty} P(l,t)e^{-ilk}\ dl\int_{-\infty}^{+\infty} \hat{\theta}(v)\hat{I}(k-v)\ dv \\ &- \frac{1}{2\pi}\int_{-\infty}^{+\infty} P(l',t)e^{-il'k}\ dl'\int_{-\infty}^{+\infty} \hat{\theta}(-v)\hat{I}'(v-k)\ dv \end{aligned} \tag{178}$$

From the definition of the Fourier transform as in equation 157, we may then see that a

simplification of equation 178 is possible:

$$\tau\hat{\Gamma}(k,t) = \frac{\hat{P}(k,t)}{2\pi}\left[\int_{-\infty}^{+\infty}\hat{\theta}(v)\hat{I}(k-v)\ dv - \int_{-\infty}^{+\infty}\hat{\theta}(-v)\hat{I}'(v-k)\ dv\right] \tag{179}$$

We have transformed from a convolution in untransformed space, to a convolution in transformed space. This has not been a fruitless exercise, as equation 179 seems immediately more tractable; as we do not convolve with the transform of the distribution, $\hat{P}(k,t)$, we may understand the flux in transformed space entirely in terms of the square-bracketed expression. Equation 179 may be simplified further by recalling that $\theta(x)$ is the Heaviside function, which has the Fourier transform, $\hat{\theta}(k)$, as:

$$\hat{\theta}(k) = \pi\delta(k) - \frac{i}{k} \tag{180}$$

Where $\delta(k)$ is the Dirac delta distribution, with the usual definition:

$$\delta(x) = \begin{cases} \infty & x = 0 \\ 0 & otherwise \end{cases} \tag{181}$$

and:

$$\int \delta(x)dx = 1 \tag{182}$$

We consider the first term in the square brackets:

$$\int_{-\infty}^{+\infty}\hat{\theta}(v)\hat{I}(k-v)\ dv = \pi\int_{-\infty}^{+\infty}\delta(v)\hat{I}(k-v)\ dv - i\int_{-\infty}^{+\infty}\frac{\hat{I}(k-v)}{v}\ dv \tag{183}$$

Given the definition of the Dirac delta, we may simplify to:

$$\int_{-\infty}^{+\infty} \hat{\theta}(v)\hat{I}(k-v)\ dv = \pi\hat{I}(k) - i\int_{-\infty}^{+\infty} \frac{\hat{I}(k-v)}{v}\ dv \tag{184}$$

Similarly, we may address the second term in the square brackets:

$$\int_{-\infty}^{+\infty} \hat{\theta}(-v)\hat{I}'(v-k)\ dv = \pi\hat{I}'(-k) + i\int_{-\infty}^{+\infty} \frac{\hat{I}'(v-k)}{v}\ dv \tag{185}$$

And so:

$$\tau\hat{\Gamma}(k,t) = \frac{\hat{P}(k,t)}{2\pi}\left[\pi\left(\hat{I}(k) - \hat{I}'(-k)\right) - i\int_{-\infty}^{+\infty} \frac{\hat{I}(k-v) + \hat{I}'(v-k)}{v}\ dv\right] \tag{186}$$

To simplify further, we must then find $I(x_n)$ and $I'(x_n)$ by recalling the definitions in equation 126 & 127. Then:

$$\begin{aligned}\hat{I}(k) &= \int_{-\infty}^{+\infty} e^{-ikx_n}\int_{x_n}^{+\infty} q(\Delta x)d\Delta x\ dx_n \\ &= \int_{-\infty}^{+\infty} e^{-ikx_n}\int_{-\infty}^{+\infty} \theta(\Delta x - x_n)q(\Delta x)d\Delta x\ dx_n\end{aligned} \tag{187}$$

defining:

$$l \equiv \Delta x - x_n \tag{188}$$

so:

$$\hat{I}(k) = \iint_{-\infty}^{+\infty} e^{-ik(\Delta x - l)}\theta(l)q(\Delta x)d\Delta x\ dl \tag{189}$$

so by rearranging the expression:

$$\hat{I}(k) = \int_{-\infty}^{+\infty} e^{-ik\Delta x} q(\Delta x)\ d\Delta x \quad \int_{-\infty}^{+\infty} e^{ikl}\theta(l)\ dl = \hat{q}(k)\hat{\theta}(-k) \tag{190}$$

Similarly:

$$\hat{I}'(-k) = \hat{q}(k)\hat{\theta}(k) \tag{191}$$

This then allows us to deal with the first and second terms within the brackets of Eqn. 186:

$$\hat{I}(k) - \hat{I}'(-k) = \hat{q}(k)\left[\hat{\theta}(-k) - \hat{\theta}(k)\right] \tag{192}$$

$$\hat{I}(k) - \hat{I}'(-k) = \hat{q}(k)\left[\pi\delta(k) + \frac{i}{k} - \pi\delta(k) + \frac{i}{k}\right] \tag{193}$$

so:

$$\hat{I}(k) - \hat{I}'(-k) = \frac{2i\hat{q}(k)}{k} \tag{194}$$

Then for the second term in equation 190:

$$\hat{I}(k-v) + \hat{I}'(v-k) = 2\pi\hat{q}(k-v)\delta(k-v) \tag{195}$$

Allowing us to write:

$$\tau\hat{\Gamma}(k,t) = i\hat{P}(k,t)\left[\frac{\hat{q}(k)}{k} - \int_{-\infty}^{+\infty} \frac{\hat{q}(k-v)\delta(k-v)}{v}\ dv\right] \tag{196}$$

By substitution, we may simplify the integral on the RHS in equation 196 using the properties of the Dirac delta distribution:

$$\int_{-\infty}^{+\infty} \frac{\hat{q}(k-v)\delta(k-v)}{v}\, dv = \frac{\hat{q}(0)}{k} \tag{197}$$

Finally, we find ourselves with the Fourier transform pair of the stochastic flux equation:

$$\tau\hat{\Gamma}(k,t) = i\hat{P}(k,t)\frac{\hat{q}(k)-\hat{q}(0)}{k} \tag{198}$$

We note a restriction on the jump function which may be inferred from equation 198 and the assumption that $P(x,t)$ and $\Gamma(x,t)$ must be real-valued: if a function, $f(x)$, is real for all values of x, the Fourier transform, $\hat{f}(k)$, has Hermitian symmetry as defined in equation 204.

$$\overline{\hat{f}(k)} = \hat{f}(-k) \tag{199}$$

Where the over-bar operator represents the complex conjugate. Given that the complex conjugate is distributive over addition, subtraction, multiplication and division, (and given i/k evidently has Hermitian symmetry) we can then see that for $\Gamma(x,t)$ to be real valued, $\hat{q}(k)$ must also possess Hermitian symmetry - equivalent to saying that $q(\Delta x)$ must be real for all values of Δx, which is perhaps not surprising given the physical meaning of $q(\Delta x)$ as being a probability distribution of particle jumps. It is clearly simpler to consider flux in Fourier space, so a simple restriction on $\hat{q}(k)$ to keep analysis grounded in physics is to consider only functions which possess Hermitian symmetry.

If the transform of the stochastic flux equation is correct, it should return Fick's first law in the case of a Gaussian jump function. Let us verify this quickly. The Fourier transform of the Gaussian jump function is:

$$\hat{q}(k) = e^{-\frac{1}{2}\sigma^2 k^2} \tag{200}$$

Consequently, we may write the transform of the stochastic flux equation for the Gaussian case as:

$$\tau\hat{\Gamma}(k,t) = i\hat{P}(k,t)\frac{e^{-\frac{1}{2}\sigma^2 k^2} - 1}{k} \tag{201}$$

By using the full Taylor series expansion, we may then write:

$$\tau\hat{\Gamma}(k,t) = -\frac{\sigma^2}{2}ik\hat{P}(k,t) + \frac{\sigma^4}{8}ik^3\hat{P}(k,t) - O(k^5) \tag{202}$$

And then by inverse transformation, we find:

$$\Gamma(x,t) = -\frac{\sigma^2}{2\tau}\frac{\partial P(x,t)}{\partial x} + \frac{\sigma^4}{8\tau}\frac{\partial^3 P(x,t)}{\partial x^3} - O(\frac{\partial^5 P(x,t)}{\partial x^5}) \tag{203}$$

Which for low order is identical to Fick's first law, satisfying us that our transform is indeed correct.

It is evident that the Fourier transform of the stochastic flux equation results in a much simpler representation. Provided that a time-invariant jump function is well-defined for a system, and the distribution of particles is known, then we may calculate the flux over an observation interval τ quite straightforwardly. From inspection of the transform of the stochastic flux equation, it is apparent that if $\hat{q}(k)$ contains terms with non-integer exponents, then the flux will feature non-integer derivatives or integrals. As such, all three reasons for finding the Fourier transform of the stochastic flux equation are justified, and it would seem that this allows further analysis.

Now consider the net flow into a volume for the conserved quantity P:

$$\frac{\partial P}{\partial t} + \oint \Gamma \cdot d\mathbf{S} = 0 \tag{204}$$

Consequently, by the application of the divergence theorem:

$$\frac{\partial P}{\partial t} + \nabla \cdot \Gamma = 0 \tag{205}$$

Considering in 1-D and then finding the spatial Fourier transform:

$$\frac{\partial \hat{P}}{\partial t} + ik\hat{\Gamma} = 0 \tag{206}$$

Then combining with equation 198, we find:

$$\frac{\partial \hat{P}}{\partial t} = \hat{P}(k,t)\frac{\hat{q}(k) - \hat{q}(0)}{\tau} \tag{207}$$

Equation 207 then is a transport equation for arbitrary $q(\Delta x, \tau)$.

Note that provided that the jump function belongs to a continuous distribution and is a PDF, then by Bochner's theorem [174], $\hat{q}(0) = 1 \; \forall \; \hat{q}$. Then using Eqn. 207, we may perform an inverse transform and find:

$$\tau\frac{\partial P}{\partial t} = \int_{-\infty}^{\infty} P(x - \Delta x, t)q(\Delta x, \tau)d\Delta x - P(x,t) \tag{208}$$

The analysis in this chapter should make it clear that any non-locality originates in the flux term.

6.4 Transport equations from the Levy-α Stable Distribution using the SFE

We have derived our stochastic flux equation (equation 125) and found its Fourier transform (equation 198). While it is clear that this can be calculated generally, it is useful to consider the behaviour in equilibrium systems. The family of Levy-α distributions (or stable distributions) are an attractor for distributions, as a consequence of the general central limit theorem; consequently, we expect the jump function for equilibrium systems to be characterised by such a distribution.

We may write the complementary function (or Fourier space representation) of the Levy-α stable distribution [174] as:

$$L\alpha S(k;\alpha,\gamma,\beta,\delta) = \begin{cases} e^{-ik\delta}e^{-|\gamma k|^{\alpha}\left[1-i\beta\tan\frac{\pi\alpha}{2}sgn(k)\right]} & \alpha \neq 1 \\ e^{-ik\delta}e^{-|\gamma k|\left[1-i\frac{2}{\pi}\beta\log|k|sgn(k)\right]} & \alpha = 1 \end{cases} \tag{209}$$

Where δ is a displacement parameter (recall the shift identity for Fourier transforms!), γ is a scale parameter (corresponding directly to a spatial width parameter for $\alpha = 2$) with $\gamma \geq 0$, β is a shape parameter not dissimilar to skewness with $\beta \in [-1, 1]$, and α is a shape parameter called the characteristic exponent with $\alpha \in (0, 2]$. The special cases of Eqn. 209 are for $\alpha = 1, \ \beta = 0$, which is the Cauchy-Lorentz distribution; and the case $\alpha = 2, \ \beta = 0$, which is the Gaussian distribution. We are also satisfied that Eqn. 209 possesses Hermitian symmetry, so will always correspond to real components for the flux in untransformed space. The flux for any equilibrium case may then be written using equation 209. We first consider the impact of the first shape parameter, α, and the scale parameter, γ on the flux, and so set $\hat{q}(k) = L\alpha S(k;\alpha,\gamma,0,\delta)$:

$$\tau\hat{\Gamma}(k,t) = i\hat{P}(k,t)\frac{e^{-ik\delta}e^{-|\gamma k|^{\alpha}} - 1}{k} \tag{210}$$

Before we proceed with any analysis or further manipulation, it is useful to attempt to understand what equation 210 actually tells us about flux for equilibrium cases. Now, Fick's first law is a local law - it is a statement that Flux is dependent solely on the local parameters

of the distribution, such that the flux at x is dependent only on $P(x)$. We have shown Fick's first law is valid if the jump function is Gaussian, $\alpha = 2$. However if the jump function may belong to the class of symmetric Levy-α distributions, it is not obvious that flux should be dependent on local parameters only. We may consider $k \longrightarrow 0$ to correspond to $x \longrightarrow \infty$ and vice versa, which is simply a statement that small wavenumbers correspond to large spatial scales. Understood in such terms, we may understand that the contribution of $\hat{P}(k \longrightarrow 0, t)$ to the flux corresponds to the dependency of the flux on features which are spatially distant from the point of interest, and conversely, the contribution of $\hat{P}(k \longrightarrow \infty, t)$ to the flux corresponds to the dependency of the flux on local features of the distribution. By considering the impact of the symmetric Levy-α distribution in the asymptotic limits of $k \longrightarrow 0$ and $k \longrightarrow \infty$, we may understand the extent (non-)local features contribute to the Flux.

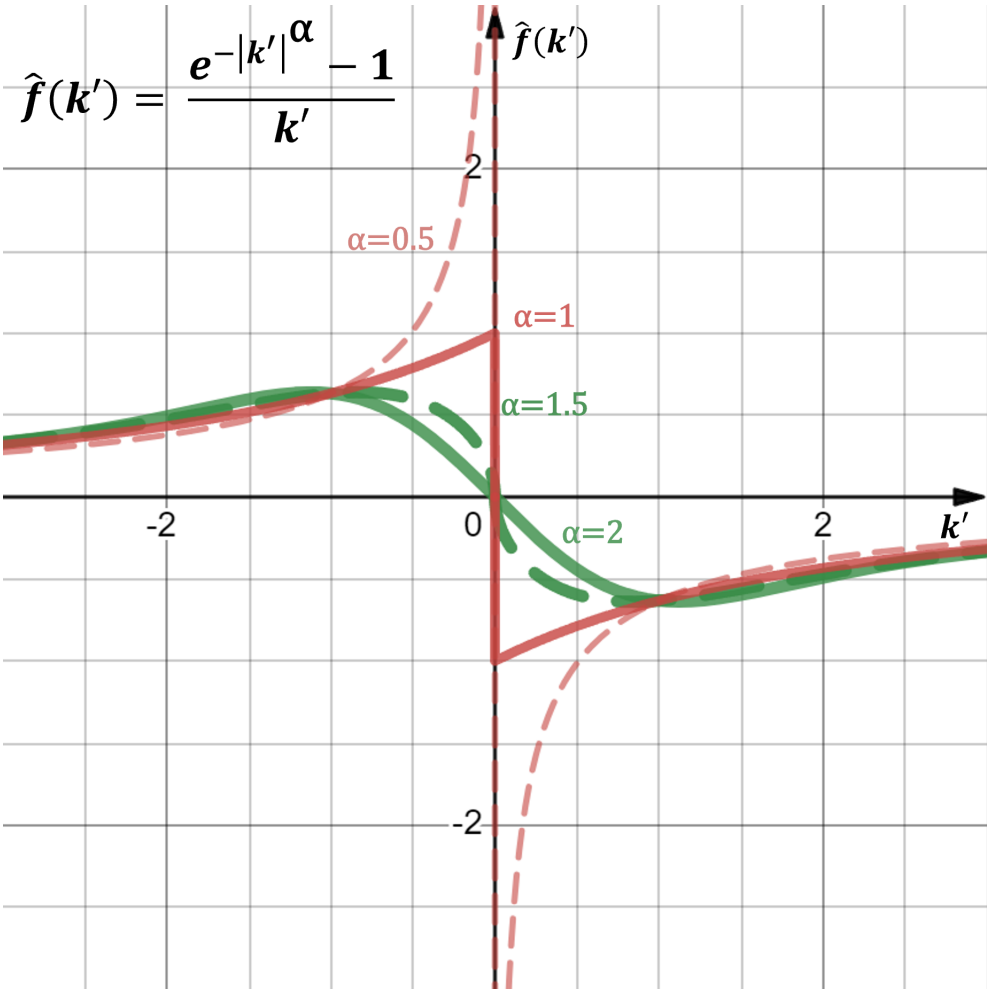

Figure 28: $f(k')$ plotted for $\alpha = 0.5, 1.0, 1.5,$ and 2 in the range $-3 < k' < 3$

To simplify matters for now, we consider the equation 210 for the case of $\delta = 0$, and make

a simple substitution $k' = \gamma k$. This allows us to consider only the impact of the scale parameter and α on the flux.

$$\tau\hat{\Gamma}(k,t) = i\gamma\hat{P}(k,t)f(k') \qquad where \qquad f(k') = \frac{e^{-|k'|^\alpha} - 1}{k'} \tag{211}$$

We see that the contribution of $\hat{P}(k \longrightarrow \infty, t)$ and $\hat{P}(k \longrightarrow 0, t)$ and all intermediate values is fundamentally restricted by $f(k')$. We plot $f(k')$ for a few α in figure 28. There are two distinct areas of behaviour: the first occurs for $\alpha > 1$, for which the contribution of $\hat{P}(0,t)$ to the flux is always zero. The second behaviour occurs for $1 > \alpha \geq 0$, where the contribution of $\hat{P}(k,t)$ to the flux as $k \longrightarrow 0$ predominate over any other contribution - that is, spatially distant features dictate the local flux, so we may call the regime $1 > \alpha \geq 0$ strongly non-local. As $k' \longrightarrow \infty$, $f(k')$ for various α tend to converge.

In figure 29 we examine $\log f(k')$ for $0.1 < k' < 10$. This demonstrates clearly the divergence of behaviour for $ck < 1$ for various α, and converging behaviour for $\gamma k > 1$. This also shows the importance of γ, the scale parameter. In any real space, the smallest wavenumber that may contribute to the flux is fixed by the largest spatial scale. Consequently there is a lower limit on k, which we name k_L. We see from figure 29 that provided γ is such that $\gamma k_L > 1$, then the flux will be similar regardless of α. If the converse is true, then the specific α becomes important in determining the flux. We also see that if we have multiple scales present in a system, it is possible to have quite different flux behaviours as a consequence, even if α is similar.

It is convenient to have a real space representation of the flux and how it is affected by the jump function. We have already looked at the special case of $\alpha = 2$, and will now look at the case for arbitrary $\alpha \in \mathbb{R}^+$. The series representation of equation 209 is:

$$e^{-ik\delta}e^{-|\gamma k|^\alpha} = \sum_{n=0}^{\infty} \frac{(-i\delta k - |\gamma k|^\alpha)^n}{n!} \tag{212}$$

Noting that the value of the $n = 0$ term is 1, we then write:

$$e^{-ik\delta}e^{-|\gamma k|^\alpha} - 1 = \sum_{n=1}^{\infty} \frac{(-i\delta k - |\gamma k|^\alpha)^n}{n!} \tag{213}$$

Then we write:

$$\tau\hat{\Gamma}(k,t) = \hat{P}(k,t)\frac{i}{k}\sum_{n=1}^{\infty} \frac{(-i\delta k - |\gamma k|^\alpha)^n}{n!} \tag{214}$$

In the limit of small k, we need consider first order terms only:

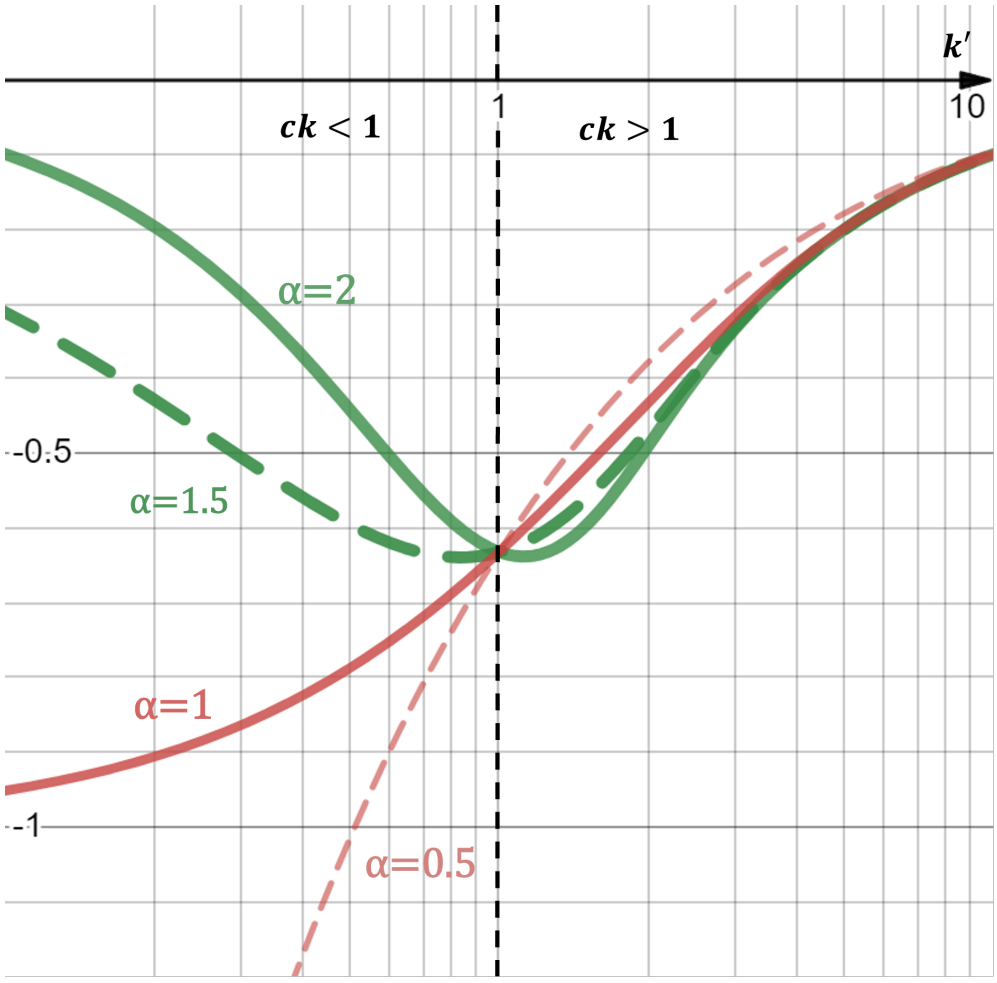

Figure 29: $\log f(k')$ *plotted for* $\alpha = 0.5, 1.0, 1.5,$ *and* 2 *in the range* $0.1 < k' < 10$

$$\tau\hat{\Gamma}(k,t) \approx \delta\hat{P}(k,t) - i|\gamma|^{\alpha}\frac{|k|^{\alpha}}{k}\hat{P}(k,t) \tag{215}$$

Applying the divergence theorem:

$$\tau\frac{\partial\hat{P}}{\partial t} \approx \delta ik\hat{P}(k,t) - |\gamma|^{\alpha}|k|^{\alpha}\hat{P}(k,t) \tag{216}$$

Performing the inverse transform:

$$\tau\frac{\partial P}{\partial t} \approx \delta\frac{\partial P(x,t)}{\partial x} + |\gamma|^{\alpha}FT^{-1}\{|k|^{\alpha}\hat{P}(k,t)\} \tag{217}$$

The last term on the RHS of Eqn. 217 is evidently a convolution of $|k|^{\alpha}$ with our $\hat{P}(k,t)$ in real space. If α is an even integer, the inverse transform would correspond to even derivatives. It is not obvious what the inverse transform should be for arbitrary $\alpha \in \mathbb{R}^{+}$ - we discuss this in Appendix B. The conclusion of that Appendix is that it may be shown [190] that:

$$FT^{-1}\{-|k|^{\alpha}\hat{f}(k)\} = D^{a}_{|x|}f(x) \tag{218}$$

Where $D^{\alpha}_{|x|}f(x)$ is the Reisz derivative, defined as:

$$D^{\alpha}_{|x|}f(x) = -\frac{1}{2cos\frac{\pi\alpha}{2}}\left[{}_{-\infty}D^{\alpha}_{x} + {}_{x}D^{\alpha}_{\infty}\right]f(x) \tag{219}$$

And ${}_{-\infty}D^{\alpha}_{x}$, ${}_{x}D^{\alpha}_{\infty}$ denote the Left- and Right- fractional Riemann-Louiville Derivatives, where:

$${}_{a}D^{\alpha}_{x}f(x) \equiv \frac{1}{\Gamma(m-\alpha)}\frac{d^{m}}{dx^{m}}\int_{a}^{x}\frac{f(\xi)}{(x-\xi)^{\alpha+1-m}}d\xi, \quad \alpha > 0, \quad m-1 \leq \alpha < m \tag{220}$$

and:

$$ {}_xD_b^\alpha f(x) \equiv \frac{(-1)^m}{\Gamma(m-\alpha)} \frac{d^m}{dx^m} \int_x^b \frac{f(\xi)}{(\xi - x)^{\alpha+1-m}} d\xi, \quad \alpha > 0, \quad m-1 \leq \alpha < m \tag{221} $$

This allows us to write Eqn. 217 as:

$$ \tau \frac{\partial P}{\partial t} \approx \delta \frac{\partial P(x,t)}{\partial x} + \gamma^\alpha D_{|x|}^\alpha P(x,t) \tag{222} $$

.

Consequently α determines the nature of the transport operator we obtain in our transport equation. Note that non-zero displacement, δ, results in the usual advection term.

If the β parameter, which we call the skewness for brevity, is zero, then we can see from equation 209 that $\hat{q}(k)$ is symmetric in k. What happens to our transport equation for non-zero skewness? We neglect the displacement parameter in this case, and consider arbitrary $\beta,\ \alpha \neq 1$:

$$ \hat{q}(k) = e^{-|\gamma k|^\alpha \left[1 - i\beta \tan \frac{\pi\alpha}{2} sgn(k)\right]} \tag{223} $$

So:

$$ \tau \frac{\partial \hat{P}}{\partial t} = \hat{P}(k,t) \left[e^{-|\gamma k|^\alpha \left[1 - i\beta \tan \frac{\pi\alpha}{2} sgn(k)\right]} - 1 \right] = \hat{P}(k,t) \sum_{n=1}^{\infty} \frac{\left(-|\gamma k|^\alpha + i|\gamma k|^\alpha \beta \tan \frac{\pi\alpha}{2} sgn(k)\right)^n}{n!} \tag{224} $$

And again, considering only the first order term:

$$ \tau \frac{\partial \hat{P}}{\partial t} \approx -\hat{P}(k,t)\gamma^\alpha |k|^\alpha + \beta \tan \frac{\pi\alpha}{2} \gamma^\alpha i \hat{P}(k,t) |k|^\alpha sgn(k) \tag{225} $$

The first term on the RHS is easily resolved given the definition of the Reisz derivative. As

for the second term [25], we may write $sgn(k)$ as:

$$sgn(k) = \frac{k}{|k|} \tag{226}$$

for $k \neq 0$. Therefore:

$$\tau \frac{\partial \hat{P}}{\partial t} \approx -\hat{P}(k,t)\gamma^{\alpha}|k|^{\alpha} + \beta \tan\frac{\pi\alpha}{2}\gamma^{\alpha} ik\hat{P}(k,t)|k|^{\alpha-1} \tag{227}$$

We may then inverse transform to:

$$\tau \frac{\partial P}{\partial t} \approx \gamma^{\alpha} D^{\alpha}_{|x|} P(x,t) - \beta \tan\frac{\pi\alpha}{2}\gamma^{\alpha}\frac{\partial}{\partial x}\left(D^{\alpha-1}_{|x|}P(x,t)\right) \tag{228}$$

We then find a new term, which we refer to as the *fractional advection* term as it originates from the odd component of the Levy-α distribution, and by way of analogy to the advection term, which originates as the odd component of $\hat{q}(k)$ in the case we have a non-zero δ.

The fractional advection term is unprecedented in the literature, as far as we can tell - presumably because it is not obvious as to why it should ever be relevant[26].

6.5 Validity of Truncation to Low Order

In the previous section we have arrived at our various forms of fractional differential equation by using the SFE and then finding a Taylor series of the resulting equation, which we then truncate. In this section, we consider whether this is reasonable, or whether there are certain circumstances in which we should be cautious. In Eqn. 224, we see the general form of the series which we extract below (for the case $\alpha \neq 1$):

[25] NB: Note that $-isgn(k)\cdot\hat{f}(k)$ is the Fourier space representation of the Hilbert transform. Fortunately, in this case, it is relatively straightforward to deal with

[26] the author hopes that this thesis sufficiently demonstrates the relevancy of this term

$$\sum_{n=1}^{\infty} a_n = \sum_{n=1}^{\infty} \frac{Q^n}{n!} = \sum_{n=1}^{\infty} \frac{\left(-|k'|^\alpha + i|k'|^\alpha \beta \tan\frac{\pi\alpha}{2} sgn(k')\right)^n}{n!} \tag{229}$$

Where:

$$Q \equiv -|k'|^\alpha + i|k'|^\alpha \beta \tan\frac{\pi\alpha}{2} sgn(k') \tag{230}$$

And we have set $k' = \gamma k$, as we did previously. First, we consider whether the series converges. We consider convergence to occur for:

$$\lim_{n\to\infty} \left| \frac{a_{n+1}}{a_n} \right| < 1 \tag{231}$$

Using our definition of Q, we may write that:

$$\frac{a_{n+1}}{a_n} = \frac{Q^{n+1}}{(n+1)!} \frac{n!}{Q^n} = \frac{Q}{n+1} \tag{232}$$

In the limit $n \longrightarrow \infty$, it is clear that Eqn. 232 tends towards zero except in the case that $Q \longrightarrow \infty$, which occurs only for non-finite k'. The series is then conditionally convergent.

We are justified in discarding higher-order terms if they are smaller in magnitude than the lower order terms, such that:

$$\frac{|Q|}{n+1} \ll 1 \tag{233}$$

We may write:

$$|Q| = \sqrt{|Q|^2} = \sqrt{Q^* Q} \tag{234}$$

Where Q^* denotes the complex conjugate of Q. $|Q|^2$ may be found to be:

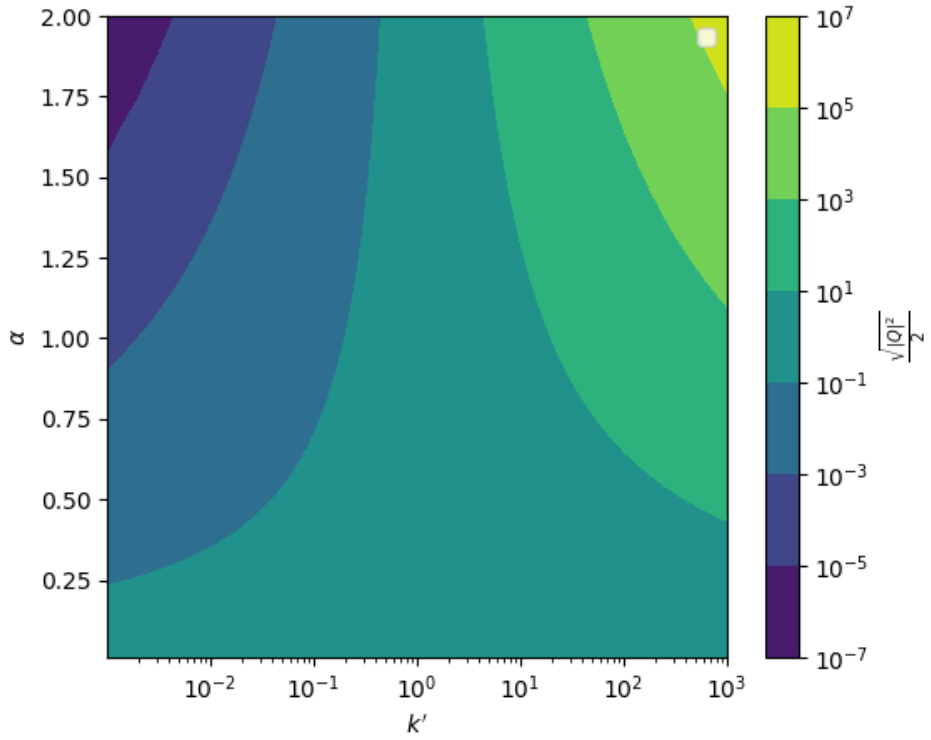

Figure 30: $\frac{|Q|}{2}$ *plotted for* $\alpha \in [0, 2]$*, with* $10^{-3} < k' < 10^{3}$*, for the case* $\beta = 0$

$$|Q|^2 = |k'|^{2\alpha}(1 + \beta^2 tan^2\left(\frac{\pi\alpha}{2}\right)) \tag{235}$$

It would be interesting to see for what k', α, β that Eqn. 233 is satisfied. We plot the function $\frac{|Q|}{n+1}$ for the case $n = 1$, in the range $\alpha \in [0, 2]$ and $k' \in [10^{-3}, 10^{3}]$ for both $\beta = 0$ and $\beta = 1$, which may be seen in Figs. 30 and 31.

While the symmetric case with $\beta = 0$ seems to have quite a well defined region in which the inequality is satisfied, generally for $k' < 10^{-1}$ and $\alpha > 0.9$, there seems to be something of an incursion which occurs in the region $\alpha \sim 1$ for the asymmetric case $\beta = 1$, which otherwise seems quite similar - in both cases, the inequality is satisfied for $k' \longrightarrow 0$. Recalling that $k' \equiv \gamma k$, this again emphasises the importance of the scale parameter in determining system behaviour.

In the case that the higher order terms are not vanishing, then we end up with terms of order $O(|k'|^{\alpha n})$ - when transformed, this corresponds to αn order derivatives of $P(x, t)$. Conse-

quently, provided that our $P(x,t)$ is such that the higher order derivatives are decreasing sufficiently fast, then we are indeed justified in considering the lowest order contributions only.

In the case that higher order derivatives of $P(x,t)$ are non-vanishing, then we may have a problem with neglecting the higher order contributions. This may occur if we have a periodic P, or are considering a system which has $P(x,t) \neq 0$ for $x \in [-\infty, \infty]$, and in such cases care should be taken.

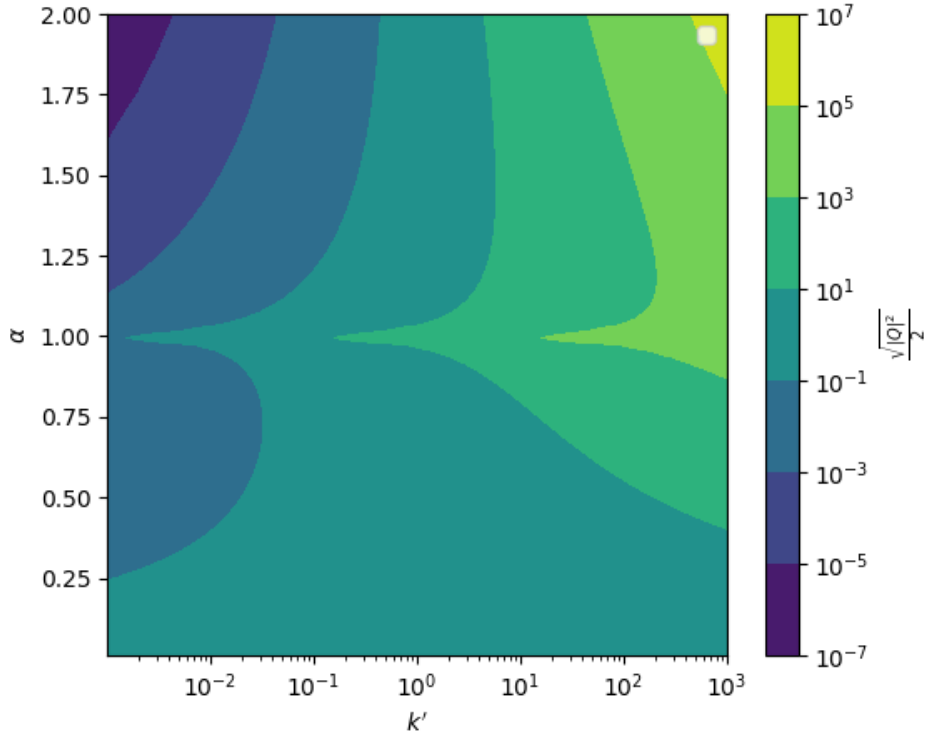

Figure 31: $\frac{|Q|}{2}$ *plotted for* $\alpha \in [0,2]$*, with* $10^{-3} < k' < 10^{3}$*, for the case* $\beta = 1$

7 Numerical Solution of Fractional Advection Diffusion Equations

We have seen in chapter 5 that we may observe non-Gaussian jump functions associated with the movement of Lagrangian tracers in drift-wave systems, and have seen in chapter 6 that if the jump function belongs to a Levy-α Stable (LαS) distribution, this may result in transport equations with diff-integrals of non-integer order (fractional derivatives) - consequently, this may justify the use of fractional advection-diffusion equations (FADEs) with the form as in Eqn. 228 in the case that the observed jump function belongs to a LαS distribution with non-zero β.

This brings a challenge - searches of the literature provide solutions to specific cases [191, 192, 193], however to the authors knowledge, there are no general solutions that have been published. Generally, finding solutions to fractional differential equations is not trivial. Some more recent methods assaulting general systems of fractional differential equations have been proposed using methods such as Adomian decomposition [194], however further work is required before these methods can be applied in this case. Consequently, we take a numerical approach to the solution of FADEs, which we will test in this chapter and apply in chapter 8.

It is possible to consider our problem a spectral shooting problem of general form as in Eqn. 207. However, it is not at all clear how to include 'standard' boundary conditions (such as Dirichlet, Neumann, or Robin conditions) in a satisfactory way while retaining the useful properties of the Fourier/Laplace transforms. This is certainly worth further investigation, as the solution to our problems in Fourier space would be significantly easier than the solution in real space. Nonetheless, the spectral approach does allow solution of an initial value problem, which may be approached using Fourier-Laplace methods.

We recall Fick's second law in terms of the jump function:

$$\frac{\partial \hat{P}}{\partial t} = \hat{P}(k,t)\frac{1}{\tau}\left[\hat{q}(k) - \hat{q}(0)\right] \tag{236}$$

We set τ equal to unity, for convenience, which does not fundamentally impact the solution.

Defining the Laplace transform as (see [195] section 17):

$$\widetilde{f}(s) \equiv L\{f(t)\}(s) \equiv \int_0^\infty f(t)e^{-st}dt, \quad \Re(s) > 0 \tag{237}$$

With inverse:

$$f(t) = L^{-1}\{f(s)\}(t) = \frac{1}{2\pi i}\int_{\varsigma-i\infty}^{\varsigma+i\infty} \widetilde{f}(s)e^{st}ds, \qquad \widetilde{f}(s) \sim O(s^{-k}),\ with\ k > 1 \tag{238}$$

Taking the Laplace transform of Eqn. 236:

$$s\widetilde{\hat{P}}(k,s) - \hat{P}(k,0) = \widetilde{\hat{P}}(k,s)\left[\hat{q}(k) - \hat{q}(0)\right] \tag{239}$$

Where $\hat{P}(k,0)$ represents the initial frequencies present. We may then write:

$$\widetilde{\hat{P}}(k,s) = \frac{1}{s - [\hat{q}(k) - \hat{q}(0)]}\hat{P}(k,0) \tag{240}$$

We may use the identity:

$$L\{e^{-at}\} = \frac{1}{s+a} \tag{241}$$

To find the inverse Laplace transform of Eqn. 240:

$$\hat{P}(k,t) = e^{[\hat{q}(k)-\hat{q}(0)]t}\hat{P}(k,0) \tag{242}$$

Assuming we have $\hat{q}(k)$ belonging to the LαS distribution, and truncating to lowest order, we may then write:

$$\hat{P}(k,t) = e^{-t|\gamma k|^{\alpha}\left[1-i\beta\tan\frac{\pi\alpha}{2}sgn(k)\right]}\hat{P}(k,0) \tag{243}$$

As $t > 0$, it may be seen that $t|f(x)| = |tf(x)|$. So:

$$\hat{P}(k,t) = e^{-|\gamma t^{\frac{1}{\alpha}} k|^{\alpha}\left[1-i\beta\tan\frac{\pi\alpha}{2}sgn(k)\right]}\hat{P}(k,0) = L\alpha S(k;\alpha,\gamma',\beta,0)\hat{P}(k,0) \tag{244}$$

Where $\gamma' \equiv t^{\frac{1}{\alpha}}\gamma$. The inverse fourier transform corresponds to:

$$P(x,t) = FT^{-1}\{L\alpha S(k;\alpha,\gamma',\beta,0)\} * P(x,0) \tag{245}$$

Consequently we see that the solution to the initial value problem is simply the convolution of the initial conditions with the LαS distribution - the evolution is then well-defined in Fourier space, and in order to compare to a numerical solution, we need only invert using a DFT to compare. Incidentally, it should be noted (again) that there is no closed form representation of the $L\alpha S$ distribution in terms of elementary functions [27] - the series representations are aggressively non-convergent, and it is best to simply find the PDF using some form of numerical Fourier inversion.

Numerically, this should be equivalent to solving the FADE, Eqn. 228 (note: we set τ to 1), repeated here for convenience:

$$\frac{\partial P}{\partial t} = \gamma^{\alpha} D^{\alpha}_{|x|} P(x,t) - \beta\tan\frac{\pi\alpha}{2}\gamma^{\alpha}\frac{\partial}{\partial x}\left(D^{\alpha-1}_{|x|}P(x,t)\right) \tag{246}$$

While there are implicit methods of solving certain classes of fractional differential equations, there were none found to deal with this particular form of the problem. Hence, for temporal discretisation we use both an (explicit) forward-Euler scheme:

$$\frac{\partial P}{\partial t} \simeq \frac{P_{i+1} - P_i}{\Delta t} \tag{247}$$

[27] hypergeometric functions are not typically considered 'elementary'

And also an explicit Runge-Kutta (global) 4th order accurate method, which is a standard predictor-corrector method.

The spatial discretisation is less straightforward.

7.1 Spatial Discretisation of Fractional Differential equation

We would like to discretise the fractional derivative, such that we may write:

$$D^{\alpha}_{|x|}P(x,t) \simeq M^{\alpha}P_j \tag{248}$$

Where M^{α} is a tensor of order $N \times N$ where N is our number of grid-points, and P_j is a column vector containing values of P at each grid point $j \in N$. In this case, we take a finite difference approach. The discretisation of the fractional derivative can be found by using the Grünwald-Letnikov representation of the fractional derivative [191, 196]:

$$G^{\alpha}f(x) = \lim_{h\to 0^+} \frac{1}{h^{\alpha}} \sum_{k=0}^{\infty} (-1)^k \binom{\alpha}{k} f(x-kh) \tag{249}$$

The Grünwald-Letnikov representation may be derived by considering the fundamental definition of the derivative as a limit:

$$f'(x) = \lim_{h\to 0^+} \frac{f(x+h) - f(x)}{h} \tag{250}$$

And applying recursively, such that:

$$f^{(n)}(x) = \lim_{h\to 0^+} \frac{f^{(n-1)}(x+h) - f^{(n-1)}(x)}{h} \tag{251}$$

Particularly useful is the theorem proved in references [196, 192], which establish that the

Grünwald-Letnikov derivative is equivalent to the Cauchy formula for derivatives such that:

$$\lim_{h\to 0^+} \frac{1}{h^\alpha} \sum_{k=0}^{\infty} (-1)^k \binom{\alpha}{k} f(x-kh) = \frac{\Gamma(\alpha+1)}{2\pi i} \int_C f(\xi) \frac{1}{(\xi - x)^{\alpha+1}} \tag{252}$$

Here, Γ denotes the gamma-function rather than the flux. As can be seen in appendix A regarding the Reisz identity, there is therefore a clear relation of the Grünwald-Letnikov derivative to the fractional (Reisz) derivative, and so a fractional (centred) difference discretisation may be found [197]. This may be expressed in a matrix as follows:

$$M^\alpha = \frac{1}{h^\alpha} \begin{bmatrix} \omega_0^\alpha & \omega_1^\alpha & \omega_2^\alpha & \dots & \omega_{N-1}^\alpha & \omega_N^\alpha \\ \omega_1^\alpha & \omega_0^\alpha & \omega_1^\alpha & \dots & \omega_{N-2}^\alpha & \omega_{N-1}^\alpha \\ \omega_2^\alpha & \omega_1^\alpha & \ddots & & & \vdots \\ \vdots & \vdots & & \ddots & & \vdots \\ \omega_{N-1}^\alpha & \omega_{N-2}^\alpha & \dots & \dots & \omega_0^\alpha & \omega_1^\alpha \\ \omega_N^\alpha & \omega_{N-1}^\alpha & \dots & \dots & \omega_1^\alpha & \omega_0^\alpha \end{bmatrix} \tag{253}$$

Where M^α is symmetric, $M^\alpha = (M^\alpha)^T$, and h denotes the spatial distance between grid-points. The values of ω_k^α are given as:

$$\omega_k^\alpha = \frac{(-1)^k \Gamma(\alpha+1) sgn(\cos\frac{\alpha\pi}{2})}{\Gamma(\frac{\alpha}{2}-k+1)\Gamma(\frac{\alpha}{2}+k+1)} \tag{254}$$

This works for arbitrary $\alpha \in [0,2]$ (except 1) which is convenient, and one may be satisfied that this is the case by computing M^α for the second-order accurate central difference, and observe that it returns the expected stencil. It was found in later work [198] that this fractional centred difference approach is accurate to $O(h^2)$.

Now, in our FADE we have a fractional 'advection' term too, not simply the symmetric fractional diffusion as in Eqn. 248:

$$\frac{\partial}{\partial x}\left(D_{|x|}^{\alpha-1} P(x,t)\right) \simeq A^{\alpha-1} P_j \tag{255}$$

We may write the second-order accurate central difference approximation for the first-order derivative as:

$$f'_j(x) = \frac{f_{j+1} - f_{j-1}}{2h} = \frac{1}{2h}\begin{bmatrix}\dots & 0 & -1 & 0 & 1 & 0 & \dots\end{bmatrix}\begin{bmatrix}\vdots \\ f_{j-2} \\ f_{j-1} \\ f_j \\ f_{j+1} \\ f_{j+2} \\ \vdots\end{bmatrix} \tag{256}$$

We may then represent the first-order difference as a tridiagonal $N \times N$ asymmetric matrix, F, using Eqn. 256 [28]. We may then express $A^{\alpha-1}$ as:

$$A^{\alpha-1} = FM^{\alpha-1} \tag{257}$$

As $A^{\alpha-1}$ is the product of a symmetric and an asymmetric matrix, it is therefore asymmetric. $A^{\alpha-1}$ is, however, the discretisation of the 'fractional' advection component. We denote the members of the matrix $A^{\alpha-1}$ as a_k^α, in the same manner as in Eqn. 253 - to represent the asymmetry, we permit $a_k^\alpha,\ k \in\ [-N, N]$ rather than solely $N > 0$ as was the case for the M^α matrix.

We therefore have a discretisation for the operations in our FADE, and so can solve it using quite straightforward methods. But first, we should give some thought to boundary conditions.

7.2 Treatment of Boundary Conditions

The FADE is an equation which, as we have shown, originates from the assumption of a system in which there exists a jump function, $q(\Delta x)$, which applies uniformly and homogeneously over the space such that it is independent of x and is independent of time t, and

[28] except at the boundaries, of course

which belongs to the $L\alpha S$ distribution. It has operators which mean that there is a non-local dependence of flux on the distribution of the transported quantity - and as we have seen, the matrices which we use (see Eqn. 253) to provide central difference approximations of the required operators are typically dense; that is, have non-zero values for each entry.

This key difference between a local difference operator (such as in Eqn. 256) and a non-local operator such as we must use to solve FADEs is highlighted most distinctly in visual format - see Figs 32 and 33.

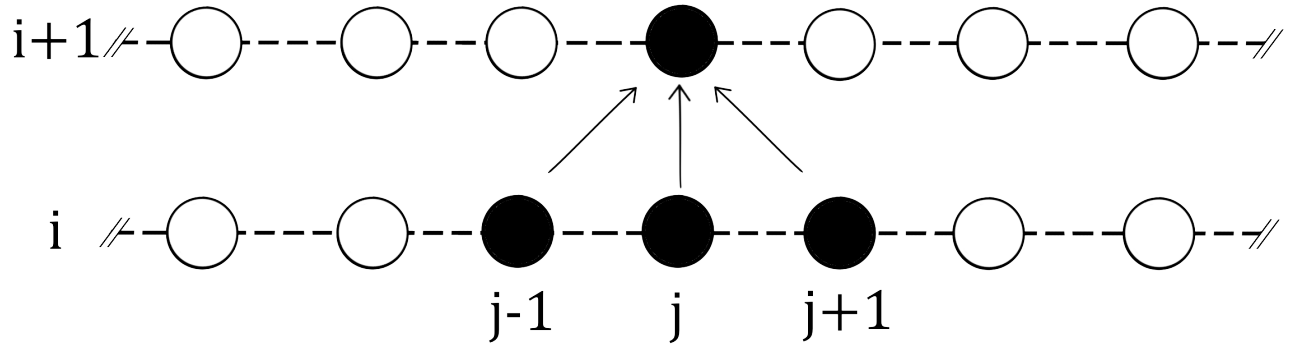

Figure 32: The contribution to a node at time $i+1$ and position j using an explicit scheme where the operator is some 3-point stencil

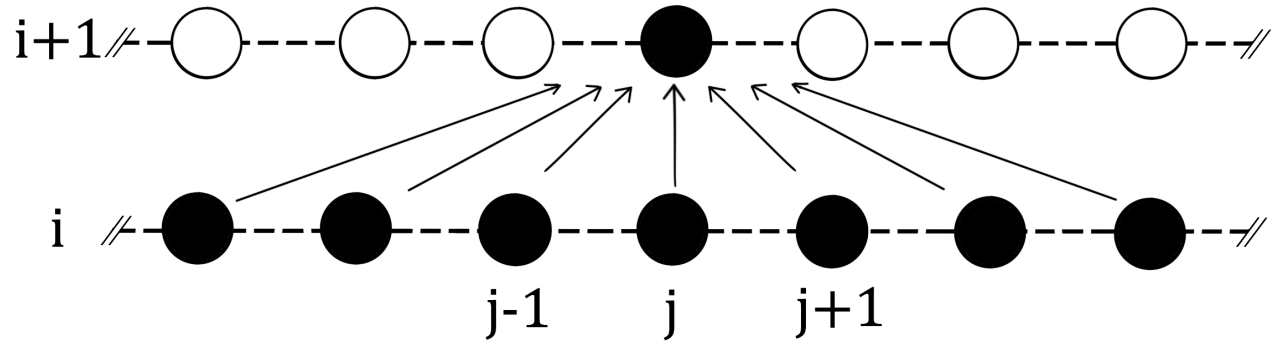

Figure 33: The contribution to a node at time $i+1$ and position j using an explicit scheme where the operator is nonlocal

Boundary conditions require a little extra consideration if we wish to solve FADE problems. Commonly used boundary conditions are Dirichlet boundary conditions, in which the boundary is set at a specified value, and Neumann boundary conditions, in which the gradient at the boundary is set at a specified value - or some combination thereof. In the finite difference case which concerns us specifically, we use ghost grid-points to set the boundary conditions; this is equivalent to having a number of grid points which are set at the value

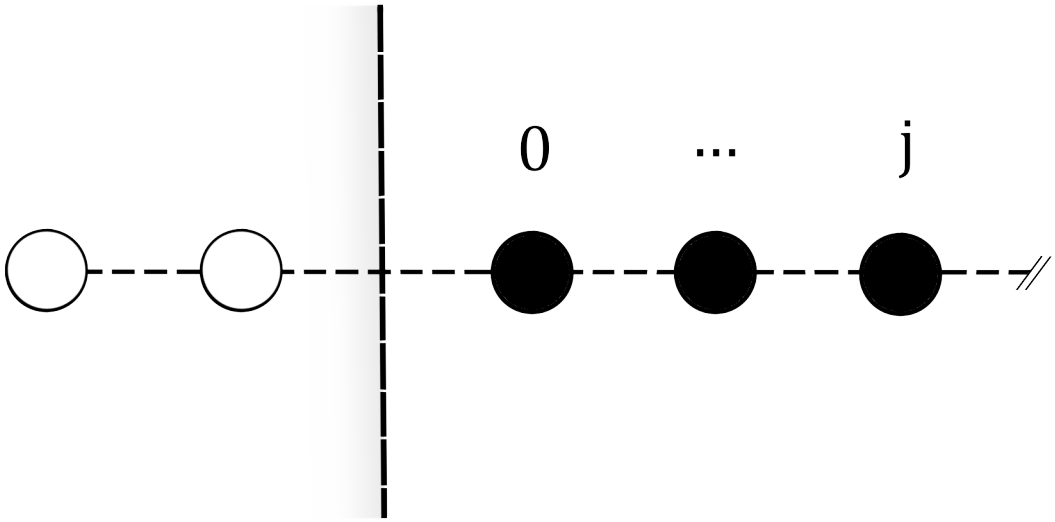

Figure 34: An image of a set of grid points featuring nodes, a number of which are 'ghost' grid points (white points); these are used solely to enforce boundary conditions

of the boundary condition in the case of a Dirichlet condition, or can be altered to enforce Neumann conditions if required. The grid points then appear as in Fig. 34.

There are three situations into which problems may be classified:

The first case is a closed system - If it is the case that our boundary is solid or otherwise impermeable, it is quite reasonable to use whatever boundary condition that may be reasonably physically imposed in the usual manner. This is because there is no transfer of the transported quantity into or out of the system. It is another matter entirely to consider what might be physically reasonable boundary conditions for a non-local fluid quantity, and we do not concern ourselves with these details here.

The second case is an open system with local transport into the system, and non-local transport out of the system. In this system, the transported quantity may enter and is then transported with a FADE, and so is non-local within the system. It should be pointed out that this implicitly requires no non-local transport from outside the system into the system, and so implies a non-local jump function *within the region only* - and therefore a spatially varying jump function (for some reason). As it is an open system, a non-local jump function would suggest non-local transport of the quantity of interest outside the system; therefore equilibrium would have to be maintained by a source term or local transport into the system region. It would be possible to represent this with standard boundary conditions at the

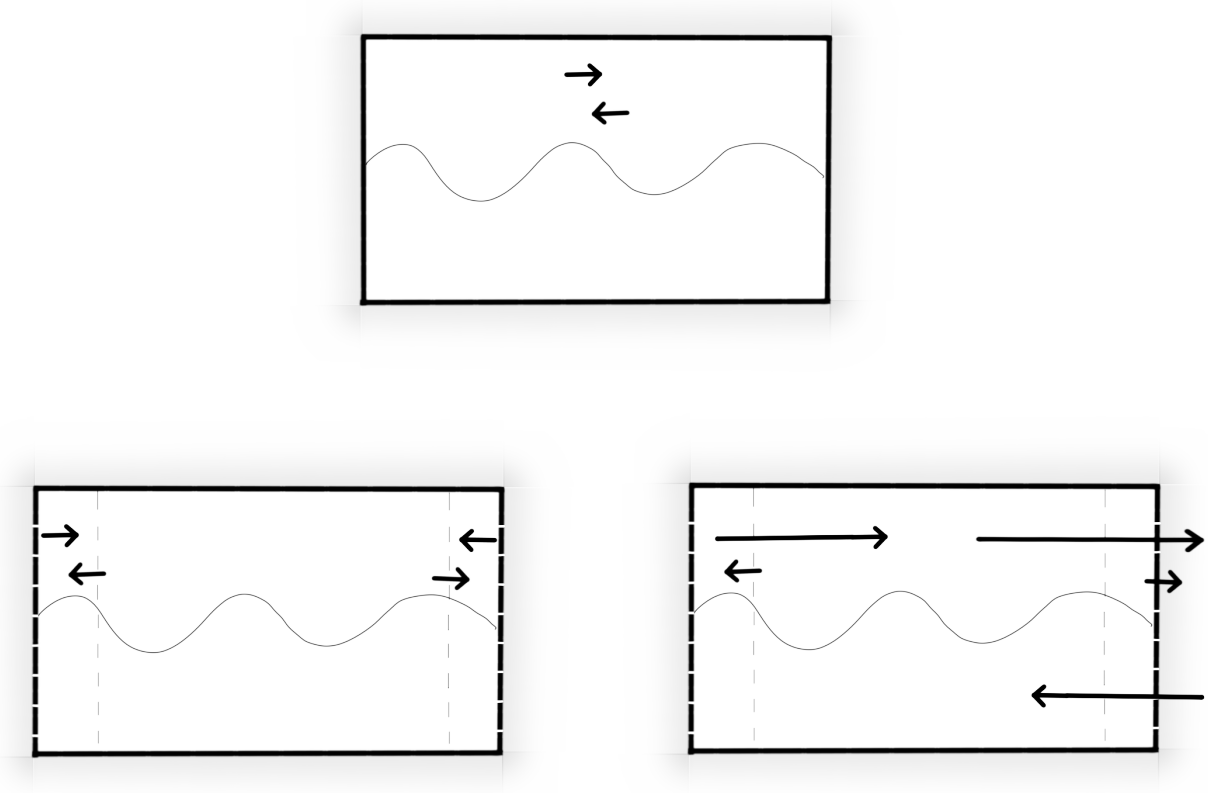

Figure 35: Top: A closed system. Left: An open system with local boundary conditions. Right: An open system with non-local boundary conditions

relevant boundaries.

The third case is an open system with non-local transport both into and out of the system. This then allows for a spatially uniform and homogeneous jump function, and the region of the system which we are considering is only a subset of the system as a whole. This particular case is the case of interest, and we shall consider a method for dealing with this.

We use the non-local fractional derivative operator as an example. To calculate the solution of the fractional derivative at a particular grid point, $D^{\alpha}_{|x|,j}$, we use Eqn. 248 - and so:

$$D^{\alpha}_{|x|,j} f(x,t) = \frac{1}{h^{\alpha}} \begin{bmatrix} \omega^{\alpha}_{N} & \dots & \omega^{\alpha}_{1} & \omega^{\alpha}_{0} & \omega^{\alpha}_{1} & \dots & \omega^{\alpha}_{N} \end{bmatrix} \begin{bmatrix} f_{j-N} \\ \vdots \\ f_{j-1} \\ f_{j} \\ f_{j+1} \\ \vdots \\ f_{j+N} \end{bmatrix} \tag{258}$$

If our domain is infinite such that $N = \infty$, this poses no problem to solve, apart from dealing with the $N \times N$ matrix. However, this would have no boundaries. We therefore say that the system is bounded at the lower end by p_{-} and at the upper end by p_{+}, such that:

$$D^{\alpha}_{|x|,j} f(x,t) = \frac{1}{h^{\alpha}} \left[\begin{array}{ccc|ccc|ccc} \dots & \omega^{\alpha}_{p_{-}+1} & | & \omega^{\alpha}_{p_{-}} & \dots & \omega^{\alpha}_{0} & \dots & \omega^{\alpha}_{p_{+}} & | & \omega^{\alpha}_{p_{+}+1} & \dots \end{array} \right] \begin{bmatrix} \vdots \\ f_{j-p_{-}-1} \\ \hline f_{j-p_{-}} \\ \vdots \\ f_{j} \\ \vdots \\ f_{j+p_{+}} \\ \hline f_{j+p_{+}+1} \\ \vdots \end{bmatrix} \tag{259}$$

Where the lines represent the separation between the region within the boundary and the region without. We may still have $N = \infty$, but now finite p restricts the size of the region we care about. What becomes clear when the problem is presented as it has been, is that there is a contribution from all grid-points outside the boundary to the point j.

This may be expressed succinctly by grouping the contributions as follows:

$$h^{\alpha} D^{\alpha}_{|x|,j} f(x,t) = \sum_{k=0}^{p_-,\ p_+} \omega_k^{\alpha} f_{j\mp k} + \sum_{k=p_-+1}^{N} \omega_k^{\alpha} f_{j-k} + \sum_{k=p_++1}^{N} \omega_k^{\alpha} f_{j+k} \tag{260}$$

The first summation represents the contribution to the computation from within the space. The last two summations represent the contribution to the operator from outside the space. If we do not consider the last two sums and only consider the first sum, then we are saying that we do not have non-local transport into the domain, and therefore the jump function is not spatially uniform and homogeneous.

The expression as in Eqn. 260 permits us to apply both Dirichlet and Neumann conditions.

Dirichlet conditions are set by $f_{j-k} = \zeta_-$, for $k > p_- + 1$ and $f_{j+k} = \zeta_+$, for $k > p_+ + 1$, where $\zeta_{\mp}$ are constants. This then permits:

$$h^{\alpha} D^{\alpha}_{|x|,j} f(x,t) = \sum_{k=0}^{p_-,\ p_+} \omega_k^{\alpha} f_{j\mp k} + \zeta_- \sum_{k=p_-+1}^{N} \omega_k^{\alpha} + \zeta_+ \sum_{k=p_++1}^{N} \omega_k^{\alpha} \tag{261}$$

One may observe that we are still assuming $N = \infty$. The last two terms then require truncation at an n - we suggest n such that:

$$|\zeta_{\mp} \omega_n^{\alpha}| \ll 1 \tag{262}$$

This introduces a small truncation error. Numerically, we see that accounting for non-local transport into the system requires that for each j, two additional sums must be computed, which are $\sum_{k=p_++1}^{n} \omega_k^{\alpha}$ and $\sum_{k=p_-+1}^{n} \omega_k^{\alpha}$.

A similar process may be applied to take into account Neumann conditions, which fixes the gradient at the boundary. Neumann conditions specify that the gradients are fixed at the boundary such that:

$$f'|_{j-k} = \psi_-, \quad f'|_{j+k} = \psi_+ \tag{263}$$

where $k > p_- \pm 1$, and of course we still have $f_{j\mp k} = \zeta_\mp$, but they are not constant (if the values are fixed at the boundary, then we have Robin or mixed boundary conditions). Again, if we are to assume non-local transport into the domain as before, we then need to define the values of f beyond the boundary, for the non-local operator to operate upon:

$$f_{j-k} = \zeta_- + k\psi_-, \quad k > p_- + 1 \tag{264}$$

$$f_{j+k} = \zeta_+ - k\psi_+, \quad k > p_+ + 1 \tag{265}$$

We then write Eqn. 260 as:

$$h^\alpha D^\alpha_{|x|,j} f(x,t) = \sum_{k=0}^{p_-,\ p_+} \omega_k^\alpha f_{j\mp k} + \zeta_- \sum_{k=p_-+1}^{N} \omega_k^\alpha + \psi_- \sum_{k=p_-+1}^{N} k\omega_k^\alpha + \zeta_+ \sum_{k=p_++1}^{N} \omega_k^\alpha - \psi_+ \sum_{k=p_++1}^{N} k\omega_k^\alpha \tag{266}$$

Where the last four terms are due to the nonlocal flux into the domain. Again we should truncate with n such that:

$$|\zeta_\mp \omega_n^\alpha \pm \psi_\mp \omega_n^\alpha n| \ll 1 \tag{267}$$

Note also that it is straightforward to enforce mixed/Robin boundary conditions with equation 266As noted previously, one should ensure that the lowest-order truncation of the FADE is still valid.

7.3 Comparison of the Numerical Solution of FADEs and the Spectral Solution

We solve the FADE numerically, and compare to the spectral shooting problem for a variety of $\alpha,\ \beta$. We use both forward Euler (FE) time discretisation as well as an RK4 scheme. We find that they typically result in near identical solutions for the problems considered in

this section, however the FE scheme typically requires far shorter Δt to produce reasonable results. We take Eqn. 245, and propagate it for the initial condition:

$$P(x,0) = A\frac{1}{\sqrt{2\pi\sigma^2}}e^{-\frac{(x-\mu)^2}{2\sigma^2}} \tag{268}$$

In the limit $1 \ll t$, we see from Eqn. 244 that we expect $\hat{P}(k,t) \to 0$ for $k \neq 0$, and we expect $\hat{P}(0,t) = \hat{P}(0,0)$. Therefore we expect:

$$\hat{P}(k,t) \to A\delta(k), \quad t \to \infty \tag{269}$$

So for a space of size Nh, where N is the number of nodes and h is our spatial separation, we expect:

$$P(x,t) \to \frac{A}{Nh}, \quad t \to \infty \tag{270}$$

As $nh \to \infty$, we expect $P(x,t) \to 0$. As we are not yet concerned with the effects of boundary conditions, for the numerical FADE we will set the initial boundary with zero value, and allow them to evolve in time - in essence, we then allow the FADE an infinite space while the spectral solution has a finite space. Consequently, the error between the two should converge to $\frac{A}{nh}$ due to the periodic nature of the spectral solution.

We will first examine cases for which $\beta = 0$ and $\alpha \in (0,2], \alpha \neq 1$ - that is, the pure fractional 'diffusion' case, as in Eqn. 271. Then, satisfied with that we will examine the more interesting case for which $\beta = 1$ [29] and $\alpha \in (1,2)$, as in Eqn. 272, for which we have our fractional 'advection' term in addition to our fractional diffusion term. We explore potential stability issues, establish their causes, and determine what can be done to improve the solution of FADEs in the general case. Note that we have simply set $\gamma = 1$ for all cases, as this is simply a spatial scaling parameter

[29] NB: we could equally have picked $\beta = -1$, the cases are numerically identical for this test problem, simply mirrored

$$\frac{\partial P}{\partial t} = D^{\alpha}_{|x|} P(x,t) \tag{271}$$

$$\frac{\partial P}{\partial t} = D^{\alpha}_{|x|} P(x,t) - \tan\frac{\pi\alpha}{2}\frac{\partial}{\partial x}\left(D^{\alpha-1}_{|x|} P(x,t)\right) \tag{272}$$

For the test problem, we select $nh = 10$, with $h = 0.01$ and $P(x,0)$ with parameters $A = 0.1$, $\sigma = 0.1$, $\mu = 5$, which are selected as it places the initial Gaussian in the centre of the domain, an appropriate distance from the boundary.

We compare the spectral problem to the solution of the FADE using a measure of normalised error:

$$\varepsilon(x,t) = \frac{1 + P_{FADE}(x,t)}{1 + P_{spectral}(x,t)} - 1 \tag{273}$$

and take the root-mean-squared (RMS) average over space to get error with time:

$$\varepsilon_{RMS}(t) = \sqrt{\frac{1}{n}\sum_{i=0}^{n} \varepsilon(x_i,t)} \tag{274}$$

Consequently, due to our selection of A, n and h, we expect $\varepsilon_{RMS}(t) = 0.01$ as $t \to \infty$.

7.3.1 FADE for $\beta = 0$, $\alpha \in (0,2]$

Here we consider the solution of the FADE for the case β, the 'skewness' parameter, is zero. This is then simply the fractional 'diffusion' problem as in Eqn. 271. Given this derives from the even component, we expect the solution to consist of (non-local) symmetric spreading in the x-direction (and so on for higher dimensions). We find that this is indeed the case, with an example evolution of the Gaussian initial condition (see Eqn. 268), as may be seen in Figs. 36 and 37. We note especially from Fig. 37 that the agreement of the numerical FADE and the inversion is qualitatively good, although it diverges for later times.

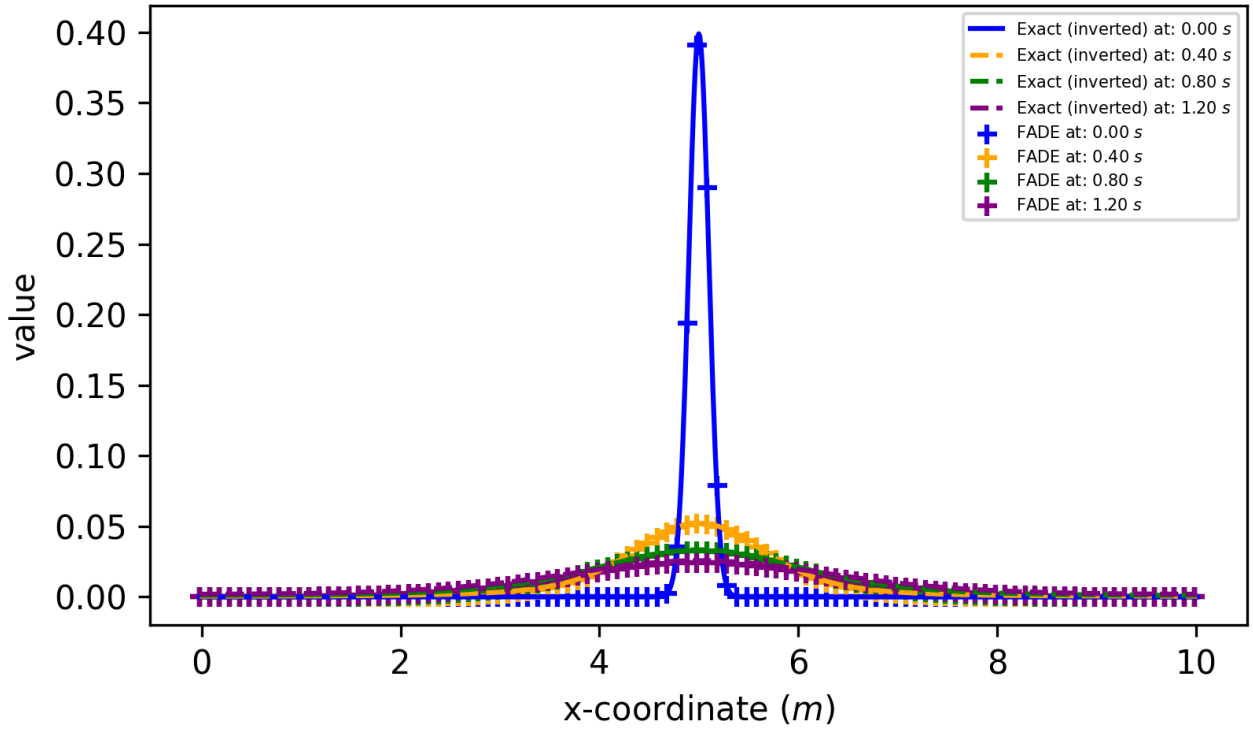

Figure 36: Evolution of the FADE for $\alpha = 1.5$, $\beta = 0$ (dotted line) with an RK4 scheme, vs inversion of the spectral shooting problem with same parameters (dashed line)

As discussed already, we expect a divergence of the spectral and numerical FADE due to the periodicity of the spectral solution - that is, the spectral shooting problem conserves the scalar being transported (i.e. the initial area), whereas the numerical FADE has a loss due to non-local fractional transport out of the domain. This is irreconcilable without making the spatial domain infinite, which is beyond our computational capacity, or if we wish to conserve the initial quantity being transported, some kind of inward transport or source term to maintain equilibrium[30].

We note the RMS error in Fig. 38, and observe that it is always less than the expected limit $\varepsilon_{RMS}(\infty) = 0.01$ which indicates quantitatively good agreement. We did examine error for various $\frac{h}{\Delta t}$, and noted that it was essentially identical down to $\frac{h}{\Delta t} = 15$ for $\alpha = 1.5$, below which the numerical scheme was unstable. One note from the scan in $\frac{h}{\Delta t}$ was that the required $\frac{h}{\Delta t}$ for stability increased as $\alpha \to 2$, to $\frac{h}{\Delta t} = 200$ which is expected for the standard diffusion problem solved with the forward Euler method.

[30]...fractional or otherwise

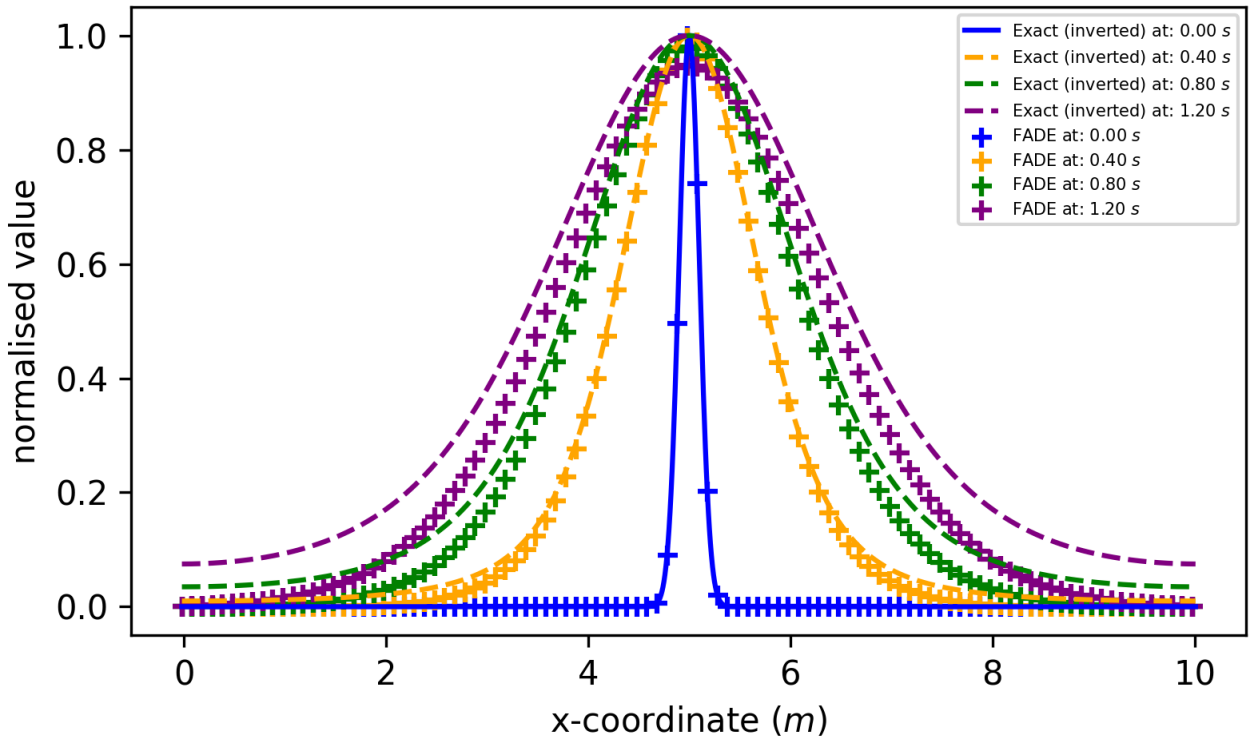

Figure 37: Evolution of the FADE for $\alpha = 1.5,\ \beta = 0$ (dotted line) with an RK4 scheme, vs inversion of the spectral shooting problem with same parameters (dashed line), normalised to the maximum value of the spectral shooting problem for each time.

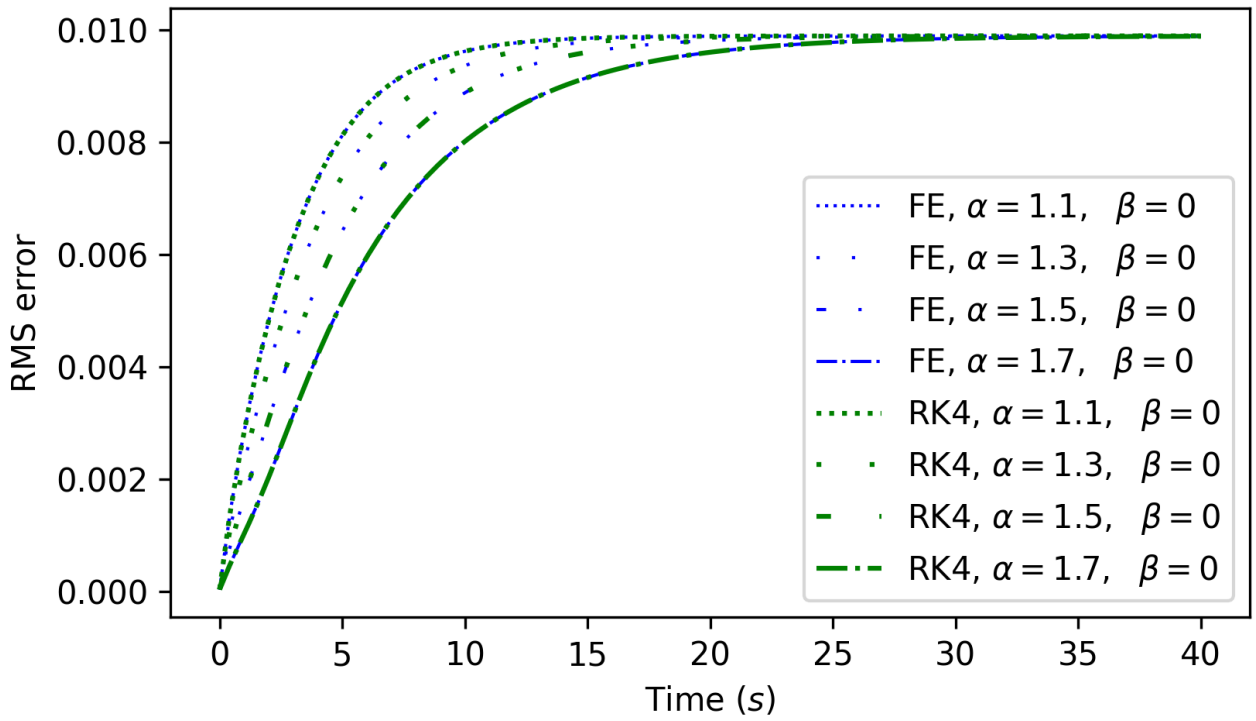

Figure 38: RMS Error with time for various values of α, and with both forward Euler and RK4 time discretisation

We see also in Fig. 38 that the convergence to $\varepsilon_{RMS}(\infty) = 0.01$ takes longer as $\alpha \to 2$. This reflects more rapid transport for lower α; this is expected, as α is the characteristic exponent determining the nature of non-locality.

When scanning in α, we examined also the accuracy of the numerical FADE for $\alpha < 1$. We note in Fig. 39 which shows the case for $\alpha = 0.7$ that the numerical FADE does not compare well to the inversion of the spectral problem. The numerical scheme clearly needs further care for $\alpha < 1$, and it is concerning that negative values are observed.

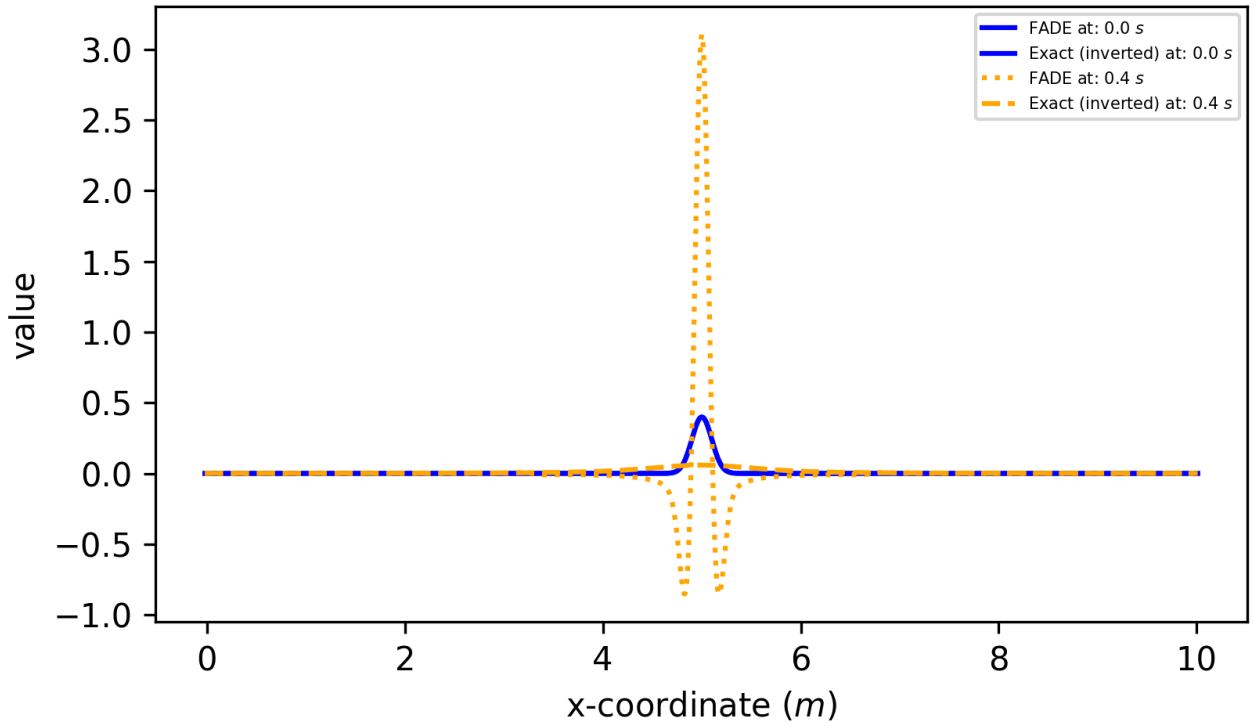

Figure 39: Comparison of numerical solution of FADE vs the solution of the spectral shooting problem for the case $\alpha = 0.7$, Forward Euler

7.3.2 FADE for $\beta = 1$, $\alpha \in (1, 2)$

Here we consider the solution of the FADE for the case β, the 'skewness' parameter, is one. Note from section 6.4 that we expect $\beta \in [-1, 1]$ given that $q(\Delta x) = L\alpha S(k)$. The key distinction here is the introduction of the fractional 'advection' term - so called as it arises from the odd-component of the $L\alpha S$ distribution, and so is analagous to the advection term. Note that for $\alpha \in [1, 2]$ - say, 1.5 - we have:

$$\frac{\partial P}{\partial t} = D^{1.5}_{|x|} P(x, t) - \tan \frac{3\pi}{4} \frac{\partial}{\partial x} \left(D^{0.5}_{|x|} P(x, t) \right) \tag{275}$$

Where the fractional 'advection' component is then calculated with the same M^α matrix as in the case that we have fractional 'diffusion' with $\alpha < 1$ - consequently, it may be the case that we have a similar problem as that observed in 39, which would then require urgent solution.

Fortunately, as can be observed from the solution of the comparison of the numerical solution of the FADE with the spectral shooting problem, both with $\alpha = 1.5$, $\beta = 1$ as depicted in Figs. 40 and 41, we may observe excellent qualitative agreement between the inversion and the numerical solution. We do note negative values of the numerical FADE, clear in Fig. 41, which are also observed in Fig. 39 for the fractional 'diffusion' case: however, it seems that the impact on the solution is limited in the full FADE. Further study of this should be completed, in case this is an issue which could result in numerical instability in certain circumstances.

It is interesting to note the contribution of the fractional 'advection' component; it does appear to be aptly named, as it does seem to cause a form of transport which resembles advection on initial inspection. We observe the impact on fractional advection for a characteristic exponent closer to 1, $\alpha = 1.1$, in Fig. 42. We see that 'increasing' the non-locality by reducing α in this way has a substantial impact on the fractional 'advection', as might be expected from the $\tan \frac{\pi\alpha}{2}$ multiplier. One observes that should a fractional 'advection', fractional 'diffusion' pulse arise in a diagnostic signature, it might be tempting to the scientist observing it to characterise it as advective; if we were to assign a velocity to the bulk of the pulse, however, it would appear to decrease with distance i.e. we would see a reducing advection coefficient that may be described as anomalous. It would be of interest to charac-

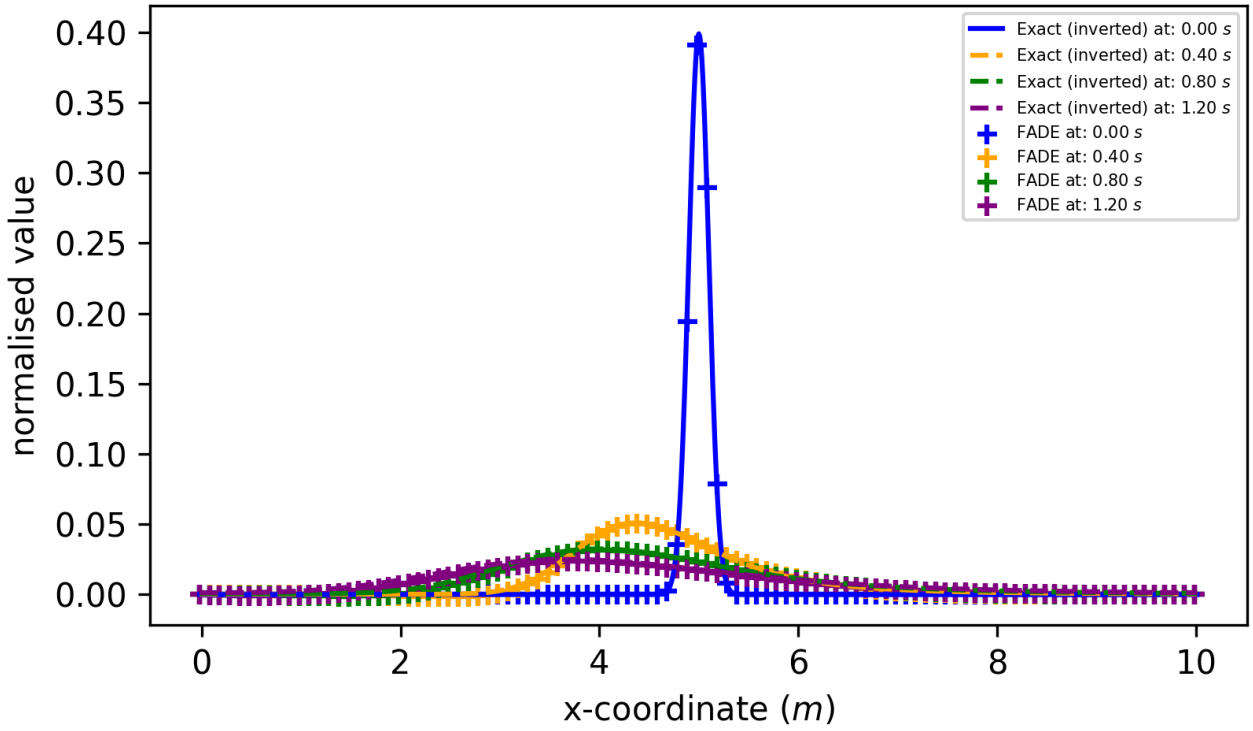

Figure 40: Evolution of the FADE for $\alpha = 1.5,\ \beta = 1$ (dotted line) with an RK4 scheme, vs inversion of the spectral shooting problem with same parameters (dashed line)

terise the signature of the effective advection that might arise, however that is not of direct relevance at this time.

We observe the RMS error for the $\beta = 1$ case in Fig. 43 for $\alpha \in [1, 2]$. The error appears to be somewhat larger for lower values of α, but we note convergence to the expected $\varepsilon_{RMS}(\infty) = 0.01$ in a very similar time, for the same α. This is expected, as it is α which determines the non-locality. Nonetheless, the error is still less than 0.01 for all cases, giving us confidence that despite some numerical issues, the numerical solution of the FADE is appropriate - although it could clearly do with some refinement.

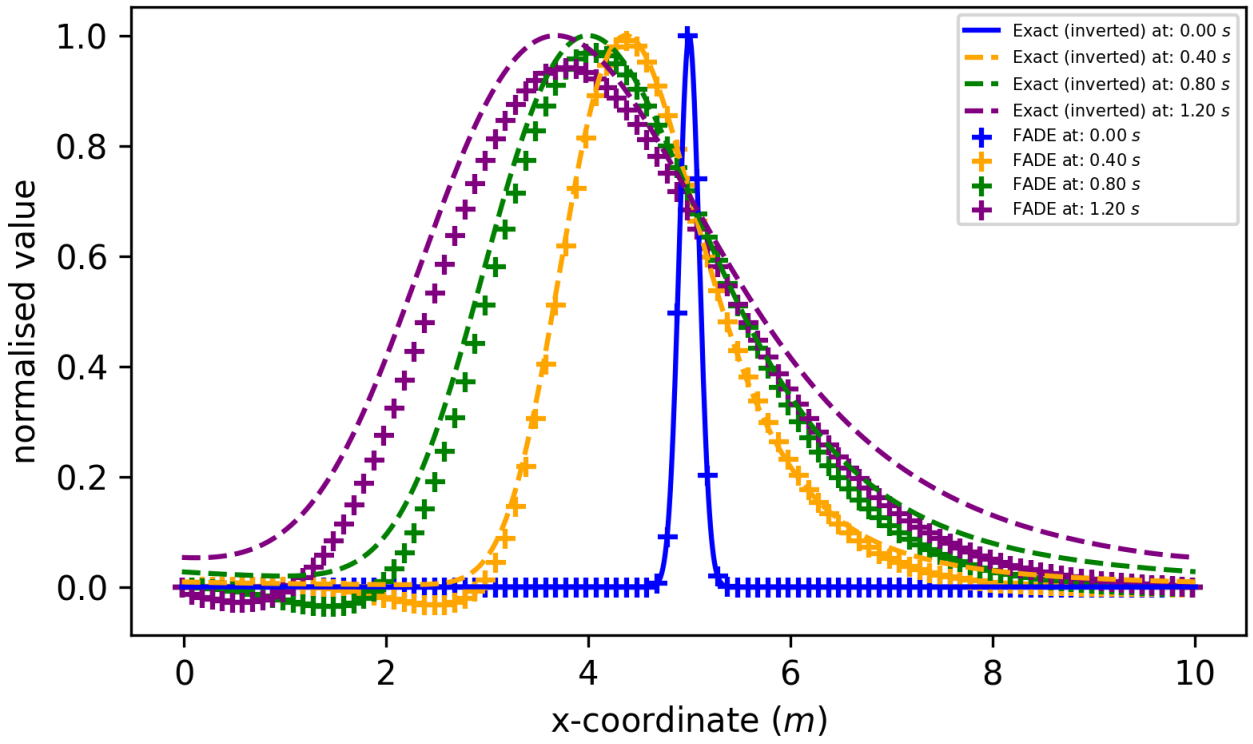

Figure 41: Evolution of the FADE for $\alpha = 1.5,\ \beta = 1$ (dotted line) with an RK4 scheme, vs inversion of the spectral shooting problem with same parameters (dashed line), normalised to the maximum value of the spectral shooting problem for each time.

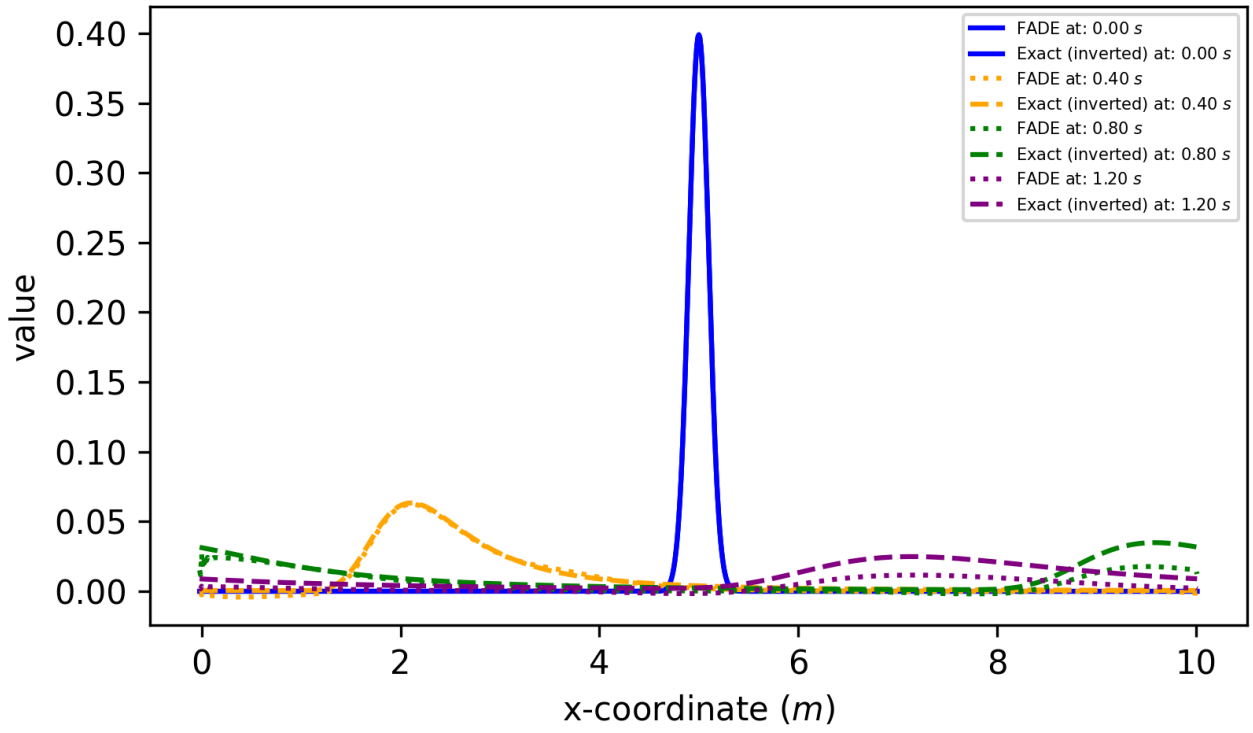

Figure 42: Evolution of the FADE for $\alpha = 1.1,\ \beta = 1$ (dotted line) with an FE scheme, vs inversion of the spectral shooting problem with same parameters (dashed line)

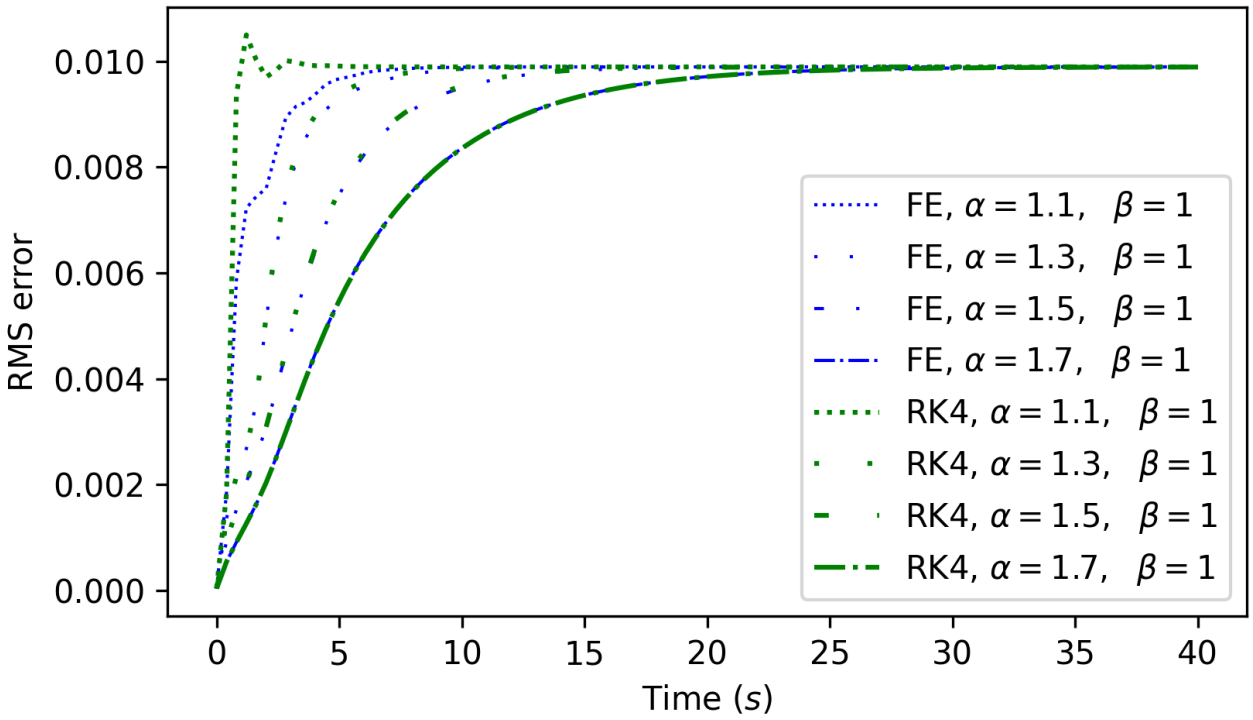

Figure 43: RMS Error with time for various values of α and $\beta = 1$

7.3.3 FADE and non-local boundary conditions

One aspect of some interest is the implementation of boundary conditions, as boundary value problems consist of the vast majority of physical problems we would like to understand. An issue discussed in section 7.2 is the implementation of boundary conditions in the case that the dynamics governing the system of interest are non-local. If we simulate only part of a domain, and yet non-local dynamics persist throughout the whole domain, then we must incorporate non-local transport into the domain. Additionally, in the solution of numerical FADEs we will always have non-local transport out of the domain. As this impacts the transport, it becomes of utmost importance to consider the 'locality' of our boundary conditions, due to the impact on conservation.

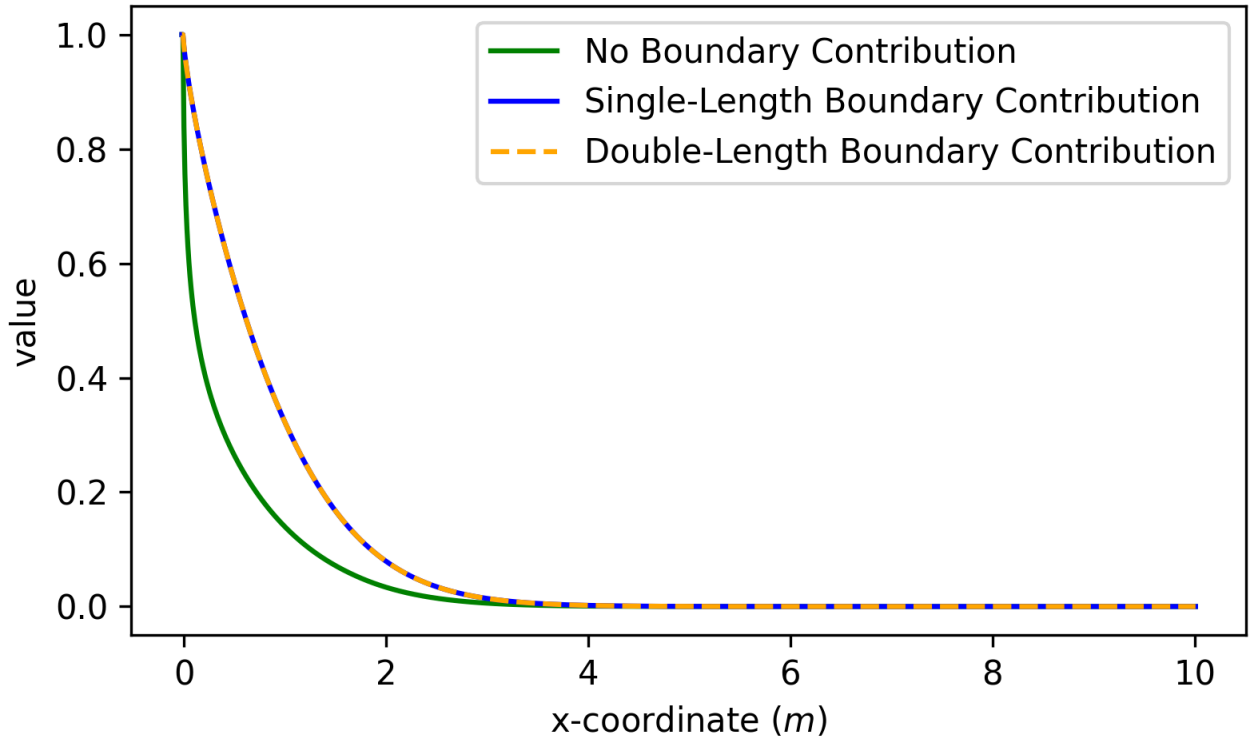

Figure 44: Solution of (dirichlet) boundary value problem with $\alpha = 1.5$, $\beta = 0$ to $t = 1.0$ s, with non-local transport into the domain equivalent to one and two lengths of the domain (blue, yellow, respectively) and without non-local transport into the domain.

In this section we implement non-local Dirichlet boundary conditions (i.e. fractional transport into the domain given that the domain continues at the fixed value) following our discussion in section 7.2, and compare to a simple Dirichlet boundary without non-local transport into the domain. We simply implement the FADE and fix the left boundary at 1

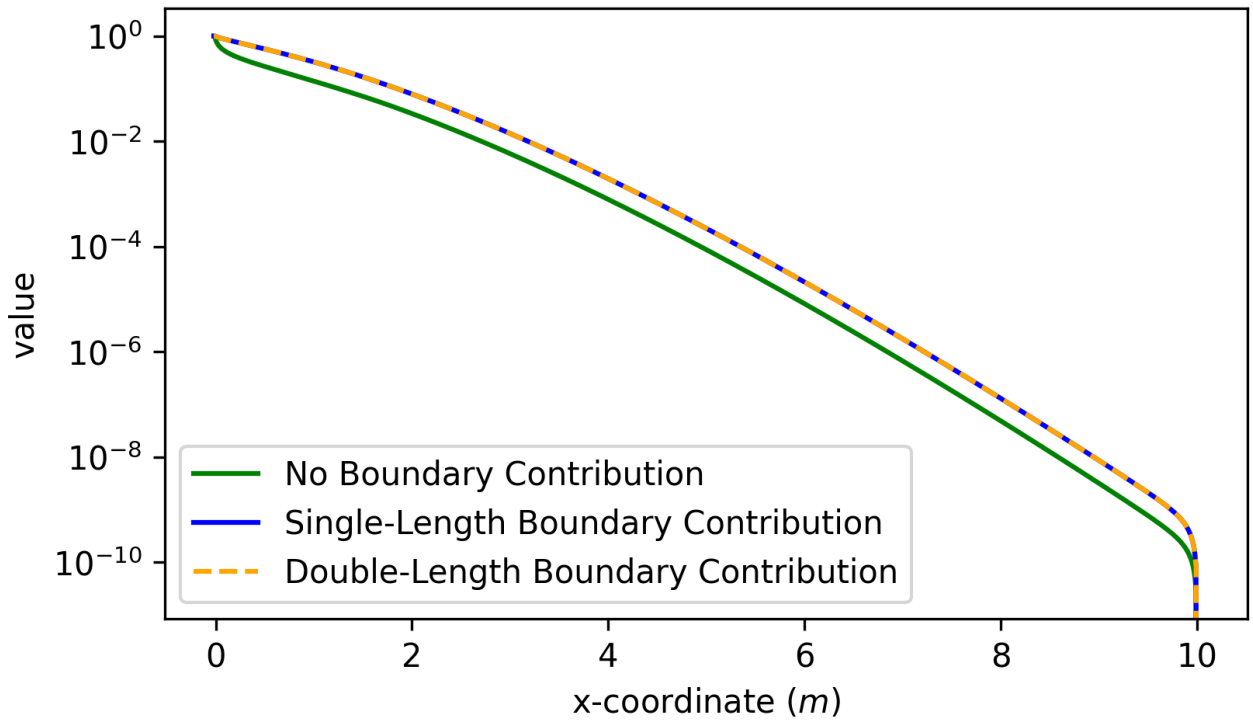

Figure 45: Solution of (dirichlet) boundary value problem with $\alpha = 1.5$, $\beta = 0$ to $t = 1.0$ s, with non-local transport into the domain equivalent to one and two lengths of the domain (blue, yellow, respectively) and without non-local transport into the domain, log-plot

and the right boundary at 0 using ghost cells, and then evolve the FADE. The results of this can be seen in Figs. 44 and 45 for time $t = 1.0$ s after initialization.

The green line, denoting Dirichlet conditions without fractional transport into the domain is clearly distinct from the blue and the yellow line, denoting various kinds of fractional transport into the domain. In log-space, the difference is less distinct over the majority of the domain, where the cases appear almost completely self similar. Nonetheless, overall the difference is distinct and significant.

7.3.4 FADE and convergence

Finally for this section, we study the convergence of a FADE with the left side fixed at 1 and the right side at 0, for both $\beta = 0$ and $\beta = 1$. As a basis of comparison to bear in mind when considering this section, the steady-state solution of the diffusion problem with the same boundary conditions is linear with gradient $-\frac{1}{L}$. In this case we use non-local Dirichlet

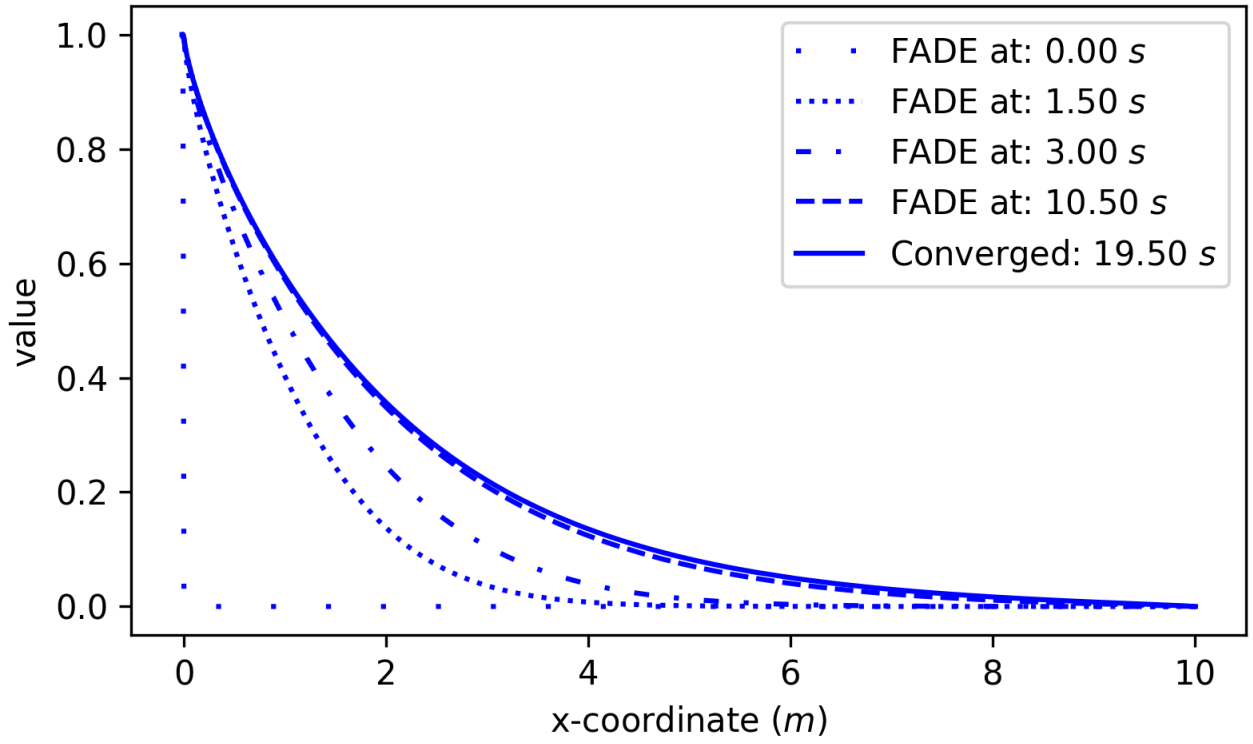

Figure 46: Solution of (dirichlet) boundary value problem with $\alpha = 1.5,\ \beta = 0$ to convergence at 19.5 s, with an RK4 scheme

boundary conditions.

It is interesting to note that the numerical FADE is convergent for both cases, and in neither case does it resemble the solution to the diffusion equation. It is worth noting that the solution to the FADE for $\beta = -1$ is non-convergent if the left boundary is fixed, but does converge in the case that the problem is mirrored exactly.

A comparison of various converged solutions may be seen in Fig. 50. There are progressively larger differences between the solutions for the same α and different β - this is due to the value of α directly impacting the magnitude of the 'fractional advective' component as may be seen in Eqn. 272.

The impact of non-locality is evident on boundary value problems such as these - it is the balance of transport into, out-of, and within the domain that determines the steady state solution of these problems, and it results in substantially different solutions.

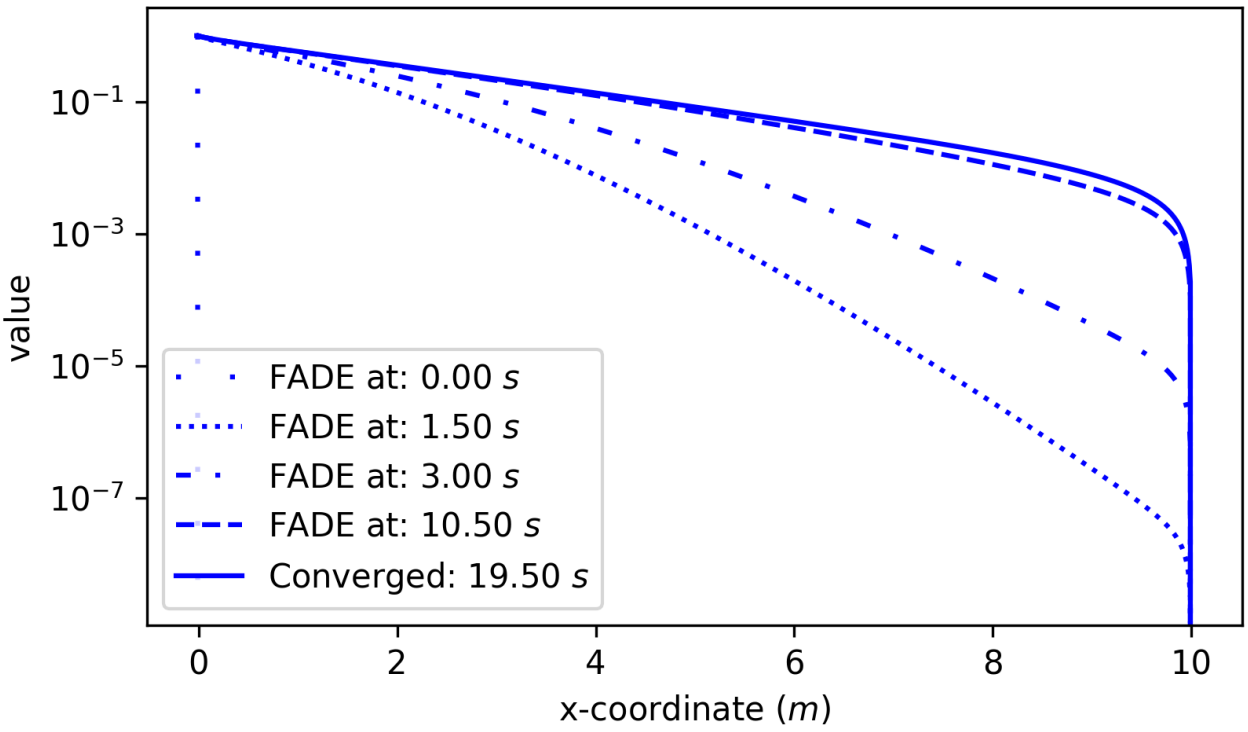

Figure 47: Solution of (dirichlet) boundary value problem with $\alpha = 1.5,\ \beta = 0$ to convergence at 19.5 s, with an RK4 scheme (log plot)

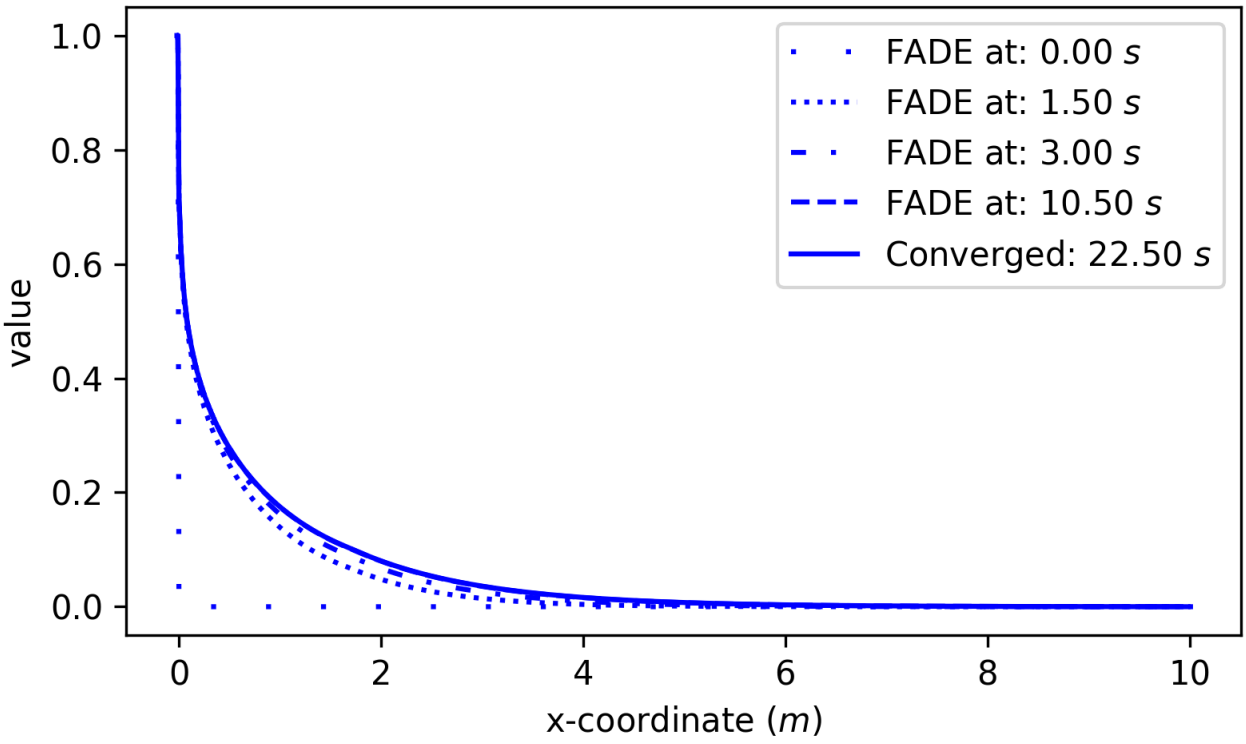

Figure 48: Solution of (dirichlet) boundary value problem with $\alpha = 1.5,\ \beta = 1$ to convergence at 22.5 s with an RK4 scheme

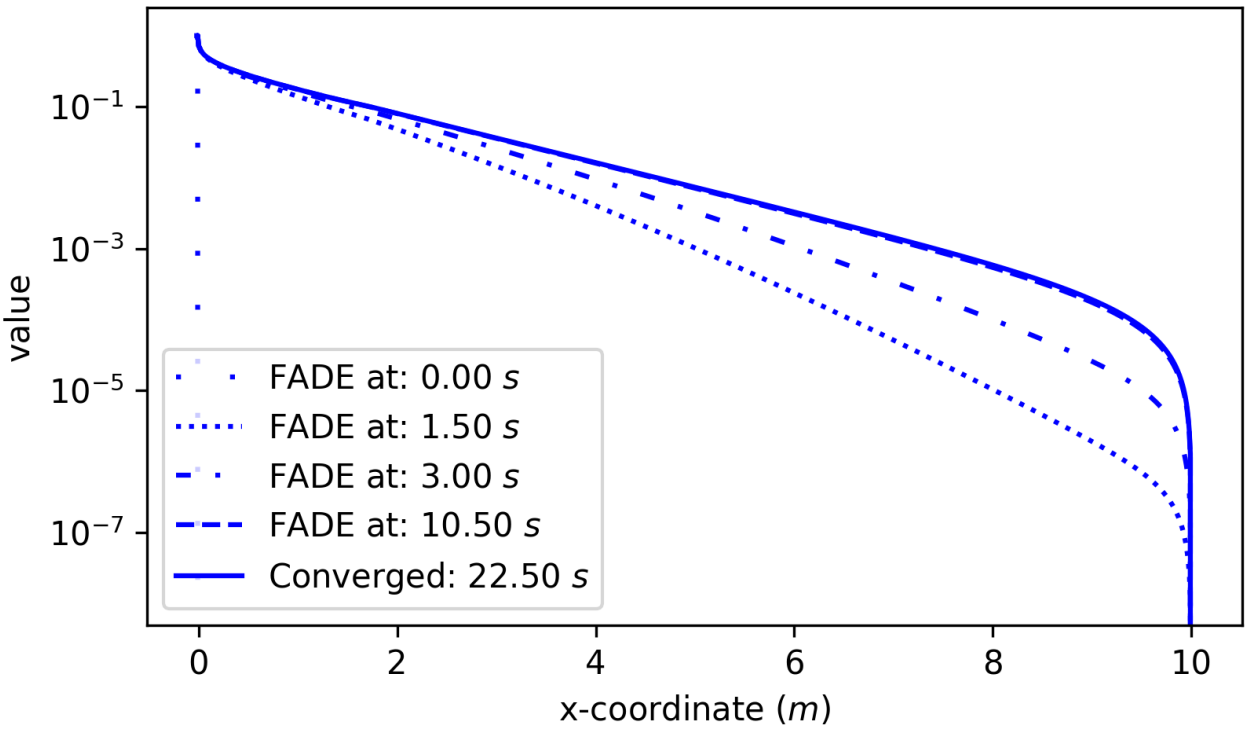

Figure 49: Solution of (dirichlet) boundary value problem with $\alpha = 1.5,\ \beta = 1$ to convergence at 22.5 s, with an RK4 scheme (log plot)

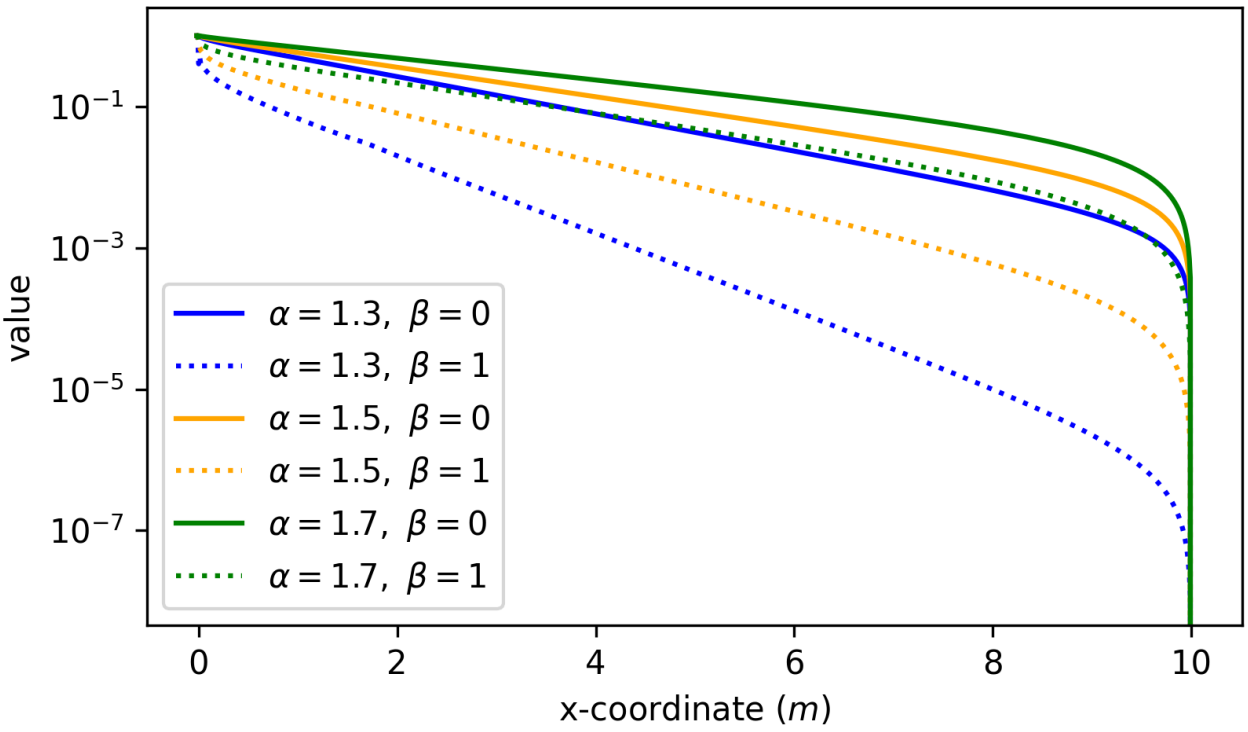

Figure 50: Comparison of converged solutions of (dirichlet) boundary value problems over a range of α and β, with an RK4 scheme (log plot)

7.4 Section Summary

In this section we have demonstrated the numerical solution of the FADE and compared it with the equivalent spectral shooting problem, as well as highlighting a few subtleties that need to be considered should one find that one has to make use of non-local models. Barring deviation due to the nature of spectral solutions, the solutions are highly comparable with only small error. One exception occurs for the case $\alpha < 1,\ \beta = 0$, where the numerical solution demonstrates a large deviation from the spectral solution. Curiously, although a similar (fractional) order operator appears for the fractional advection case, $\alpha > 1,\ \beta = 1$, the numerical solution matches the spectral solution very well. It is surmised that this is due to stabilisation of the error due to fractional diffusion: however, further investigation would be illuminating.

One final topic of interest in this section is the finding that the steady-state solutions of FADEs in the case of the 1-D boundary value problem are markedly different to that of the standard diffusive boundary value problem. As mentioned previously, analytical solution to fractional calculus problems is not trivial, and the author is not aware of any general approach to the solution of FADEs; this could do with some investigation.

8 Radial Transport in Simulations of the Scrape-Off Layer

We have the tools to be able to measure jump functions as well as solve FADEs, which occur should we have a jump function, $q(\Delta x)$, which belongs to the LαS distribution.

Our hypothesis is that the jump functions measured in SOL simulations will belong to the LαS distribution, and are not Gaussian. If this is the case, then this allows us to express the steady-state density in the SOL in a reduced form as a FADE.

In this section, we examine 2D simulations of the SOL, find radial jump functions, and then see if the observed jump functions and implied transport equation compares well to the SOL mean profile, and so determine whether our hypothesis may be justified.

8.1 The STORM2D SOL Equations

We use the STORM2D module of the BOUT++ software [185] to conduct our simulations - this is a branch of STORM, which solves 3D equations which are a drift-reduced, cold-ion, and electrostatic reduction of the Braginskii equations in the fluid limit. The equations solved in STORM2D are a 2D reduced version, similar to those used by the ESEL code to model electrostatic interchange turbulence in the SOL [199].

Previous work with this package to simulate the SOL found that despite the simplifications made in the 2D model, there is overall good agreement with the 3D model in terms of the fluctuation statistics and radial density profiles - however, there is a challenge in simultaneously matching both the density and temperature profiles [200].

Nonetheless, these transport equations are satisfactory for our purposes, which is to examine whether we may use jump functions to characterise non-local transport.

The 2D equations result from grouping all terms with a parallel dependence into effective loss terms. This results in the following systems of transport equations for density, n, vorticity, Ω, and temperature, T [200]:

$$\frac{\partial n}{\partial t} = \frac{1}{B}\{\phi, n\} + C(p) - nC(\phi) + D_n \nabla_\perp^2 n - n_{loss} + S_{n0} \tag{276}$$

$$\frac{\partial \Omega}{\partial t} = \frac{1}{B}\{\phi, \Omega\} + \frac{1}{n}C(p) + D_\Omega \nabla_\perp^2 \Omega - \Omega_{loss} \tag{277}$$

$$\frac{\partial T}{\partial t} = \frac{1}{B}\{\phi, T\} - \frac{2}{3}TC(\phi) + \frac{2}{3}\frac{T}{n}C(p) + \frac{5}{3}TC(T) + \frac{2}{3}\frac{1}{n}\kappa_\perp \nabla_\perp^2 T + \frac{2}{3}\frac{1}{n}S_{E0} - \frac{1}{n}TS - T_{loss} \tag{278}$$

and the vorticity related to the potential as:

$$\Omega = \nabla \cdot \left(\frac{\nabla_\perp \phi}{B^2}\right) \tag{279}$$

Where $C(g)$ denotes the curvature operator:

$$C(g) \equiv \nabla \times \frac{\mathbf{b}}{B} \cdot \nabla g \tag{280}$$

which may in simplified tokamak geometry at the midplane (which is indeed our case) be approximated as:

$$C(g) \approx -\frac{2}{R_0 B_0}\frac{\partial g}{\partial z} \tag{281}$$

Where $\{a, b\}$ denotes the Poisson bracket as in Eqn. 109. There are two source terms: S_n and S_E, corresponding to a density and energy source respectively. There are three sink/loss terms: n_{loss}, Ω_{loss}, and T_{loss}, corresponding to density, vorticity and temperature loss terms respectively.

In this case, the geometry is assumed to be a tokamak flux tube with (**B**-) parallel, radial and binormal directions - in the simplified STORM2D equations here in the midplane, the parallel

direction corresponds to the y-axis, the radial direction to the x-axis, and the binormal direction to the z-axis. The 2D equations are solved in the radial-binormal $(x-z)$ direction, with the parallel terms approximated (hence the grouping of the parallel terms discussed earlier) as loss terms.

For the set of simulations conducted, the parameters were selected as; $L_x = 140\ \rho_s$ with 1024 cells, and $L_z = 150\ \rho_s$ with 256 cells, and $L_y = L_\parallel = 5500\ \rho_s$. These particular settings were selected as they are similar to those used by Nicholas et al [200]. The binormal boundary conditions are periodic, and the radial conditions are Dirichlet conditions. There are three parallel loss terms; n_{loss}, Ω_{loss} and T_{loss}: we define a separatrix or LCFS, and for radii which are less than this the parallel losses are zero, and beyond which (i.e. in the SOL) the parallel loss terms apply.

The density and vorticity loss terms are determined by assuming a sheath dissipation closure [201] - density and temperature are assumed to have zero parallel gradient, and any currents flowing in the domain are closed entirely in the thin sheath, such that the sheath acts as a sink for the kinetic energy of fluctuations.

$$n_{loss} = \frac{n}{L_\parallel} V_{sh}(\phi, T) \tag{282}$$

$$\Omega_{loss} = \frac{1}{L_\parallel}(V_{sh}(\phi, T) - \sqrt{T}) \tag{283}$$

Where V_{sh} is the sheath velocity, given [200] as:

$$V_{sh}(\phi, T) = V_{prefactor}\sqrt{T}e^{-\frac{\phi}{T}} \tag{284}$$

Where $V_{prefactor}$ is the sheath prefactor, calculated as:

$$V_{prefactor} \equiv \sqrt{\frac{\mu}{2\pi}\frac{\mu}{\mu+1}} \tag{285}$$

Where $\mu \equiv \frac{m_i}{m_e}$. For the thermal loss term, we write:

$$T_{loss} = \frac{2}{3}\frac{1}{nL_{\parallel}}q_{\parallel} \tag{286}$$

Where $q_{\parallel}$ is the harmonic average of the sheath-limited and conduction-limited parallel currents [202], given respectively as:

$$q_{\parallel} = (\gamma - \frac{3}{2})nTV_{sh}(\phi, T) \tag{287}$$

$$q_{\parallel} = \frac{2}{7}\frac{1}{L}\kappa_{\parallel}T^{\frac{7}{2}} \tag{288}$$

8.1.1 Normalisation and Simulation Parameters

The Bohm normalisation is used such that:

$$\frac{x}{\rho_s} \rightarrow x, \quad \Omega_i t \rightarrow t \tag{289}$$

spatial measures are normalised to the hybrid gyroradius $\rho_s = c_s/\Omega_i$, and measures of time to the ion gyrofrequency, $\Omega_i = eB_0/m_i$. The selected normalisations result in the velocity normalisation as$c_s = (T_0/m_i)^{\frac{1}{2}}$. Temperatures are normalised to some normalising temperature, T_0, densities normalised to n_0, transport coefficients normalised to the Bohm diffusion rate, $\rho_i^2\Omega_i$, and the potential is normalised to the thermal energy:

$$\phi \equiv \frac{e\varphi}{T_0} \tag{290}$$

The dimensionless forms of the currents and sources are:

Table 4: Table of normalising parameters for SOL simulation reference case

Parameter	m_i (amu)	n_0 (m^{-3})	T_0 (eV)	B_0 (T)	R_0 (m)	$L_\parallel$ (ρ_i)
Value (Reference)	2	0.8×10^{19}	40	0.25	1.5	5500

Table 5: Table of transport parameters

Parameter	D_n	D_Ω	$\kappa_\perp$	$\kappa_\parallel$
Value (Reference)	3.6×10^{-3}	7.1×10^{-2}	1.0×10^{-2}	1.1×10^{5}

$$J = \frac{j}{en_0 c_s} \tag{291}$$

$$S_{n0} = \frac{S_{n0}}{n_0 \Omega_i} \tag{292}$$

$$S_{E0} = \frac{S_{E0}}{n_0 T_0 \Omega_i} \tag{293}$$

The normalising parameters used for the reference case are displayed in table 4. The transport parameters are calculated as in [199], and the values are given for the reference case in table 5.

8.2 Simulated SOL Properties

The simulations are set up with an initial density and energy source located within the 'separatrix' region in order to imitate a density and energy source from the core plasma. The density and energy sources occur in the density and temperature transport equations (Eqns. 276 and 278) as S_n and S_E, and the sources have a form:

$$S_n = S_{n0} norm(x - x_{Sn}, w_{Sn}^2) \tag{294}$$

$$S_E = S_{E0} norm(x - x_{SE}, w_{SE}^2) \tag{295}$$

Where $norm(\mu, \sigma^2)$ denotes the normal or Gaussian distribution with mean μ and standard deviation σ. We have x_{Sn} set such that the density source peaks 10% into the domain, and x_{SE} at 9% of the domain. In both cases, the standard deviations w are 0.25, and for the

reference cases we set $S_{n0} = 0.03$ and $S_{E0} = 0.1$, again, these are set similarly to Nicholas et al [200]. We vary the magnitude of the density and energy sources around these parameter values such that we have a set of simulations with $S_{n0} \in [0.024, 0.042], S_{E0} = 0.1$ and a set with $S_{E0} \in [0.08, 0.16], S_{n0} = 0.03$.

Once the simulations are initialised with these sources, the gradients created by the sources cause instabilities to form, which eventually produces turbulence. We allow the simulation to run for a simulated time equivalent to several milliseconds to reach a steady-state turbulence: the statistical steady state acquired for this purpose was used for analysis.

Some properties of interest include the average profiles, as well as the fluctuation statistics. It should be noted that these reproduce the properties identified and discussed in Nicholas et al. 2021 [200], so a detailed discussion of these data is not provided here.

8.3 Measuring Radial Jump Functions in the SOL

We have observed that the Flux-Gradient relation appears to be difficult to define - and certainly non-linear - which is consistent with previous results regarding the SOL as discussed in section 2.4.2. As we have seen in section 6, the stochastic flux equation and associated analysis demonstrates that a linear flux-gradient relation occurs if and only if when we have a Gaussian jump function[31].

Measuring the jump function is done with Lagrangian tracers, as in the HWE case. However, differences between the 2D SOL simulations and the HWE simulations mean that one must consider carefully how one is to determine the jump function, and what our initial seeding strategy should be. Key considerations are that:

- The 2D SOL is periodic only in the binormal direction and thus Lagrangian tracers cannot be assumed to 'wrap' around the radial direction when crossing a radial boundary
- The 2D SOL is not homogeneous

[31] see Eqn. 198 to Eqn. 203

Due to the first point, we cannot seed Lagrangian tracers uniformly over the domain and expect sensible results - as particles which are lost across the radial boundary before the observation interval τ occurs would result in a bias in the jump function. Due to the second point we cannot discount the possibility that the jump function may have to be considered as radially inhomogeneous. The only way to determine whether the jump function is radially homogeneous is to sample the jump function at various radii. Consequently, the tracer seeding strategy is as follows:

- define a number of radial sectors exhaustively covering the domain in the radial direction
- the observation interval should be selected such that tracers in sector 2 and 9 do not interfere with the radial boundaries.
- the widths of the radial extents should be constrained such that the observation interval is larger than the correlation time

In this particular case, we were able to define a width such that we were able to have 10 radial sectors, as demonstrated in Fig. 51, and were able to select an observation interval according to the criteria of, $\tau = 5 \times 10^{-5}$ s or approximately 600 periods of the ion gyrofrequency. Finally, in order to define good-quality jump functions with as minimal noise as possible, as many tracers must sample the space in as many configurations as possible. As such, the same simulations were restarted 10 times at different points in the steady-state turbulence regions, with jump functions gathered for the same radial positions. The datasets for the same radial sectors were then combined to provide a more representative picture. The data for each run then consisted of particle data from 10 different sectors, each with 10 restarts with 10^5 particles per sector[32].

8.3.1 SOL jump functions

We give example jump functions across the radius for the density source variation runs. These are shown in Fig. 52. The standard deviation is on the order of 20% of the mean

[32]...this was quite storage intensive, even for 2D - the increase in storage requirements to obtain the required data from simulation from a 3D system could be restrictive. This highlights a need for a first-principles or other heuristic approach to obtaining the jump function

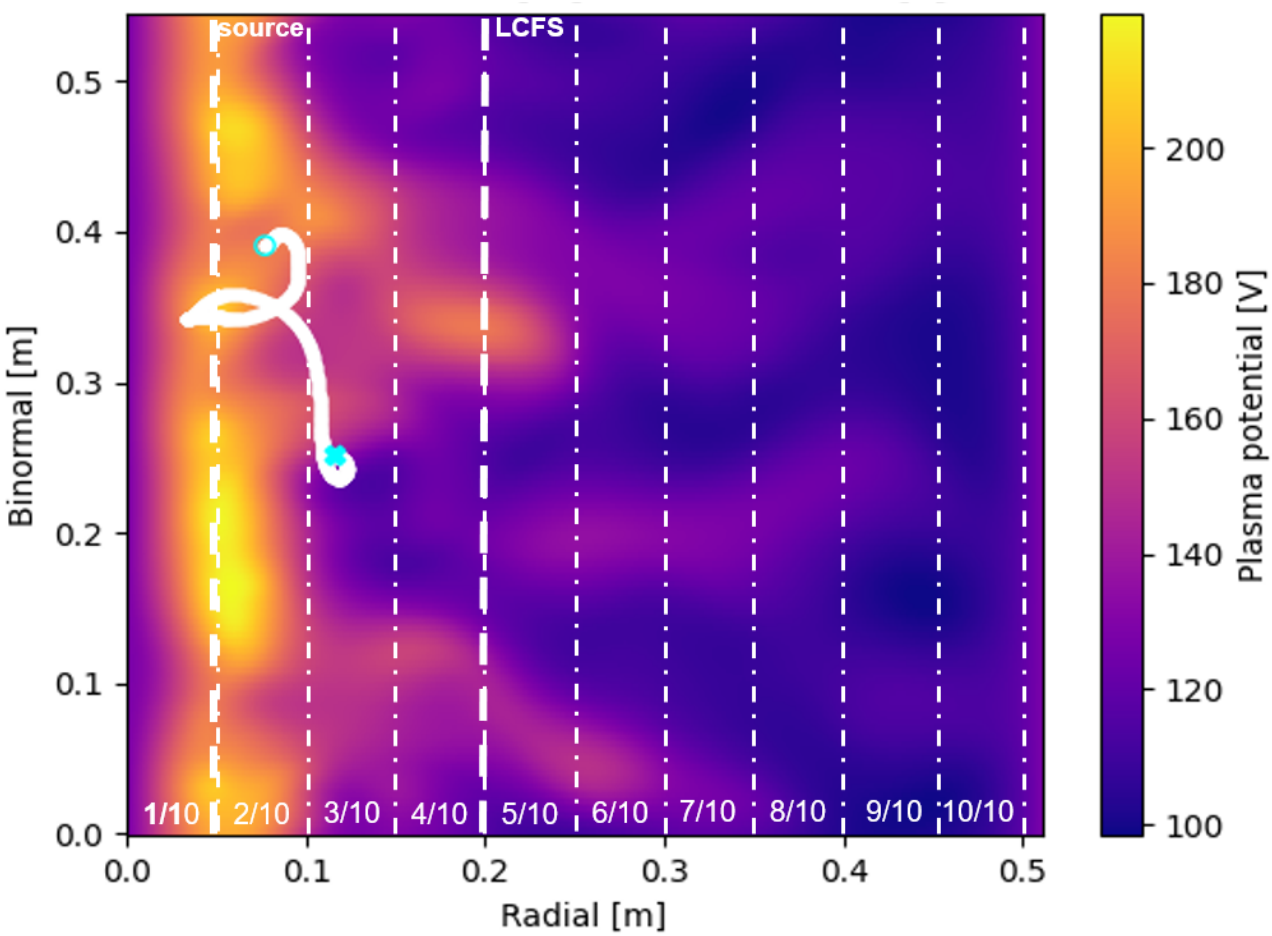

Figure 51: A particle undergoes a random walk on an example output (last frame on path shown). The radial sectors are delineated with white lines. The source and the LCFS are indicated.

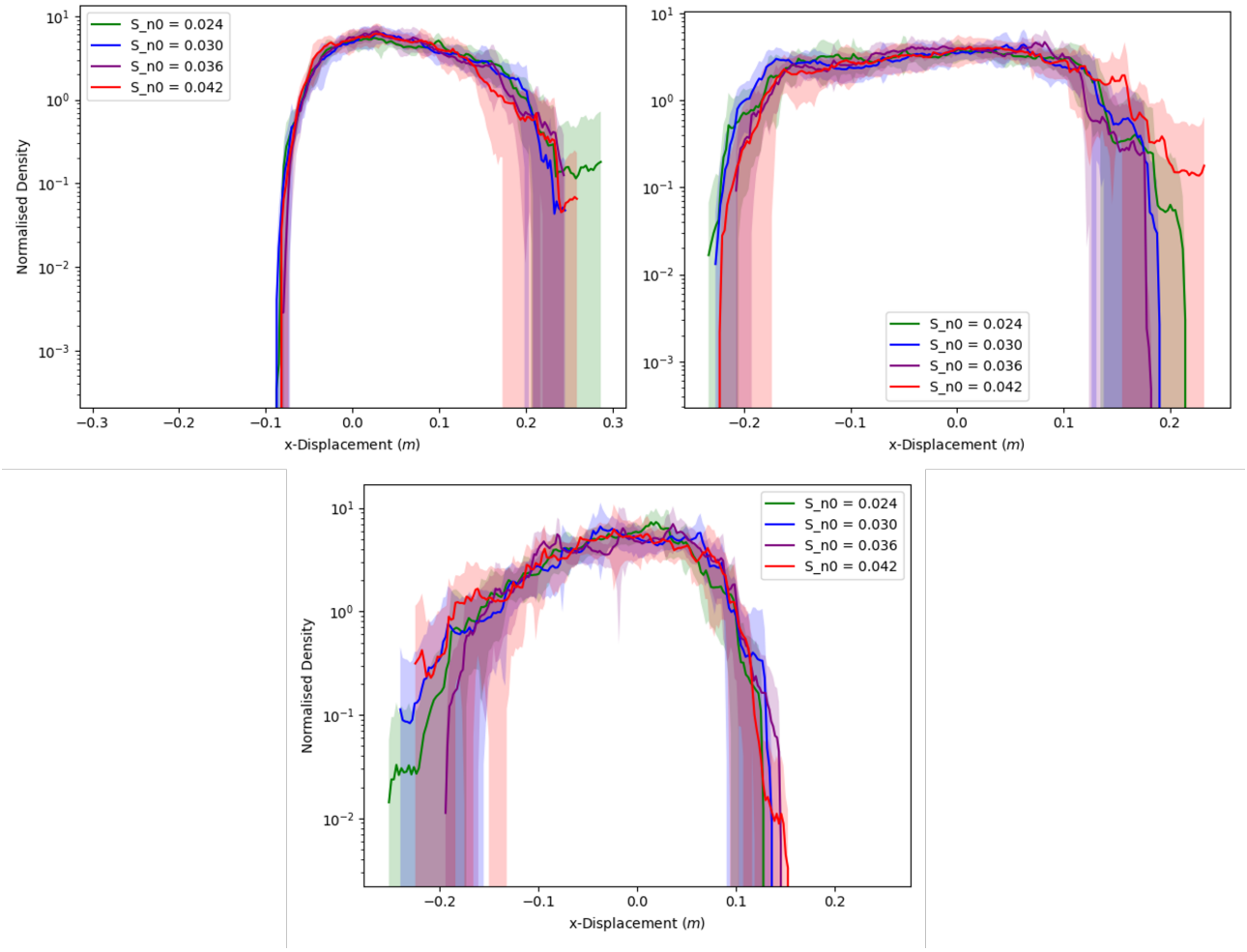

Figure 52: Ergodic jump functions for sectors 2, 5 *and* 7 *respectively (clockwise). The shaded areas denote the uncertainty in the data.*

despite measures to improve the data quality. The jump functions do appear to be largely consistent across the change in the source magnitude. There appears to be a persistent change in the jump function properties across the radius, which strongly indicates that the jump function is radially inhomogenous. The jump functions for the first and last sectors were discarded, as the data was influenced by the boundaries in an nonphysical manner: Additionally, the first sector was radially within the energy and density sources, and so not considered reflective of relevant physical conditions. We quantify this variation in terms of the mean, skewness and kurtosis of the jump functions with radius, which may be seen in Fig. 53.

We notice an almost linear decrease in the skewness with radius from positive to negative values, and a reduction of the mean to negative values. Recall that the Gaussian distribution

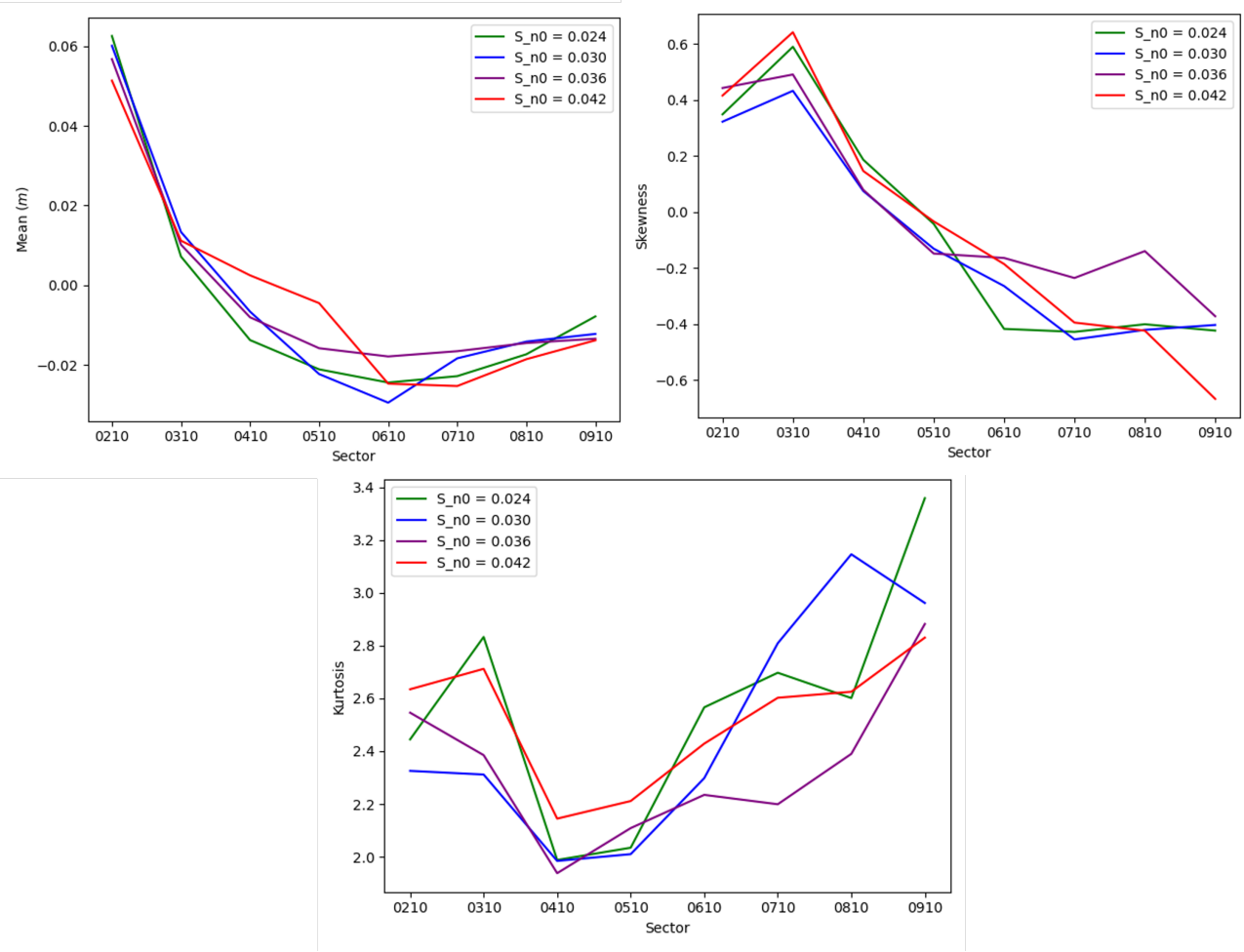

Figure 53: Variation in jump function statistics with sector for the varying density source runs. Note that sector refers to the splitting of the radial direction into 10 distinct regions

possesses a kurtosis equal to 3, so the values identified suggest that the distributions are non-Gaussian. Very similar behaviour was observed for the scan in the energy source.

The Lagrangian tracer particle data suggests two things: First, the jump functions do not appear to be Gaussian, hence once cannot justify any kind of advection-diffusion equation as a reduction of the equations; Second, as suspected, the jump function does appear to vary with radius, which may pose some difficulty as our analysis is based on a spatially uniform jump function.

To mitigate this, we must make some assumptions which leverage the physics of the system, and hope that these are sufficient. From section 8.2 it may be seen that the average density is highest at the source, and decreases rapidly. If the jump function is to be assumed to

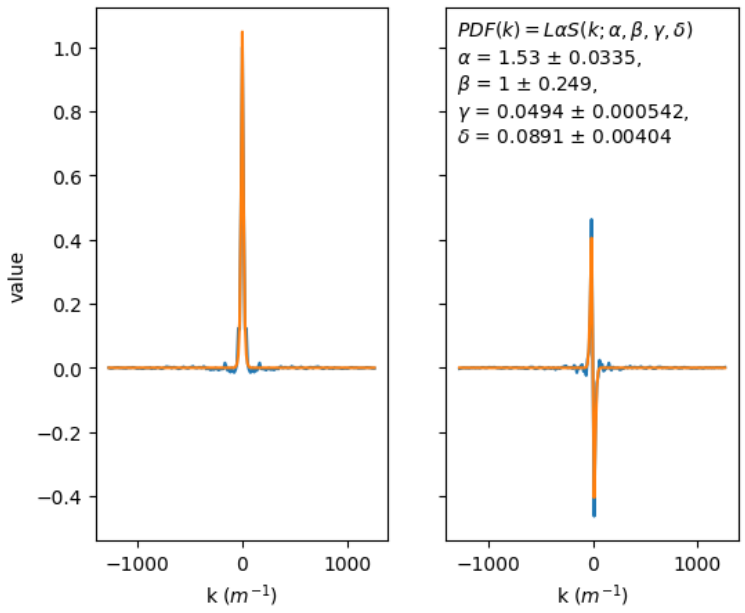

Figure 54: Fit in Fourier space of the LαS distribution to the sector 2 data for the reference case. Error in fit parameters are estimated from the covariance matrix of the fit.

be mimicking the behaviour of particles, then when considering jump functions across the radius, the contribution of any particular jump function should be weighted by the local density: Consequently, we assume that the ensemble jump function would be primarily determined by the jump function(s) closer to the density peak - note that these display a similar character. This difficulty does reveal a flaw with our Lagrangian tracers; ideally, there should be a way of weighting the particles or controlling their propagation that better reflects the actual system density, without requiring a full Particle-In-Cell simulation.

With this in mind, we then consider the jump functions for sector 2 and whether it is well-described by a LαS distribution given in Eqn. 209. As with the case in section 5, we perform the fit in Fourier space as the LαS is well-defined there. We give the example of the reference case to demonstrate the fitting, which may be seen in Figs. 54 and 55. The data demonstrates that a LαS distribution with $\alpha \approx 1.5$ and $\beta \approx 1$ is a good fit to the distribution, which is particularly well demonstrated in Fourier space. Note that, for example, sector 3 demonstrates a higher skewness and so suggests a different fit. The jump functions from further out - e.g. sectors 7 and 8 - are very flat and do not correspond well to a stable distribution. A non-integer α and non-zero β indicate that a FADE may be an appropriate description of the dynamics in this case.

We present the fits for the rest of the jump functions for the same sector across the S_{n0} and

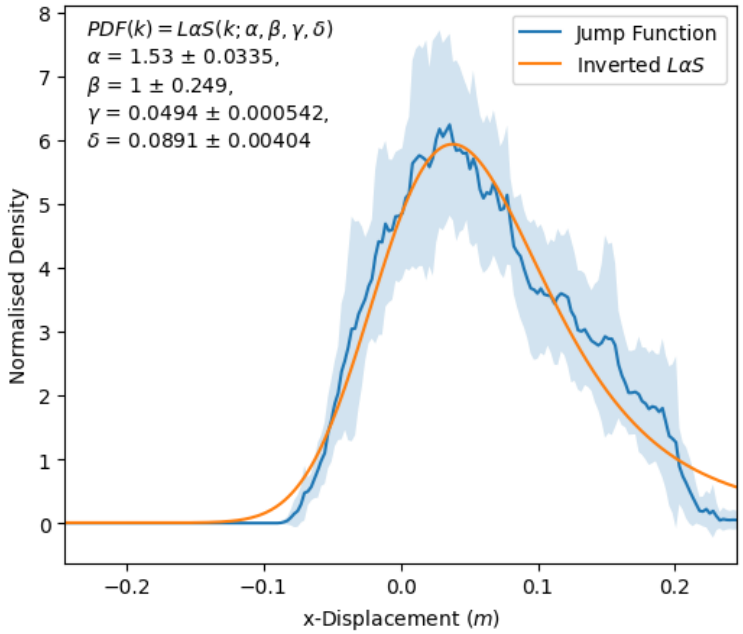

Figure 55: Inverse transform of the LαS distribution fit in comparison to the sector 2 data for the reference case

S_{e0} runs in table 6. Overall trends include ubiquitously non-integer α in the range $[1.4, 1.7]$ and error of order $\approx 2\%$, a positive skewness with error of order $\approx 20\%$, a consistent γ or 'frequency width' with error of order $\approx 1\%$, and a non-zero displacement term δ with error of order $\approx 5\%$. The persistent non-zero δ suggests a persistent advective contribution to the dynamics.

Table 6: Table of LαS parameters for sector 2 jump functions for various runs. The reference case is shown in the first row

Run	α	β	γ	δ
$S_{n0} = 0.03$ $S_{e0} = 0.10$	1.53 ± 0.0335	1 ± 0.249	0.0494 ± 0.000542	0.0891 ± 0.00404
$S_{e0} = 0.10$ and...				
$S_{n0} = 0.024$	1.6 ± 0.0487	1 ± 0.388	0.0546 ± 0.000813	0.0867 ± 0.00499
$S_{n0} = 0.036$	1.49 ± 0.0301	1 ± 0.0219	0.0473 ± 0.000497	0.0882 ± 0.00402
$S_{n0} = 0.042$	1.69 ± 0.0402	1 ± 0.0585	0.0481 ± 0.000535	0.0641 ± 0.00273
$S_{n0} = 0.03$ and...				
$S_{e0} = 0.08$	1.42 ± 0.0335	1 ± 0.238	0.0495 ± 0.000638	0.101 ± 0.00626
$S_{e0} = 0.12$	1.5 ± 0.0335	1 ± 0.159	0.0577 ± 0.000903	0.109 ± 0.00728
$S_{e0} = 0.14$	1.53 ± 0.0511	1 ± 0.0351	0.0588 ± 0.000952	0.108 ± 0.00805
$S_{e0} = 0.16$	1.54 ± 0.0503	1 ± 0.0586	0.0637 ± 0.00103	0.113 ± 0.00739

8.4 SOL modelling with FADEs

The results of the preceding section indicate that we may attempt to model the density transport in the SOL using a FADE similar to those developed in section 6 and solved in section 7. Specifically, we solve a 1D equation of the form:

$$\tau \frac{\partial n}{\partial t} = \gamma^{\alpha} D^{\alpha}_{|x|} n(x,t) - \beta \tan \frac{\pi \alpha}{2} \gamma^{\alpha} \frac{\partial}{\partial x} \left(D^{\alpha-1}_{|x|} n(x,t) \right) - \delta \frac{\partial n(x,t)}{\partial x} - n_{loss} \tag{296}$$

Key differences between the earlier FADE simulations and the SOL FADE simulations primarily relate to the boundary conditions. In the SOL FADE case, we allow floating non-local boundary conditions in the ghost cells, which are updated based on the average of the nearest cells in the domain. This was done to ensure the closest replication of the STORM2D boundary conditions. An additional difference is the addition of a density source at the same location as in the STORM2D simulations - this is located 10% of the way into the domain, at approximately $14\rho_s$. The density and energy sources in the STORM2D simulations serve the role of a source from the 'core' - so in the FADE simulations, we adjust the value of the density source to match the peak density in the SOL simulations. As we have discussed, nonlocal boundary conditions are not straightforward; while it is feasible that the source region could have been modelled as some kind of inner Robin or nonlocal Robin boundary condition, the most straightforward approach is to consider the source as the 'inner' boundary condition and match it in the FADE simulations[33].

[33]This will be of far greater importance to consider when modelling a real system

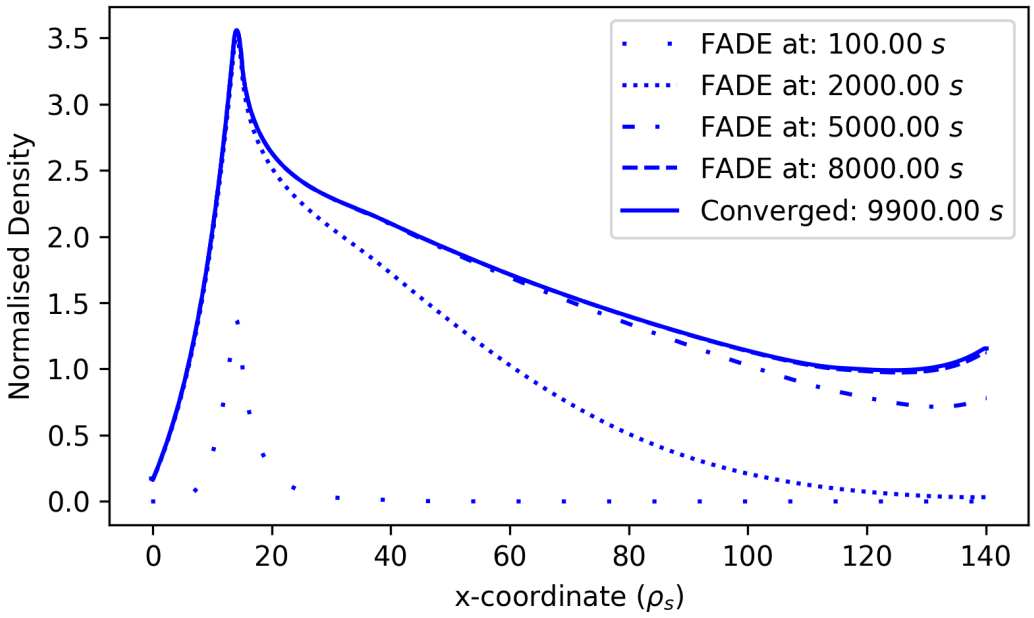

Figure 56: Convergence plot of numerical FADE to solution at ~ 9900 *seconds*

Where we apply the loss term only in the open field line region - that is in the SOL for radial values greater than the LCFS. Normalising the parameters is mostly straightforward using the convention used for STORM2D, if we recall that β and α are already dimensionless. The observation interval is normalised as $\Omega_i \tau \to \tau$, the displacement parameter as $\delta/\rho_s \to \delta$, and the 'frequency width' as $\gamma/\rho_s \to \gamma$. For the reference case then, we find that the normalised $\tau = 603$, the normalised $\gamma = 13.6$, and the normalised $\delta = 24.7$. As indicated in table 6, we use $\alpha = 1.53$ and $\beta = 1$.

The loss term is implemented in the solver as a proportional sink, with coefficients found using the estimated parameters. $L_\parallel$ is 5500, the magnitude of Eqn. 284 is estimated as being on the order of between $1 - 0.1$ in normalised units. Therefore, we estimate the loss coefficient as being on the order of $10^{-4} \sim 10^{-6}$ overall.

The convergence of the FADE for the reference case can be seen in Fig. 56. The comparison of the converged density profile to the average density profile simulated by STORM2D is shown in Fig. 57. The converged FADE solution is a good match to the average profile from the STORM2D equations. Recall that the parameters used for the FADE are taken entirely from the sector 2 jump function which we measured in the STORM2D equation.

For the rest of the cases in table 6, there was a similar match too. We include a few

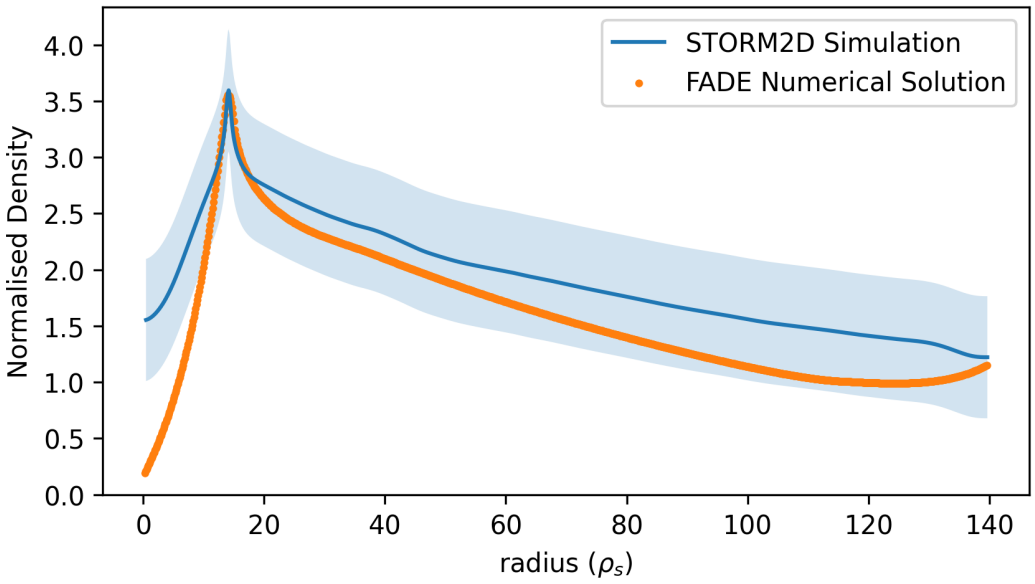

Figure 57: Comparison of mean density profile in reference case to converged FADE. The shaded blue region denotes the standard deviation in the density profile

FADE/simulation comparisons from a number of scans in order to demonstrate this - these may be seen in Figs. 58 and 59. There is typically a good match between the FADE and the simulation density profiles, with the FADE typically lying in the uncertainty region for the STORM2D profile - i.e. within 20% of the mean value.

One possible cause of these matches are that the FADE is not sensitive to variation in parameters. We solved FADEs for a number of parameters around those for the reference case to demonstrate the large variation possible. We have not shown all scans in parameters here, nor do we claim to have comprehensively scanned the whole parameter space.

We show two scans - one in α, one in β - holding all other parameters the same as in the reference case, though altering the density source value to match the peak density. These may be seen in figures 60 and 61. These scans demonstrate the significance of the characteristic exponent (α) and the 'skewness' (β) parameter in determining the properties of the solution. As can be seen the alteration of the characteristic exponent - the 'nonlocal' parameter - has an extreme effect on the solution. As noted in the section 7.2, boundary conditions must be treated very carefully in nonlocal simulations - and this appears to be demonstrated in the β scan for the right-hand boundary. Between $\beta = 0.75$ and $\beta = 1$, there is a strong change in the gradient of the profile after $\rho_s = 120$. This could suggest that the β in the earlier cases is not totally correct, and one may note that β does indeed have the largest uncertainty in

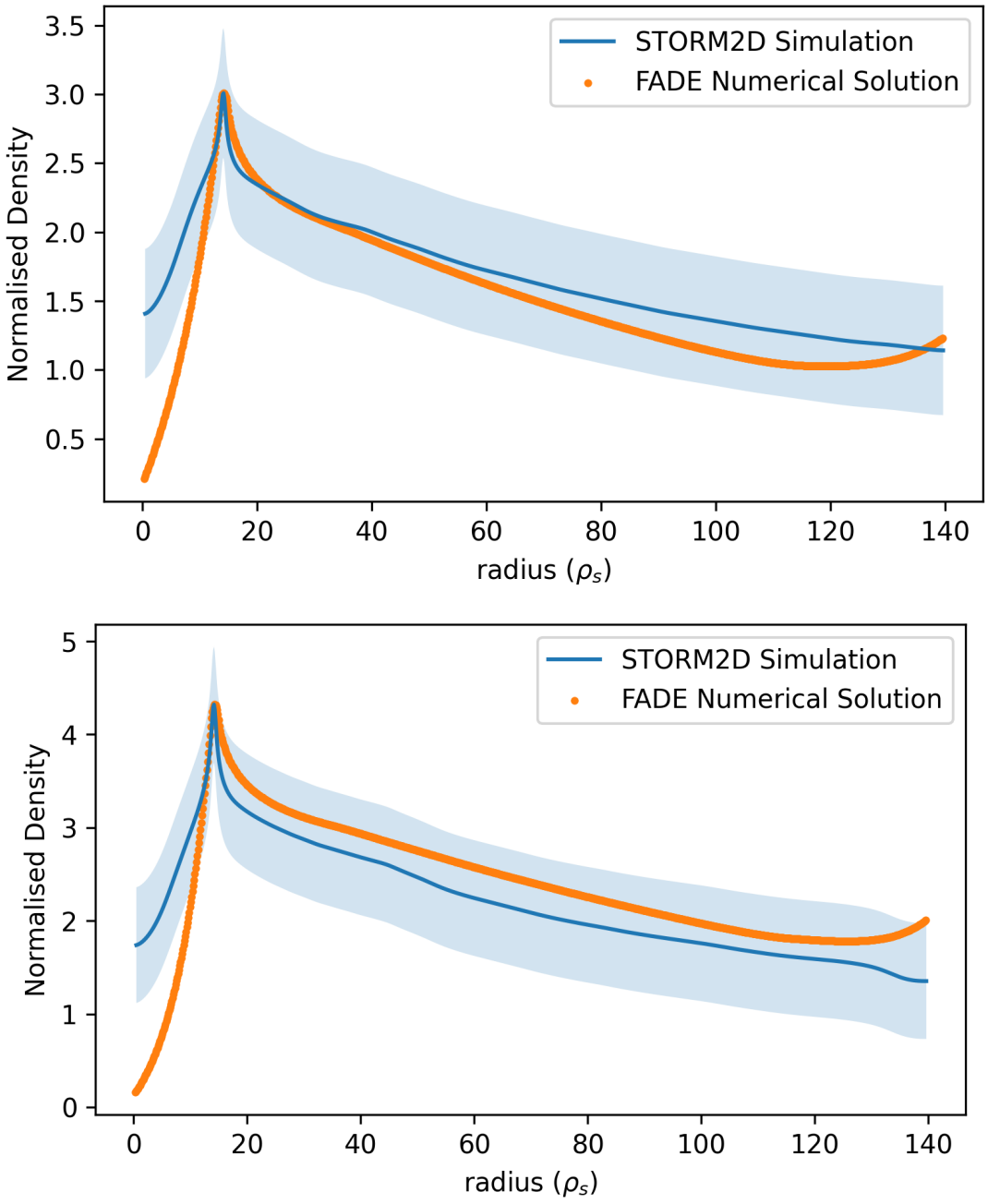

Figure 58: Comparisons of mean density profile to converged FADE with $S_{E0} = 0.10$ and top: $S_{n0} = 0.024$, bottom: $S_{n0} = 0.036$

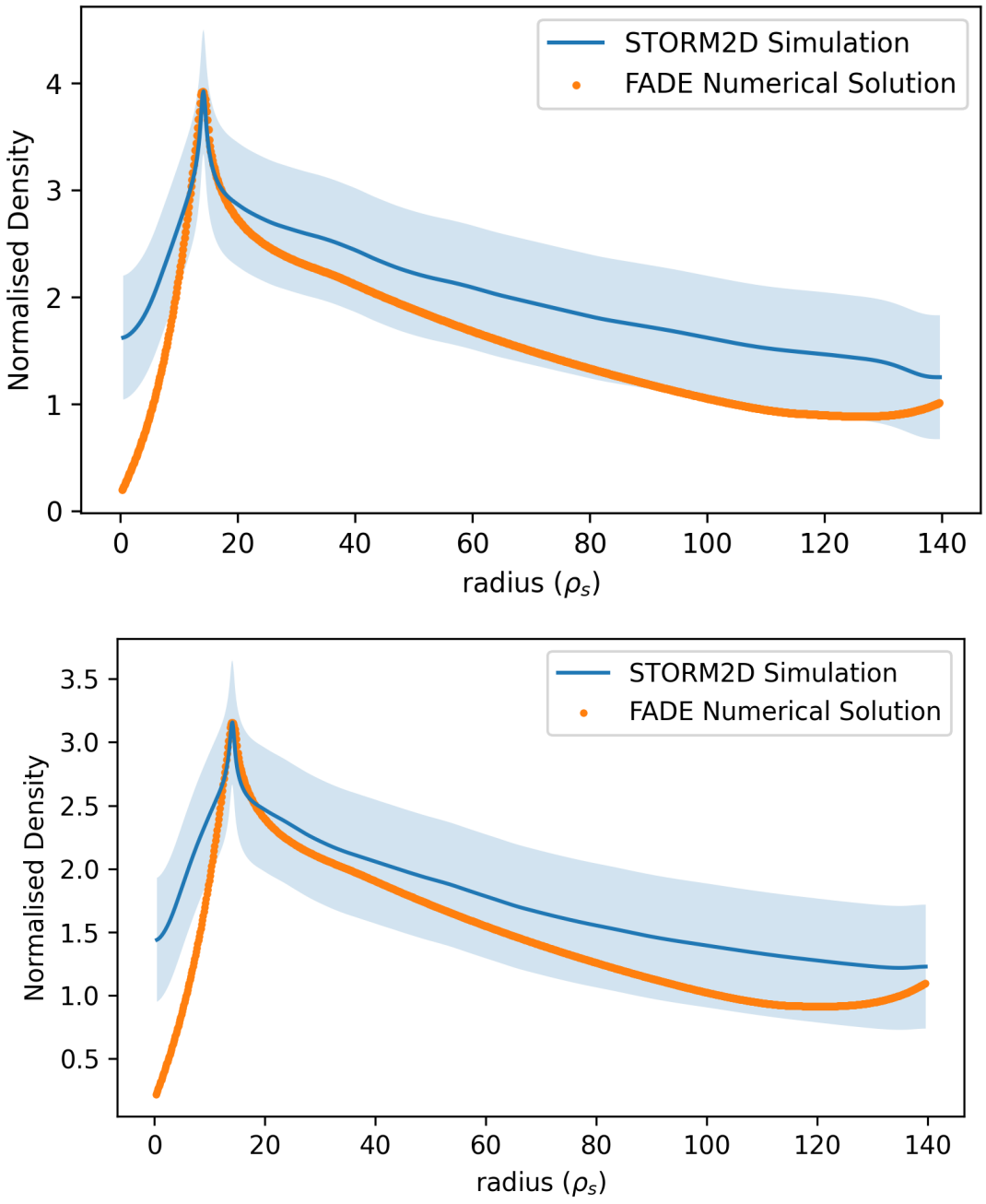

Figure 59: Comparisons of mean density profile to converged FADE with $S_{n0} = 0.03$ and top: $S_{E0} = 0.08$, bottom: $S_{E0} = 0.16$

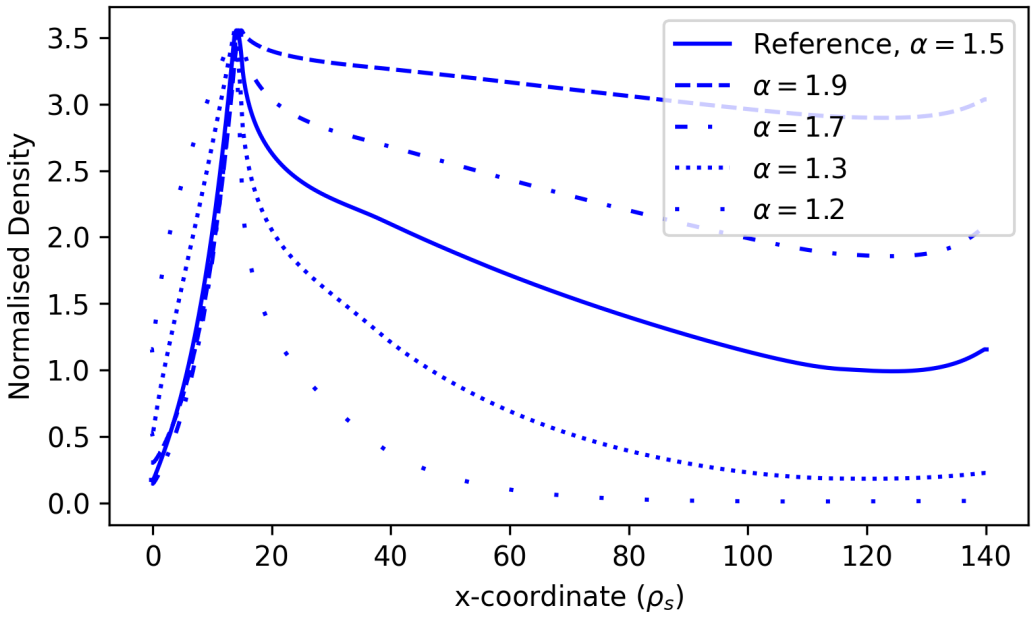

Figure 60: Scan of FADE in α around the parameters for the reference case

the fits. Note from the convergence plot (Fig. 56) that this develops later in the simulation. From the work on boundary conditions in section 7, we know that the fractional advection term can have unusual interactions with the boundaries, depending whether it is the left or right boundary. As such, there is work to be done here ensuring the boundaries are appropriate, as this would eliminate one possible source of uncertainty.

Given the match between the FADEs and the STORM2D simulations, this suggests that the approximations we made were reasonable, and it seems that we have evidence that supports the reduction of conventional transport equations to non-local FADEs in steady-state, and that a jump function can be defined and measured in order to identify said FADE parameters, at least in the regime studied here.

The scans result in slightly different steady-states - and correspondingly slightly different FADEs.

It is important to reiterate that the methods here can identify advective-diffusive, local, transport *if present*: this would occur for the case $\alpha \to 2$.

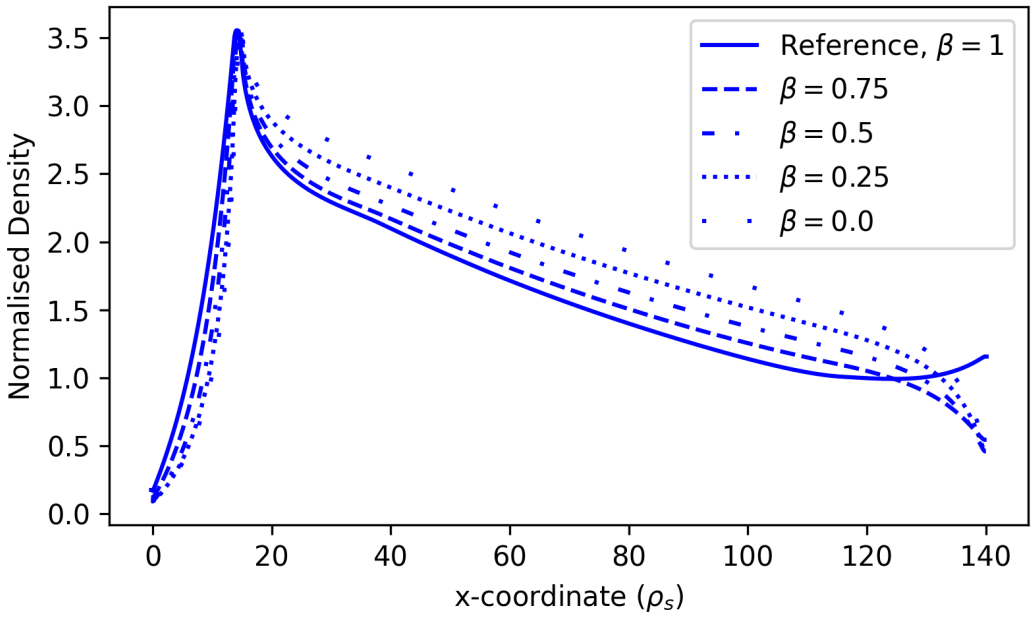

Figure 61: Scan of FADE in β around the parameters for the reference case

8.5 Section Summary

The STORM2D equations, which model aspects of interchange turbulence in the SOL, are simulated in a scan of density and temperature sources. The jump functions are then measured in these simulations. Unlike in sections 4 and 5, we have inner and outer radial boundary conditions which are non-periodic, and so particles cannot have physical behaviour past these boundaries. Additionally, due to apparent variation in behaviour with radius in the steady-state STORM2D case, we suspected that the jump function varied with radius.

Consequently, we measured the jump function by initialising particles in radial sectors and examining their propagation after the observation interval. To improve the quality of the data, we averaged over a number of observation intervals, with particles re-seeded in the sector at the start of each observation to maintain the spatial specificity of the measured jump function in that sector.

It is found that the jump functions for the STORM2D equations in the parameter regimes examined are universally non-Gaussian, and appeared to vary radially. An assumption made to simplify modelling was that the jump function in the highest density region - universally the second sector - was most representative of the jump function. A LαS jump function was well-fit to these in Fourier space, with parameters such that they justified modelling with

FADEs.

The numerical solution of FADEs with parameters taken from these jump functions demonstrated good matches with the mean profiles generated with STORM2D equations. This supports the conjecture that FADEs are viable as reduced models of non-local transport in practice, as suggested by the analysis in section 6.4.

9 Summary and Conclusion

We have outlined the phenomenology of radial scrape-off layer (SOL) transport in tokamak devices. There are a number of experiments which highlight the inadequacy of advective-diffusive reduced models of transport in the edge and SOL, and also point to the existence of nonlocal transport - in particular, there are two aspects of key importance:

- The measurement of the flux-gradient relationship in the SOL does not produce a linear relationship, which suggests that advection-diffusion models are not appropriate.
- There are long-lived coherent structures present - filaments - which propagate across the SOL, the formation of which is likely a result of turbulent processes occurring at the edge rather than local SOL properties[34].

As statistical models of transport by filaments have met with success in describing transport, and these are intrinsically a non-local model, we examined the literature with relation to non-local transport. There are various sources across the literature in neutral fluids which address coherent structures and their relation to non-locality, but there does not appear to be a unified body of work in this regard. However, the sources we did find were quite promising, as they appeared to relate to analogous situations - the generation and propagation of coherent structures. Notably, there were attempts to define some non-local eddy diffusivity which take this phenomena into account.

The most promising avenue of approach to dealing with this problem appeared to lie with the random walk approaches to transport. The key concept of the random walk models are

[34]Essentially more complicated analogues of the 'flyers' observed in Conway's game of life

the assignment of a probability distribution to the length and direction of a step a random walker makes: this is referred to as a jump function. We identified the limitations of present random walk approaches, and developed a new one - an 'observational' random walk (ORW) - which we believe synthesises the best of these approaches by introducing a characteristic observation interval independent of any specific particle's behaviour; the jump function is then additionally characterised in terms of this observation interval. We demonstrate how the jump function may be constructed for a single random walker, and the construction of the general case for an ensemble[35]. The form of the (converged, long time) jump function is then dependent on distributional limit theorems, such as the central limit theorem and general central limit theorem.

The outcome of applying random walk models is that Fick's diffusion equation, or the advection-diffusion equation, may be shown to be a consequence of a Gaussian jump function. Given that we apparently have a physical scenario in which it is not possible to characterise transport with an advection-diffusion relation, it is then reasonable to question whether non-Gaussian jump functions occur in relevant scenarios, their proximate causes, and the consequences of such a phenomenon.

The working hypothesis at this point was that coherent structures cause non-local transport, and this may be understood through the measurement and examination of jump functions.

Developed in this work is a method of measuring jump functions by observing the dispersion of Lagrangian tracer particles over an observation interval. This worked in a simple test case, so we applied it to simulations of the classical and modified (Charney-)Hasegawa-Wakatani equations. These equations, which simply model drift-wave turbulence are an ideal test case due to the formation of distinct coherent structures named zonal flows in certain cases; consequently, we expected to see a distinct difference between measured jump functions in cases with zonal flows, and without zonal flows.

The measured jump functions demonstrated a clear difference; Gaussian jump functions were observed in the cases without zonal flows, but when zonal flows were present the measured jump functions were observed to be non-Gaussian. In fact, they were found to be well-described by symmetric α-stable distributions[36].

[35] As well as how the classical random walks may be found from our 'observational' random walk

[36] The subset of Levy-α Stable distributions with $\beta = 0$

Given that non-Gaussian jump functions were observed to occur in steady state cases, there then appeared to be a justification to develop the ORW further. Later in this work the stochastic flux equation (SFE) was constructed. The SFE defines the instantaneous flux across a surface in terms of the jump function and the density field. Identifying the corresponding Fourier pair, allowed a proof of Fick's first law (and by extension the second law) directly for the case that the jump function is Gaussian. Importantly, we found that the SFE implied more general forms of Fick's law - the general central limit theorem suggests that jump functions should converge to the family of Levy α-stable (LαS) distributions. When we considered the combination of the SFE with the LαS distributions, we were able to demonstrate that the advection-diffusion equation is only a special case: more generally we can justify the existence of a transport equation with transport terms of non-integer or fractional derivative order. The terms identified we call fractional diffusion and fractional advection - these names were proposed as the fractional diffusion term originates from the even component of the jump function, and the fractional advection term originates from the odd component[37].

We termed the resultant equations fractional- advection, diffusion equations (FADEs) and demonstrated how they may be solved numerically using explicit methods. We implemented both RK4 and Forward Euler approaches, and showed that both compare favourably to the analytical solution for a particular case for $\alpha \in (1, 2]$. We considered the nature of non-local boundary conditions, and consequently emphasise the importance of understanding very carefully the (non-)locality present in our physical system as this fundamentally impacts modelling in a significant and non-trivial manner - that being said, we did propose some basic boundary conditions which may be considered non-local extensions of the Dirichlet and Neumann conditions, and we outlined the reason for their application.

Given the success in solving FADEs, the work was then at a stage where we could consider the SOL using such tools. The hypothesis at this stage was that the SOL density profile may be modelled effectively using a FADE derived from the jump function(s) measured in a representative case.

Using STORM2D, a BOUT++ module which solves a cold-ion reduced Braginskii equation which models interchange turbulence, we produced simulations which model aspects of the SOL - especially those relating to production and transport of coherent structures radially. Unlike in the HWE cases the system is not periodic in the radial direction and we had

[37]...and so may be regarded as non-local analogues to diffusion and advection

reasonable grounds to believe it may be neither homogeneous nor isotropic (in terms of a hypothetical measured jump function) - consequently, a more careful Lagrangian tracer seeding strategy was developed which allowed us to measure jump functions with some degree of spatial sensitivity and avoiding boundaries. Jump functions were universally non-Gaussian and appeared to be inhomogenous and anisotopic across the range of simulations examined. A simplifying assumption was that the jump function measured in the highest-density region was the jump function that dominated the behaviour overall.

Numerical solution of FADEs with the parameters taken directly from the jump functions generated density profiles which corresponded well with the average density profiles from the simulations. This supports the hypothesis that a FADE may indeed be used to model the SOL density profile, and furthermore suggests an equivalence between the reduced (Braginskii) equations in steady state and FADEs more generally.

We may then conclude that this thesis has been successful in advancing the hypothesis that: coherent structures are a cause of non-local transport; which may in turn be quantified by the measurement of jump functions; which may be used to generate (reduced) non-local models with which to model aspects radial SOL transport.

9.1 Future Work and Remaining Questions

In order to fully exploit the work done in this thesis for application to Tokamak modelling, the immediate work that must be done to compellingly complete the case for FADE reduced modelling is as follows:

- Experimental measurement of jump functions should be attempted through some means [38] and the resultant FADEs compared with experimental profiles. This work in itself would immediately have a significant impact on characterising and predicting SOL behaviour if successful.
- A first principles approach should be pursued. This should initially consist of the construction of the jump function from first principles based on the fundamental physics

[38] Although speculative at this point, this may be approached either by measurement of a transport kernel [203] or through examination of fluctuation statistics [204] and then conversion to a jump function.

of turbulence in the edge and the SOL, and then attempt to predict conditions based on this first principles approach[39].

More generally, there are a number of interesting questions that follow directly from the work in this thesis. In no particular order:

- We have here investigated the case of a jump function which is spatially independent. The spatially dependent case could be interesting and relevant.
- Following on and related to the previous item, it is possible to conceive physical cases where the jumps in a random walk may not be entirely independent. For example, consider the case where there is a large anisotropic change in collisionality. A particle which jumps to a region of lower collisionality, may perhaps be more likely to continue in the same direction. *Limit theorems for distributions and corresponding jump functions should be identified in such cases, which would continue the work of Kolmogoroff.*
- While it is intuitive to apply the random walk model to density transport, we are interested in the transport of other quantities, such as energy in the form of heat. While moment approaches may be adequate and extensible to this case, it would be of great intuitive value to see how the transfer of thermal energy can be obtained directly from random walk models for density by construction - possibly by appeal to other thermodynamic concepts such as entropy.
- Relatedly, and conversely, if the equations derived using jump functions (such as FADEs) and the stochastic flux equation are indeed reduction of full transport equations in certain limits, it should be possible to rigorously demonstrate this in the correct circumstances. A general method to do this would be particularly instrumentally useful in a wide variety of circumstances.
- General solutions to FADEs would be very useful in relation to the above. It seems possible and reasonable to do this, and indeed the author is working on producing such solutions. It is likely that hyper-geometric functions play a significant part in the solution thereof, but this raises the prospect of some intriguing solution methods for transport equations as a whole if indeed some (non-local) fractional transport equations are reductions of non-fractional and local transport equations

[39]It would also be beneficial to extend this in order to attempt to understand the impact on transport due to coherent structures in steady-state more generally (e.g. impact of zonal flows).

These are only a small number of immediate questions that occur during the writing of this thesis. This appears to be a fruitful and interesting area with a great deal of potential for application: only by innovative and dedicated work in the realms of experiment, theory, and pure mathematics will the full scope and application become clear.

References

[1] G. H. Miley, H. Towner, and N. Ivich, "Fusion cross sections and reactivities," *University of Illnois Nuclear Engineering Programme Report*, 1974.

[2] I. García-Cortés, R. Balbín, A. Loarte, J. Bleuel, A. Chankin, S. J. Davies, M. Endler, S. K. Erents, C. Hidalgo, G. F. Matthews, B. V. Milligen, and H. Thomsen, "Turbulent transport studies in the jet edge plasmas in limiter configuration," *Plasma Physics and Controlled Fusion*, vol. 42, pp. 389–400, 2000.

[3] R. J. Maqueda, G. A. Wurden, S. Zweben, L. Roquemore, H. Kugel, D. Johnson, S. Kaye, S. Sabbagh, and R. Maingi, "Edge turbulence measurements in nstx by gas puff imaging," *Review of Scientific Instruments*, vol. 72, pp. 931–934, 1 2001.

[4] O. E. Garcia, R. A. Pitts, J. Horacek, A. H. Nielsen, W. Fundamenski, J. P. Graves, V. Naulin, and J. J. Rasmussen, "Turbulent transport in the tcv sol," *Journal of Nuclear Materials*, vol. 363-365, pp. 575–580, 6 2007.

[5] O. E. Garcia, V. Naulin, A. H. Nielsen, and J. J. Rasmussen, "Turbulence and transport in the edge region of toroidally magnetized plasmas," *Physics AUC*, vol. 17, pp. 263–286, 2007.

[6] A. Wynn, B. Lipschultz, I. Cziegler, J. Harrison, A. Jaervinen, G. F. Matthews, J. Schmitz, B. Tal, M. Brix, C. Guillemaut, D. Frigione, A. Huber, E. Joffrin, U. Kruzei, F. Militello, A. Nielsen, N. R. Walkden, and S. Wiesen, "Investigation into the formation of the scrape-off layer density shoulder in jet iter-like wall l-mode and h-mode plasmas," *Nuclear Fusion*, vol. 58, 3 2018.

[7] B. Lipschultz, B. Labombard, C. S. Pitcher, and R. Boivin, "Investigation of the origin of neutrals in the main chamber of alcator c-mod," *Plasma Phys. Control. Fusion*, vol. 44, pp. 733–748, 2002.

[8] O. E. Garcia, R. A. Pitts, J. Horacek, J. Madsen, V. Naulin, A. H. Nielsen, and J. J. Rasmussen, "Collisionality dependent transport in tcv sol plasmas," *Plasma Physics and Controlled Fusion*, vol. 49, 12 2007.

[9] J. Flor and G. J. Heijst, "An experimental study of dipolar vortex structures in a stratified fluid," *Journal of Fluid Mechanics*, vol. 279, pp. 101–133, 1994.

[10] E. R. Weeks, J. S. Urbach, and H. L. Swinney, "Anomalous diffusion in asymmetric random walks with a quasi-geostrophic flow example," 1996.

[11] A. S. EDDINGTON, "The internal constitution of the stars," *Nature*, vol. 106, 9 1920.

[12] S. Nalley and A. LaRose, "International energy outlook 2021," tech. rep., U.S. Energy Information Administration, 10 2021.

[13] V. Masson-Delmotte, P. Zhai, A. Pirani, S. Connors, C. Pean, S. Berger, N. Caud, Y. Chen, L. Goldfarb, M. Gomis, M. Huang, K. Leitzell, E. Lonnoy, J. Matthews, T. Maycock, T. Waterfield, O. Yelekci, R. Yu, and B. Zhou, "Climate change 2021: The physical science basis," tech. rep., International Panel on Climate Change, 2021.

[14] "Key world energy statistics 2021," tech. rep., International Energy Agency, 2021.

[15] "Bp energy outlook 2023," tech. rep., British Petroleum, 2023.

[16] "Statistical review of world energy 2022," tech. rep., British Petroelum, 2022.

[17] D. Kaya, F. Çanka Kılıç, and H. H. Öztürk, *Fuels and Combustion*, pp. 227–263. Cham: Springer International Publishing, 2021.

[18] K. Vohra, A. Vodonos, J. Schwartz, E. A. Marais, M. P. Sulprizio, and L. J. Mickley, "Global mortality from outdoor fine particle pollution generated by fossil fuel combustion: Results from geos-chem," *Environmental Research*, vol. 195, p. 110754, 2021.

[19] "Renewables 2022," tech. rep., International Energy Agency, 2022.

[20] "Global renewables outlook: Energy transformation 2050," tech. rep., International Renewable Energy Agency, 2020.

[21] "Uranium resources, production and demand," tech. rep., Nuclear Energy Agency and International Atomic Energy Agency, 2020.

[22] J. Carlson, "Nuclear growth and proliferation issues," tech. rep., Australian Safeguards and Non-Proliferation Office, 10 2007.

[23] "Public attitudes to nuclear power," tech. rep., Nuclear Energy Agency, 2010.

[24] "Comparing nuclear accident risks with those from other energy sources.," tech. rep., Nuclear Energy Agency, 2010.

[25] J. Handal and J. Surowiec, "Nasa confirms dart mission impact changed asteroid's motion in space," 2022. Retrieved 19/04/2023.

[26] P. Michel, M. Küppers, A. C. Bagatin, B. Carry, S. Charnoz, J. de Leon, A. Fitzsimmons, P. Gordo, S. F. Green, A. Hérique, M. Juzi, Özgür Karatekin, T. Kohout, M. Lazzarin, N. Murdoch, T. Okada, E. Palomba, P. Pravec, C. Snodgrass, P. Tortora, K. Tsiganis, S. Ulamec, J.-B. Vincent, K. Wünnemann, Y. Zhang, S. D. Raducan, E. Dotto, N. Chabot, A. F. Cheng, A. Rivkin, O. Barnouin, C. Ernst, A. Stickle, D. C. Richardson, C. Thomas, M. Arakawa, H. Miyamoto, A. Nakamura, S. Sugita, M. Yoshikawa, P. Abell, E. Asphaug, R.-L. Ballouz, W. F. Bottke, D. S. Lauretta, K. J. Walsh, P. Martino, and I. Carnelli, "The esa hera mission: Detailed characterization of the dart impact outcome and of the binary asteroid (65803) didymos," *The Planetary Science Journal*, vol. 3, p. 160, 7 2022.

[27] A. Suárez Mascareño, E. González-Álvarez, M. R. Zapatero Osorio, J. Lillo-Box, J. P. Faria, V. M. Passegger, J. I. González Hernández, P. Figueira, A. Sozzetti, R. Rebolo, F. Pepe, N. C. Santos, S. Cristiani, C. Lovis, A. M. Silva, I. Ribas, P. J. Amado, J. A. Caballero, A. Quirrenbach, A. Reiners, M. Zechmeister, V. Adibekyan, Y. Alibert, V. J. S. Béjar, S. Benatti, V. D'Odorico, M. Damasso, J. B. Delisle, P. Di Marcantonio, S. Dreizler, D. Ehrenreich, A. P. Hatzes, N. C. Hara, T. Henning, A. Kaminski, M. J. López-González, C. J. A. P. Martins, G. Micela, D. Montes, E. Pallé, S. Pedraz, E. Rodríguez, C. Rodríguez-López, L. Tal-Or, S. Sousa, and S. Udry, "Two temperate Earth-mass planets orbiting the nearby star GJ 1002," , vol. 670, p. A5, Feb. 2023.

[28] P. Lubin, "A roadmap to interstellar flight," 4 2016.

[29] C. J. . Everett, *On a Method of Propulsion of Projectiles by Means of External Nuclear Explosions*, pp. 163–178. Berkeley: University of California Press, 1990.

[30] G. R. Schmidt, J. A. Bonometti, and C. A. Irvine, "Project orion and future prospects for nuclear pulse propulsion," *Journal of Propulsion and Power*, vol. 18, pp. 497–504, 2002.

[31] A. R. Martin and J. A. Bond, *Project Daedalus: The Propulsion System, Part I, Theoretical Considerations and Calculations*, pp. 44–62. 1978.

[32] R. W. Bussard, "Galactic matter and interstellar flight," *Astronautica Acta*, vol. 6, 1960.

[33] K. Altwegg, H. Balsiger, A. Bar-Nun, J.-J. Berthelier, A. Bieler, P. Bochsler, C. Briois, U. Calmonte, M. Combi, and e. a. J. de Keyser, "67p/churyumov-gerasimenko, a jupiter family comet with a high d/h ratio," *Science*, vol. Volume 347, 2015.

[34] H. B. Niemann, S. K. Atreya, G. R. Carignan, T. M. Donahue, J. A. Haberman, D. N. Harpold, R. E. Hartle, D. M. Hunten, W. T. Kasprzak, P. R. Mahaffy, T. C. Owen, N. W. Spencer, and S. H. Way, "The galileo probe mass spectrometer: Composition of jupiter's atmosphere," *Science*, vol. 272, no. 5263, pp. 846–849, 1996.

[35] J. D. Huba, *NRL Plasma Formulary*. Washington, DC 20375: NRL, 2018.

[36] K. S. Krane, *INTRODUCTORY NUCLEAR PHYSICS*. J. Wiley, 2nd ed., 1988.

[37] W. M. Nevins, A. Carlson, N. Rostoker, M. W. Binderbauer, and H. J. Monkhorst, "Feasibility of a colliding beam fusion reactor," *Proceedings of the Physical Society*, vol. Vol.70 (1), p.6-10, 1957.

[38] A. Pelaghia, G. Crete, and A. G. Ruggiero, "Nuclear fusion of protons with boron," 1992.

[39] F. R. Gladeck, J. H. Hallowell, E. J. Martin, F. W. McMullan, R. H. Miller, R. Pozega, W. E. Rogers, R. H. Rowland, C. F. Shelton, and L. Berkhouse, "Operation ivy, 1952 - united states atmospheric nuclear weapons tests nuclear test personnel review," tech. rep., Defence Nuclear Agency, May 13 1983.

[40] F. A. Hernández and P. Pereslavtsev, "First principles review of options for tritium breeder and neutron multiplier materials for breeding blankets in fusion reactors," *Fusion Engineering and Design*, vol. 137, pp. 243–256, 12 2018.

[41] J. Wesson, *Tokamaks*. Oxford, UK: Oxford University Press, 2011.

[42] N. Rostoker, M. W. Binderbauer, and H. J. Monkhorst, "Colliding beam fusion reactor," *Science*, vol. 278, pp. 1419–1422, 11 1997.

[43] J. D. Lawson, "Some criteria for a power producing thermonuclear reactor," *Science*, vol. Vol. 281, Issue 5375, pp. 307, 1998.

[44] L. L. N. Laboratory, "Lawrence livermore national laboratory achieves fusion ignition." `https://archive.ph/etG78`, 12 2022.

[45] J. Lindl, P. Amendt, R. L. Berger, S. G. Glendinning, and S. H. Glenzer, "The physics basis for ignition using indirect-drive targets on the national ignition facility," *Physics of Plasmas*, vol. 11, no. 339, 2004.

[46] S. Meschini, F. Laviano, F. Ledda, D. Pettinari, R. Testoni, D. Torsello, and B. Panella, "Review of commercial nuclear fusion projects," *Frontiers in Energy Research*, vol. 11, 2023.

[47] S. A. Slutz, M. C. Herrmann, R. A. Vesey, A. B. Sefkow, D. B. Sinars, D. C. Rovang, K. J. Peterson, and M. E. Cuneo, "Pulsed-power-driven cylindrical liner implosions of laser preheated fuel magnetized with an axial field," *Physics of Plasmas*, vol. 17, p. 056303, 03 2010.

[48] A. B. Sefkow, S. A. Slutz, J. M. Koning, M. M. Marinak, K. J. Peterson, D. B. Sinars, and R. A. Vesey, "Design of magnetized liner inertial fusion experiments using the Z facility," *Physics of Plasmas*, vol. 21, p. 072711, 07 2014.

[49] UKAEA, "Lithium breeding tritium innovation (librti) programme." `https://uk.eu-supply.com/ctm/Company/CompanyInformation/Index/72814`, 2024.

[50] R. Hunt, R. Abbott, M. Havstad, and A. Dunne, "Fatigue cracking of a bare steel first wall in an inertial confinement fusion chamber," *Fusion Engineering and Design*, vol. 88, pp. 311–316, 6 2013.

[51] D. A. Ehst, Y. Cha, A. M. Hassanein, S. Majumdar, B. Misra, and H. C. Stevens, "A comparison of pulsed and steady-state tokamak reactor burn cycles. part i: Thermal effects and lifetime limitations," *Nuclear Engineering and Design/Fusion*, vol. Fusion 2, pp. 305–318, 1985.

[52] D. A. Ehst, J. N. Brooks, K. Evans, and S. Kim, "A comparison of pulsed and steady-state tokamak reactor burn cycles. part ii: Magnet fatigue, power supplies, and cost analysis," *Nuclear Engineering and Design*, vol. Fusion 2, pp. 319–336, 1985.

[53] V. D. Shafranov, "On the history of the research into controlled thermonuclear fusion," *Physics-Uspekhi*, vol. 44, pp. 835–843, 8 2001.

[54] F. Wagner, "A quarter-century of h-mode studies," *Plasma Physics and Controlled Fusion*, vol. 49, 12 2007.

[55] I. P. E. G. on Confinement and Transport, "Iter physics basis chapter 2: Plasma confinement and transport," *Nucl. Fusion*, vol. 39, p. 2175, 1999.

[56] F. Wagner, G. Becker, K. Behringer, D. Campbell, A. Eberhagen, W. Engelhardt, G. Fussmann, J. Gernhardt, G. Gierke, G. Haas, M. Huang, F. Karger, M. Keilhacker, Q. Kluber, M. Kornherr, K. Lackner, G. Lisitano, G. G. Lister, H. M. Mayer, D. Meisel,

E. R. MIiller, H. Murmann, H. Niedermeyer, W. Poschenrieder, H. Rapp, H. Bohr, F. Schneider, G. Siller, E. Speth, A. Stabler, K. H. Steuer, G. Venus, O. Vollmer, and Z. Yu, "A regime of improved confinement and high beta in neutral-beam-heated divertor discharges of the asdex tokamak," *Appl. Phys. Lett*, vol. 18, p. 133, 1982.

[57] H. Zohm, "Edge localized modes (elms)," *Plasma Phys. Control. Fusion*, vol. 38, pp. 105–128, 1996.

[58] I. P. E. G. on Divertor, "Iter physics basis chapter 4: Power and particle control," *Nuclear Fusion*, vol. 39, p. 2391, 1999.

[59] F. L. Ribe, "Fusion reactor systems," *Reviews of Modern Physics*, vol. 47, 1 1975.

[60] V. A. Soukhanovskii, "A review of radiative detachment studies in tokamak advanced magnetic divertor configurations," *Plasma Physics and Controlled Fusion*, vol. 59, 4 2017.

[61] F. Militello, *Boundary Plasma Physics*, vol. 123. Springer International Publishing, 2022.

[62] S. I. Krasheninnikov and A. S. Kukushkin, "Physics of ultimate detachment of a tokamak divertor plasma," *Journal of Plasma Physics*, vol. 83, 10 2017.

[63] T. Gheorghiu, F. Militello, and J. J. Rasmussen, "On the transport of tracer particles in two-dimensional plasma edge turbulence," *Physics of Plasmas*, vol. 31, 1 2024.

[64] W. D. D'haeseleer, W. N. G. Hitchon, J. D. Callen, and J. L. Shohet, *Flux Coordinates and Magnetic Field Structure*. Springer Berlin Heidelberg, 1991.

[65] T. Eich, A. W. Leonard, R. A. Pitts, W. Fundamenski, R. J. Goldston, T. K. Gray, A. Herrmann, A. Kirk, A. Kallenbach, O. Kardaun, A. S. Kukushkin, B. Labombard, R. Maingi, M. A. Makowski, A. Scarabosio, B. Sieglin, J. Terry, and A. Thornton, "Scaling of the tokamak near the scrape-off layer h-mode power width and implications for iter," *Nuclear Fusion*, vol. 53, 9 2013.

[66] D. Brunner, B. Labombard, A. Q. Kuang, and J. L. Terry, "High-resolution heat flux width measurements at reactor-level magnetic fields and observation of a unified width scaling across confinement regimes in the alcator c-mod tokamak," *Nuclear Fusion*, vol. 58, 7 2018.

[67] P. C. Stangeby, "Basic physical processes and reduced models for plasma detachment," *Plasma Physics and Controlled Fusion*, vol. 60, 3 2018.

[68] J. Boedo, A. G. McLean, D. L. Rudakov, and J. G. Watkins, "A review of direct experimental measurements of detachment," *Plasma Physics and Controlled Fusion*, vol. 60, 2 2018.

[69] B. Labombard, M. V. Umansky, R. L. Boivin, J. A. Goetz, J. Hughes, B. Lipschultz, D. Mossessian, C. S. Pitcher, J. L. Terry, and A. Group, "Cross-field plasma transport and main chamber recycling in diverted plasmas on alcator c-mod," *Nuclear Fusion*, vol. 40, 2000.

[70] H. Sun, "Broadening of sol width at high collisional plasma edge and its impact on machine operation," Layering in Magnetic Plasmas (conference), 2024.

[71] P. C. Stangeby, *The plasma boundary of magnetic fusion devices*. Institute of Physics Pub, 2000.

[72] F. F. Chen, *Introduction to Plasma Physics and Controlled Fusion*. Springer International Publishing, 2016.

[73] J. WESSON, *Tokamaks 3rd Edition by John Wesson, Oxford University Press 2004, 749pp, Hardback 0 19 850922*, vol. 71. Oxford University Press, third ed., 6 2005.

[74] S. J. Zweben and R. W. Gould, "Structure of edge-plasma turbulence in the caltech tokamak structure of edge-plasma turbulence in the caltech tokamak*," 1985.

[75] A. J. Wootton, B. A. Carreras, H. Matsumoto, K. McGuire, W. A. Peebles, C. P. Ritz, P. W. Terry, and S. J. Zweben, "Fluctuations and anomalous transport in tokamaks," *Physics of Fluids B*, vol. 2, pp. 2879–2903, 1990.

[76] M. Endler, "Turbulent sol transport in stellarators and tokamaks," *Journal Of Nuclear Materials*, vol. 266-269, pp. 84–90, 1999.

[77] B. LaBombard, R. L. Boivin, M. Greenwald, J. Hughes, B. Lipschultz, D. Mossessian, C. S. Pitcher, J. L. Terry, and S. J. Zweben, "Particle transport in the scrape-off layer and its relationship to discharge density limit in alcator c-mod," *Physics of Plasmas*, vol. 8, pp. 2107–2117, 5 2001.

[78] J. Horacek, R. A. Pitts, and J. P. Gravesécole, "Overview of edge electrostatic turbulence experiments on tcv," *Czechoslovak Journal of Physics*, vol. 55, pp. 271–283, 2005.

[79] D. L. Rudakov, J. A. Boedo, R. A. Moyer, P. C. Stangeby, J. G. Watkins, D. G. Whyte, L. Zeng, N. H. Brooks, R. P. Doerner, T. E. Evans, M. E. Fenstermacher, M. Groth, E. M. Hollmann, S. I. Krasheninnikov, C. J. Lasnier, A. W. Leonard, M. A. Mahdavi, G. R. McKee, A. G. McLean, A. Y. Pigarov, W. R. Wampler, G. Wang, W. P. West, and C. P. Wong, "Far sol transport and main wall plasma interaction in diii-d," *Nuclear Fusion*, vol. 45, pp. 1589–1599, 12 2005.

[80] Y. H. Xu, S. Jachmich, and R. R. Weynants, "On the properties of turbulence intermittency in the boundary of the textor tokamak," *Plasma Physics and Controlled Fusion*, vol. 47, pp. 1841–1855, 10 2005.

[81] G. Y. Antar, S. I. Krasheninnikov, P. Devynck, R. P. Doerner, E. M. Hollmann, J. A. Boedo, S. C. Luckhardt, and R. W. Conn, "Experimental evidence of intermittent convection in the edge of magnetic confinement devices," *Physical Review Letters*, vol. 87, pp. 65001–1–65001–4, 8 2001.

[82] F. Militello, P. Tamain, W. Fundamenski, A. Kirk, V. Naulin, and A. H. Nielsen, "Experimental and numerical characterization of the turbulence in the scrape-off layer of mast," *Plasma Physics and Controlled Fusion*, vol. 55, 2 2013.

[83] G. Y. Antar, G. Counsell, Y. Yu, B. Labombard, and P. Devynck, "Universality of intermittent convective transport in the scrape-off layer of magnetically confined devices," *Physics of Plasmas*, vol. 10, pp. 419–428, 2 2003.

[84] J. A. Boedo, D. L. Rudakov, R. A. Moyer, G. R. McKee, R. J. Colchin, M. J. Schaffer, P. G. Stangeby, W. P. West, S. L. Allen, T. E. Evans, R. J. Fonck, E. M. Hollmann, S. Krasheninnikov, A. W. Leonard, W. Nevins, M. A. Mahdavi, G. D. Porter, G. R. Tynan, D. G. Whyte, and X. Xu, "Transport by intermittency in the boundary of the diii-d tokamak," *Physics of Plasmas*, vol. 10, pp. 1670–1677, 5 2003.

[85] S. I. Krasheninnikov, "On scrape off layer plasma transport," *Physics Letters A*, vol. 283, pp. 368–370, 2001.

[86] O. E. Garcia, J. Horacek, R. A. Pitts, A. H. Nielsen, W. Fundamenski, J. P. Graves, V. Naulin, and J. J. Rasmussen, "Interchange turbulence in the tcv scrape-off layer," *Plasma Physics and Controlled Fusion*, vol. 48, 1 2006.

[87] D. A. D'Ippolito, J. R. Myra, and S. J. Zweben, "Convective transport by intermittent blob-filaments: Comparison of theory and experiment," *Physics of Plasmas*, vol. 18, 6 2011.

[88] J. Harrison, G. Fishpool, and B. Dudson, "Filamentary transport in the private flux region in mast," *Journal of Nuclear Materials*, vol. 463, 8 2015.

[89] X. Bonnin, A. S. Kukushkin, and D. P. Coster, "Code development for iter edge modelling - solps5.1," *Journal of Nuclear Materials*, vol. 390-391, pp. 274–277, 6 2009.

[90] B. Lipschultz, D. Whyte, and B. LaBombard, "Comparison of particle transport in the scrape-off layer plasmas of alcator c-mod and diii-d," *Plasma Physics and Controlled Fusion*, vol. 47, pp. 1559–1578, 10 2005.

[91] V. Naulin, "Turbulent transport and the plasma edge," *Journal of Nuclear Materials*, vol. 363-365, pp. 24–31, 6 2007.

[92] O. E. Garcia, V. Naulin, A. H. Nielsen, and J. J. Rasmussen, "Computations of intermittent transport in scrape-off layer plasmas," *Physical Review Letters*, vol. 92, 4 2004.

[93] K. W. Gentle, R. V. Bravenec, G. Cima, H. Gasquet, G. A. Hallock, P. E. Phillips, D. W. Ross, W. L. Rowan, A. J. Wootton, T. P. Crowley, J. Heard, A. Ouroua, P. M. Schoch, and C. Watts, "An experimental counter-example to the local transport paradigm," *Physics of Plasmas*, vol. 2, pp. 2292–2298, 1995.

[94] K. W. Gentle, R. V. Bravenec, G. Cima, G. A. Hallock, P. E. Phillips, D. W. Ross, W. L. Rowan, A. J. Wootton, T. P. Crowley, A. Ouroua, P. M. Schoch, and C. Watts, "The evidence for nonlocal transport in the texas experimental tokamak," *Physics of Plasmas*, vol. 4, pp. 3599–3613, 1997.

[95] K. Ida, Z. Shi, H. J. Sun, S. Inagaki, K. Kamiya, J. E. Rice, N. Tamura, P. H. Diamond, G. Dif-Pradalier, X. L. Zou, K. Itoh, S. Sugita, O. D. Gürcan, T. Estrada, C. Hidalgo, T. S. Hahm, A. Field, X. T. Ding, Y. Sakamoto, S. Oldenbürger, M. Yoshinuma, T. Kobayashi, M. Jiang, S. H. Hahn, Y. M. Jeon, S. H. Hong, Y. Kosuga, J. Dong, and S. I. Itoh, "Towards an emerging understanding of non-locality phenomena and non-local transport," *Nuclear Fusion*, vol. 55, 1 2015.

[96] C. Angioni, E. Fable, F. Ryter, P. Rodriguez-Fernandez, and T. Pütterich, "The local nature of the plasma response to cold pulses with electron and ion heating at asdex upgrade," *Nuclear Fusion*, vol. 59, 8 2019.

[97] P. Rodriguez-Fernandez, C. Angioni, and A. E. White, "Local transport dynamics of cold pulses in tokamak plasmas," *Reviews of Modern Plasma Physics*, vol. 6, 12 2022.

[98] G. M. Staebler, J. E. Kinsey, and R. E. Waltz, "A theory-based transport model with comprehensive physics," *Physics of Plasmas*, vol. 14, 2007.

[99] P. A. Politzer, "Observation of avalanchelike phenomena in a magnetically confined plasma," *Physical Review Letters*, vol. 84, 2000.

[100] P. A. Politzer, M. E. Austin, M. Gilmore, G. R. McKee, T. L. Rhodes, C. X. Yu, E. J. Doyle, T. E. Evans, and R. A. Moyere, "Characterization of avalanche-like events in a confined plasma," *Physics of Plasmas*, vol. 9, pp. 1962–1969, 2002.

[101] A. J. H. Donné, J. Sánchez-Sanz, B. P. V. Milligen, E. D. L. Luna, F. L. Tabarés, E. Ascasíbar, T. Estrada, F. Castejón, J. Castellano, I. García-Cortés, J. Herranz, C. Hidalgo, J. A. Jimenez, F. Medina, M. Ochando, I. Pastor, M. A. Pedrosa, D. Tafalla, L. García, R. Sánchez, A. Petrov, K. Sarksian, and N. Skvortsova, "Ballistic transport phenomena in tj-ii you may also like ballistic transport phenomena in tj-ii," *Nuclear Fusion*, vol. 42, pp. 787–795, 2002.

[102] J. Schmittbuhl, J.-P. Vilotte, and S. Roux, "Reliability of self-affine measurements," *Physical Review E*, vol. 51, 1995.

[103] K. Ida, "Non-local transport nature revealed by the research in transient phenomena of toroidal plasma," *Reviews of Modern Plasma Physics*, vol. 6, 12 2022.

[104] D. G. Whyte, B. L. Lipschultz, P. C. Stangeby, J. Boedo, D. L. Rudakov, J. G. Watkins, and W. P. West, "The magnitude of plasma flux to the main-wall in the diii-d tokamak," *Plasma Physics and Controlled Fusion*, vol. 47, pp. 1579–1607, 10 2005.

[105] O. Garcia, J. Horacek, R. Pitts, A. Nielsen, W. Fundamenski, V. Naulin, and J. J. Rasmussen, "Fluctuations and transport in the tcv scrape-off layer," *Nuclear Fusion*, vol. 47, pp. 667–676, 7 2007.

[106] T. T. Team, N. Vianello, C. Tsui, C. Theiler, S. Allan, J. Boedo, B. Labit, H. Reimerdes, K. Verhaegh, W. A. Vijvers, N. Walkden, S. Costea, J. Kovacic, C. Ionita, V. Naulin, A. H. Nielsen, J. J. Rasmussen, B. Schneider, R. Schrittwieser, M. Spolaore, D. Carralero, J. Madsen, B. Lipschultz, and F. Militello, "Modification of sol profiles and fluctuations with line-average density and divertor flux expansion in tcv," *Nuclear Fusion*, vol. 57, 8 2017.

[107] F. Militello, L. Garzotti, J. Harrison, J. T. Omotani, R. Scannell, S. Allan, A. Kirk, I. Lupelli, and A. J. Thornton, "Characterisation of the l-mode scrape off layer in mast: Decay lengths," *Nuclear Fusion*, vol. 56, 11 2016.

[108] N. Yan, L. Chen, G. S. Xu, X. Q. Wu, S. C. Liu, Y. F. Wang, L. Y. Meng, G. H. Hu, N. Zhao, H. Lan, V. Naulin, A. H. Nielsen, J. J. Rasmussen, K. D. Li, L. Wang, Q. Q. Yang, M. H. Li, Y. Ye, R. Ding, Y. Q. Tao, Y. Z. Qian, J. L. Hou, X. Liu, and J. B. Liu, "Dependence of upstream sol density shoulder on divertor neutral pressure observed in l-mode and h-mode plasmas in the east superconducting tokamak," *Nuclear Fusion*, vol. 61, 7 2021.

[109] D. Carralero, H. W. Müller, M. Groth, M. Komm, J. Adamek, G. Birkenmeier, M. Brix, F. Janky, P. Hacek, S. Marsen, F. Reimold, C. Silva, U. Stroth, M. Wischmeier, and E. Wolfrum, "Implications of high density operation on sol transport: A multimachine investigation," *Journal of Nuclear Materials*, vol. 463, pp. 123–127, 7 2015.

[110] N. Vianello, D. Carralero, C. K. Tsui, V. Naulin, M. Agostini, I. Cziegler, B. Labit, C. Theiler, E. Wolfrum, D. Aguiam, S. Allan, M. Bernert, J. Boedo, S. Costea, H. D. Oliveira, O. Fevrier, J. Galdon-Quiroga, G. Grenfell, A. Hakola, C. Ionita, H. Isliker, A. Karpushov, J. Kovacic, B. Lipschultz, R. Maurizio, K. McClements, F. Militello, A. H. Nielsen, J. Olsen, J. J. Rasmussen, T. Ravensbergen, H. Reimerdes, B. Schneider, R. Schrittwieser, E. Seliunin, M. Spolaore, K. Verhaegh, J. Vicente, N. Walkden, and W. Zhang, "Scrape-off layer transport and filament characteristics in high-density tokamak regimes," *Nuclear Fusion*, vol. 60, 2020.

[111] N. Asakura, Y. Koide, K. Itami, N. Hosogane, K. Shimizu, S. Tsuji-Iio, S. Sakurai, and A. Sakasai, "Sol plasma profiles under radiative and detached divertor conditions in jt-60u," *Journal of Nuclear Materials*, pp. 559–563, 1997.

[112] H. J. Sun, S. A. Silburn, I. S. Carvalho, D. B. King, C. Giroud, G. Fishpool, G. F. Matthews, R. B. Henriques, D. L. Keeling, F. G. Rimini, L. Garzotti, D. Frigione, D. V. Eester, M. Groth, J. Flanagan, D. Kos, B. Viola, A. Boboc, P. Shi, M. L. Mayoral, J. Mailloux, C. Maggi, A. Huber, D. Douai, N. Vianello, P. J. Lomas, M. Lennholm, M. Maslov, K. Kirov, P. Jacquet, C. G. Lowry, M. Baruzzo, C. Stuart, J. Mitchell, L. Horvath, and D. C. McDonald, "The broadening of sol profiles in jet tritium plasma and its impact on machine operation," *Nuclear Fusion*, vol. 63, 1 2023.

[113] J. R. Myra and D. Russell, "Collisionality and magnetic geometry effects on tokamak edge turbulent transport: I. a two-region model with application to blobs," *Physics of Plasmas*, vol. 13, 2006.

[114] T. Farley, N. R. Walkden, F. Militello, M. Sanna, J. Young, S. S. Silburn, J. Harrison, L. Kogan, I. Lupelli, S. S. Henderson, A. Kirk, and J. W. Bradley, "Filament identification in wide-angle high speed imaging of the mega amp spherical tokamak," *Review of Scientific Instruments*, vol. 90, 9 2019.

[115] G. Fuchert, D. Carralero, P. Manz, U. Stroth, and E. Wolfrum, "Towards a quantitative prediction of the blob detection rate," *Plasma Physics and Controlled Fusion*, vol. 58, 4 2016.

[116] C. Wersal, P. Ricci, and J. Loizu, "A comparison between a refined two-point model for the limited tokamak sol and self-consistent plasma turbulence simulations," *Plasma Physics and Controlled Fusion*, vol. 59, 3 2017.

[117] F. Militello, N. R. Walkden, T. Farley, W. A. Gracias, J. Olsen, F. Riva, L. Easy, N. Fedorczak, I. Lupelli, J. Madsen, A. H. Nielsen, P. Ricci, P. Tamain, and J. Young, "Multi-code analysis of scrape-off layer filament dynamics in mast," *Plasma Physics and Controlled Fusion*, vol. 58, 8 2016.

[118] O. E. Garcia, "Stochastic modeling of intermittent scrape-off layer plasma fluctuations," *Physical Review Letters*, vol. 108, 6 2012.

[119] F. Militello and J. T. Omotani, "Scrape off layer profiles interpreted with filament dynamics," *Nuclear Fusion*, vol. 56, 8 2016.

[120] N. R. Walkden, A. Wynn, F. Militello, B. Lipschultz, G. Matthews, C. Guillemaut, J. Harrison, and D. Moulton, "Interpretation of scrape-off layer profile evolution and first-wall ion flux statistics on jet using a stochastic framework based on filamentary motion," *Plasma Physics and Controlled Fusion*, vol. 59, 6 2017.

[121] F. Militello, T. Farley, K. Mukhi, N. Walkden, and J. T. Omotani, "A two dimensional statistical framework connecting thermodynamic profiles with filaments in the scrape off layer and application to experiments," *Physics of Plasmas*, vol. 25, 2018.

[122] J. M. Losada, A. Theodorsen, and O. E. Garcia, "Stochastic modelling of blob-like plasma filaments in the scrape-off layer: Theoretical foundation," 10 2022.

[123] T. Wu, P. H. Diamond, L. Nie, M. Xu, Y. Yu, R. J. Hong, Y. H. Chen, J. Q. Xu, T. Long, Y. Zhang, Q. H. Yan, R. Ke, J. Cheng, W. Li, Z. H. Huang, L. W. Yan, X. Chu, Z. H. Wang, and C. Hidalgo, "How turbulent transport broadens the heat flux width: local sol production or edge turbulence spreading?," *Nuclear Fusion*, vol. 63, 12 2023.

[124] T. Long, P. Diamond, R. Ke, Z. Chen, M. Cao, X. Xu, M. Xu, R. Hong, W. Tian, J. Yuan, Y. Liu, Q. Yan, Q. Yang, C. Shen, W. Guo, L. Wang, L. Nie, Z. Wang, G. Hao, N. Wang, Z. Chen, Y. Pan, J. Li, W. Chen, and W. Zhong, "On how structures convey non-diffusive turbulence spreading," *Nuclear Fusion*, vol. 64, p. 064002, 6 2024.

[125] W. D. McComb, *The Physics of Fluid Turbulence*. Oxford University Press, 1st ed., 1990.

[126] J. O. Hinze, *Turbulence: An introduction to its mechanism and theory*, vol. 1. McGraw-Hill Book Company, 2 ed., 1959.

[127] R. H. Kraichnan, "Inertial ranges in two-dimensional turbulence," *Physics of Fluids*, vol. 10, pp. 1417–1423, 1967.

[128] G. G. Plunk and T. Tatsuno, "Energy transfer and dual cascade in kinetic magnetized plasma turbulence," *Physical Review Letters*, vol. 106, 4 2011.

[129] E. Lindborg, "Can the atmospheric kinetic energy spectrum be explained by two-dimensional turbulence?," *Journal of Fluid Mechanics*, vol. 388, pp. 259–288, 6 1999.

[130] K. Ida and T. Fujita, "Internal transport barrier in tokamak and helical plasmas," *Plasma Physics and Controlled Fusion*, vol. 60, p. 033001, 3 2018.

[131] N. R. Walkden, B. D. Dudson, and G. Fishpool, "Characterization of 3d filament dynamics in a mast sol flux tube geometry," *Plasma Physics and Controlled Fusion*, vol. 55, 10 2013.

[132] S. J. Kline, W. C. Reynolds, F. A. Schraub, and P. W. Runstadler, "The structure of turbulent boundary layers," *Journal of Fluid Mechanics*, vol. 30, pp. 741–773, 12 1967.

[133] A. K. Gupta and R. E. Kaplan, "Statistical characteristics of reynolds stress in a turbulent boundary layer," *Physics of Fluids*, vol. 15, pp. 981–985, 1972.

[134] W. W. Willmarth and T. J. Bogar, "Survey and new measurements of turbulent structure near the wall," *Physics of Fluids*, vol. 20, 1972.

[135] G. L. Brown and A. Roshko, "On density effects and large structure in turbulent mixing layers," *Journal of Fluid Mechanics*, vol. 64, no. 4, pp. 775–816, 1974.

[136] J. C. McWilliams and J. B. Weiss, "Anisotropic geophysical vortices," *Chaos*, vol. 4, pp. 305–311, 1994.

[137] A. K. Hussain, "Coherent structures - reality and myth," *Physics of Fluids*, vol. 26, pp. 2816–2850, 1983.

[138] J. Weiss, "The dynamics of enstrophy transfer in two-dimensional hydrodynamics," *Physica D*, vol. 48, pp. 273–294, 1991.

[139] J. B. Weiss and J. C. McWilliams, "Lagrangian dynamics in high-dimensional point-vortex systems," 1998.

[140] A. Babiano, "Elementary topology of two-dimensional turbulence from a lagrangian viewpoint and single-particle dispersion," *Journal of Fluid Mechanics*, vol. 257, pp. 533–558, 1993.

[141] A. Provenzale, "Transport by coherent barotropic vortices," *Annual Review of Fluid Mechanics*, vol. 31, 1999.

[142] A. Okubo, "Horizontal dispersion of floatable particles in the vicinity of velocity singularities such as convergences," *Deep Sea Research and Oceanographic Abstracts*, vol. 17, no. 3, pp. 445–454, 1970.

[143] G. Haller and G. Yuan, "Lagrangian coherent structures and mixing in two-dimensional turbulence," *Physica D*, vol. 147, 2000.

[144] L. F. Richardson, "Atmospheric diffusion shown on a distance-neighbour graph," *Proceedings of the Royal Society A*, pp. 709–737, 1926.

[145] S. Corrsin, "Limitations of gradient transport models in random walks and in turbulence," *Advances in geophysics*, vol. 18, pp. 25–60, 1975.

[146] S. Goldstein, "On diffusion by discontinuous movements, and on the telegraph equation," *The Quarterly Journal of Mechanics and Applied Mathematics*, vol. 4, pp. 129–156, 1951.

[147] F. Toschi and E. Bodenschatz, "Lagrangian properties of particles in turbulence," *Annual Review of Fluid Mechanics*, vol. 41, pp. 375–404, 1 2009.

[148] B. H. Fiedler, "An integral closure model for the vertical turbulent flux of a scalar in a mixed layer," *Journal of the Atmospheric Sciences*, vol. 41, pp. 674–680, 1983.

[149] R. Berkowicz and L. P. Prahm, "On the spectral turbulent diffusivity theory for homogeneous turbulence," *Journal of Fluid Mechanics*, vol. 100, pp. 433–448, 1980.

[150] E. E. Ebert, U. Schumann, and R. B. Stull, "Nonlocal turbulent mixing in the convective boundary layer evaluated from large-eddy simulation," *Journal of the Atmospheric Sciences*, vol. 46, 1989.

[151] R. B. Stull, "Transilient turbulence theory part i: The concept of eddy-mixing across finite distances," *American Meteorological Society*, pp. 3351–3367, 1984.

[152] R. B. Stull, "Review of non-local mixing in turbulent atmospheres: Transilient turbulence theory," *Boundary-Layer Meteorology*, vol. 62, pp. 21–96, 1993.

[153] F. Hamba, "Nonlocal analysis of the reynolds stress in turbulent shear flow," *Physics of Fluids*, vol. 17, pp. 1–9, 2005.

[154] F. Hamba, "Analysis and modelling of non-local eddy diffusivity for turbulent scalar flux," *Journal of Fluid Mechanics*, vol. 950, 11 2022.

[155] M. B. Isichenko, "Percolation, statistical topography, and transport in random media," *Reviews of Modern Physics*, vol. 64, pp. 961–1043, 1992.

[156] V. E. Lynch, B. A. Carreras, D. del Castillo-Negrete, K. M. Ferreira-Mejias, and H. R. Hicks, "Numerical methods for the solution of partial differential equations of fractional order," *Journal of Computational Physics*, vol. 192, pp. 406–421, 12 2003.

[157] D. Del-Castillo-Negrete, B. A. Carreras, and V. E. Lynch, "Nondiffusive transport in plasma turbulence: A fractional diffusion approach," *Physical Review Letters*, vol. 94, 2 2005.

[158] D. Del-Castillo-Negrete, "Fractional diffusion models of nonlocal transport," *Physics of Plasmas*, vol. 13, no. 8, 2006.

[159] P. Manz, C. Hufnagel, A. Zito, D. Carralero, M. Griener, T. Lunt, O. Pan, M. Passoni, B. Tal, M. Wischmeier, and E. Wolfrum, "The diffusion limit of ballistic transport in the scrape-off layer," *Physics of Plasmas*, vol. 27, 2 2020.

[160] P. Manz, T. T. Ribeiro, B. D. Scott, G. Birkenmeier, D. Carralero, G. Fuchert, S. H. Müller, H. W. Müller, U. Stroth, and E. Wolfrum, "Origin and turbulence spreading of plasma blobs," *Physics of Plasmas*, vol. 22, 2 2015.

[161] R. Metzler and J. Klafter, "The random walk's guide to anomalous diffusion: A fractional dynamics approach," 2000.

[162] R. Kutner and J. Masoliver, "The continuous time random walk, still trendy: fifty-year history, state of art and outlook," *European Physical Journal B*, vol. 90, 3 2017.

[163] K. PEARSON, "The problem of the random walk," *Nature*, vol. 72, 7 1905.

[164] E. W. Montroll and G. H. Weiss, "Random walks on lattices. ii," *Journal of Mathematical Physics*, vol. 6, pp. 167–181, 1965.

[165] R. V. Noorden, B. Maher, and R. Nuzzo, "The top 100 papers." `https://www.nature.com/news/the-top-100-papers-1.16224`, 2014.

[166] S. Chandrasekhar, "Stochastic problems in physics and astronomy," *Reviews of Modern Physics*, vol. 15, 1 1943.

[167] L. Vlahos, H. Isliker, Y. Kominis, and K. Hizanidis, "Normal and anomalous diffusion: A tutorial," 5 2008.

[168] S. L. Lauritzen, "Time series analysis in 1880: A discussion of contributions made by t.n. thiele," *International Statistical Review / Revue Internationale de Statistique*, vol. 49, 12 1981.

[169] L. Bachelier, "Théorie de la spéculation," *Annales scientifiques de l'É.N.S.*, vol. 17, pp. 21–86, 1900.

[170] J.-M. Courtault, Y. Kabanov, B. Bru, P. Crépel, I. Lebon, and A. L. Marchand, "Louis bachelier on the centenary of thÉorieth´thÉorie de la spÉculationsp´spÉculation *," 2000.

[171] A. Einstein, "On the movement of small particles suspended in stationary liquids required by the molecular-kinetic theory of heat," *Annalen der Physik*, vol. 17, pp. 549–560, 1905.

[172] E. of Mathematics, "Stirling formula." `http://encyclopediaofmath.org/index.php?title=Stirling_formula&oldid=44695`, 2020.

[173] M. F. Shlesinger, "Fractal time in condensed matter," *Ann. Rev. Phys. Chern*, vol. 39, pp. 269–90, 1988.

[174] J. P. Nolan, *Univariate Stable Distributions*. Springer, first edition ed., 9 2020.

[175] B. V. Gnedenko and A. N. Kolmogorov, *Limit Distributions For Sums of Independent Random Variables*. Addison-Wesley Publishing, first ed., 1952.

[176] M. Pettini, A. Vulpiani, P. A. Moro, I. H. J. Misguich, M. D. Leener, J. Orban, and R. Balescu, "Chaotic diffusion across a magnetic field in a model of electrostatic turbulent plasma," *Physical Review A*, vol. 38, 1988.

[177] L. Patruno and M. Ricci, "A systematic approach to the generation of synthetic turbulence using spectral methods," *Computer Methods in Applied Mechanics and Engineering*, vol. 340, pp. 881–904, 10 2018.

[178] R. Basu, V. Naulin, and J. J. Rasmussen, "Particle diffusion in anisotropic turbulence," *Communications in Nonlinear Science and Numerical Simulation*, vol. 8, pp. 477–492, 9 2003.

[179] M. Vlad, F. Spineanu, J. H. Misguich, and R. Balescu, "Diffusion with intrinsic trapping in two-dimensional incompressible stochastic velocity fields," *Physical Review E*, vol. 58, 1998.

[180] B. Kadoch, D. del Castillo-Negrete, W. J. T. Bos, and K. Schneider, "Lagrangian conditional statistics and flow topology in edge plasma turbulence," *Physics of Plasmas*, vol. 29, p. 102301, 10 2022.

[181] P. H. Diamond, S. I. Itoh, K. Itoh, and T. S. Hahm, "Zonal flows in plasma - a review," *Plasma Physics and Controlled Fusion*, vol. 47, 5 2005.

[182] A. Hasegawa and K. Mima, "Stationary spectrum of strong turbulence in magnetized nonuniform plasma," *Physical Review Letters*, vol. 39, 7 1977.

[183] A. Yoshizawa, S.-I. Itoh, K. Itoh, and N. Yokoi, "Turbulence theories and modelling of fluids and plasmas," *Plasma Phys. Control. Fusion*, vol. 43, pp. 16337–16339, 2001.

[184] G. W. Hammett, M. A. Beer, W. Dorland, S. C. Cowley, and S. A. Smith, "Developments in the gyrofluid approach to tokamak turbulence simulations," *Plasma Phys. Control. Fusion*, vol. 35, p. 973, 1993.

[185] B. D. Dudson, P. A. Hill, D. Dickinson, J. Parker, A. Dempsey, and et al., "BOUT++." `https://github.com/boutproject/BOUT-dev`, 10 2020.

[186] A. B. A. Elhmaidi, D; Provenzale, "Elementary topology of two-dimensional turbulence from a lagrangian viewpoint and single-particle dispersion," *Journal of Fluid Mechanics*, vol. 257, pp. 533–558, 1993.

[187] W. Bos, B. Kadoch, S. Neffaa, and K. Schneider, "Lagrangian dynamics of drift-wave turbulence," *Physica D: Nonlinear Phenomena*, vol. 239, pp. 1269–1277, 7 2010.

[188] R. Sánchez, D. E. Newman, J. N. Leboeuf, V. K. Decyk, and B. A. Carreras, "Nature of transport across sheared zonal flows in electrostatic ion-temperature-gradient gyrokinetic plasma turbulence," *Physical Review Letters*, vol. 101, 11 2008.

[189] R. Basu, T. Jessen, V. Naulin, and J. J. Rasmussen, "Turbulent flux and the diffusion of passive tracers in electrostatic turbulence," *Physics of Plasmas*, vol. 10, pp. 2696–2703, 7 2003.

[190] R. Balescu, "V-langevin equations, continuous time random walks and fractional diffusion," *Chaos, Solitons and Fractals*, vol. 34, pp. 62–80, 2007.

[191] K. B. Oldham and J. Spanier, *The Fractional Calculus: Theory and Applications of Differentiation and Integration to Arbitrary Order*. Academic Press, 1st ed., 1974.

[192] I. Podlubny, *Fractional Differential Equations: An Introduction to Fractional Derivatives, Fractional Differential Equations, to Methods of their Solution and some of their Applications*. Academic Press, 1st ed., 1998.

[193] H. J. Haubold and A. M. Mathai, *An introduction to fractional calculus*. Nova Science Publishers, 1st ed., 2017.

[194] V. Daftardar-Gejji and H. Jafari, "Adomian decomposition: A tool for solving a system of fractional differential equations," *Journal of Mathematical Analysis and Applications*, vol. 301, pp. 508–518, 1 2005.

[195] I. Gradshteyn and I. Ryzhik, *Table of Integrals, Series, and Products*. Academic Press, seventh edition ed., 2007.

[196] M. D. Ortigueira and F. Coito, "From differences to derivatives," *Fractional Calculus and Applied Analysis*, vol. 7, 2004.

[197] M. D. Ortigueira, "Riesz potential operators and inverses via fractional centred derivatives," *International Journal of Mathematics and Mathematical Sciences*, vol. 2006, 2006.

[198] C. Çelik and M. Duman, "Crank-nicolson method for the fractional diffusion equation with the riesz fractional derivative," *Journal of Computational Physics*, vol. 231, pp. 1743–1750, 2012.

[199] W. Fundamenski, O. E. Garcia, V. Naulin, R. A. Pitts, A. H. Nielsen, J. J. Rasmussen, J. Horacek, and J. P. Graves, "Dissipative processes in interchange driven scrape-off layer turbulence," *Nuclear Fusion*, vol. 47, pp. 417–433, 2007.

[200] T. E. G. Nicholas, J. Omotani, F. Riva, F. Militello, and B. Dudson, "Comparing two- and three-dimensional models of scrape-off-layer turbulent transport," *Plasma Physics and Controlled Fusion*, vol. 64, 3 2022.

[201] O. E. Garcia, N. H. Bian, and W. Fundamenski, "Radial interchange motions of plasma filaments," *Physics of Plasmas*, vol. 13, 2006.

[202] J. R. Myra, D. A. Russell, D. A. D'Ippolito, J. W. Ahn, R. Maingi, R. J. Maqueda, D. P. Lundberg, D. P. Stotler, S. J. Zweben, J. Boedo, and M. Umansky, "Reduced model simulations of the scrape-off-layer heat-flux width and comparison with experiment," *Physics of Plasmas*, vol. 18, 1 2011.

[203] G. Dif-Pradalier, P. H. Diamond, V. Grandgirard, Y. Sarazin, J. Abiteboul, X. Garbet, P. Ghendrih, A. Strugarek, S. Ku, and C. S. Chang, "On the validity of the local diffusive paradigm in turbulent plasma transport," *Physical Review E - Statistical, Nonlinear, and Soft Matter Physics*, vol. 82, 3 2010.

[204] T. Tork, P. Manz, N. Bian, F. Reimold, G. Grenfell, C. Killer, and W. Zholobenko, "Estimation of turbulent transport coefficients by the conditional variance method," *Nuclear Fusion*, vol. 65, p. 016054, 1 2025.

[205] J. Hoffmann-Jorgensen, "Stable densities," *Theory of Probability and Its Applications*, vol. 38, pp. 350–355, 1994.

[206] V. M. Zolotarev, "On representation of densities of stable laws by special function," *Theory of Probability and its Applications*, vol. 39, pp. 197–362, 1995.

[207] K. Arias-Calluari, F. Alonso-Marroquin, and M. S. Harré, "Closed-form solutions for the lévy-stable distribution," *Physical Review E*, vol. 98, 7 2018.

Appendices

A Fractional Derivatives: An Introduction

Fractional calculus seems to be regarded as somewhat exotic by numerous physicists with whom I have spoken. I therefore present a compact explanation of the origin of fractional calculus, and would like to direct the reader to several authoritative books on the subject: First, "The Fractional Calculus" [191] which is very practical and approachable. Second, "Fractional Differential Equations" [192], which is both rigorous and comprehensive. Third, "An introduction to Fractional Calculus" [193], which is a more recent addition containing some additional results and applications. These sources are the basis of this appendix.

The fractional derivative is an operator which takes the concept of the integer-order derivative, and generalises it such that the derivative to any, arbitrary, non-integer order may be taken. This may sound strange. The fractional derivative may also be thought of as an operator, which, applied the inverse-order number of times, obtains the integer order derivative, such that:

$$\frac{d}{dx}f(x) \equiv \frac{d^{1/2}}{dx^{1/2}}\frac{d^{1/2}}{dx^{1/2}}f(x) \equiv \frac{d^{1/n}}{dx^{1/n}} \overset{n}{\cdot\cdot\cdot} \frac{d^{1/n}}{dx^{1/n}}f(x) \tag{297}$$

This is all well and good - however, specifying that the fractional derivative should possess this property, does not immediately give us an operator or function which calculates the fractional derivative. We must first find such an operator. To do this, a number of definitions of the fractional derivative have been created which satisfy the property in Eqn. 297. We consider one particular kind of fractional derivative first: the Reimann-Liouville fractional derivative. To arrive at the Riemann-Liouville fractional derivative, we first begin with fractional integration. The nth integral of a function may be written as:

$${}_aI_x^n f(x) = \int_a^x \int_a^{x_1} \overset{n}{\cdot\cdot\cdot} \int_a^{x_{n-1}} f(x_n)\, dx_n \overset{n}{\cdot\cdot\cdot} dx_1 \tag{298}$$

And due to Cauchy, if $f(x)$ is continuous in $[a, x]$ we may write:

$$ {}_aI_x^n f(x) = \frac{1}{(n-1)!}\int_a^x \frac{f(\zeta)}{(x-\zeta)^{1-n}}\, d\zeta \tag{299} $$

This form can be deduced by repeatedly integrating a test function of your choice, and may be proved for arbitrary $f(x)$ by induction. This may be generalised by using the definition of the Gamma function for positive integers:

$$ \Gamma(x) = (x-1)! \tag{300} $$

or, due to Bernoulli, for arbitrary x:

$$ \Gamma(x) = \int_0^\infty \zeta^{x-1}e^{-\zeta}\, d\zeta \tag{301} $$

...which extends the concept of the factorial. As such we may write:

$$ {}_aI_x^\alpha f(x) = \frac{1}{\Gamma(\alpha)}\int_a^x \frac{f(\zeta)}{(x-\zeta)^{1-\alpha}}\, d\zeta \tag{302} $$

Which is the Riemann-Liouville fractional integral for real α. It may be verified to be commutative, such that ${}_aI_{x\,a}I_x^\varphi f(x) =_a I_{x\,a}^\varphi I_x^\varsigma f(x) =_a I_x^{\varsigma+\varphi} f(x)$.

We may then use this to construct the Riemann-Liouville fractional derivative by taking the nth (integer) order derivative of the fractional integral:

$$ {}_aD_x^\alpha f(x) = \frac{d^n}{dx^n}\ {}_aI_x^{n-\alpha} f(x), \quad \alpha > 0 \quad n-1 < \alpha \leq n \tag{303} $$

This may be considered as taking the '$n-\alpha$'th fractional integral of $f(x)$, and then differentiating 'n' times, leaving us with a fractional derivative of α order. The non-local nature of the fractional derivative manifests here, as it has as an essential component the integral over the singular function, with the properties of the singularity controlled by α.

Continuing, it is important to ensure that when α is an integer, p, we end up with the integer-order derivative of $f(x)$. Using the inequalities restricting n in Eqn. 303, we may set $m \equiv \alpha + 1$, and so write the Riemann-Liouville left-fractional derivative:

$$ {}_aD_x^{\alpha} f(x) = \frac{1}{\Gamma(m-\alpha)} \frac{d^m}{dx^m} \int_a^x \frac{f(\zeta)}{(x-\zeta)^{\alpha+1-m}} \, d\zeta \tag{304} $$

And by switching the limits, we may obtain the right-fractional Riemann-Liouville derivative:

$$ {}_xD_b^{\alpha} f(x) = \frac{(-1)^m}{\Gamma(m-\alpha)} \frac{d^m}{dx^m} \int_x^b \frac{f(\zeta)}{(\zeta-x)^{\alpha+1-m}} \, d\zeta \tag{305} $$

For the purposes of this thesis, the most useful property is the Fourier transform, which we discuss in Appendix B.

It should be noted also that the Riemann-Liouville fractional derivative is not the sole definition - indeed there are a number of functions which posses the properties required to be a fractional difference operators. One definition of particular note is the Grunwald-Letnikov (GL) fractional derivative, which is essential for numerical purposes - and is possibly the most assumption-light forms of the fractional difference operator, as well as one of the earliest forms [191].

The essential intuition behind the GL fractional derivative is very simple - consider the fundamental definition of the derivative:

$$ f'(x) = \lim_{h \to 0^+} \frac{f(x+h) - f(x)}{h} \tag{306} $$

Then the second derivative is:

$$ f''(x) = \lim_{h \to 0^+} \frac{f'(x+h) - f'(x)}{h} \tag{307} $$

$$f''(x) = \lim_{h\to 0^+} \frac{\frac{f(x+2h)-f(x+h)}{h} - \frac{f(x+h)-f(x)}{h}}{h} \tag{308}$$

$$f''(x) = \lim_{h\to 0^+} \frac{f(x+2h) - 2f(x+h) + f(x)}{h^2} \tag{309}$$

One can continue this process indefinitely, and therefore find the GL derivative by induction:

$$f^n(x) = \lim_{h\to 0^+} \frac{1}{h^\alpha} \sum_{k=0}^{\infty} (-1)^k \binom{\alpha}{k} f(x-kh) \tag{310}$$

Which may also be written:

$${}_aD_x^{-p} f(x) = \lim_{h\to 0^+} \frac{1}{h^p} \sum_{k=0}^{\infty} \binom{p}{k} f(x-kh), \quad kh = x-a \tag{311}$$

Particularly useful is the theorem proved in ref. [196], which establishes that the Grünwald-Letnikov derivative is equivalent to the Cauchy formula for derivatives such that:

$$\lim_{h\to 0^+} \frac{1}{h^\alpha} \sum_{k=0}^{\infty} (-1)^k \binom{\alpha}{k} f(x-kh) = \frac{\Gamma(\alpha+1)}{2\pi i} \int_C f(\xi) \frac{1}{(\xi - x)^{\alpha+1}} \tag{312}$$

Or, equivalently, it may be shown [192] that:

$${}_aD_x^{-p} f(x) = \frac{1}{(p-1)!} \int_a^x (x-\xi)^{p-1} f(\xi) d\xi \tag{313}$$

And therefore there is a clear link between the GL definition and RL definition of the fractional differential operator, which may be exploited to develop numerical schemes.

B The Reisz Identity

We introduced the Reisz identity in Eqn. 218, and now discuss where it, and the Reisz derivative come from. The Reisz identity is:

$$FT^{-1}\{-|k|^{\alpha}\hat{f}(k)\} = D^{a}_{|x|}f(x) \tag{314}$$

Where $D^{\alpha}_{|x|}f(x)$ is the Reisz derivative, defined as:

$$D^{\alpha}_{|x|}f(x) = -\frac{1}{2cos\frac{\pi\alpha}{2}}\left[{}_{-\infty}D^{\alpha}_{x} +_{x} D^{\alpha}_{\infty}\right]f(x) \tag{315}$$

Where these come from, and why we should need these definitions, is not immediately obvious. Additionally, while the Reisz identity appears to be used occasionally, a search of the literature did not reveal a proof of it excepting what appears to be a circular proof. As such, here we provide a non-circular one.

Let us first define the Fourier transform:

$$\hat{f}(k) \equiv FT\{f(x)\}(k) \equiv \int_{-\infty}^{\infty} f(x)e^{-ikx}dx \tag{316}$$

Which has inverse:

$$f(x) \equiv FT^{-1}\{\hat{f}(k)\}(x) \equiv \frac{1}{2\pi}\int_{-\infty}^{\infty} \hat{f}(k)e^{ikx}dk \tag{317}$$

Then, we write G&R identity 17.23.25 [195]:

$$FT\{|x|^{\nu}\} = 2cos\left(\frac{\pi(\nu+1)}{2}\right)\Gamma(\nu+1)|k|^{-\nu-1}, \quad -1 < \nu < 0 \tag{318}$$

First let us find the inverse transform of $|k|^{\alpha-m}\hat{f}(k)$. The convolution theorem, written as:

$$FT\{f * g\} = \hat{f}(k)\hat{g}(k) = FT\{\int_{-\infty}^{\infty} f(\varepsilon)g(x-\varepsilon)d\varepsilon\} \tag{319}$$

Comes in useful, as in conjunction with Eqn. 318 and making the substitution that $-\nu-1 = \alpha - m$ we may then write:

$$FT^{-1}\{|k|^{\alpha-m}\hat{f}(k)\} = \frac{1}{2cos\left(\frac{\pi(m-\alpha)}{2}\right)}\frac{1}{\Gamma(m-\alpha)}\int_{-\infty}^{\infty}\frac{f(\xi)}{|x-\xi|^{\alpha+1-m}}d\xi \tag{320}$$

Note that selecting $-\nu - 1 = \alpha - m$ requires us to impose some specific requirements on α and m. First, we allow $\alpha \in \mathbb{R}$. Then, we require $m \in \mathbb{Z}$. Given the range of validity in Eqn. 318, this then requires $\alpha < m < \alpha + 1$ - or that m is the closest integer larger than α. We may separate the integral in Eqn. 320 as follows by using the properties of the absolute value function:

$$\int_{-\infty}^{\infty}\frac{f(\xi)}{|x-\xi|^{\alpha+1-m}}d\xi = \int_{-\infty}^{x}\frac{f(\xi)}{(x-\xi)^{\alpha+1-m}}d\xi + \int_{x}^{\infty}\frac{f(\xi)}{(\xi-x)^{\alpha+1-m}}d\xi \tag{321}$$

We may then write:

$$2cos\left(\frac{\pi(m-\alpha)}{2}\right)FT^{-1}\{|k|^{\alpha-m}\hat{f}(k)\} = \frac{1}{\Gamma(m-\alpha)}\int_{-\infty}^{x}\frac{f(\xi)}{(x-\xi)^{\alpha+1-m}}d\xi + \tag{322}$$

$$\frac{1}{\Gamma(m-\alpha)}\int_{x}^{\infty}\frac{f(\xi)}{(\xi-x)^{\alpha+1-m}}d\xi \tag{323}$$

At this point, please note the similarity of Eqn. 325 to the definitions of the Left- and Right- RL fractional derivatives, Eqns. 303 and 305. The key difference is then the m order derivative, which we have already implied we will use in our notation. Now:

$$FT\{\frac{d^m f'(x)}{dx^m}\} = (ik)^m\hat{f}'(k) \tag{324}$$

Then, if $\hat{f}'(k) = |k|^{\alpha-m}\hat{f}(k)$, we find (after some manipulation):

$$FT^{-1}\{|k|^{\alpha}\hat{f}(k)\} = \frac{1}{2cos\left(\frac{\pi(\alpha-m)}{2}\right)}\left[\frac{1}{\Gamma(m-\alpha)}\frac{d^m}{dx^m}\int_{-\infty}^{x}\frac{f(\xi)}{(x-\xi)^{\alpha+1-m}}d\xi\right. \tag{325}$$

$$\left.+\frac{1}{\Gamma(m-\alpha)}\frac{d^m}{dx^m}\int_{x}^{\infty}\frac{f(\xi)}{(\xi-x)^{\alpha+1-m}}d\xi\right. \tag{326}$$

Note that $\alpha - m$ is always ≤ 1, so strictly should feature in the definition of the Reisz derivative. This is not a problem provided one recalls that the coefficient should be positive for all use cases. This last equation then leads us naturally to the Reisz fractional derivative in Eqn. 315, with the transform property in Eqn. 314.

C Representation of the LαS Distribution as a Probability Density Function

The Levy-α Stable ($L\alpha S$) distribution was introduced in section 6.4, and repeated here:

$$L\alpha S(k;\alpha,\gamma,\beta,\delta) = \begin{cases} e^{-ik\delta}e^{-|\gamma k|^{\alpha}\left[1-i\beta\tan\frac{\pi\alpha}{2}sgn(k)\right]} & \alpha \neq 1 \\ e^{-ik\delta}e^{-|\gamma k|\left[1-i\frac{2}{\pi}\beta\log|k|sgn(k)\right]} & \alpha = 1 \end{cases} \tag{327}$$

The key feature is that the $L\alpha S$ is defined in Fourier space, and so is a complementary function (CF). Now, the CF may be understood as the Fourier transform of the probability density function (PDF) in general. What distinguishes the $L\alpha S$ distribution from other distributions is that it is defined by its CF primarily, rather than its PDF. The PDF therefore has to be found as follows:

$$PDF_{L\alpha S}(x) = FT^{-1}\{L\alpha S(k;\alpha,\gamma,\beta,\delta)\} \tag{328}$$

A closed form PDF for the $L\alpha S$ distribution - or at least an approximation - would be very useful to aid understanding, as it is a matter of convention to study PDFs of various

distributions. Numerous people have attempted to find an appropriate PDF of the $L\alpha S$ distribution, with some of the most recent results given by Hoffman-Jorgenson and Zolotarev [205, 206], and they have been very ingenious in the attempt - however the convergence of these representations are bad, in that they tend to suddenly vary either towards ∞ or $-\infty$. The most recent approach has addressed this problem specifically [207], and appears to return a reasonable approximation of the PDF of the $L\alpha S$ distribution which has appropriate convergence properties.

While this effort is important and significant, in practice, it is both trivial and useful to simply perform the inverse fast-Fourier transform (i.e. numerically invert) the $L\alpha S$ distribution to acquire the PDF. This is the approach adopted by the author.